The Eigenvalue Spectrum of the Fermion Matrix in Lattice Higgs Systems

Thesis by

David Henty

for the degree of

Doctor of Philosophy

Department of Physics and Astronomy,

University of Glasgow.

 September 1990.

To my family

Acknowledgements

I would like to thank my supervisor Christine Davies for her continual interest in my work and her informative and good natured advice throughout my studies. I would also like to thank Iain Barbour who has given me much enthusiastic and valuable guidance. I am grateful to the SERC for their financial support and also for the use of the IBM 3090-600E/VF and Cray X-MP/416 computers at the Atlas Centre, Rutherford Laboratory under grant GR/0095.2. Work was also done on Glasgow University's IBM 3090-150E/VF under the Kelvin Project supported by IBM.

The number of people who have helped to make my stay in Glasgow the most enjoyable of my academic career are too numerous to mention, but here goes. Thanks go to all my flatmates of the past three years for being such good company outside the confines of the department - Damascus, Haris, Jonathon and Panos who made settling in so easy and Anne, Graeme and Mandy for putting up with my erratic attendance at Airlie Street. I am forever grateful to Honda C90 GGT-307X for showing me round Glasgow at the outset, but mainly for coming off worst in our disagreement with Peugout NNS-292V. I would like to thank all my fellow theory students over the years for making the department such an enjoyable place in which to work and for making the lunchtime pool sessions so long. Special regards go to Zoheir for being such a good friend and office-mate. Last, but by no means least, I am grateful to Peigi both for having a flat and a washing machine and for looking after me so well.

Declaration

Except where specific reference is made to the work of others, this thesis has been composed by the author. It has not been accepted in any previous application for a degree. I further state that no part of this thesis has already been or is being submitted for any degree or qualification at any other university.

David Henty

Contents

Acknowledgements i

Declaration ii

Contents iii

Abstract vii

Chapter 1
Introduction

1.1 Field Theory and Path Integrals 1
1.2 Evaluation of the Path Integral 2
1.3 Lattice Regularisation 3
1.4 Gauge Theories 4
1.5 Lattice Fermions 5
1.6 Gauge Interactions 8
1.7 Simulation Techniques 9
1.7.1 Heatbath and Metropolis 9
1.7.2 Hybrid Monte Carlo 10

Chapter 2
Fermion Matrix Inversion

2.1 The Need for Efficient Fermion Matrix Inversion 12
2.2 The Conjugate Gradient Algorithm 13
2.3 The Lanczos Algorithm 14
2.4 Block Algorithms 15
2.4.1 The Block CG Algorithm 16
2.4.2 The Block LA Algorithm 17
2.5 Expected Advantages of the Block Forms 18

2.6 Inversion of the Kogut Susskind Fermion Matrix 20
2.6.1 Results on a 4^4 Lattice 22
2.6.2 Results on an 8^4 Lattice 25
2.7 Inversion of Diagonal Matrices 26
2.7.1 Results for Linear Eigenvalue Distributions 27
2.7.2 Results for Logarithmic Eigenvalue Distributions 28
2.8 Conclusions 29

Chapter 3
Lattice Higgs Models

3.1 The Continuum Higgs Mechanism 31
3.2 Lattice Higgs Systems 33
3.3 The Quenched Phase Diagram 36
3.4 Inclusion of Dynamical Fermions 38
3.5 The Crossover Region 39
3.6 The Ising Limit 41

Chapter 4
Quenched Simulations

4.1 The Model and its Symmetries 43
4.2 Simulating the Ising Model 44
4.3 The Fermion Matrix M 46
4.3.1 The Free Case 47
4.3.2 The Interacting Case 47
4.4 The Non-Hermitian Lanczos Algorithm 48
4.4.1 Use of Symmetries of M 50
4.4.2 Implementation in Real Arithmetic 52
4.4.3 Tests of Numerical Accuracy 53
4.5 The Eigenvalue Spectrum of M for Local Coupling 54
4.5.1 The PM Phase 55
4.5.2 The FM Phase 57
4.5.3 Coping with Degenerate Eigenvalues 58
4.5.4 The AFM Phase 59

4.6 The Eigenvalue Spectrum of M for Hypercubic Coupling 60
4.6.1 The PM Phase 60
4.6.2 The FM Phase 60
4.6.3 The AFM Phase 61
4.7 Obtaining m_f from the Eigenvalue Spectrum of M 61
4.8 Conclusions 62

Chapter 5
Fermion Masses with Local Coupling

5.1 Introduction 64
5.2 The Propagator Mass 65
5.3 Evaluation of the Lattice Propagator 66
5.4 The Condensate Mass 68
5.5 The M' Fermion Matrix 71
5.6 The Non-Hermitian Lanczos Algorithm for M' 74
5.7 The Eigenvalue Spectrum of M' 76
5.8 The Phase Diagram and the M' Condensate Mass 79
5.9 Numerical Results for the Fermion Mass 83
5.10 Conclusions 85

Chapter 6
The Quenched Infinite Volume Limit

6.1 Introduction 86
6.2 The Hermitian Lanczos Algorithm 86
6.2.1 Sturm Sequencing 87
6.2.2 Implementation for $M^\dagger M$ 89
6.2.3 Convergence of the Eigenvalues 90
6.3 Numerical Results 91
6.3.1 Behaviour of the Small Eigenvalues 92
6.3.2 The Density of Zero Modes 93
6.4 The Large κ Limit 94
6.5 Conclusions 96

Chapter 7
Dynamical Simulations

7.1	Introduction	97
7.2	Simulating the Dynamical Theory	99
	7.2.1 Rank Annihilation	100
	7.2.2 The Dynamical Heatbath Algorithm	101
	7.2.3 Numerical Details	102
7.3	Results at $\kappa = -0.15$	103
	7.3.1 The Eigenvalue Spectrum of M	106
7.4	Results for $\kappa > 0$	107
7.5	Comparison with Mean Field Theory	107
7.6	The Renormalised Fermion Mass	109
7.7	The PM1 / PM2 Phase Boundary	111
	7.7.1 The Eigenvalue Spectrum of M	112
7.8	Use of the Block Algorithm in Dynamical Simulations	113
7.9	Conclusions	115

Chapter 8
Conclusion 117

References 122

Abstract

In the first part of this thesis we consider the performance of various block algorithms for the inversion of large sparse matrices. By computing the eigenvalue spectra of the matrices under consideration we are able to directly relate the performance of the algorithms to the difficulty of the calculation. We find that the block Lanczos algorithm is superior to all others considered for the inversion of the Kogut Susskind fermion matrix. Furthermore we investigate the performance of the block Lanczos algorithm on matrices constructed to have specific eigenvalue spectra. From this study we are able to make quantitative predictive statements about the number of iterations that the algorithm will take to converge given the form of the eigenvalue spectrum of the matrix whose inversion is attempted.

The rest of this thesis is concerned with lattice Higgs systems. Specifically we study a model where staggered fermions are coupled to Ising spins via an on-site Yukawa term with coupling constant y. This is a very simple model that seems to embody most of the relevant phenomena observed in more complicated systems. Most importantly there are two symmetric regions PM1 and PM2 where the renormalised fermion mass m_f is non-zero for large y in the PM2 region despite the scalar field having zero expectation value. We study the model in the quenched approximation and by examining the distribution of the eigenvalues of the fermion matrix M in the complex plane we qualitatively explain the features of the model as being due to the transition of eigenvalues from the imaginary to the real axis via the origin as y is increased. An approximate method for calculating m_f from the value of a fermion condensate is developed and we reproduce the values for m_f obtained by other authors who calculate it using the standard method involving the fermion propagator. However, our method has the advantage that it is applicable on very small volumes where the propagator definition breaks down. We investigate the behaviour in the quenched infinite volume limit by evaluating the low lying

eigenvalues of the matrix $M^\dagger M$. We show that the small eigenvalues observed in the spectrum of M at intermediate y on finite lattices imply that there is a finite density of zero modes in the infinite volume limit.

By performing dynamical simulations on a small lattice we determine the phase diagram of the model and demonstrate the validity of mean field calculations of the phase boundaries. From calculations of m_f we identify the PM1 and PM2 phases. It is shown that the inclusion of fermion dynamics eliminates the small eigenvalues of M present in the quenched model and as y is increased the eigenvalues now transfer from the real to imaginary axis via a path avoiding the origin. It is only by using the block Lanczos algorithm that simulations in certain regions of the phase plane are feasible, and only by our method of considering a fermion condensate can we calculate m_f on such a small volume.

Chapter 1

Introduction

1.1 Field Theory and Path Integrals

The aim of any calculational technique in quantum field theory is to compute the expectation value of some operator $\hat{O}$ over a representative ensemble of field configurations generically denoted $\{\phi\}$. By an analogy with ordinary 1-D quantum mechanics first exploited by Feynman [1] we can write this expectation value as

$$<\hat{O}> = \frac{1}{Z} \int \{d\phi\}\, \hat{O}\{\phi\}\, exp\,(\frac{2\pi i}{h} S\{\phi\}\,) \tag{1.1}$$

$$Z = \int \{d\phi\}\, exp\,(\frac{2\pi i}{h} S\{\phi\}\,) \tag{1.2}$$

where $\{d\phi\}$ is some measure on the space of the field variables, $S\{\phi\}$ is the action which is a real valued function of the field and its spatial and temporal derivatives and Z is the partition function. It is the action which defines the field theory and gives the equations of motion via the action principle (from now on we work in units where $h/2\pi = c = 1$, and it will be dimensionless). We can write the action as a four dimensional integral

$$S\{\phi\} = \int d^4x\; L\,(x) \tag{1.3}$$

where $L(x)$ is the Lagrangian density.

As it stands eqns. 1.1 and 1.2 are purely formal due to the oscillatory nature of the integrand. By continuing to imaginary time $\tau = i\,t$ and by performing a Wick rotation of $\frac{\pi}{2}$ so that the τ integration lies along the real axis we can write 1.3 as

$$S\{\phi\} = i \int d^4x\; L_E\,(x) = i\, S_E\,\{\phi\} \tag{1.4}$$

where L_E and S_E are the Euclidean space Lagrangian and action respectively. We can now write our defining formula for calculating $<\hat{O}>$ as

$$<\hat{O}> = \frac{1}{Z} \int \{d\phi\}\, \hat{O}\{\phi\}\, exp\,(-S_E\{\phi\}) \tag{1.5}$$

$$Z = \int \{d\phi\}\, exp\,(-S_E\{\phi\}) \tag{1.6}$$

From now on we work exclusively in Euclidean space and omit the subscript 'E'.

1.2 Evaluation of the Path Integral

For the sake of definiteness let us consider a real scalar field theory with a Lagrangian made up of a free and interacting part $L = L_0 + L_I$ where

$$L_0 = \frac{1}{2}\, \partial_\mu \phi\, \partial^\mu \phi + m^2 \phi^2 + J\phi \tag{1.7}$$

$$L_I = \frac{\lambda}{4!} \phi^4 \tag{1.8}$$

For $\lambda = 0$ we can evaluate eqn. 1.6 exactly and by continued differentiation with respect to the source term J can compute the time ordered products of field variables necessary to calculate scattering amplitudes in this (non-interacting) theory. We can successively improve this calculation to any order in the coupling λ by expanding the term $\exp(-S_I)$ as a power series in λ. Although this is a perfectly rigorous technique for any renormalisable theory, it can obscure the real non-perturbative physics which may not be accessible via any finite order expansion. Indeed, although we can 'solve' eqn. 1.5 to many orders and calculate non-zero scattering amplitudes, non-perturbative studies indicate complete charge screening at long distances giving a non-interacting physical theory.

There are many other ways to evaluate eqn 1.5, for example mean field and saddle point techniques. However, the method on which this thesis rests is based on the observation that eqn. 1.5 is formally equivalent to the expression in statistical mechanics for the equilibrium value of some thermodynamic quantity $F\{\phi\}$

$$<F> = \frac{1}{Z} \int \{d\phi\}\, F\{\phi\}\, \exp(-\beta\, H\{\phi\}) \tag{1.9}$$

where the inverse temperature β is set to unity and we identify the Euclidean space action with some Hamiltonian H defined on a four dimensional space. This equivalence of our 3+1 dimensional field theory with a 4 dimensional statistical system allows us to use all the calculational techniques developed in statistical mechanics. Our approach will be to define the theory on a 4-D hypercubic lattice with lattice spacing 'a' and evaluate eqn. 1.5 on a computer. We will hope to retrieve the continuum theory by taking the $a \rightarrow 0$ infinite volume limit in some controlled fashion.

1.3 Lattice Regularisation

Our discretisation scheme for eqns. 1.7 and 1.8 will be a very simple one. We only define ϕ on lattice sites labelled by some integers n_μ, $\mu = 0,1,2,3$ and make the substitutions

$$\phi(x) \rightarrow \phi(n) \tag{1.10}$$

$$\partial_\mu \phi(x) \rightarrow \frac{1}{a} \left(\phi(n+\mu) - \phi(n) \right) \tag{1.11}$$

$$\int d^4x \rightarrow a^4 \sum_n \tag{1.12}$$

where $n+\mu$ is the neighbouring site to n in the μ^{th} direction. Such a scheme preserves the discrete Z(2) symmetry $\phi(x) \rightarrow - \phi(x)$ of the original action (and would also preserve the global U(1) symmetry of the corresponding theory with a complex scalar field). This lattice implementation of the continuum symmetry is trivial in this simple example, but will be a crucial consideration when discretising theories with gauge fields and/or fermions.

From now on we will work in units where $a = 1$ and all quantities are dimensionless. If we transform to momentum space, the variables $\phi(p)$ are only defined within the first Brillouin zone $-\pi < p \leq \pi$. This illustrates how the lattice acts as a momentum cutoff and controls ultra-violet divergences. In addition we can control infra-red divergences by having antiperiodic boundary conditions in at least one direction such that $|p| \geq \frac{\pi}{L}$ where L is the extent of the lattice in that direction.

We have obviously broken the O(4) rotational invariance of the original Euclidean action, but we would hope to retrieve this in the continuum limit.

Having defined the theory on a finite set of field variables via eqns. 1.10, 1.11 and 1.12 we can attempt to evaluate eqn 1.5 on a computer using one of the standard techniques described below.

1.4 Gauge Theories

Any continuum gauge theory will be invariant under some set of local gauge transformations of the field variables. For an SU(N) Yang-Mills theory the euclidean action is

$$S\{A_\mu\} = \frac{1}{2} Tr\,(F_{\mu\nu}F_{\mu\nu}) \tag{1.13}$$

$$F_{\mu\nu} = \partial_\mu A_\nu - \partial_\nu A_\mu - i\,g\,[\,A_\mu, A_\nu] \tag{1.14}$$

where $A^\mu(x) \in$ SU(N). The gauge transformation is

$$A_\mu(x) \rightarrow U(x)\,\{\,A_\mu(x) - \frac{i}{g}\partial_\mu\,\}\,U^{-1}(x) \tag{1.15}$$

where $U(x) \in$ SU(N). It is this invariance that leads to certain Ward identities that make the theory renormalisable. If any regularisation scheme violates these symmetries then it will be plagued by uncontrollable divergences. Unfortunately, a naive discretisation such as eqns. 1.10 to 1.12 only preserves gauge invariance to lowest order in 'a' for a non-abelian gauge group (ie N>1) and the violation of the Ward identities will make it impossible to take the limit $a \rightarrow 0$ in a smooth manner.

Wilson [2] proposed an action built out of plaquette variables $P_{\mu\nu}$ which on the lattice take the form

$$U_\mu(n) = exp\,(\,i\,a\,g\,A_\mu(n)\,) \tag{1.16}$$

$$P_{\mu\nu}(n) = U_\mu(n)\,U_\nu(n+\mu)\,U_\mu^\dagger(n+\mu)\,U_\nu^\dagger(n) \tag{1.17}$$

The trace of this quantity is invariant under the lattice gauge transformation

$$U_\mu(n) \rightarrow V(n)\,U_\mu(n)\,V^\dagger(n+\mu) \tag{1.18}$$

where $V(n) \in$ SU(N) and hence $V(n)^\dagger V(n) = 1$. The Wilson action Sw is

$$S_W = -\frac{\beta}{N}\sum_{P_{\mu\nu}} Re\,(Tr\,(P_{\mu\nu}(x))) \tag{1.19}$$

where $\beta = \frac{2N}{g^2}$. This reproduces the continuum action 1.13 to leading order in 'a' and has an exact gauge invariance due to the compact nature of the variables U_μ.

We have absorbed all dimensionful parameters by re-scaling fields and coupling constants. Our only variable is the coupling β, so to set the scale of 'a' we must measure at least one physical dimensionful quantity in units of 'a' and compare to the real world. Such a quantity could be the nucleon mass or the string tension for SU(3). In the case of non-abelian gauge theories, asymptotic freedom indicates that the $a \to 0$ limit is achieved by taking $g^2 \to 0$ but the situation may not be so clear for other theories. Without asymptotic freedom the theory defined around zero bare coupling may well be free at long distances. This situation is believed to arise for the scalar field theory of eqns. 1.7 and 1.8. Unless a fixed point other than the Gaussian one exists the theory may well only be an effective one, valid down to some finite minimum lattice spacing 'a'.

1.5 Lattice Fermions

The continuum Lagrangian for one flavour of free fermion is

$$L = \overline{\Psi}\,\gamma_\mu\,\partial^\mu\,\Psi + m\,\overline{\Psi}\Psi \tag{1.20}$$

where Ψ is a four component Dirac spinor and γ_μ are the usual gamma matrices. An important symmetry of the action at $m = 0$ is the chiral one

$$\Psi_L^R \to exp\,(i\,\alpha_L^R)\,\Psi_L^R \tag{1.21}$$

$$\overline{\Psi}_L^R \to \overline{\Psi}_L^R\,exp\,(-i\,\alpha_R^L) \tag{1.22}$$

where $\Psi_L^R = \frac{1}{2}(1\pm\gamma_5)\,\Psi$. We would like to retain this in our lattice theory. If we make the replacement

$$\partial_\mu\,\Psi(x) \to \frac{1}{2}\,(\,\Psi(n+\mu) - \Psi(n-\mu)\,) \tag{1.23}$$

where we take a central difference to maintain anti-hermiticity at $m = 0$, we can write the fermionic action as

$$S = \sum_n \sum_\mu \frac{1}{2}(\overline{\Psi}(n)\gamma_\mu\Psi(n+\mu) - \overline{\Psi}(n)\gamma_\mu\Psi(n-\mu)) + m\,\overline{\Psi}(n)\Psi(n) \quad (1.24)$$

This action has the full continuum chiral symmetry. However, it suffers from the infamous fermion doubling problem. This is evident if we transform to momentum space and calculate the inverse propagator $S^{-1}(p)$ at $m = 0$

$$S^{-1}(p) = \sum_{p_\mu} \sum_\mu i\,\gamma_\mu\, sin(p_\mu) \quad (1.25)$$

We will have a pole in the propagator not only at $p = 0$ but at all $2^D = 16$ points where $p_\mu = 0$ or π. Hence there will be 16 physical fermions in our lattice theory.

There are two standard solutions to this problem. As mentioned above we would like to retain the continuum chiral symmetry, but this cannot be done by a reasonable action without species doubling due to the no-go theorems of Nielsen and Ninomiya [3]. One procedure is due to Wilson [4] where we add to the action a second derivative term proportional to the arbitrary Wilson parameter r. Although irrelevant in the naive continuum limit, this term removes the unphysical poles at $p_\mu = \pi$ leaving one propagating fermion in the spectrum. The action is now

$$S = -\kappa \sum_n \sum_\mu \overline{\Psi}(n)\,(r-\gamma_\mu)\,\Psi(n+\mu) + \overline{\Psi}(n+\mu)\,(r+\gamma_\mu)\,\Psi(n)$$

$$+ \sum_n \overline{\Psi}(n)\Psi(n) \quad (1.26)$$

where the hopping parameter κ is given in this free theory by $\kappa^{-1} = (2m+8r)$.

The price we pay is the explicit breaking of the chiral symmetry at $m = 0$ and in addition we have to sweep in κ to find this massless limit (at $\kappa = \kappa_c$) when gauge interactions are included. All that is known a priori about this critical value of the hopping parameter is that, for $r = 1$, it lies between the weak and strong coupling limits of $\frac{1}{8}$ and $\frac{1}{4}$ respectively [5].

The solution we will adopt is due to Kogut and Susskind [6] and relies on thinning the degrees of freedom to reduce the number of continuum species. If we make a judicious choice of a change of variables in eqn. 1.24 via the unitary transformations [7]

$$\Psi(n) \rightarrow A(n)\,\chi(n) \tag{1.27}$$

$$\overline{\Psi}(n) \rightarrow \overline{\chi}(n)\,A^{\dagger}(n) \tag{1.28}$$

$$A(n) = \gamma_0^{n0}\,\gamma_1^{n1}\,\gamma_2^{n2}\,\gamma_3^{n3} \tag{1.29}$$

then the the action becomes diagonal in spin space and the only remnant of the γ matrices is a site dependent phase $\alpha_\mu(n)$. We retain only one of the 4 decoupled fermion actions by considering only one of the components of χ. The staggered fermion action can then be written

$$S = \sum_n \sum_\mu \frac{1}{2}\left(\alpha_\mu(n)\,\overline{\chi}(n)\,\chi(n+\mu) - \alpha_\mu(n-\mu)\,\overline{\chi}(n)\,\chi(n-\mu) \right) + m\,\overline{\chi}(n)\chi(n)$$

$$\alpha_\mu(n) = (-1)^{n_0 + n_1 + \ldots\ n_{\mu-1}} \tag{1.30}$$

The operators of our theory can be written in terms of the single component anti-commuting χ fields by using the transformation laws in eqns. 1.27 to 1.29. This unfortunately gives rise to rather complicated meson and baryon operators [8]. The continuum chiral symmetry is replaced by the symmetry

$$\chi_O^E \rightarrow exp\,(\,i\,\alpha_O^E\,)\,\chi_O^E \tag{1.31}$$

$$\overline{\chi}_O^E \rightarrow \overline{\chi}_O^E\,exp\,(-i\,\alpha_E^O\,) \tag{1.32}$$

The subscripts 'E' and 'O' refer to the fields on even and odd lattice sites n where $(-1)^{n0+n1+n2+n3} = +1$ or -1 respectively. This indicates that the chiral degrees of freedom are distributed over different sites of our lattice and that χ fields on neighbouring sites have opposite chiralities. A mass term forces $\alpha_E = \alpha_O$ by coupling even to even and odd to odd sites. This is a consequence of the fact that a mass term in the continuum Lagrangian forbids independent rotations of the left and right handed fermionic components by coupling right to right and left to left modes.

As opposed to the Wilson formulation (eqn. 1.26) we have a lattice symmetry that is a remnant of the continuum chiral symmetry, even for finite lattice spacing.

Since the need for the Higgs mechanism in the standard model is a result of the chiral nature of the electroweak couplings we will use the staggered formulation throughout to allow us to study chiral fermionic properties.

1.6 Gauge Interactions

The gauge transformation on the fermionic χ fields (which still carry a colour SU(N) index) is

$$\chi(n) \rightarrow V(n)\,\chi(n) \tag{1.33}$$

$$\overline{\chi}(n) \rightarrow \overline{\chi}(n)\,V^{\dagger}(n) \tag{1.34}$$

where $V(n) \in$ SU(N). Since the staggered action (eqn. 1.30) only couples nearest neighbour sites, and noting the gauge transformation on the gauge fields (eqn. 1.18), it is evident that if we replace all terms in the action of the form $\overline{\chi}(n)\,\chi(n+\mu)$ by $\overline{\chi}(n)\,U_{\mu}(n)\,\chi(n+\mu)$ then the resulting expression will be gauge invariant. This prescription is equivalent to the minimal coupling prescription used in continuum field theory.

By writing the action in the form $\overline{\chi}(m)M_{KS}(m,n)\chi(n)$ we arrive at the following form for the Kogut Susskind fermion matrix

$$M_{KS}(m,n) = \frac{1}{2}\sum_{\mu} \alpha_{\mu}(m)\,U_{\mu}(m)\,\delta_{n,\,m+\mu} - \alpha_{\mu}(m-\mu)\,U_{\mu}^{\dagger}(m-\mu)\,\delta_{n,\,m-\mu} + m\,\delta_{m,n} \tag{1.35}$$

Since the Grassmann nature of the χ fields is not easily implemented on a computer we integrate out the fermions fields analytically to obtain an effective action for the theory that depends only on the gauge degrees of freedom $\{U_{\mu}\}$

$$S_{EFF}\{U_{\mu}\} = S_{W}\{U_{\mu}\} + Tr\,(\,ln\,(M_{KS}\{U_{\mu}\}\,)\,) \tag{1.36}$$

Fermion observables can be written in terms of the fermion matrix. For example, the two point function is given by

$$\langle \overline{\Psi}_i \Psi_j \rangle = \frac{1}{Z}\int \{dU_{\mu}\}\,M_{KS}^{-1}(j,i)\,exp\,(\,-S_{EFF}\{U_{\mu}\}\,) \tag{1.37}$$

1.7 Simulation Techniques

Having defined our theory on a lattice we require a method of generating field configurations $\{\phi\}$ in order to evaluate eqn. 1.5. On anything but the smallest discrete systems it is impossible to average over all configurations. If we were to generate configurations with equal probability we could average the value of an operator weighted by the Boltzmann factor $\exp(-S\{\phi\})$ over many different $\{\phi\}$. However, most of these would have such a large exponential suppression as to make their contribution to the average negligible. Such a procedure would take a prohibitively long time to implement. Only those configurations close to a minimum of $S\{\phi\}$ have a significant weight, and it is this observation that leads us to importance sampling. In this approach we generate configurations with the required probability distribution $P\{\phi\} = exp(-S\{\phi\})$ and the expectation value of some operator $\hat{O}$ becomes a simple average over a large number N of independent configurations $\{\phi\}_i$.

$$< \hat{O} > = \frac{1}{N} \sum_{i=1}^{N} \hat{O}\{\phi\}_i \tag{1.38}$$

To generate such a set $\{\phi\}_i$ it is sufficient to have an updating scheme that takes $\{\phi\} \rightarrow \{\phi'\}$ whilst ensuring that the conditions of detailed balance are satisfied, ie

$$\frac{P(\{\phi\} \rightarrow \{\phi'\})}{P(\{\phi'\} \rightarrow \{\phi\})} = \frac{exp(-S\{\phi\})}{exp(-S\{\phi'\})} \tag{1.39}$$

The only condition is that the update must be ergodic.

1.7.1 Heatbath and Metropolis

To use a heatbath algorithm we must be able to compute analytically the probability distribution for a give field variable ϕ_n while the background set of all other fields $\{\phi_0\} = \{\phi\} - \phi_n$ is held constant. If we know the value of

$$P(\{\phi_n, \phi_0\}) = \frac{exp(-S\{\phi_n, \phi_0\})}{\int d\phi_n \; exp(-S\{\phi_n, \phi_0\})} \tag{1.40}$$

then we can choose a new ϕ_n with exactly the required probability at each update.

If we cannot evaluate eqn. 1.40 then an alternative is to use the Metropolis algorithm [9]. We propose small random changes ('hits') to some ϕ_n in the original configuration $\{\phi\}$ and accept the new configuration $\{\phi'\}$ with probability

$$P(\{\phi\} \rightarrow \{\phi'\}) = min [1 , exp (- (S\{\phi'\}-S\{\phi\}))] \qquad (1.41)$$

This procedure satisfies eqn. 1.39, the drawback being that if our proposed changes increase the action too much then none will be accepted. In the limit of an infinite number of hits the Metropolis algorithm becomes identical to the heatbath algorithm, ie we are numerically evaluating the integral 1.39.

1.7.2 Hybrid Monte Carlo

The problem with the heatbath and Metropolis and heatbath algorithms is that it is necessary to evaluate the the new action $S\{\phi'\}$ for each local field update. When fermions are included this is prohibitively costly in computer time except for extremely small lattice volumes. The reason is that the highly non-local nature of the fermion contribution to the effective action, $Tr(ln(M_{KS}))$, makes a global re-evaluation of S necessary even for local field changes. What is required is a method of choosing global updates to the lattice which have a reasonable acceptance probability via eqn. 1.41. To do this we construct a Hamiltonian $H = P^2/2 + L$ from our original Lagrangian and then define a new action S' which is the volume integral of this Hamiltonian. Our partition function is defined as

$$Z = \int \{dP\} \{d\phi\} exp (- S'\{P,\phi\}) \qquad (1.42)$$

which coincides with eqn. 1.2 due to the trivial nature of the momentum integration. However, if we propose field changes by evolving the system $\{P,\phi\}$ in some fictitious time τ with time step $d\tau$ using some molecular dynamics algorithm [10] which preserves the 'energy' function S' we can move quickly through phase space and yet still have a good acceptance rate via eqn 1.41. In such a scheme the fermionic contribution to S need only be calculated once per entire sweep of the lattice which amounts to a huge saving in computer time. To ensure

Chapter 2

Fermion Matrix Inversion

2.1 The Need for Efficient Fermion Matrix Inversion

In any dynamical updating algorithm it is necessary to calculate columns of the inverse lattice Dirac operator M^{-1} to include the effects of fermion loops. It is the efficiency with which this is performed that limits the speed at which independent field configurations can be generated. Even in quenched simulations an efficient inversion algorithm is often required to calculate particle masses from the decay of the associated propagator or to estimate the value of the chiral condensate $<\overline{\Psi}\Psi>$.

It is frequently useful to calculate several columns of the inverse simultaneously. This occurs when all the columns of M^{-1} on a given site corresponding to different colours and spins are required for a hadron propagator, and also in updating algorithms [12] where the change in some link variable changes several columns of M^{-1}. A calculation of the action of M^{-1} on multiple vectors is also useful to obtain improved estimates of the chiral condensate [13].

Motivated by this we investigate an important generalisation of the standard inversion algorithms which is to write them in 'block' form [14, 15]. A block algorithm with block size B can be used to obtain B columns of M^{-1} simultaneously. The scalar variables in the algorithm, typically the coefficients in the expansion of the solution as a sum of orthogonal vectors, are replaced by **full** square matrices of dimension B. The vectors of length N are replaced by matrices of dimension $N \times B$ which we shall refer to as block vectors.

First we briefly describe the standard implementations of the algorithms under consideration. All the algorithms are iterative which is essential for such a large matrix. At each iteration step the current approximation to the solution is improved by some linear update. The matrix M itself only appears when multiplying a vector which allows us to take full advantage of its sparse nature.

2.2 The Conjugate Gradient Algorithm

The conjugate gradient (CG) algorithm [16] is used to solve the equation

$$H\psi = \eta \tag{2.1}$$

for ψ where η is known and H is some hermitian positive definite matrix. We shall assume without any loss of generality that $|\eta|^2 = 1$ throughout. The CG algorithm is derived by noting that solving eqn. 2.1 is equivalent to minimising the scalar functional

$$F(\psi) = \frac{1}{2}(\psi, H\psi) - (\eta, \psi) \tag{2.2}$$

where (u,v) is the inner product of the vectors u and v. This is obvious since

$$\frac{\partial F(\psi)}{\partial \psi} = 0 \quad \Rightarrow \quad H\psi - \eta = 0 \tag{2.3}$$

The simplest choice for minimising F would be some steepest descent algorithm where at each iteration we update our approximate solution ψ_i by the equation

$$\psi_{i+1} = \psi_i + \lambda_i \nabla F(\psi_i) \tag{2.4}$$

where λ_i is chosen to minimise F along the local direction of the gradient. This is, however, a very bad choice [17]. Each update to the solution is orthogonal only to its immediate predecessor and this can mean that we minimise along a given direction many times before reaching the required solution. Due to this the algorithm may take many iterations to traverse small distances if there are long shallow 'valleys' in F (see fig. 2.1). What is required is a procedure that remembers the prior directions of minimisation and if possible chooses a new direction orthogonal them all.

In the CG algorithm we allow more freedom in the updating of ψ_i to implement this. We update according to

$$\psi_{i+1} = \psi_i + \lambda_i p_i \tag{2.5}$$

$$p_{i+1} = \alpha_i p_i + \nabla F(\psi_i) \tag{2.6}$$

and choose α_i and λ_i such that

$$(p_{i+1}, Hp_i) = 0 \tag{2.7}$$

$$(\nabla F(\psi_{i+1}), \nabla F(\psi_i)) = 0 \tag{2.8}$$

The remarkable fact is that this choice ensures that eqns. 2.7 and 2.8 hold not only locally but also globally for any pairs p_i, p_j and ψ_i, ψ_j (the proof is a simple inductive one). This then implies that for some $j \leq N$, $\nabla F(\psi_j) = 0$. Eqn. 2.3 will then be satisfied and ψ_j will be the required solution ψ.

In exact arithmetic the CG algorithm will converge in at most N iterations. This is achieved by ensuring the H-orthogonality of the minimisation directions (eqn. 2.7) and the orthogonality of the 'residuals' $H\psi_i - \eta$ (eqn. 2.8).

2.3 The Lanczos Algorithm

The Lanczos (LA) algorithm [18] has a completely different philosophy to the CG algorithm. It was originally developed to extract the eigenvalues of large sparse matrices, but can be readily modified to solve equations of the form of eqn. 2.1. We attempt to transform the hermitian (but not necessarily positive definite) matrix H into a symmetric tridiagonal form T using a unitary matrix X, ie. we attempt to solve

$$X^{\dagger} H X = T \tag{2.9}$$

We write X as a series of N column vectors x_i (the Lanczos vectors) which are mutually orthonormal due to the unitarity of X. T is written as

$$\begin{vmatrix} \alpha_1 & \beta_1 & 0 & 0 & . & . & 0 \\ \beta_1 & \alpha_2 & \beta_2 & 0 & . & . & 0 \\ 0 & \beta_2 & \alpha_3 & \beta_3 & . & . & 0 \\ 0 & 0 & \beta_3 & \alpha_4 & . & . & 0 \\ . & . & . & . & . & . & 0 \\ . & . & . & . & . & \alpha_{N-1} & \beta_{N-1} \\ 0 & 0 & 0 & 0 & 0 & \beta_{N-1} & \alpha_N \end{vmatrix} \tag{2.10}$$

The LA algorithm rests on the observation that all the x_i, α_i and β_i^2 are uniquely determined once one of the Lanczos vectors (x_1 say) has been arbitrarily chosen subject only to the normalisation condition $x_1^{\dagger} x_1 = 1$. The resulting recurrence

relations for x_i, α_i and β_i ensure that the Lanczos vectors are mutually orthonormal and that α_i and β_i are real.

The solution of eqn. 2.1 via the LA algorithm consists of using the x_i as a basis in which to expand the required solution ψ having first set $x_1 = \eta$ [19]. Despite the very different philosophies behind the two algorithms it is well known [19, 20] that they are equivalent for a given hermitian positive definite matrix H. This means that they will give exactly the same solution vector step by step in exact arithmetic. However, rounding errors on a computer will make the the two methods inequivalent in practice.

2.4 Block Algorithms

As mentioned above, it is often necessary to solve eqn. 2.1 several times for different sources η but for the same matrix H. Suppose we require the solution to a set of B equations of the form

$$H\psi_n = \eta_n , \quad n = 1,2 \ldots B \tag{2.11}$$

We could achieve this by running the standard LA or CG algorithm B times. We can however solve eqns. 2.11 by using a block algorithm with block size B. To do this we write the vectors ψ and η as block vectors of dimension $N \times B$. The B columns of the block vector η are set equal to the η_n. When the block algorithm has converged the columns of the block solution vector ψ will be the required solution vectors ψ_n.

It is quite straight forward to obtain the block forms of the CG and LA algorithms. The only complication is that what were previously scalar variables are now square matrices and do not commute. The order of these variables now matters. For the CG algorithm the required ordering is the one that preserves eqns. 2.7 and 2.8 for the block vectors. For the LA algorithm, one imagines transforming the matrix H of eqn. 2.9 into a block tridiagonal form T such that the α_i and β_i in eqn. 2.10 are square matrices of dimension B. Note that in the block form it is $\beta^\dagger$ that appears below the diagonal to preserve the hermiticity of T.

Having obtained the block forms we require some scalar variable to monitor the progress of the algorithm. In the single ($B = 1$) algorithms the norm of the solution vector and the norm of the residue vector $r_i = \eta - H\psi_i$ are used. For the block algorithms we take the norm of an $N \times B$ block vector to be

$$norm(v) = \sqrt{\frac{Trace(v^\dagger v)}{B}} \tag{2.12}$$

which is the RMS norm for all the single vectors in the block. This ensures that the norm of the residue is dominated by those solution vectors in the block solution that have converged the least.

The residue will be small when the algorithm has converged but $|r_i|$ is not necessarily a good estimator of the error in the solution. This is because the residue is insensitive to those components of ψ_i which are eigenvectors of H with small eigenvalue. We always run until $|r_i| <<$ smallest eigenvalue of H and there is a long plateau in $|\psi_i|$ so this does not concern us. It is however an important consideration when deciding on a stopping condition for an implementation of the algorithms within some real simulation [21].

2.4.1 The Block CG Algorithm

The block version of the CG algorithm used to solve $H\psi = \eta$ comprises the following iterative scheme [15]:

$$r_{i+1} = r_i - H p_i a_i \tag{2.13}$$

$$p_{i+1} = p_i b_i + r_{i+1} \tag{2.14}$$

$$\psi_{i+1} = \psi_i + p_i a_i \tag{2.15}$$

$$a_i = (p_i^\dagger H p_i)^{-1} (r_i^\dagger r_i) \tag{2.16}$$

$$b_i = (r_i^\dagger r_i)^{-1} (r_{i+1}^\dagger r_{i+1}) \tag{2.17}$$

$$p_1 = r_1 = \eta - H\psi_1 \tag{2.18}$$

r, p and ψ are $N \times B$ block vectors and a and b are $B \times B$ matrices. ψ_1 is arbitrary and taken to be the null vector, r_i is the residue $\eta - H\psi_i$ whose norm we check for convergence. The vectors r_i and p_i satisfy the following important

relationships

$$r_i^\dagger r_j = 0 \quad for\ i \neq j. \tag{2.19}$$

$$(p_i, Hp_j) = 0 \quad for\ i \neq j. \tag{2.20}$$

By rewriting eqn. 2.11 in the form $M^\dagger M\psi = M^\dagger\eta$, the usual CG algorithm can be modified to calculate columns of the inverse of the non-hermitian fermion matrix M. The algorithm (MDMCG) is

$$r_{i+1} = r_i - M p_i a_i \tag{2.21}$$

$$p_{i+1} = p_i b_i + M^\dagger r_{i+1} \tag{2.22}$$

$$\psi_{i+1} = \psi_i + p_i a_i \tag{2.23}$$

$$a_i = ((M p_i)^\dagger (M p_i))^{-1} (M^\dagger r_i)^\dagger (M^\dagger r_i) \tag{2.24}$$

$$b_i = ((M^\dagger r_i)^\dagger (M^\dagger r_i))^{-1} (M^\dagger r_{i+1})^\dagger (M^\dagger r_i) \tag{2.25}$$

$$p_1 = M^\dagger r_1,\ r_1 = \eta - M\psi_1 \tag{2.26}$$

ψ_1 is arbitrary and taken to be the null vector, r_i is the residue $\eta - M\psi_i$.

2.4.2 The Block LA algorithm

The recurrence relations for the block Lanczos vectors x_i which are the columns of some unitary matrix are

$$\alpha_i = x_i^\dagger H x_i \tag{2.27}$$

$$U_i = Hx_i - x_{i-1}\beta_{i-1}^\dagger - x_i \alpha_i \tag{2.28}$$

$$\beta_i^\dagger \beta_i = U_i^\dagger U_i \tag{2.29}$$

$$x_{i+1} = U_i \beta_i^{-1} \tag{2.30}$$

where U_i and x_i are both $N \times B$ block vectors and α_i and $\beta^2{}_i$ are $B \times B$ hermitian matrices. The initial Lanczos vector must satisfy $x_1{}^\dagger x_1 = 1$ and we take $\beta_0 = 0$. Eqn. 2.29 only defines $\beta^2{}_i$ whereas eqn. 2.30 requires β_i itself. We can choose the β_i to be upper triangular with real diagonal elements, and they can then be readily extracted from eqn. 2.29 by a simple iterative procedure.

It is important to note that only the α_i will change for matrices H that differ

solely by the addition of a multiple of the identity matrix. The Lanczos vectors themselves and the β_i will remain unaltered. This has some useful consequences described below. The Lanczos vectors satisfy the orthonormality condition

$$x_i^\dagger x_j = \delta_{i,j} \tag{2.31}$$

Having generated this orthonormal set we can construct the solution to eqn. 2.11 in the following iterative procedure:

$$A_{k+1} = -\alpha_{k+1}(\beta_k^{-1})^\dagger A_k + B_k \tag{2.32}$$

$$B_{k+1} = -\beta_{k+1}(\beta_k^{-1})^\dagger A_k \tag{2.33}$$

$$y_{k+1} = y_k + A_{k+1}^{-1} t_k \tag{2.34}$$

$$t_{k+1} = -B_{k+1}A_{k+1}^{-1}t_k \tag{2.35}$$

$$U_{k+1} = U_k + x_{k+1}(\beta_k^{-1})^\dagger A_k \tag{2.36}$$

$$V_{k+1} = V_k - U_{k+1}A_{k+1}^{-1}t_k \tag{2.37}$$

$$\psi_k = -V_k(y_k+\alpha_1\beta_1^{-1})^{-1} \tag{2.38}$$

where A, B, y and t are $B \times B$ matrices and U, V and ψ are $N \times B$ block vectors. The residue $r_i = \eta - M\psi_i$ is not given directly by the LA algorithm. However, the parameter t_i is related to r_i via

$$r_i^\dagger r_i = (d_i t_i)^\dagger (d_i t_i) \quad \textit{where} \quad d_i = (y_i + \alpha_1\beta_1^{-1})^{-1} \tag{2.39}$$

and we know the norm of the residue without storing the residue vector explicitly.

2.5 Expected Advantages of the Block Forms

The advantages of blocking the vectors in the CG and LA algorithms are obvious in exact arithmetic. The major computational task in the algorithms is to generate a complete set of mutually orthogonal vectors (the x_i in LA, the r_i in CG). If we solve eqns. 2.11 with the conventional $B = 1$ algorithm we generate a completely new set of such vectors for each of the B runs of the algorithm. This is extremely wasteful since the same complete set could be used to construct all B solution vectors simultaneously. This is precisely what is achieved in the block

forms, where the matrix nature of the expansion parameters ensures that the individual solution vectors in the block solution receive contributions from all B single vectors in a given block basis vector.

If the above argument is correct we would expect convergence of the block algorithms after approximately N/B iterations. This corresponds to N matrix-vector multiplications which is exactly the number required for convergence of the single algorithm. For the same number of such operations we have constructed B solution vectors. This, however, corresponds to less than a factor of B in computer time due to the overheads of inverting the $B \times B$ parameter matrices (for example eqns. 2.24 and 2.34).

The above argument will not hold in most practical implementations of the algorithms since N will be very large. In such cases eqns. 2.19, 2.20 and 2.31 only hold in some local region and we rapidly lose orthogonality. In addition, the single algorithm typically converges to some acceptable solution in many less than N iterations by choosing the directions in the solution space most appropriate to the particular source η. However, we might expect some gain for the block algorithms for the following reasons.

Firstly, by imposing eqns. 2.19, 2.20 and 2.31 on whole block vectors at a time we might expect to increase the number of iterations over which global orthogonality is maintained.

Secondly, we might expect the block algorithm to be much more efficient when there are small eigenvalues present in the eigenvalue spectrum of H. This is apparent if we consider a decomposition of a single solution vector ψ in terms of the orthonormal eigenvectors e_i of H with corresponding eigenvalues λ_i

$$\psi = \sum_{i=1}^{N} \frac{1}{\lambda_i} (e_i, \eta)\, e_i \tag{2.40}$$

and we view the aim of the algorithms as computing these eigenvalues and eigenvectors. This is a natural viewpoint for the LA algorithm and is therefore also valid for CG due to their equivalence. If all the eigenvalues in the spectrum are of

the same order of magnitude so that the condition number $\kappa = \lambda_{max} / \lambda_{min}$ is of order unity then the most important eigenvectors will be those with largest overlaps with the source. The important point is that the eigenvectors that the algorithm needs to find are, for small κ, dependent on the source. There will be little 'mixing' between the solutions ψ_n corresponding to different sources η_n and the block algorithm will be a costly implementation of B decoupled single algorithms.

If we take the other limit where κ is large due to the presence of one very small eigenvalue λ_j, then the only relevant eigenvector is e_j. The sum in eqn. 2.40 is dominated by this particular eigenvector for any choice of source except in the rare case where $(e_j, \eta) = 0$. We can construct a good approximation to all B solutions once we have found this single eigenvector and we would expect a gain in performance due to the blocking procedure.

Numerical analysis suggests that the number of iterations required for the single algorithm to converge should depend simply on the square root of the condition number [22] and also that this generalises to a simple dependence on the square root of the block condition number $\kappa_B = \lambda_{max}/\lambda_B$ [23] for a block algorithm with block size B. However, these arguments involve assumptions about the form of the eigenvalue spectrum (smooth and dense) that may not apply in the situations that arise in lattice QCD. What we can say without doubt is that for a given general form of the eigenvalue spectrum the number of iterations taken to converge will rise with the condition number, but not necessarily in a linear fashion.

2.6 Inversion of the Kogut Susskind Fermion Matrix

For all our studies we use SU(3) gauge configurations generated in the quenched approximation and use the Kogut Susskind form of the lattice Dirac operator (eqn. 1.35) which is

$$M_{KS}(m,n) = \frac{1}{2} \sum_{\mu} \alpha_\mu(m)\, U_\mu(m)\, \delta_{n,\, m+\mu} - \alpha_\mu(m\text{-}\mu)\, U_\mu^{\dagger}(m\text{-}\mu)\, \delta_{n,\, m\text{-}\mu} + m\, \delta_{m,n} \qquad (2.41)$$

where U_μ are the SU(3) link variables and α_μ the usual phases ± 1. We use antiperiodic boundary conditions on the fermion fields in all directions.

As explained above, the nature of the eigenvalue spectrum has implications for the speed at which columns of the inverse can be calculated and in particular the presence of small eigenvalues. The condition number κ is important but also the density of eigenvalues around λ_{min}. Since the spectrum depends on the gauge field this leads to a change in performance with the coupling constant β as well as with the quark mass parameter m. We investigate this behaviour since it is important when comparing the algorithms to study their convergence on matrices of differing and *known* degrees of difficulty.

For M_{KS} the eigenvalues have the form $m \pm i\lambda$ where $i\lambda$ are the eigenvalues of the anti-hermitian massless part of the matrix and λ is real and positive. λ can take very small values on large lattices at low β but is never zero in practical simulations on a finite lattice. It is possible, however, to construct special configurations that are an exception to this rule [24]. The sum over λ^2 is constant being half the product of the number of sites, directions and colours in the theory. The largest value of λ is about 2 independently of β.

It is important to note that the massless part of M_{KS} only connects even to even and odd to odd sites. Only half the storage space will be required if we can arrange for all the vectors to be purely even or purely odd and all matrix multiplications will be twice as fast. We therefore choose the RHS of eqn. 2.11 to be a purely even vector η_{even} and solve [25]

$$MM^\dagger \phi_{even} = \eta_{even} \tag{2.42}$$

$$\psi = M^\dagger \phi_{even} \tag{2.43}$$

Eqn. 2.42 is solved straight forwardly using either the CG or LA algorithms since $MM^\dagger$ is hermitian and positive definite. It connects even to even and odd to odd sites even at finite m and so we have halved the storage and computation required. The LA algorithm has the advantage that it can solve for the inverse at several

masses simultaneously which is very useful for quenched hadron propagators. We can generate the Lanczos vectors from the massless piece of $M_{KS}M_{KS}^{\dagger}$ and simply add m^2 to the α_i. Since generating the vectors is the major computational cost we thereby save in computer time at the price of additional storage. The LA algorithm described here is exactly equivalent to the one described in refs. [12, 19, 26] but is rather easier to implement. They will both agree step by step with the CG algorithm in exact arithmetic. Note that the residue of eqn. 2.42 is precisely the required residue η - $M\psi_i$.

2.6.1 Results on a 4^4 Lattice

Although a 4^4 lattice is too small for practical calculations it is still a useful volume on which to test algorithms. We will describe the results on two configurations, one thermalised at β = 5.3 and the other at β = 5.7. The m=0 eigenvalue spectra of M_{KS} on these configurations are quite different (see fig. 2.2 where we plot the number of eigenvalues below λ against λ). At β = 5.3 there are many small eigenvalues whereas at β = 5.7, above the chiral transition, these low modes have moved away from the origin. This is as we would expect from the expression for the chiral condensate

$$<\bar{\Psi}\Psi> \; = \; \pi N_C \rho(\lambda=0) \qquad (2.44)$$

where N_C is the number of colours and $\rho(\lambda)$ is the normalised eigenvalue density around λ. From the preceding discussion we expect the algorithms to find the configuration at β = 5.3 much harder to deal with and the performance will be strongly mass dependent since the smallest eigenvalue of M_{KS} will be largely governed by the mass. We have studied configurations other than those described in detail here and we find the same qualitative behaviour although the exact values for the eigenvalues and the number of iterations depends on the individual configuration.

Some typical curves for the residue as a function of the number of multiplications by M_{KS} ($2 \times$ iterations $\times B$) are shown in fig. 2.3 for the LA

algorithm. For large m and small B the residue drops monotonically. However, as m is decreased the appearance of small eigenvalues introduces a characteristic initial plateau to the curves. For B=1 we can use the Lanczos algorithm to monitor the convergence of the eigenvalues as the algorithm progresses and, as expected, it is exactly at the point where the lowest eigenvalues begin to converge that the plateau ends and the residue starts to drop. At large B there is also a plateau in the curves but for a different reason. By monitoring the orthogonality of the Lanczos vectors x_i with the initial vector we see that eqn. 2.31 is satisfied to a very high degree of accuracy right up to the point where the whole solution space has been spanned at iteration 768. At this point the solution is almost completely determined and only a few more iterations are necessary until convergence is achieved.

Fig. 2.4 shows the computer time taken per column of the inverse at the two different couplings and with two masses 0.1 and 0.01. A very strict convergence criterion of $|r_i| < 10^{-10}$ was used. For large B the number of iterations drops like B^{-1} but this is adjusted by the overheads of inverting the $B \times B$ parameter matrices which can be significant compared to operations of the form $M_{KS} \times vector$ on such a small lattice. It is clear from fig. 2.4 that the block LA algorithm is far less sensitive to the eigenvalue spectrum than the single algorithm and as a results outperforms it significantly at low β and low m. It is important to see if this holds on larger lattices where even the block algorithm will not be able to maintain global orthogonality right up to the point of convergence.

Although the CG algorithm with $B = 1$ is numerically identical to the LA algorithm over many iterations, the CG algorithm becomes numerically unstable as B is increased. The residue never reaches 10^{-10} for large values of B ($B > 8$ for $\beta = 5.3$ and $B > 15$ for $\beta = 5.7$ at $m = 0.01$) and the degree of convergence becomes dependent on B and the source η.

The reason for this is that the block vectors in LA are orthonormal and hence they and the expansion matrices constructed from them have elements always much larger than machine precision. In CG, however, the corresponding vectors are the

residue vectors themselves which are orthogonal but not normalised to unity. When the residue becomes small the parameter matrices will have very small elements. For large B and small m inverting these matrices with Gaussian elimination to calculate the parameters a_i and b_i in eqns. 2.24 and 2.25 introduces large relative errors preventing reliable convergence. These rounding errors affect the CG algorithm even in 64-bit precision. When 32-bit precision is used throughout the convergence of the block LA algorithm is also affected, but to a lesser degree.

In fact the block CG algorithm does not behave so badly on larger lattices [23]. Although the residue vectors still become small the convergence is more gradual and there is no critical point at which all the solutions converge suddenly. It is at this critical point of convergence on small lattices that it is most essential to be numerically accurate. This is supported by the fact that convergence on 4^4 was particularly bad when B was an exact multiple of N. Then after N/B iterations convergence will be particularly sudden and numerical accuracy most important.

As described above the MDMCG algorithm could be used directly with the matrix M_{KS} to calculate rows of the inverse when η is a mixed even/odd vector. For B=1 this algorithm takes exactly the same number of iterations to converge as LA or CG. When B>1 it takes approximately twice as many for such a mixed starting vector. This is because the block algorithm is unable to exploit the two fold degeneracy in the eigenvalue spectrum of $M_{KS}^{\dagger}M_{KS}$ at $m = 0$. In general the algorithms described here need only search directions containing a single eigenvector from each degenerate pair. For B=1 this happens automatically since degenerate eigenvectors of an hermitian matrix can always be chosen such that all but one are orthogonal to the starting vector and then the algorithm need never explore these directions. When B>1 all the single vectors in the block starting vector η must belong to the same degenerate subspace otherwise the algorithm is forced to search through all directions. Two degenerate eigenvectors with eigenvalue λ^2 can be chosen to purely even or odd. Hence odd and even vectors belong to two degenerate sub-spaces. If we do choose a purely even starting vector

the MDMCG algorithm takes the same number of iterations to converge as the CG and LA algorithms for any B. However it is a costly implementation since the vectors p_i are mixed even/odd for finite m and we are unable to halve the size of the vectors to decrease the computer time.

The CG and MDMCG algorithms were not pursued any further since we have shown that the LA algorithm is superior. It is more numerically stable than the CG algorithms and has the added benefit that it allows us to compute the residue at several masses simultaneously.

2.6.2 Results on an 8^4 Lattice

For larger lattices we do not expect sudden convergence after N/B iterations, but from the previous discussion we would expect some gain when there are low eigenvalues present in the spectrum. We studied two 8^4 configurations thermalised at $\beta = 5.5$ and the other at $\beta = 5.8$ where the smallest eigenvalues were 0.0007 and 0.014 respectively. The spectra of the lowest eigenvalues are shown in fig. 2.5. It would be expected that the inversion at $\beta = 5.8$ would be more rapid than that at $\beta = 5.5$ since the condition number is smaller and the density of small eigenvalues is much lower.

The computer time taken per column of the inverse is shown in fig. 2.6 which confirms this prediction. It can be seen that at small mass the block form of LA is far superior to the single algorithm and there is little mass dependence for sufficiently large B. At large mass $m>0.1$ we find a very slow rise of the curve with B due to the increased computer time taken to calculate block vector dot products, which grows as B^2. For this mass there is no improvement due to the blocking since the mass term dominates the low eigenvalues of M_{KS}. It is when very small eigenvalues are present (low mass, low β) that the block algorithm is most effective. For $B = 24$ (the maximum blocking possible due to memory limitations) at $\beta = 5.5$ and $m = 0.01$ there is a factor of 6 improvement over the single algorithm which takes nearly 2500 iterations to converge. There is an even

larger improvement at smaller masses, but once the mass becomes smaller than the smallest eigenvalue it has little physical meaning. At a block size of 24 inversion at all masses requires almost the same amount of computation.

By monitoring the orthogonality of the Lanczos vectors it was again observed that the effect of larger blocking is to significantly increase the number of multiplications by M_{KS} over which orthogonality is maintained.

When low eigenvalues were present in the spectrum, there was again a characteristic plateau in the residue/iterations plot. For B=1 the point at which convergence sets in rapidly was again identified with the convergence of these small modes. The plateau persists in the block forms, presumably for the same reason.

2.7 Inversion of Diagonal Matrices

Although there is no practical value in inverting a diagonal matrix it is useful to study the performance of the algorithms on such matrices since we can easily construct them to have specific eigenvalue spectra. This gives us more control over the structure of the 'fermion' matrix than using real gauge configurations, and allows us to go to much more extreme limits of ill-conditioning in order to test the algorithms more thoroughly.

We use the block LA algorithm to solve eqn. 2.11 where the $N \times N$ hermitian matrix H is taken to be

$$H(m, n) = \lambda_n \delta_{m,n} \qquad (2.45)$$

and λ_n comes from the required eigenvalue distribution. We consider two generic types of distribution parameterised solely by the condition number. The first is a linear distribution of eigenvalues where we have a distribution $\lambda_1 \rightarrow \lambda_N$ with λ_n given by

$$\lambda_n = \lambda_{min} + (1-\lambda_{min}) \frac{n-1}{N-1} \qquad (2.46)$$

The second is a logarithmic distribution given by

$$\lambda_n = (\lambda_{min})^{\frac{N-n}{N-1}} \qquad (2.47)$$

In both cases $\lambda_1 = \lambda_{min}$ and $\lambda_N = 1$, and hence $\kappa = 1/\lambda_{\min}$. The low lying

eigenvalues of these two distributions are shown in fig. 2.7 for a condition number $\kappa = 10^3$. It is evident that the logarithmic distribution causes the eigenvalues to be highly concentrated around λ_{min}, whereas the linear distribution leaves λ_{min} as a fairly isolated small mode.

We cannot take the source η to be a delta function since this is an eigenfunction of the diagonal matrix, so we generate a random source and normalise it to unity. The fact that all the eigenvalues are real allows us to work in real arithmetic throughout if we choose η to be real. We have checked that this does not alter the results. This means a four fold increase in speed.

Studies were performed for $N = 8^4$ for a range of κ values, and the convergence criterion was taken to be $|r_i| < 10^{-6}$. This is not as small as was taken before since we wish to go to very large values of κ where, for large B, we run into numerical problems even with the LA algorithm.

2.7.1 Results for Linear Eigenvalue Distributions

Some typical curves for the residue versus the number of iterations are shown in fig. 2.8 for B=1 and $\kappa = 10^3$, 10^4 and 10^5. We see that at large κ there is the characteristic point associated with the convergence of the lowest eigenvalues where the residue starts to drop monotonically after a long plateau region during which the residue does not decrease. If the previous arguments about the effects of low eigenvalues are correct it will be during this plateau that the lowest eigenvalue and corresponding eigenvector are being sought. Although the residue is not decreasing we expect that the major contributions to the solution vector are being found. This is supported by the fact that if we monitor the norm of the solution vector along with the residue we see that the solution is rapidly changing throughout this plateau but becomes stable exactly at the point where the residue starts to decrease. We therefore expect the block algorithm to be superior to the single algorithm.

The results obtained for various values of B at a range of κ from 10 to 10^{10} are shown in fig. 2.9 and show that there is a dramatic improvement as B is increased.

At higher values of κ numerical problems were encountered for $B \geq 20$. To check whether the convergence rate follows the expected form (number of iterations $\approx \sqrt{\kappa_B}$, with the block condition number given by $\kappa_B = \lambda_{max}/\lambda_B$) we plot the ratio of the number of iterations to $\sqrt{\kappa_B}$ against the condition number in fig. 2.10. For $\kappa \leq 10^3$ the relationship holds reasonably well - for a given condition number the ratio is fairly constant for all B, and it does not change significantly with κ in this range. However, the relationship breaks down completely at larger κ values where the major feature is that the $B = 1$ algorithm performs far better than the naive formula would predict.

To try and determine the behaviour for large κ as a function of B we normalise by the number of iterations taken by the $B = 1$ algorithm. We plot the gain (the number of iterations at block size 1 divided by the number at block size B) divided by $\sqrt{B}$ against κ in fig. 2.11. We see that for $\kappa > 10^3$ the gain in the block algorithm is given approximately by $\sqrt{B}$ with the agreement becoming more exact with increasing κ.

At low m and low β the eigenvalue spectrum of M_{KS} resembles that of a linear distribution at large κ where there is an overall smooth distribution with a few very small eigenvalues. The general features of the LA algorithm are the same in these two cases. There is a long plateau in the residue before convergence suddenly sets in, and there is a large improvement in performance with B.

2.7.2 Results for Logarithmic Eigenvalue Distributions

Some typical curves for the residue versus the number of iterations at B=1 are shown in fig. 2.12 for $\kappa = 10^3$, 10^4 and 10^5. There is no plateau in the residue and experience would tell us that on large volumes there will be little to be gained by going to larger values of B. This is borne out in fig. 2.13 where we plot the number of iterations for various B as a function of κ from 10 to 2000. For $\kappa > 500$ numerical problems were encountered at B=20 and convergence was never achieved. This upper limit on the condition number is much lower than for the

linear distribution, presumably because the much higher density of low eigenvalues requires a correspondingly higher numerical accuracy.

In fig. 2.14 we plot the same data against the square root of the condition number. The B=1 curve follows the $\sqrt{\kappa}$ relationship expected for smooth, dense distributions and the points lie on a straight line through the origin. There is a slight reduction in the number of iterations as B is increased, presumably due to the increased degree of orthogonality of the Lanczos vectors. Although small, the reduction is much greater than would be predicted by the $\sqrt{\kappa_B}$ relationship since the block condition number changes by only one or two percent over the whole range of B.

The logarithmic distribution has a very high concentration of low eigenvalues. This causes the performance of the block algorithm to be no better than the single algorithm and also makes the block algorithm numerically unstable at relatively low values of κ. Any reduction in the number of iterations taken to converge is outweighed by the computational overheads of the block form.

2.8 Conclusions

We have calculated columns of the inverse Kogut-Susskind fermion matrix using a variety of different algorithms. Since we have also found the eigenvalue spectra of the different matrices we can directly relate the performance of the algorithms to the degree of difficulty of the calculation.

When only a single column of the inverse is required, the CG and LA algorithms perform identically. The MDMCG algorithm is not as good since it requires more storage and computation than the other algorithms.

When more than one column of the inverse is required the block LA algorithm out-performs the block CG and MDMCG algorithms. The latter two are not numerically stable in their simplest form for large values of the block size. Improvements have been suggested [6, 23] but these are unlikely to make the performance superior to that of LA.

By considering the performance of the LA algorithm on matrices with specifically constructed eigenvalue spectra we have identified the conditions under which the block form of the algorithm is most efficient. The required conditions are fulfilled by a linear distribution of eigenvalues with a large condition number where the improvement factor over the single algorithm is given by the square root of the block size. More generally, we expect the block form to be useful in any situation where there are a few small eigenvalues present in an otherwise smooth spectrum.

This situation arises for Kogut Susskind fermions at small mass in a background SU(3) gauge field in the phase of broken chiral symmetry. This is a physically interesting regime. For an 8^4 configuration at $\beta = 5.5$ we find an improvement factor of 5 or more. Use of the block LA algorithm therefore offers the opportunity of increasing the speed of many calculations involving lattice fermions, particularly those hampered by critical slowing down.

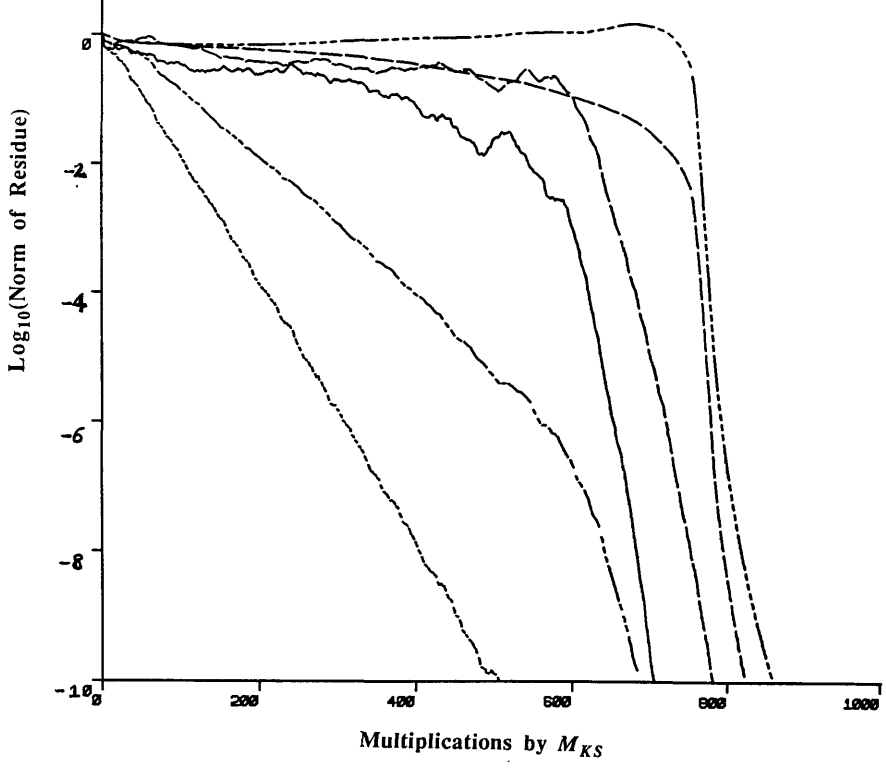

Fig. 2.3 Residue of the block LA algorithm vs. the number of multiplications by M_{KS} for various m and B. In order of convergence:
$m = 0.1$, $B = 1$; $m = 0.1$, $B = 2$; $m = 0.01$, $B = 1$;
$m = 0.01$, $B = 2$; $m = 0.1$, $B = 18$; $m = 0.01$, $B = 18$.

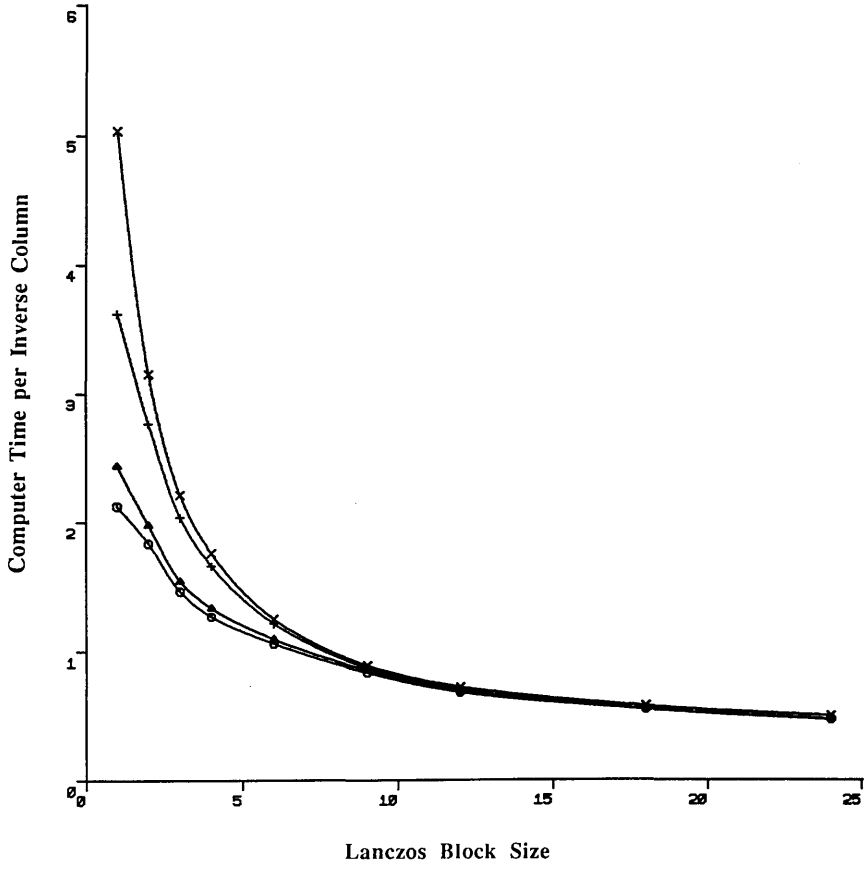

Fig. 2.4 The time (in seconds) taken to calculate one column of the inverse fermion matrix for the block LA algorithms vs. the block size on a 4^4 lattice. Convergence condition is $|r| < 10^{-10}$.
(x) $\beta = 5.3$, $m = 0.01$; (+) $\beta = 5.3$, $m = 0.1$;
(Δ) $\beta = 5.7$, $m = 0.01$; (o) $\beta = 5.7$, $m = 0.1$;

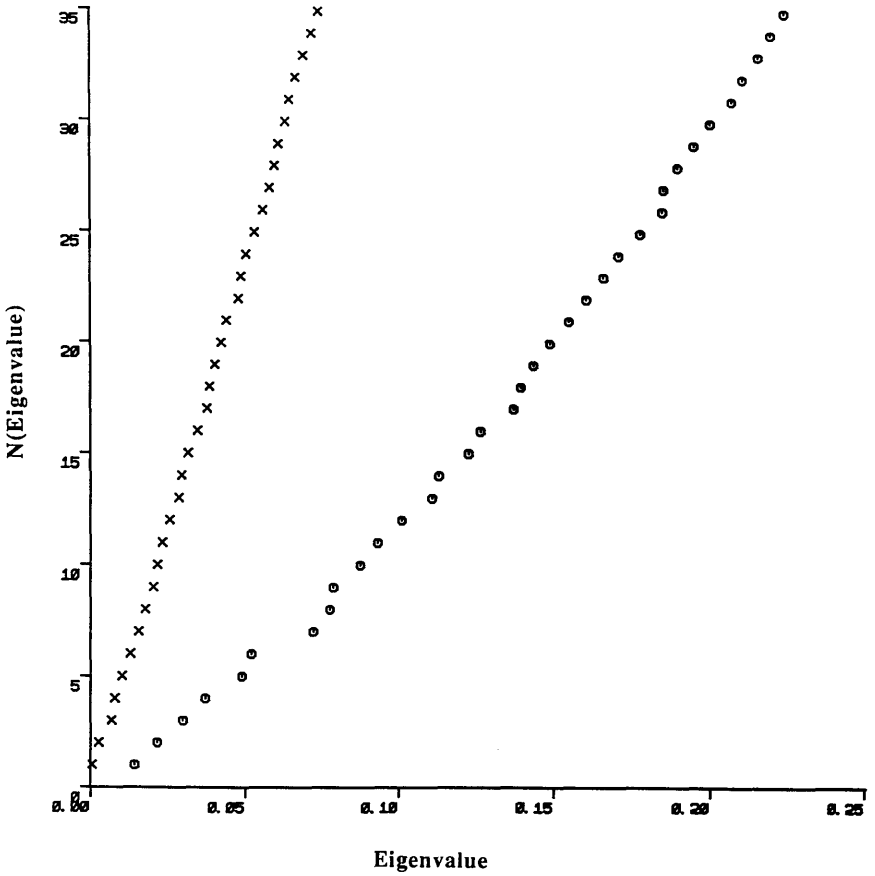

Fig. 2.5 The eigenvalues close to zero for the massless Kogut-Susskind fermion matrix on an 8^4 lattice. (x) $\beta = 5.5$, (o) $\beta = 5.8$.

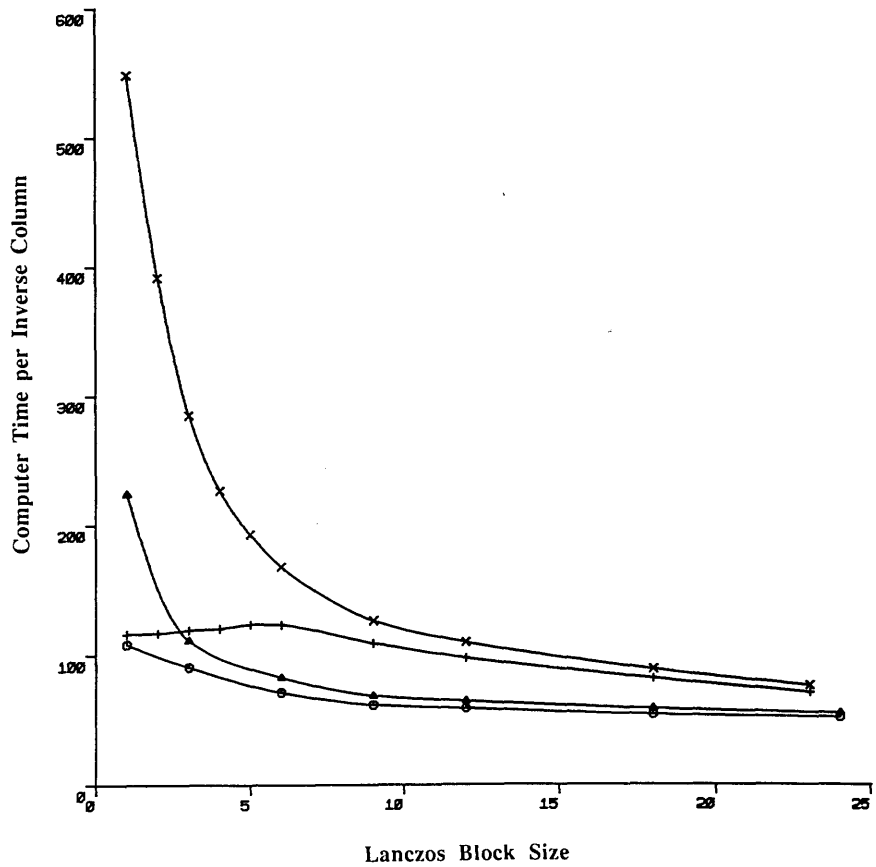

Fig. 2.6 The time (in seconds) taken to calculate one column of the inverse fermion matrix for the block LA algorithms vs. the block size on an 8^4 lattice. Convergence condition is $|r| < 10^{-10}$.
(x) $\beta = 5.5$, $m = 0.01$; (+) $\beta = 5.8$, $m = 0.05$;
($\triangle$) $\beta = 5.5$, $m = 0.01$; (o) $\beta = 5.8$, $m = 0.05$;

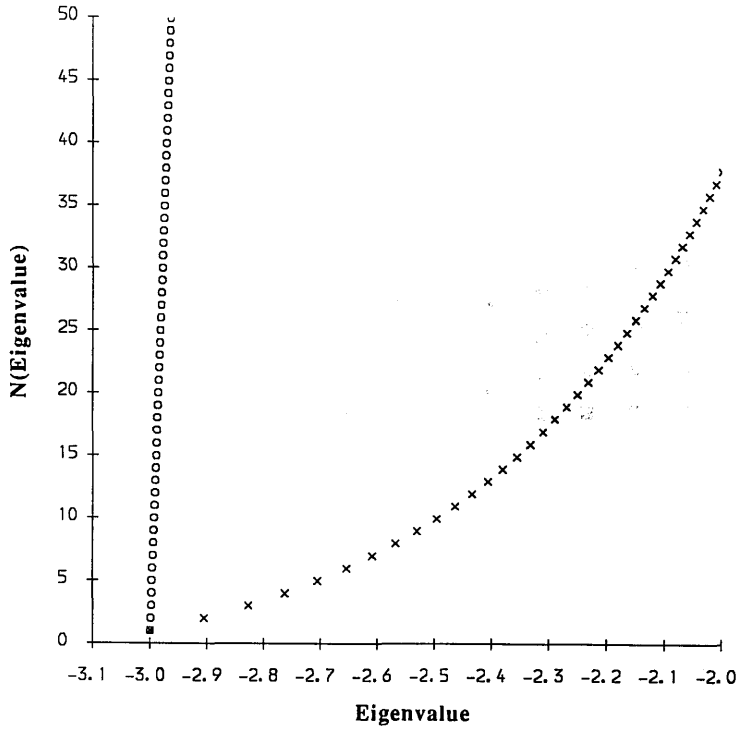

Fig. 2.7 The eigenvalues close to zero for logarithmic and linear distributions with condition number $\kappa = 10^3$. (o) logarithmic, (x) linear.

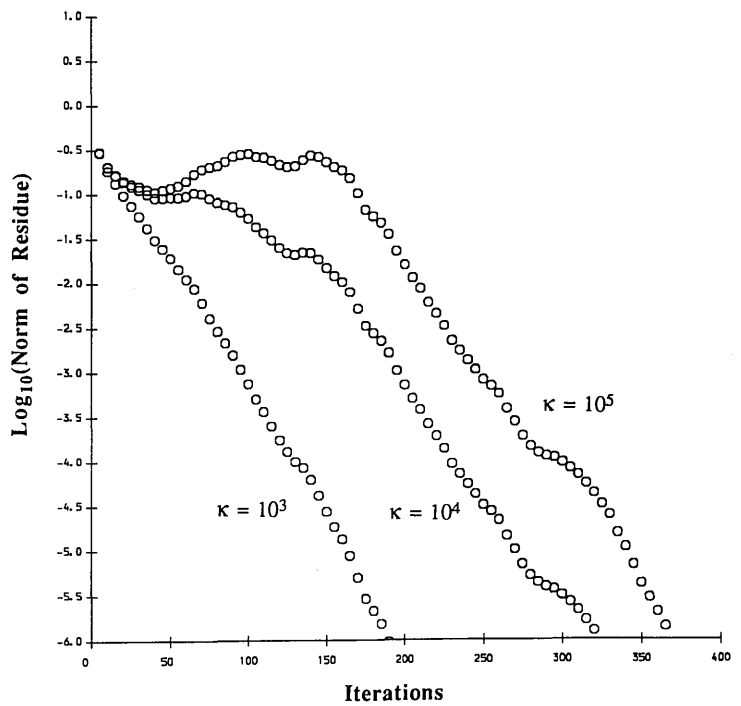

Fig. 2.8 Residue of the $B = 1$ LA algorithm vs. the number of iterations for linear eigenvalue distributions with various condition numbers.

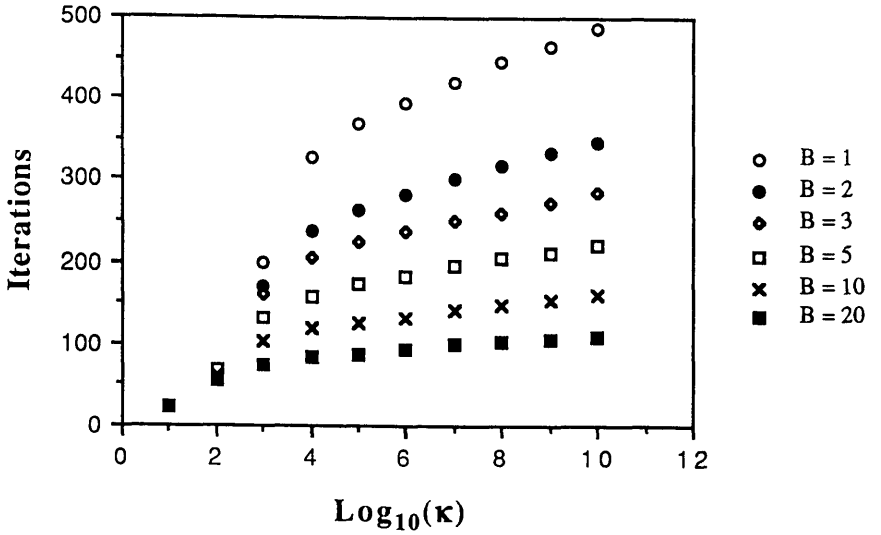

Fig. 2.9 The number of iterations taken for the block LA algorithm to converge vs. the log of the condition number for linear eigenvalue distributions. The convergence condition is $|r| < 10^{-6}$.

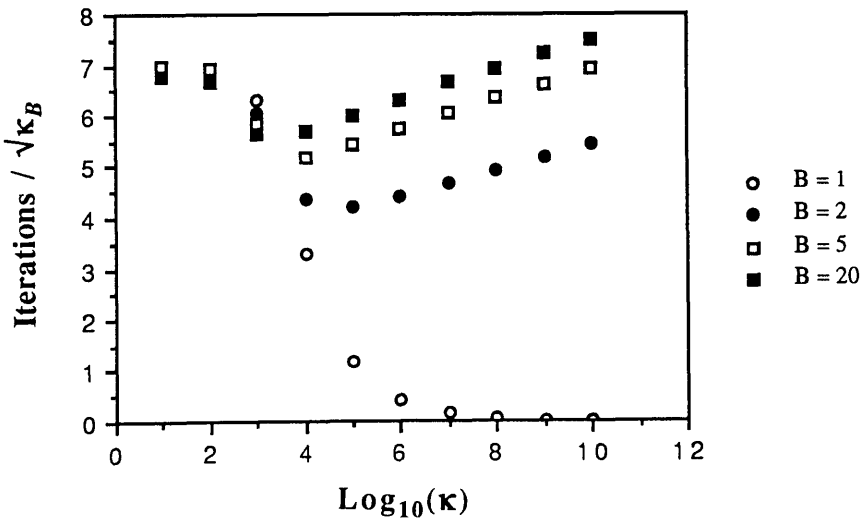

Fig. 2.10 The number of iterations taken for the block LA algorithm to converge divided by the square root of the block condition number κ_B vs. the log of the condition number for linear eigenvalue distributions.

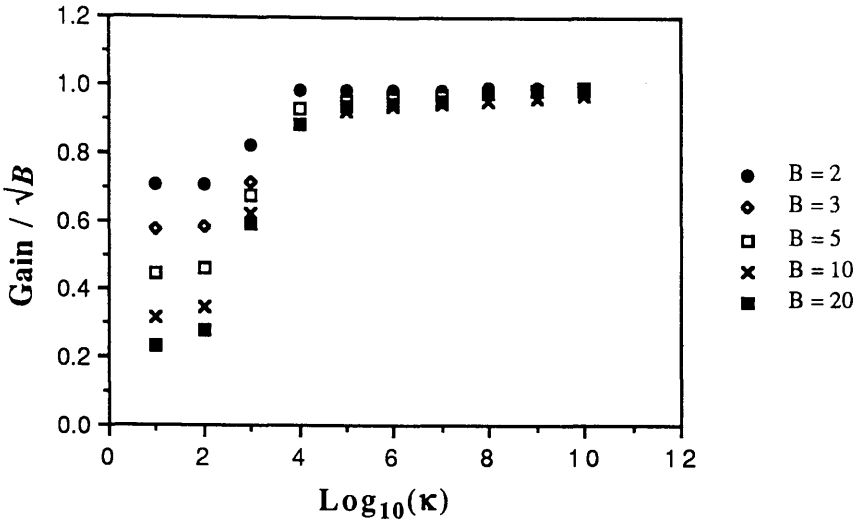

Fig. 2.11 Gain for the block LA algorithm over the square root of the block size vs. the log of the condition number for linear eigenvalue distributions.

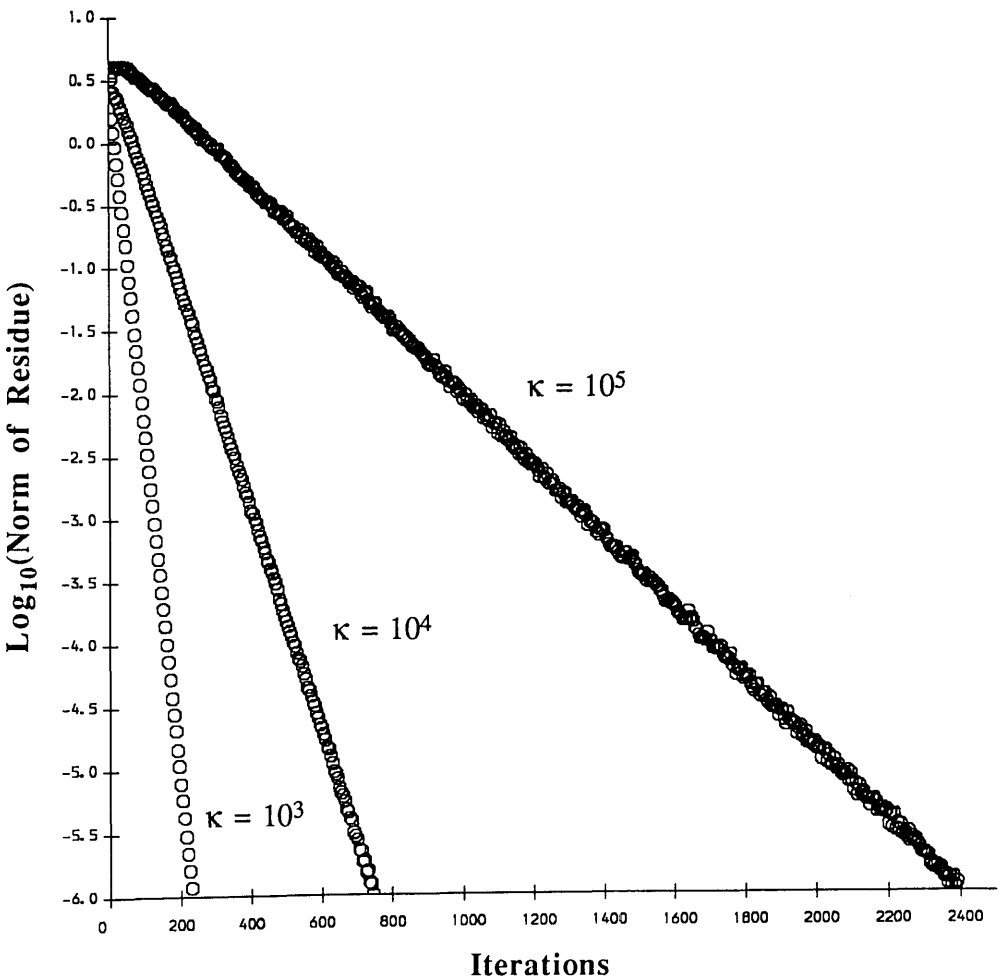

Fig. 2.12 Residue of the $B = 1$ LA algorithm vs. the number of iterations for logarithmic eigenvalue distributions with various condition numbers.

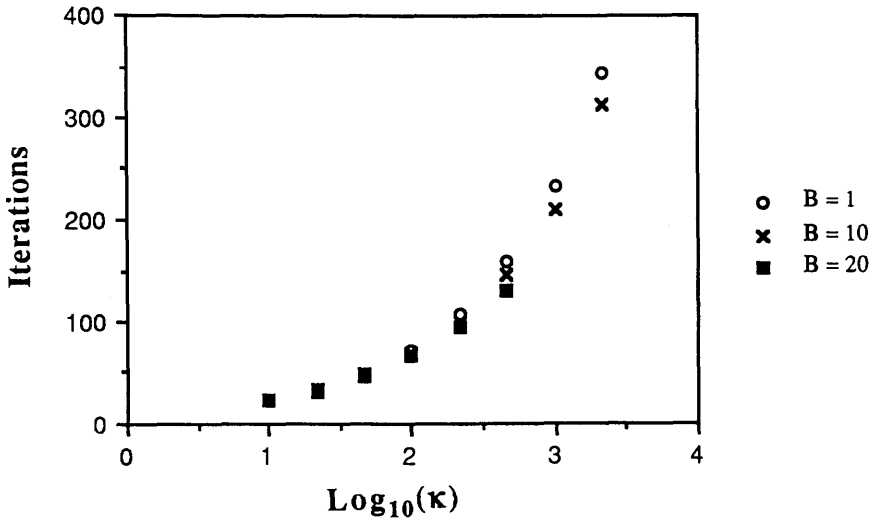

Fig. 2.13 The number of iterations taken for the block LA algorithm to converge against the log of the condition number for logarithmic eigenvalue distributions. The convergence condition is $|r| < 10^{-6}$.

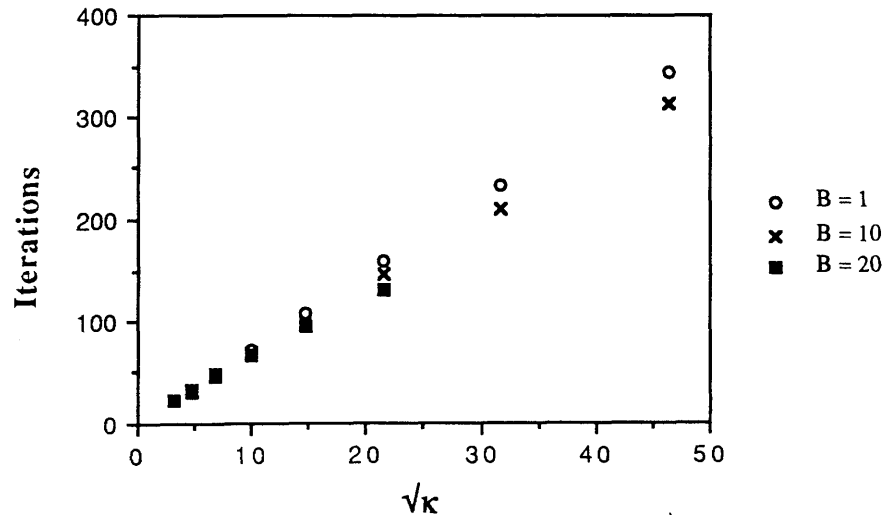

Fig. 2.14 The number of iterations taken for the block LA algorithm to converge against the square root of the condition number for logarithmic eigenvalue distributions. The convergence condition is $|r| < 10^{-6}$.

Chapter 3

Lattice Higgs Models

3.1 The Continuum Higgs Mechanism

An integral part of the standard model is the electroweak sector described by the Glashow-Weinberg-Salam model [27] which unifies the electromagnetic and weak interactions by introducing an SU(2) × U(1) gauge symmetry mediated by the W^+, W^- and Z gauge bosons and the photon. The problem which will concern us here is the need to dynamically generate particle masses within the theory. The weak forces are very short range implying masses for the gauge bosons of order 100 GeV, and the top quark mass is of a comparable order of magnitude. However, any bare mass term in the Lagrangian for either the bosons or the fermions breaks the gauge symmetry and consequently renders the theory un-renormalisable.

The way to generate mass terms is through the introduction of an auxiliary scalar field which transforms non-trivially under the electroweak gauge group and hence couples to the gauge bosons. If we then arrange for this field to spontaneously break the SU(2) gauge symmetry and acquire a non-zero vacuum expectation value then the Higgs mechanism [28] generates masses for the W^+, W^- and Z bosons. By leaving the U(1) electromagnetic symmetry unbroken the photon will remain massless. In the standard model the Higgs field is a complex iso-doublet with four degrees of freedom. Of these, three are 'eaten' by the gauge bosons so they acquire the extra longitudinal degree of freedom needed for massive spin-1 particles.The remaining degree of freedom manifests itself as the neutral scalar Higgs particle, which has not yet been observed despite many extensive searches [29]. The Higgs mass is a free parameter of the theory and the fact that it has not been detected suggests that its value is very large.

Once we have introduced the Higgs field and unavoidably generated the required massive gauge bosons by allowing it to develop a non-zero VEV, we can

generate fermion masses in a rather more straightforward manner. We add Yukawa terms to the Lagrangian of the form

$$\overline{\Psi}\, Y_a\, \Phi_a\, \Psi \tag{3.1}$$

where Y_a are Yukawa coupling matrices in flavour space and Φ_a the components of the Higgs field. Such a term mixes the left and right handed fermion components but is still gauge invariant due to the presence of the Φ field.

When the Φ field spontaneously breaks the gauge symmetry we can always choose a gauge such that classically only one of its components is non-zero and equal to the VEV [30]. If we apply this gauge transformation to eqn. 3.1 and then diagonalise the resulting Yukawa matrix Y in flavour space we will find the physical fermion fields which are mass eigenstates. In this unitary gauge the Lagrangian contains terms of the form

$$y_i <\Phi> \overline{\Psi}_i \Psi_i \tag{3.2}$$

where the y_i are the (real and positive) eigenvalues of Y and 'i' labels the fermion flavour. Such a term is a mass term for the fermion Ψ_i and hence, to lowest order, the fermions acquire a mass m_i given by

$$m_i = y_i <\Phi> \tag{3.3}$$

This mass has been dynamically generated from a gauge invariant interaction term and hence does not spoil the renormalisability of the theory.

The only remaining problem is how to arrange for the Higgs field to break the gauge symmetry. This is straightforward if we consider a single component real scalar field with a Lagrangian in Minkowski space of the form of

$$L = \frac{1}{2}\partial_\mu\phi\partial^\mu\phi - V(\phi) \tag{3.4}$$

$$V(\phi) = \frac{1}{2}\mu^2\phi^2 + \frac{1}{4}\lambda\phi^4 \tag{3.5}$$

We must have $\lambda > 0$ so that the potential V is bounded from below, but the choice of sign for μ^2 is undetermined. If we take $\mu^2<0$ then the potential develops two degenerate minima away from the origin at the points where

$$\frac{\partial V}{\partial \phi} = 0 \Rightarrow \phi = \pm\sqrt{\frac{-\mu^2}{\lambda}} \qquad (3.6)$$

The sign of ϕ is undetermined and unimportant. We will always take it to be positive such that a positive Yukawa coupling will give a positive mass. To lowest order the VEV of the scalar field will be the value of ϕ at this minimum. If we use a Lagrangian of the general form of eqn. 3.4 for the Higgs field Φ of the standard model then we can arrange for the gauge symmetry to be spontaneously broken. We can tune the Higgs VEV by tuning μ^2 to some appropriate (negative) value.

The gauge boson masses are given in terms of this VEV, and one can therefore derive the following expression for $<\Phi>$ [31]

$$<\Phi> = \frac{2m_W}{em_Z}\sqrt{(m_Z^2 - m_W^2)} \qquad (3.7)$$

where e is the electronic charge and m_W and m_Z the W and Z boson masses. Taking the values of the vector boson masses from the UA1 and UA2 experiments [32] gives a VEV of the order of 250 GeV.

3.2 Lattice Higgs Systems

There are three major reasons for investigating Higgs models on the lattice. Firstly, if we are to have a completely non-perturbative (lattice) definition of the full standard model [33, 34] we must generate all particle masses via the Higgs mechanism. Decoupling the unwanted doubled fermions using some variant of Wilson's method (eqn. 1.26) has to be done in a gauge invariant manner involving the lattice Higgs field. This involves using Wilson-Yukawa couplings [35] which spontaneously generate the Wilson term in a manner analogous to the generation of mass terms in the continuum, and this mechanism has to be understood.

Secondly, even if we content ourselves with a perturbative definition of the standard model we may still require non-perturbative knowledge of the Higgs mechanism. Like all other particles the top quark will acquire its mass via a Yukawa coupling, but if $m_t > 100$ GeV eqn. 3.7 implies that $y_t > 0.4$. This value may well

be outside the valid bounds of perturbation theory and hence eqn. 3.3 may not hold. More critically, it might be true that a non-perturbative upper bound exists for masses generated via Yukawa couplings and that it is impossible to accommodate a very heavy top in the standard model.

Thirdly, we can also look for new fixed points in the lattice model well away from the one around zero coupling. The theory defined around such a non-perturbative fixed point might well have a very different continuum limit from the perturbative theory. The existence of this alternative continuum theory would be of great interest.

Hence we would like to define a simple lattice Higgs system with which to study dynamical fermion mass generation. Our first approximation is to ignore all gauge interactions. This will be a good approximation for the heavy quarks in which we are interested since they will have large bare Yukawa couplings. Secondly we consider a single component real scalar field for simplicity. The Euclidean form of the Lagrangian is the same as eqns. 3.4 and 3.5 except that the sign of the potential term is reversed. We discretise the resulting action by eqns. 1.10 and 1.11 to obtain the purely bosonic lattice action S_B

$$S_B = \sum_n \phi^2(n) - 2\kappa \sum_n \sum_\mu \phi(n)\phi(n+\mu) + \lambda \sum_n (\phi^2(n) - 1)^2 \qquad (3.8)$$

This action is invariant under the $Z(2)$ transformation

$$\phi(n) \rightarrow -\phi(n) \qquad (3.9)$$

Eqn. 3.8 reduces to the continuum Euclidean form of eqn. 3.4 if we make the identifications

$$\phi_c = \frac{\sqrt{2\kappa}}{a}\phi \qquad (3.10)$$

$$\mu_c^2 = a^{-2}\left(\frac{1 - 2\lambda}{\kappa} - 2d\right) \qquad (3.11)$$

$$\lambda_c = \kappa^{-2}\lambda \qquad (3.12)$$

where d is the number of space-time dimensions and the subscript 'c' refers to the continuum action.

Such a model spontaneously magnetises and breaks the $Z(2)$ symmetry in certain regions of the (κ, λ) phase plane. In four dimensions there are three distinct phases characterised by the value of the field on even and odd sites (ϕ_e and ϕ_o). We define the usual magnetisation $\langle\phi\rangle = \langle\phi_e + \phi_o\rangle$ and the 'staggered' magnetisation $\langle\phi_{st}\rangle = \langle\phi_e - \phi_o\rangle$. The phase structure is, for a given λ

$$\begin{aligned}
\kappa < -\kappa_c &\quad \text{Antiferromagnetic (AFM) phase:} \quad \langle\phi\rangle = 0,\ \langle\phi_{st}\rangle \neq 0 \\
-\kappa_c < \kappa < \kappa_c &\quad \text{Paramagnetic (PM) phase:} \quad \langle\phi\rangle = 0,\ \langle\phi_{st}\rangle = 0 \\
\kappa > \kappa_c &\quad \text{Ferromagnetic (FM) phase:} \quad \langle\phi\rangle \neq 0,\ \langle\phi_{st}\rangle = 0
\end{aligned}$$

The fact that the PM / FM and PM / AFM phase transitions happen at $\pm\kappa_c$ and not at two independent values is due to the symmetry of the action 3.8 under the simultaneous transformations

$$\kappa \rightarrow -\kappa, \quad \phi_e \rightarrow \phi_e, \quad \phi_o \rightarrow -\phi_o \tag{3.13}$$

since this symmetry implies $\langle\phi_{st}(-\kappa)\rangle = \langle\phi(\kappa)\rangle$.

The critical value $\kappa_c(\lambda)$ is a very slowly varying function of the self-coupling λ. For $\lambda = 0$ we have a free field theory and eqn. 3.11 shows that the massless continuum theory with $\mu^2 = 0$ is obtained at $\kappa^{-1} = 2d$. We identify this as a phase transition point since the theory has zero mass gap and hence infinite correlation length, ie. $\kappa_c(0) = (2d)^{-1}$. For $\lambda = \infty$ the theory reduces to the Ising model (see section 3.6) and a simple mean field calculation (see for example ref. [36]) gives the result $\kappa_c(\infty) = (4d)^{-1}$, valid to leading order in $1/d$.

We can use this action as the basis for our lattice Higgs system since all we require to study the generation of fermion masses is some scalar field that can acquire a non-zero VEV. Fermions are introduced by adding the term

$$S_F = \sum_{i=1}^{n_f} \sum_{m,\, n} \overline{\chi}_i(m)\, M_{KS}(m,\, n)\, \chi_i(n) \tag{3.14}$$

where M_{KS} is the staggered fermion matrix of eqn. 1.35 with $U_\mu(m)$ set to unity. This introduces n_f species of free staggered fermions. To couple these to the scalar field we add a Yukawa term to the action of the form

$$S_Y = \sum_{i=1}^{n_f} \sum_n y_i \, \phi(n) \, \overline{\chi}_i(n) \chi_i(n) \tag{3.15}$$

where we have allowed for a different coupling y to each fermion species. This is the naive transcription of the continuum form given by eqn. 3.1 and is, for obvious reasons, called a local Yukawa coupling.

Such actions (and ones closely related to them) have been the subject of many studies both in the quenched approximation [37], and in full dynamical simulations in the cases of radially fixed [38] and radially free [39, 40] Higgs fields. Since our interest is in spontaneous mass generation for the fermions, the bare mass m in S_F is set to zero. The basic features that have emerged seem to be common to all Higgs models that use a local Yukawa term of the form of eqn. 3.15.

3.3 The Quenched Phase Diagram

The phase diagram is particularly simple in the quenched approximation (see fig. 3.1). There can be no phase transition as a function of y since the quenched partition function is y-independent, so the two phase boundaries are independent of y and occur at the values $\pm\kappa_c$ given by the pure bosonic theory. However, the values of fermionic observables can vary significantly with y and it is found that the PM phase divides into two regions characterised by different values of the fermion mass.

For $y << \sqrt{2}$ the system is in the PM1 region where the renormalised fermion mass m_f measured from the two point function is zero [40]. As κ is increased across the PM1/FM phase boundary the fermion mass increases. This is a 'perturbative' phase where the perturbative relationship for the mass (eqn. 3.3) holds for small y.

For $y >> \sqrt{2}$ the system is in the PM2 region where the renormalised fermion mass is non-zero even though $<\phi> = 0$. As κ is increased across the PM2/FM phase boundary the fermion mass decreases despite the fact that $<\phi>$ is an increasing function of κ. This is a non-perturbative region and to obtain some insight into the strange behaviour of the fermion mass we can perform a hopping expansion to obtain the fermion propagator from eqn. 1.37, where the hopping parameter is $1/y$ [40]. We define the fermion energy E_f as

$$E_f = - lim_{n \to \infty} n^{-1} ln (|<\chi(0) \overline{\chi}(ne_\mu)>|) \tag{3.16}$$

where e_μ is a unit vector in the μ^{th} direction, and calculate m_f from the relation

$$m_f = sinh(E_f) \tag{3.17}$$

The two point function is given by eqn 1.37

$$|<\chi(0) \overline{\chi}(ne_\mu)>| = |<M^{-1}(0, ne_\mu)>| \tag{3.18}$$

and we expand $M^{-1} = (M_{KS} + y\phi)^{-1}$ as a power series in $1/y$ to give

$$(M_{KS} + y\phi)^{-1} = (y\phi)^{-1} \sum_{r=0}^{\infty} (-1)^r (M_{KS}(y\phi)^{-1})^r \tag{3.19}$$

Since M_{KS} hops between neighbouring sites the inverse comprises a series of hops each carrying a factor of $1/y$. The contribution to the required inverse element to leading order in $1/y$ comes from the straight line path between 0 and ne_μ. Remembering that each hop also carries a factor of 1/2 from the fermion matrix and ignoring the phases α_μ that contribute an irrelevant overall sign we have

$$|<M^{-1}(0, ne_\mu)>| \approx y^{-(r+1)} 2^{-r} |<\prod_{r=0}^{n} \phi^{-1}(re_\mu) >| \tag{3.20}$$

From now on we take $n+1$ to be even since the RHS of eqn. 3.20 vanishes in the PM2 region for $n+1$ odd. We make the further approximation that the multiple bosonic correlation function in eqn. 3.20 factorises into a product of two point functions, ie we assume

$$<\prod_{r=0}^{n} \phi^{-1}(re_\mu) > = z^{n+1}, \quad z^2 = <\phi^{-1}(n)\phi^{-1}(n+\mu)> \tag{3.21}$$

Putting eqns. 3.16 and 3.20 into eqn. 3.21 gives the following result for E_f

$$E_f = ln\,(2y) - ln\,(z) \tag{3.22}$$

and using eqn. 3.17 we obtain the final result

$$m_f = \frac{y}{z} \tag{3.23}$$

valid to leading order in $1/y$. Unlike $<\phi>$, z^2 is $Z(2)$ invariant and is non-zero for all positive κ. Since z increases with κ and is continuous across κ_c, eqn. 3.23 qualitatively explains the observed behaviour of the fermion mass for large y. Despite the fact that we have very massive fundamental fermions for large y in the PM phase the chiral symmetry remains unbroken. In this region the chiral symmetry is not realised by massless fermions but rather by parity doubled pairs of massive fermions. This behaviour is not completely novel and has already been observed in numerical studies of the purely fermionic 2-d Gross-Neveu model at large four-fermi coupling [41].

Fermions are massive throughout the FM phase where both $<\phi>$ and z are large and chiral symmetry is broken. The κ dependence of the mass varies with y from the small y behaviour of eqn. 3.3 to the large y behaviour of eqn. 3.23. The AFM phase has no smooth continuum limit and although it is of theoretical interest we do not consider the behaviour of the fermion mass in this region.

The PM1 and PM2 regions are distinguished by the very different behaviour of the fermion mass but there can be no true phase transition separating the two in the quenched model since the dynamics of the theory are governed purely by the bosonic action S_B. We therefore refer to the region around $y = \sqrt{2}$ as the crossover region since it is in this region that the behaviour of the fermion mass crosses over from following the small to the large y expressions.

3.4 Inclusion of Dynamical Fermions

In the dynamical theory the phase diagram is not yet completely determined. In the limiting cases of very small y (weakly coupled fermions) and very large y (fermions so heavy that they decouple) the quenched phase diagram will be recovered. In the intermediate region the symmetry of eqn. 3.13 is broken by the

Yukawa term and, for a given y, the PM / FM and PM / AFM phase transitions need not be symmetric about $\kappa = 0$. An analytic study [40] which expands about the points $y = 0$ and $y = \infty$ indicates that the effect of the fermionic action is always to favour ferromagnetic ordering. Hence both the phase boundaries turn downwards as they approach the crossover region. However, such expansions fail to converge in the crossover region itself.

Fig. 3.2 shows the proposed phase diagram at some arbitrary λ [40]. Although the positions of the phase boundaries may change with λ there will be no qualitative difference in the phase structure. Whether the PM1/PM2 boundary persists in the dynamical model or if there is some intervening phase is unknown. If it exists, then it is presumably a bona fide phase transition unlike the quenched crossover region.

3.5 The Crossover Region

The interesting region as far as the fermion dynamics is concerned is the region close to $y = \sqrt{2}$. In dynamical studies it becomes very difficult to invert the fermion matrix (the number of conjugate gradient iterations required in the hybrid monte carlo algorithm peaks dramatically [42]) making this region difficult to simulate. In quenched studies the same basic problem manifests itself as an inability to define the fermion mass from the two point function [37]. In addition, the domains of convergence of small and large y expansions do not include this region of y. These are signs that the fermion matrix is developing zero modes and hence the partition function is behaving in a singular fashion.

The difficulty of simulating the theory dynamically near the crossover region has lead to the introduction of a modified Yukawa term [43] which smears the local interaction of eqn. 3.15 over a hypercube.

$$S_Y = \sum_{i=1}^{n_f} \sum_{n} y_i \phi(n) \left(\frac{1}{2^d} \sum_{h} \bar{\chi}_i(n+h)\chi(n+h) \right) \tag{3.24}$$

This is the hypercubic form where $\{h\}$ are the 2^d vectors that span a hypercube and have elements $h_\mu = 0$ or 1. This reduces to the local form of eqn. 3.15 in the

naive $a \rightarrow 0$ limit with slowly varying fields, but removes the singular behaviour near $y = \sqrt{2}$. Other types of non-local Yukawa coupling have been considered (see ref. [44] for a definition using non-overlapping hypercubes) but we restrict our studies to that of eqn. 3.24.

This modification makes dynamical simulations possible in the crossover region but alters the phase structure for large y. We can see this if we write the local and hypercubic couplings in a more similar way than eqns 3.15 and 3.24. Both actions are of the form

$$S_Y = \sum_{i=1}^{n_f} \sum_n Y_i(n)\, \bar{\chi}_i(n)\chi_i(n) \tag{3.25}$$

where $Y_i(n)$ takes the values

$$Y_i(n) = y_i\, \phi(n) \tag{3.26}$$

for the local form and

$$Y_i(n) = y_i \left(\frac{1}{2^d} \sum_h \phi(n-h) \right) \tag{3.27}$$

for the hypercubic form.

In the large y limit we neglect the free fermion action S_F (eqn. 3.14) and the fermionic integration can be done to leave the effective partition function

$$Z_{EFF} = \int \{d\phi\} \prod_n Y^2(n)\, exp\, (-S_B) \tag{3.28}$$

where we have set $n_f = 2$, $y_1 = y_2 = y$ and dropped the subscript 'i'. For simplicity we now consider the case of a radially fixed Higgs field. With the local form of Y of eqn. 3.26, Y^2 is a constant and we recover the purely bosonic theory. However, with the hypercubic form of Y (eqn. 3.27) this is not true. There can be no pure AFM phase since this would mean $Y(n) = 0$ (the average field over a hypercube being zero) and hence AFM configurations have zero weight in the partition function via eqn. 3.28. Paramagnetic configurations have $\langle Y(n) \rangle = 0$ and hence will be heavily suppressed.

The hypercubic form favours ferromagnetic ordering as $y \rightarrow \infty$. Numerical

studies [43] have shown that there is no PM2 phase and that the AFM phase at large negative κ is replaced by a ferrimagnetic (FI) phase at large y. This phase has simultaneous ferromagnetic and antiferromagnetic ordering with both $<\phi>$ and $<\phi_{st}>$ non-zero. The proposed phase diagram for hypercubic coupling is shown in fig. 3.3 [43].

The true nature of the crossover region with local coupling has been left unclear by previous numerical and analytic studies. It needs to be investigated since it is a very general feature of Higgs systems with a local Yukawa interaction. It is clear that the dynamics are dominated in the crossover region by the fermionic part of the action, and even in the quenched theory the fermionic observables are rapidly changing functions of y.

This current lack of understanding motivates us to study the eigenvalue spectrum of the fermion matrix. Such a study will hopefully explain the reasons for the singular behaviour in the crossover region (which points to an ill conditioned fermion matrix and hence the presence of small fermionic eigenvalues) and for the spontaneous generation of mass at large y in the symmetric phase. We would also hope to be able to explain exactly why the hypercubic form of the coupling alleviates these problems near $y = \sqrt{2}$. Since we are mainly interested in the qualitative features inherent in all lattice Higgs systems with local Yukawa couplings we study the simplest model that contains all the relevant physics.

3.6 The Ising Limit

The lattice form of the action for a real scalar field, eqn. 3.8, makes it clear that the self interaction term proportional to λ tends to radially fix the ϕ field to unit length to reduce the action. In the limit $\lambda \rightarrow \infty$ this forces $\phi^2 = 1$. The self interaction term vanishes and the quadratic mass term is an irrelevant constant. The action reduces to

$$S_B = -2\kappa \sum_n \sum_\mu \phi(n)\phi(n+\mu) \qquad (3.29)$$

where $\phi = \pm 1$. This is the well known Ising model [45].

The pure Ising model has the same three phases (AFM, PM and FM) as the model defined at finite λ via eqn. 3.8. A mean field calculation [36] gives the value of the critical hopping parameter $\kappa_c = (4d)^{-1} = 0.0625$, whereas a full monte carlo computer simulation [46] gives $\kappa_c = 0.07483(2)$. There are many simplifications which can be made due to the constraint that the 'spin ' variables ϕ satisfy $\phi = \pm 1$, making it an attractive model to simulate in the quenched approximation. There are, however, problems in simulating the full theory due to the discrete nature of the Ising spins. Since the spins are not continuous we cannot define a continuous momentum by differentiation of the action with respect to the field. We are therefore unable to easily use the Hybrid Monte-Carlo algorithm described in section 1.7.2 since this relies on the introduction of a continuous momentum variable to implement the molecular dynamics equations of motion that evolve the system through phase space. We must use some alternative method which will be computationally more costly, but dynamical simulations will still be possible in sufficiently small volumes. It is worth noting that difficulties with the Hybrid Monte-Carlo algorithm were encountered at large finite λ in ref. [47], so this problem is not restricted to the pure Ising limit.

We choose the Ising limit for reasons of simplicity. However, the mounting evidence for the triviality of the action 3.8 [48] would suggest that the same results will be obtained in the continuum limit for any value of λ. The next step is to couple fermions to the Ising spins with local and hypercubic Yukawa couplings of the form of eqns 3.15 and 3.24 and to compute the eigenvalue spectrum of the fermion matrix.

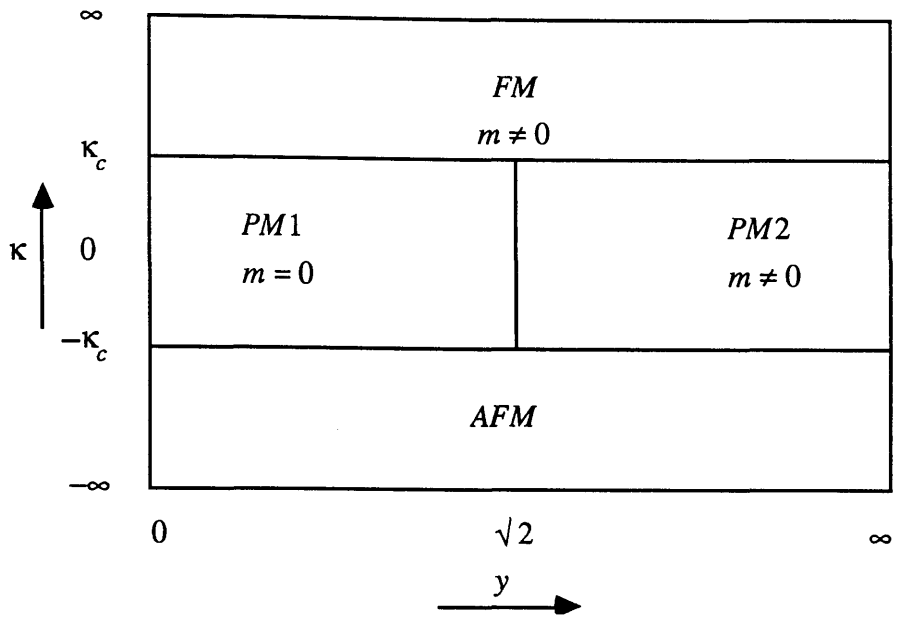

Fig. 3.1 The phase diagram of the quenched fermion / Higgs system with local Yukawa coupling y at some arbitrary λ. κ_c is the critical point in the purely bosonic theory with $y = 0$.

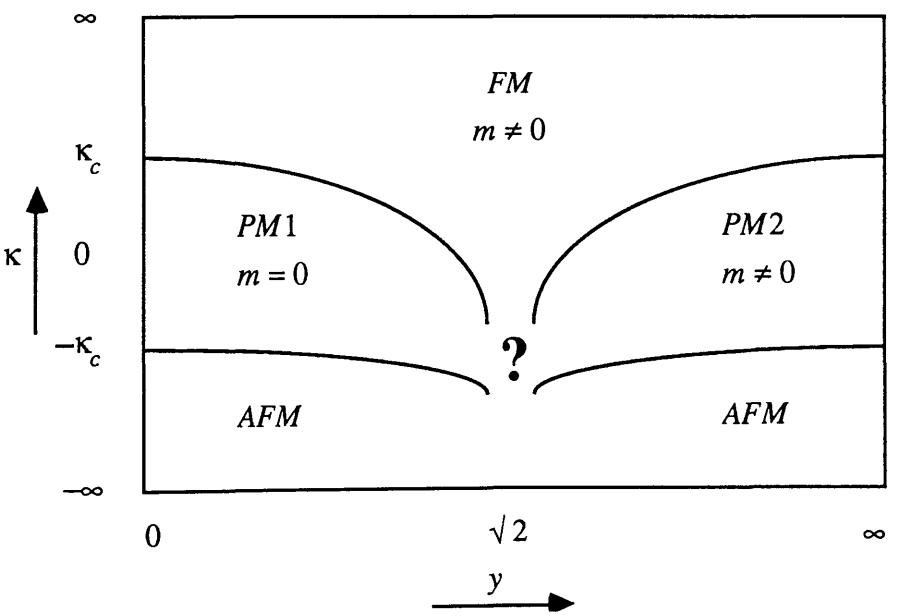

Fig. 3.2 The phase diagram of the full fermion / Higgs system with local Yukawa coupling y at some arbitrary λ. κ_c is the critical point in the purely bosonic theory with $y = 0$. The structure at large negative κ is unknown.

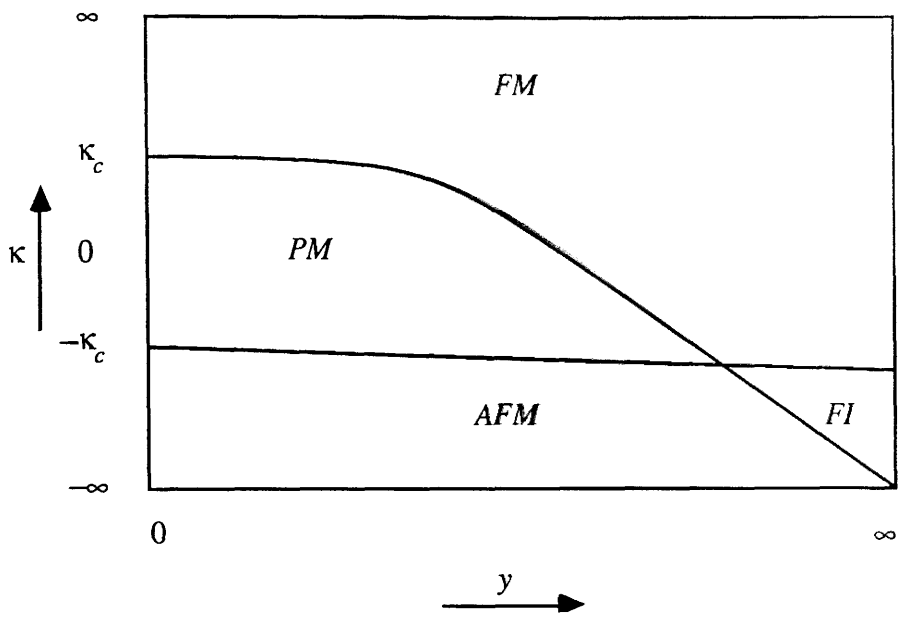

Fig. 3.3 The phase diagram of the full fermion / Higgs system with hypercubic Yukawa coupling y at some arbitrary λ. κ_c is the critical point in the purely bosonic theory with $y = 0$.

From now on we will refer to the fermion matrix $M_{KS}+Y_i$ as M_i. Having integrated out the fermions we obtain

$$Z = \int d\{\phi\} \prod_{i=1}^{n_f} det(M_i\{\phi\} + m_i)\, exp\,(-S_B) \tag{4.7}$$

The expression for a fermionic variable such as the chiral condensate is

$$\langle\bar{\chi}_j\chi_j\rangle = \frac{\partial}{\partial m_j} ln\, Z \,|_{m_j=0} = \frac{1}{Z}\int d\{\phi\}\, Tr(M_j^{-1}) \prod_{i=1}^{n_f} det(M_i) exp\,(-S_B) \tag{4.8}$$

Expressing the trace as the sum of the inverse eigenvalues of M_j immediately shows the importance of the eigenvalue spectrum.

For our initial studies we use the quenched approximation, which is to assume that all the fermionic determinants are independent of the configuration $\{\phi\}$. The quenched average of eqn. 4.8 is

$$\langle\bar{\chi}_j\chi_j\rangle_Q = \frac{1}{Z_B}\int d\{\phi\}\, Tr(M_j^{-1})\, exp\,(-S_B) \tag{4.9}$$

where Z_B is the purely bosonic (Ising) partition function. The different fermion species have decoupled since they have no dynamics associated with them. From now on we consider the behaviour of only one fermion species in the background ϕ field and drop the species subscript.

4.2 Simulating the Ising Model

To evaluate quenched expectation values such as eqn. 4.9 we simply have to generate spin configurations with the weight $exp(-S_B)$ and average the fermionic variable over them. Due to the simplicity of the Ising model we use a heatbath algorithm. The probability of a particular variable $\phi(n)$ being 'up' (having value +1) is, from eqn. 1.40,

$$P_{up}(n) = \frac{exp\left(2\kappa \sum_m \phi(m)\right)}{2\, cosh\left(2\kappa \sum_m \phi(m)\right)} \tag{4.10}$$

where the sum runs over the $2d$ nearest neighbour sites of the site n.

The Ising model only couples even to odd and odd to even sites and we can update all the even or odd sites simultaneously without altering eqn. 4.10. We therefore store the lattice in 'red/black' order [49] where the sites $n = 1 \rightarrow N/2$ are all even and the remainder $n = N/2+1 \rightarrow N$ odd. This makes the algorithm very fast on a vector machine since each loop over $N/2$ sites is vectorisable with a stride of 1. Since the sum over nearest neighbours in eqn. 4.10 can only take $2d+1$ values, the possible values of P_{up} are calculated once and stored in a look-up table.

The heatbath algorithm is very fast for the Ising model and makes the generation of spin configurations a negligible overhead compared to the evaluation of fermionic observables. However, it becomes very inefficient near criticality. At the second order phase transition points $\kappa = \pm\kappa_c$ the spins become correlated over long distances of the order of the lattice size. A local updating procedure is unable to flip these large domains of aligned spins. The system proceeds very slowly through phase space and the number of sweeps taken to produce a statistically independent configuration becomes very large. The solution is to use cluster algorithms [50] which identify and flip whole clusters of spins at once. The computational overheads of identifying the clusters in each configuration are far outweighed by the large reduction in the autocorrelation time near criticality. However, as long as we work on relatively small volumes and/or in regions well away from criticality where the correlation length is small the heatbath algorithm will suffice.

Figure 4.1 shows the values of the most important bosonic quantities $<\phi>$ and $<\phi(n)\phi(n+\mu)>$ as a function of κ on an 8^4 lattice. We always average the absolute value of the magnetisation so we can never obtain zero on a finite lattice even in the PM phase. In the FM phase we observe tunneling between the two degenerate minima where the system is magnetised either up or down. This is a finite volume effect and in the infinite volume limit it would not be necessary to average the absolute values of $Z(2)$ non-invariant quantities in order to obtain non-zero expectation values. In this limit $<\phi>$ is discontinuous across κ_c whereas $<\phi(n)\phi(n+\mu)>$ is continuous across and non-zero at the phase transition.

4.3 The Fermion Matrix M

We first consider the properties of the eigenvalue spectrum of M. M is a non-hermitian matrix and hence has complex eigenvalues. It is instructive to write the fermion matrix in even/odd form, which is the order in which we store the lattice sites for the Ising spins. In this form the fermion matrix is

$$M = \begin{pmatrix} 0 & \tilde{M} \\ -\tilde{M}^{\dagger} & 0 \end{pmatrix} + \begin{pmatrix} Y_e & 0 \\ 0 & Y_o \end{pmatrix} \tag{4.11}$$

where $\tilde{M}$ is the part of M_{KS} that hops from odd to even sites and the even and odd parts of Y are diagonal. The important symmetry is generated by the even/odd projectors P_e and P_o which in the form of eqn 4.11 are given by

$$P_e = \begin{pmatrix} I & 0 \\ 0 & 0 \end{pmatrix}, \; P_o = \begin{pmatrix} 0 & 0 \\ 0 & I \end{pmatrix} \tag{4.12}$$

where I is the $N/2$ x $N/2$ unit matrix. It is easy to see that the hermitian operator $P_e - P_o$ anticommutes with the fermionic derivative M_{KS} and commutes with the diagonal Yukawa coupling matrix Y. Hence we have the relationships

$$(P_e - P_o)\, M_{KS}\, (P_e - P_o)^{\dagger} = -M_{KS} = M_{KS}^{\dagger} \tag{4.13}$$

$$(P_e - P_o)\, Y\, (P_e - P_o)^{\dagger} = Y = Y^{\dagger} \tag{4.14}$$

and therefore

$$(P_e - P_o)\, M\, (P_e - P_o)^{\dagger} = M^{\dagger} \tag{4.15}$$

Since M is unitarily related to $M^{\dagger}$ they both possess the same eigenvalues. The eigenvalues of $M^{\dagger}$ are the complex conjugates of those of M and this means that the eigenvalues of M must either come in complex conjugate pairs or be exactly real. This is in fact trivial in our case since M is purely real and must possess the (λ,λ^*) symmetry to ensure that the determinant is real. However, eqn. 4.15 will hold even when M_{KS} is a covariant derivative including complex gauge fields since all that is required for the relation to hold is that M_{KS} be anti-hermitian and connect only nearest neighbour sites.

4.3.1 The Free Case

At $y = 0$ we only have the free part M_{KS}. This is anti-hermitian and hence has purely imaginary eigenvalues $i\lambda_0$ with λ_0 real. The eigenvalues come in $\pm i\lambda_0$ pairs due to the (λ,λ^*) symmetry. The eigenvalues of these free modes are given by

$$\lambda_0 = \sqrt{\sum_\mu sin^2 p_\mu} \tag{4.16}$$

The allowed values of the momenta p_μ are determined by the dimensions of the lattice L_μ and the boundary conditions.

$$p_\mu = 2n_\mu \frac{\pi}{L_\mu} \quad \text{for periodic boundary conditions in the } \mu \text{ direction.} \tag{4.17}$$

$$p_\mu = (2n_\mu+1) \frac{\pi}{L_\mu} \quad \text{for anti-periodic boundary conditions.} \tag{4.18}$$

where $n_\mu = 0, 1, \ldots L_\mu\text{-}1$ to restrict the momenta to the region $0 \le p_\mu < \pi$. There is a large degeneracy in the free spectrum which will hopefully be broken by the Yukawa interactions. In the extreme case of a 4^4 lattice with antiperiodic boundary conditions in all directions there is only one distinct eigenvalue with $\lambda_0 = \sqrt{2}$, but on larger volumes there are many more free modes.

4.3.2 Interacting Case

The (λ,λ^*) symmetry means that $det(M)$ is real. However, it is not necessarily positive since M can have exactly real eigenvalues that have no complex conjugate partner. If there is an odd number of negative real eigenvalues then the determinant will be negative. In such a case we cannot interpret $det(M)$ as a probability and a dynamical simulation algorithm will fail at the metropolis accept/reject step unless we have two species of fermion with the same Yukawa coupling matrix Y to square up the determinant. This does not matter in the quenched approximation but forces n_f to be even for the full model.

For certain special spin configurations $\{\phi\}$ we can evaluate the the eigenvalue spectrum analytically. If we have a pure ferromagnetic configuration with $\langle\phi\rangle = 1$ ($\kappa = +\infty$) the matrix Y reduces to yI in both the local and hypercubic cases. Hence the eigenvalues are given by $\lambda = y \pm i\lambda_0$.

In a purely antiferromagnetic configuration with $\langle\phi_{st}\rangle = 1$ ($\kappa = -\infty$) the hypercubic Yukawa coupling vanishes and we recover the free ($m = 0$) case. For the local form we can write the fermion matrix M as $M_{KS} + y(P_e - P_o)$. Hence

$$M^2 = M_{KS}^2 + \{M_{KS}, P_e - P_o\} + y^2 = M_{KS}^2 + y^2 \qquad (4.19)$$

since M_{KS} anticommutes with $(P_e - P_o)$. The eigenvalues of M are of the form

$$\lambda = \sqrt{y^2 - \lambda_0^2} \qquad (4.20)$$

with λ_0 given by eqn. 4.16. The eigenvalues are purely real or imaginary and there are exact zero modes whenever $y = \pm\lambda_0$.

For any finite value of κ between these limits we need to extract the eigenvalues by some numerical method. This is done with the non-hermitian Lanczos algorithm since M is a non-hermitian matrix.

4.4 The Non-Hermitian Lanczos Algorithm

The non-hermitian Lanczos algorithm [51] uses the fact that any matrix M can be tri-diagonalised by a similarity transformation generated by some matrix X and its inverse, ie we try to solve

$$X^{-1} M X = T \qquad (4.21)$$

for X where T is some symmetric tridiagonal form with complex entries. In the special case where M is hermitian then X can be chosen to be unitary and $X^{-1} = X^\dagger$. The tridiagonal form then has real entries and the algorithm becomes the hermitian Lanczos algorithm described in section 2.3. As in the hermitian case we write X as a series of N column vectors x_i (the x Lanczos vectors). However, since X is not unitary we must also calculate its inverse. For convenience we choose to generate $Y = (X^{-1})^\dagger$ which we write as a series of N column vectors y_i (the y Lanczos vectors). Since $Y^\dagger X = I$ the x and y Lanczos vectors must satisfy

$$y_i^\dagger x_j = \delta_{i,j} \qquad (4.22)$$

The algorithm rests on the observation that the x and y Lanczos vectors are

completely determined once we have chosen x_1 and y_1 subject only to eqn. 4.22. If we write T in the form of eqn. 2.10 but allow for the α_i and β_i to be complex then the recurrence relations for the x_i are

$$X_i = M x_i - \alpha_i x_i - \beta_{i-1} x_{i-1} \tag{4.23}$$

$$x_{i+1} = X_i \beta_i^{-1} \tag{4.24}$$

and the conjugate relations for the y_i

$$Y_i = M^\dagger y_i - \alpha_i^* y_i - \beta_{i-1}^* y_{i-1} \tag{4.25}$$

$$y_{i+1} = Y_i (\beta_i^*)^{-1} \tag{4.26}$$

The α_i and β_i are found at each step from

$$\alpha_i = y_i^\dagger M x_i \tag{4.27}$$

$$\beta_i^2 = Y_i^\dagger X_i \tag{4.28}$$

where we set $\beta_0 = 0$ so that the same equations apply for i=1.

The iterative procedure ends (in exact arithmetic) when we encounter $\beta_i = 0$ for some $i \leq N$. Termination will occur in less than N iterations for $i = N - n$ either if x_1 (y_1) is orthogonal to n of the right (left) eigenvectors of M, or if there is an n-fold degeneracy in the eigenvalue spectrum of M. In a practical implementation on a computer we will never have $\beta_{N-n} = 0$ due to rounding errors which grow exponentially and spoil the relationship 4.22. In order to preserve the global mutual orthogonality of the x and y Lanczos vectors we must store all of them and reorthogonalise each new vector against its predecessors. The reorthogonalisation step is

$$x_i \rightarrow x_i - \sum_{j=1}^{i-1} (y_j^\dagger x_i)\, x_j \tag{4.29}$$

$$y_i \rightarrow y_i - \sum_{j=1}^{i-1} (x_j^\dagger y_i)\, y_j \tag{4.30}$$

and now we do achieve $|\beta_{N-n}|$ sufficiently small to terminate. In practice, where we choose x_1 and y_1 at random, it is always a degeneracy that causes early termination of the algorithm rather than some problem with the initial conditions.

Once we have generated the tridiagonal form T, we still require to find the eigenvalues. This is done by the QL algorithm which applies judiciously chosen rotations to T of the form $T \rightarrow R^{\dagger}T\,R$ to reduce it to diagonal form. The form of the algorithm that we implement has 'implicit shifts' [52] which minimises rounding errors and increases the numerical stability.

Assuming no degeneracy in the spectrum of M, the non-hermitian Lanczos algorithm will require $2N$ operations of the form M x *vector* along with a total of $N(N+1)$ individual reorthogonalisations of one vector against another. Since M is sparse the matrix/vector operations are of order N, and reorthogonalisation becomes the major computational task for large N with the time taken growing as N^3. The time needed for the QL algorithm is again negligible for large N. The storage required is dominated by the need to store all $2N$ Lanczos vectors simultaneously, which requires the storage of $2N^2$ complex numbers. Due to the limited availability of computer time and storage the algorithm described above is only practicable for volumes of the order of 4^4, and it is necessary to consider ways of improving the algorithm given the specific form of the fermion matrix.

4.4.1 Use of Symmetries of M

The fact that M and $M^{\dagger}$ are unitarily related by eqn. 4.15 suggests that we might be able to directly relate the x and y Lanczos vectors since they are generated by M and $M^{\dagger}$ respectively. This would halve the storage and computation required. To this end we suppose we can find some unitary hermitian matrix U which satisfies

$$U\,M\,U^{\dagger} = M^{\dagger},\; U^{\dagger}U = \mathbf{1},\; U = U^{\dagger} \tag{4.31}$$

We now consider the Lanczos algorithm at some step 'i' and assume that β_j^2 is real for $1 \leq j \leq i\text{-}1$ and that the relationship between y_i and x_i is of the form

$$y_i = \prod_{j=1}^{i-1} sgn(\beta_j^2)\, Ux_i = s_i\, Ux_i \tag{4.32}$$

where sgn(x) is +1(-1) if x is greater (less) than 0 for some real number x. Hence $s_i = \pm 1$. We will eventually take $U = P_e - P_o$ to satisfy eqn 4.31 but we shall keep the proof as general as possible. By substituting this expression for y_i in eqn 4.27 we have

$$\alpha_i = x_i^\dagger (UM) x_i \tag{4.33}$$

and α_i is real since UM is hermitian by eqn. 4.31. Using this in eqn. 4.25 gives

$$\begin{aligned} Y_i &= s_i (M^\dagger - \alpha_i) Ux_i - \beta_{i-1}^* s_{i-1} Ux_{i-1} \\ &= s_i U(M - \alpha_i) x_i - \beta_{i-1} s_i Ux_{i-1} \\ &= s_i UX_i \end{aligned} \tag{4.34}$$

where we have used $\beta_{i-1}^* = sgn(\beta_{i-1}^2)\, \beta_{i-1}$ since β_{i-1}^2 is real by assumption. Hence by eqn. 4.28

$$\beta_i^2 = s_i X_i^\dagger UX_i \tag{4.35}$$

and is real. Finally we find that the new y Lanczos vector from eqn. 4.26 is

$$\begin{aligned} y_{i+1} &= Y_i (\beta_i^*)^{-1} \\ &= s_i\, sgn(\beta_i^2)\, UX_i\, \beta_i^{-1} \\ &= s_{i+1}\, Ux_{i+1} \end{aligned} \tag{4.36}$$

Hence the assumption is true for i+1 if it is true for i. We can ensure the assumption is true trivially for i=1 if we set $y_1 = s_1 Ux_1$ where we are free to choose $s_1 = \pm 1$. The only restriction is that the orthogonality condition (eqn. 4.22) must hold. Hence by induction eqn. 4.32 is true for all i and we only have to generate and store the x Lanczos vectors since we can easily derive the y vectors from them. An added bonus of this particular choice of initial conditions is that all α_i are real and β_i purely real or imaginary. The only overhead is that we have to keep track of the value of s_i which changes sign whenever β^2 is less than zero.

The reorthogonalisation of the x Lanczos vectors via eqn. 4.29 is simple using eqn. 4.32 and we do not have to reorthogonalise the y vectors. The choice of U that we require is $U = P_e - P_o$. This means that the typical dot products that have

to be computed are particularly straightforward when we store the lattice in even/odd order, ie

$$y^\dagger Ux = y^\dagger(P_e - P_o)x = y_e^\dagger x_e - y_o^\dagger x_o \tag{4.37}$$

is easy to calculate and vectorisable since we store the even and odd parts of each vector separately.

The fact that we can relate the y Lanczos vectors to the x Lanczos vectors means we save a factor of 2 in computer time and storage, making it possible to extract the eigenvalues of M on lattices as large as 6^4.

4.4.2 Implementation in Real Arithmetic

We can make further use of the symmetry of eqn. 4.31 if we choose the first Lanczos vector x_1 to be real. Since the α_i are real and the β_i purely real or imaginary, the x_i will have purely real or imaginary elements. This is also true for the X_i which are constructed from them. We therefore only have to deal with the absolute value of β and real vectors v' defined as

$$v = v' \text{ if } v \text{ is real} \tag{4.38}$$

$$v = iv' \text{ if } v \text{ is imaginary} \tag{4.39}$$

All we have to do is keep track of whether particular Lanczos vectors and β's are real or imaginary and insert any resulting minus signs by hand. This can be done simply by comparing s_i with its initial value s_1 and checking the signs of the most recent values of β^2.

The recurrence relations for the real Lanczos vectors x_i' are derived by considering all possible combinations of the various signs of s_i and β^2 and are given by

$$X_i' = Mx_i' - \alpha_i x_i + |\beta_{i-1}|x_{i-1} \quad \text{if } s_i = s_1 \text{ and } \beta_{i-1}^2 < 0 \tag{4.40}$$

$$= Mx_i' - \alpha_i x_i - |\beta_{i-1}|x_{i-1} \quad \text{otherwise.} \tag{4.41}$$

$$x_{i+1}' = -X_i' |\beta_i^{-1}| \quad \text{if } s_i = s_1 \text{ and } \beta_i^2 < 0 \tag{4.42}$$

$$= X_i' |\beta_i^{-1}| \quad \text{otherwise} \tag{4.43}$$

The α_i and β_i are calculated from eqns. 4.27 and 4.28 as before, since these equations are unaffected by factors of $\pm 1, \pm i$ in the x_i. Although only the absolute value of beta is needed for the Lanczos algorithm we must store the full complex value for subsequent use by the QL algorithm.

The reorthogonalisation procedure goes through unchanged. After each iteration we make the replacement

$$x'_i \rightarrow x'_i - \sum_{j=1}^{i-1} s_j \, (x'^{\dagger}_j U \, x'_i) \, x'_j \qquad (4.44)$$

There seems to be no further room for improvement of the algorithm other than fine tuning of the computer program that implements it. By making full use of the symmetry of M expressed in eqn. 4.15 we are able to find all the eigenvalues of M using an algorithm that works almost entirely in real arithmetic. On large volumes, where the time required for reorthogonalisation is much greater than that required for all the other Lanczos steps and for the QL algorithm, the storage grows as N^2 and the time as N^3. By halving the number of vectors and working in real arithmetic this results in a four-fold reduction in storage and an eight-fold increase in speed over the original algorithm of eqns. 4.23 to 4.30.

4.4.3 Tests of Numerical Accuracy

We need an independent check on the eigenvalues that we compute in order to monitor numerical stability. An obvious check is that the absolute value of the last beta is very small and that the (λ,λ^*) symmetry is realised in the spectrum. This is not sufficient, however, since this symmetry is guaranteed by the reality of the α_i and β^2_i. If the symmetry were violated it would be a failure of the QL algorithm and we have never encountered problems with this part. Having a very small value for β_N is also no guarantee that the eigenvalues are correct since this would be the case for any (random !) set of Lanczos vectors due to the reorthogonalisation steps.

In practice we check the sum and the sum of the squares of the eigenvalues.

These values are known since it is obvious from eqn. 4.11 that the trace of the fermion matrix is given by

$$Tr(M) = \sum_{i=1}^{N} \lambda_i = \sum_{n=1}^{N} Y(n) \tag{4.45}$$

This expression only involves the real parts of the eigenvalues since the imaginary part is zero due to the (λ,λ^*) symmetry. Hence we also compute

$$Tr(M^2) = \sum_{i=1}^{N} \lambda_i^2 = -\frac{Nd}{2} + \sum_{n=1}^{N} Y^2(n) \tag{4.46}$$

The RHS of eqn. 4.46 is the sum of two terms. The first is the contribution from the $2d$ ways of hopping from each site to a neighbouring one and back again, which carries a weight of $-\frac{1}{4}$. The second is simply the contribution from staying on a given site. We could of course calculate higher order traces which would involve more hops and more complicated functions of the vector Y, but we regard eqns 4.45 and 4.46 as being sufficient.

4.5 The Eigenvalue Spectrum of M for Local Coupling

The eigenvalue spectra of M in the three phases (PM, FM and AFM) of the Ising model on a 6^4 lattice are shown in figures 4.2 to 4.16 where we display the data in the form of both scatter and 'lego' plots. The scatter plots make the general form of the distributions clear but since it is impossible to resolve closely packed eigenvalues the density of the eigenvalues is not apparent. To reveal the density distribution we bin the data and plot the the number of eigenvalues in each bin on the vertical scale of a 3D plot of the complex eigenvalue plane. Each figure is the superposition of 4 spectra taken from 4 different configurations separated by 10000 heatbath sweeps. The configurations are definitely independent since tunneling was observed in the FM phase and the spins had to be rotated to align all the magnetisations. The values of y are chosen to lie below, in and above the expected location of the crossover region around $\sqrt{2}$. We use the local form of the Yukawa coupling (eqn. 3.26) so the Yukawa term on each site is $\pm y\,\bar{\chi}\chi$. The fermionic

boundary conditions are chosen to be periodic in the three spatial dimensions and antiperiodic in the temporal one, which simply involves changing the sign of $\alpha_\mu(n)$ in eqn. 4.4 whenever $n_0 = L_0$. The sum and sum of the squares of the eigenvalues were always checked using eqns. 4.45 and 4.46. Some typical numbers are given in table 4.1.

	$\kappa = 0.04$, $y = 0.5$	$\kappa = 0.08$, $y = 2.0$
$Tr(M)$	0.9999998	1175.99999998
Eqn. 4.45 gives	1.0000000	1176.00000000
$Tr(M^2)$	-2268.0002	2591.99998904
Eqn. 4.46 gives	-2268.0000	2592.00000000

Table 4.1 Tests of the numerical accuracy of the computed eigenvalues of M on a 6^4 lattice compared to the exact analytic results.

Given that each trace is the sum of 1296 separately calculated quantities we see from table 4.1 that the agreement is very good and we conclude that the eigenvalues are being computed correctly. We discuss the three Ising phases in turn.

4.5.1 The PM Phase

The spectra in the PM phase obtained at $\kappa = 0.04$ and $y = 0.5$, 1.2, 1.4 and 1.6 are shown in figs. 4.2 to 4.5. These figures immediately clarify the distinction between the PM1 (small y) and PM2 (large y) regions in terms of the eigenvalues of M. For small y the eigenvalues are perturbed slightly from their free values $\pm i\lambda_0$, where for our choice of lattice volume and boundary conditions λ_0 can take the values 0.50, 1.00, 1.32, 1.58 and 1.80. By choosing a very small value of y much smaller that the minimum separation between the free modes we have checked that the multiplicity of the eigenvalues corresponding to a given λ_0 is given by the multiplicity of λ_0 predicted by eqn. 4.16.

As y is increased from zero the eigenvalues move away from their free values

as seen in figure 4.2. The distribution spreads out with the direction of flow varying from being parallel to the real axis to being directly towards it. The overall effect is to broaden the spectrum symmetrically about the imaginary axis and to move it closer to the real axis. Throughout the small y region ($y < 1.2$) there are purely imaginary eigenvalues present in the spectrum but no purely real ones, and hence the fermionic determinant will be positive due to the (λ, λ^*) symmetry.

As we approach the crossover region figures 4.3 and 4.4 show that there are many small eigenvalues present. The purely imaginary eigenvalues of the small y region transfer to the real line by meeting at a point on the real axis very close to the origin. Typically these eigenvalues then move off in different directions along the real axis. There will therefore be exact zero modes on a given configuration for the values of y at which one of these real eigenvalues crosses the origin. Apart from these exact zeroes, there will be a high density of eigenvalues about zero for any value of y close to $y^* \approx 1.4$. Eigenvalues that meet on the real axis far from the origin take up distinct real values but both move away from the origin in the same direction with increasing y.

Exactly real eigenvalues are of special significance since their appearance can cause the determinant to change sign and also cause a singularity in the chiral condensate as a function of the bare fermion mass m. Although no computed eigenvalue will have an exactly zero imaginary part due to rounding errors we can still identify the real eigenvalues since the imaginary part will be very small. More importantly they will appear with no complex conjugate partner. At the point in the crossover region where an eigenvalue and its mirror image coalesce there must be an exact degeneracy. However, as y increases the two eigenvalues take up different values on the real axis and are free to move independently. Once an eigenvalue has joined the real axis it cannot leave as y is increased since to do so it has to have a complex conjugate partner. This constraint does not apply to the imaginary eigenvalues since there is no exact $(\lambda,-\lambda)$ symmetry, and they are free to leave the imaginary axis at any time.

For larger y figure 4.5 shows that there are no purely imaginary eigenvalues, and the spectrum consists of two distinct vertical bands well away from the origin. There is a slightly increased density of exactly real eigenvalues compared to those with small imaginary part as can be seen from figure 4.6. The sign of the determinant depends on the particular configuration being studied but will not change for a given configuration as y is increased further.

In the symmetric phase we observe an approximate symmetry in the eigenvalue spectrum about the imaginary axis. If we consider a particular set of spins and replace ϕ by $-\phi$ then this this takes M to $-M^{\dagger}$. Since $\langle\phi\rangle = 0$ the spin reversed configuration occurs with the same probability as the original one which means that $-\lambda^*$ occurs equally with λ when we take an ensemble average. This explains the approximate reflection symmetry in the PM phase which we would expect it to be broken in the FM phase. As a result $\langle\bar{\chi}\chi\rangle$ is zero throughout the PM phase.

Figures 4.2 and 4.5 show that the PM1 and PM2 phases are distinguished by the fact that there are imaginary eigenvalues but no real ones in PM1, and real eigenvalues but no imaginary ones in PM2. Figure 4.4 shows that the crossover region is the region of y where small fermionic eigenvalues are present and it is therefore no surprise that it is difficult to invert the fermion matrix for $y \approx \sqrt{2}$.

4.5.2 The FM Phase

The spectra in the FM phase were taken at $\kappa = 0.08$ (where $\langle\phi\rangle = 0.54$) and at $y = 0.5$, 1.2, 1.4 and 1.6. These are shown in figures 4.7 to 4.11. Due to the spontaneous magnetisation there is always an excess of eigenvalues with positive real part for all finite values of y. Other than this the qualitative features are the same as in the PM phase with some eigenvalues still making the transition from the imaginary to the real axis via the region around the origin for $y \approx 1.4$ (see fig. 4.9). However, more of the eigenvalues initially flow horizontally to the right away from the imaginary axis and never hit the real axis as is evident from fig. 4.7. We therefore expect the number of small modes when y is around y^* to be reduced.

The fact that we are far from a pure FM state at this value of κ is reflected in the fact that there are still many eigenvalues with negative real part at $y = 1.6$ (see figs. 4.10 and 4.11). For a pure FM state the free ($y = 0$) eigenvalues would simply be shifted a distance y along the real axis and none would have a negative real part. Although we do not observe this extreme behaviour, the overall asymmetry of the spectrum about the imaginary axis still means that $<\bar{\chi}\chi>$ is non-zero throughout the FM phase.

At κ values larger than 0.08 the Lanczos algorithm terminated before the N^{th} iteration with a very small β value. This was due to a degeneracy in the spectrum and not to a failure of the algorithm since the number of distinct eigenvalues did not change as the choice for the initial Lanczos vector x_1 was varied. This is no surprise since we know that as $\kappa \rightarrow \infty$ and $<\phi> \rightarrow 1$ the eigenvalues will tend to $y \pm i\lambda_0$ and we will encounter the enormous degeneracy of the free spectrum. We would, however, like to know the degeneracy of each eigenvalue in order to plot meaningful density distributions.

4.5.3 Coping with Degenerate Eigenvalues

It is possible to compute the eigenvalue degeneracies at large κ values by slightly perturbing the fermion matrix M_{KS} away from the free one. To do this we use the form given in eqn. 2.41 with $U_\mu(n) = exp(i\theta_\mu(n))$. If we take the θ_μ to be non-zero we can break the degeneracy at large κ. By taking θ_μ sufficiently small we can perturb the $\theta_\mu = 0$ eigenvalues by such a small amount that we can match the two spectra and identify degenerate $\theta_\mu = 0$ eigenvalues that have been perturbed into a cluster of very closely spaced eigenvalues. We therefore know the degeneracy of a particular eigenvalue by counting the number of eigenvalues in the corresponding cluster for $\theta_\mu \neq 0$. In practice we take the phase of this fictitious $U(1)$ gauge field to be

$$\theta_\mu(n) = \pi \frac{\delta_\mu(n)}{\Delta} \tag{4.47}$$

where δ_μ are random numbers in the interval (-1,1) and Δ is large, typically around 500. By having chosen U_μ such that $U_\mu^\dagger U_\mu = 1$, eqns. 4.45 and 4.46 are still true and we can easily check that the eigenvalues are correct. However M is no longer real and we must deal with complex Lanczos vectors. The price we pay in computer time makes the small perturbation approach impractical for large volumes so we have to run at relatively low values of the magnetisation if we require all N eigenvalues.

In models with gauge fields the degeneracy problem will be eradicated since the perturbations that we have had to introduce into the fermion matrix by hand will be generated by quantum fluctuations of the gauge fields present in the covariant fermionic derivative. The degeneracy problem is also less severe in models with continuous bosonic degrees of freedom [53] since this means that there are small fluctuations in the ϕ field even at high magnetisation that are enough to break the degeneracy present in the free spectrum. The degeneracy is reduced as the volume is increased since the fluctuations in the magnetisation are smaller, and the system is less likely to be in a highly magnetised (degenerate) state for a given value of κ.

4.5.4 The AFM Phase

The spectra in the AFM phase were taken at $\kappa = -0.08$ (where $\langle\phi_{st}\rangle = 0.54$) and at $y = 0.5$, 1.2, 1.6 and 1.9. These are displayed in figures 4.12 to 4.16. For larger values of $\langle\phi_{st}\rangle$ the same degeneracy problem encountered in the FM phase occurred. Just as the eigenvalue spectrum in the FM phase show signs of being that of a pure FM state by becoming asymmetric about the imaginary axis, the spectra in figs. 4.12 to 4.16 are showing signs of becoming those of a pure AFM state given by eqn. 4.20. There is an extremely high density of imaginary eigenvalues for $y << y^*$ and of real ones for $y >> y^*$ (see fig. 4.16 for a density plot at $y = 1.9$). However, the region around $y = y^*$ where small eigenvalues are present is much larger than in the FM or PM phases as is evident from figures 4.13, 4.14 and 4.15. The fact that we are still far from a pure AFM state is reflected in the fact that there

are still many eigenvalues at the four extreme corners of the spectrum as was observed in the PM phase (compare figs. 4.14 and 4.5), whereas for a pure AFM state all the eigenvalues are purely real or imaginary. The symmetry of the spectrum about the imaginary axis means that $<\bar{\chi}\chi>$ is zero throughout the AFM phase.

4.6 The Eigenvalue Spectrum of M for Hypercubic Coupling

The scatter plots of the eigenvalue spectrum of M in the three phases (PM, FM and AFM) of the Ising model are shown in figures 4.17 to 4.21 where we have used the hypercubic form of the Yukawa coupling (eqn. 3.27). The data was taken from the same configurations used in the study of the local coupling at κ values of 0.04, 0.08 and -0.08 respectively.

4.6.1 The PM phase

Figures 4.17 and 4.18 clarify why there is no crossover region in the PM phase around $y = \sqrt{2}$ for hypercubic coupling. There is no qualitative change in the shape of the eigenvalue spectrum as a function of y except that it is smeared out while remaining centred on the imaginary axis. All the eigenvalues move roughly horizontally and none show any sign of moving towards the real axis. Since this latter behaviour was the cause of the zero modes in M for local coupling we see that the hypercubic form eliminates the numerical problems associated with having an ill conditioned fermion matrix. Rather than simply making the local model well behaved through the crossover region, the introduction of the hypercubic form has removed this region altogether by removing the zero modes of M.

4.6.2 The FM Phase

Figures 4.19 and 4.20 show immediately that in the FM phase the spectrum at a given y is a smeared free spectrum displaced a distance of approximately $y<\phi>$ along the real axis. There are no zero modes and this explains why it is possible to define m_f from the fermion propagator for all values of the Yukawa coupling and

why it exhibits such smooth behaviour. Although there are still a few eigenvalues with negative real part there are far less than for local coupling, and there is no sign of any of the eigenvalues approaching the origin or the real axis.

In these studies the value of κ was taken to be the same as in the studies of the local Yukawa coupling so that direct comparisons could be made. For the local form, κ was chosen so the system was as deep as possible in the FM phase without there being any degeneracy in the spectrum of M. However, it is possible to go to much higher magnetisations with the hypercubic coupling before any degeneracy is observed because smearing the Yukawa interaction over a hypercube allows $Y(n)$ to have 2^d+1 distinct values between +1 and -1. This is sufficient to break the degeneracy present for the local form where $Y(n)$ can only take the values ± 1.

Although there are no signs of small eigenvalues in the fermion matrix for the parameters considered above, they do in fact appear for sufficiently large y. Fig. 4.21 shows the spectrum at $\kappa = 0.08$ and $y = 8.0$ and we see that eigenvalues have started to transfer to the real axis and small modes are present. However, this is probably not of any physical relevance since in the dynamical theory the system will be in a much more highly magnetised state at this value of y and the spectrum will change.

4.6.3 The AFM Phase

Figure 4.22 shows that in the AFM phase the eigenvalues remain close to their free values even for relatively large values of y. There is no sign of the appearance of zero modes as opposed to the very high number seen for local coupling, and we therefore expect fermionic variables to vary smoothly throughout this phase.

4.7 Obtaining m_f from the Eigenvalue Spectrum of M

We know that in a theory of completely free fermions with a bare mass term m_f the eigenvalues of M will be $m_f \pm i\lambda_0$ with the allowed values of λ_0 given by eqn. 4.16. In the infinite volume limit the spectrum will consist of a single vertical

band in the complex plane intercepting the real axis at m_f. Knowing this we can say that if the spectrum of M in some interacting theory is a vertical band of eigenvalues (or something approximating it) then the renormalised fermion mass will simply be the displacement of this band along the real axis.

Using this approach we can readily see that, at least for values of y less than 8.0, the hypercubic form of the Yukawa coupling gives a renormalised fermion mass of approximately $y\langle\phi\rangle$ since this is always the displacement of the eigenvalues along the real axis observed in the simulations in both the PM phase ($\langle\phi\rangle = 0$) and FM phase ($\langle \phi \rangle = 0.54$) (see figs. 4.18 and 4.20). Although the spectrum is rather smeared, there is always a high concentration of eigenvalues whose real part is $y\langle\phi\rangle$ and from additional simulations we find that the interacting spectrum rapidly approaches a free spectrum as κ is increased further into the FM phase. This explains why the fermion mass with hypercubic coupling follows the perturbative relationship $m_f = y\langle\phi\rangle$ for a large range of y and why there is no problem with defining m_f in the region $y \approx \sqrt{2}$ (see ref. [54] for data for m_f with hypercubic coupling at $y = 5$). Fig. 4.22 also supports the analytic result [54] that m_f vanishes for hypercubic coupling for all y in the AFM phase.

For the case of local coupling the situation is somewhat more complicated. Although at small y we observe what appears to be a smeared free spectrum, the eigenvalues in the FM phase are heavily concentrated around a vertical line that would intersect the real line at y. This might lead us to conclude that $m_f = y$ whereas we know from studies of the fermion propagator [37] that the perturbative relation $m_f = y\langle\phi\rangle$ holds in this region. At large y in both the FM and PM2 regions we observe two vertical lines of eigenvalues rather than the single line expected in a free theory. If we ignore the eigenvalues with negative real part and attempt to identify m_f as the intercept on the positive half of the real axis we obtain incorrect results (m_f shows almost no κ dependence which is inconsistent with ref. [37]). We postpone the question of how to consistently define m_f from the eigenvalue spectrum for local coupling to chapter 5.

4.8 Conclusions

By using the non-hermitian Lanczos algorithm we have been able to calculate all the complex eigenvalues of the fermion matrix on lattices as large as 6^4. Our studies of the eigenvalue spectrum of M on Ising spin configurations generated in the quenched approximation have shown that many of the known results concerning $Z(2)$ Higgs models defined with either local or hypercubic Yukawa coupling are easily explainable in terms of the fermionic eigenvalues.

For local coupling the paramagnetic phase is divided into two regions, PM1 and PM2, at small and large y. In PM1 the fermion matrix has exactly imaginary eigenvalues but no real ones, whereas in PM2 there are exactly real eigenvalues but no imaginary ones. The FM and AFM phases are similarly split into two regions. It has been noted previously that in an intermediate region of y around $\sqrt{2}$ the model becomes difficult to simulate dynamically due to difficulty with the inversion of the fermion matrix. In the same region in quenched simulations it becomes impossible to define the renormalised fermion mass m_f via the fermion propagator. Our studies have shown that both these problems are associated with the appearance of very small modes in this region of y regardless of the bosonic field configurations as eigenvalues transfer from the imaginary to the real axis via the origin.

The introduction of the hypercubic form for the Yukawa coupling has been observed to result in a model that has no PM2 phase and where no problems are encountered concerning dynamical simulation or the definition of m_f from the fermion propagator. We have shown that this is due to the complete absence of small eigenvalues in the range of y that has been considered and we can obtain values for m_f directly from the eigenvalue spectrum that are in agreement with the values derived from the propagator. It is however possible that problems may arise for very large values of y ($y > 8.0$) due to the appearance of small fermionic modes.

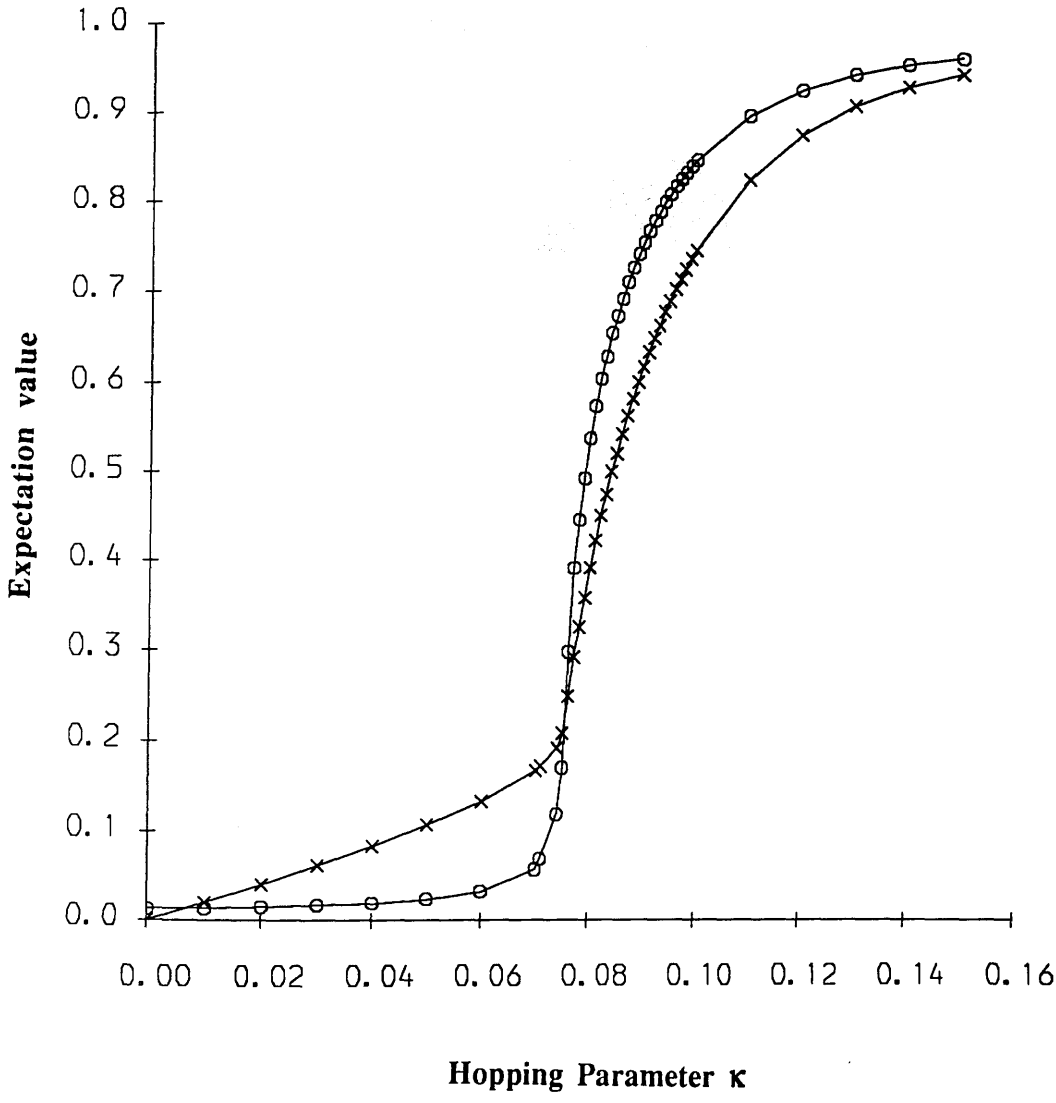

Fig. 4.1 The values of relevant observables vs.the hopping parameter for the Ising model on an 8^4 lattice: (o) $\langle\phi\rangle$, (×) $\langle z^2\rangle = \langle\phi(n)\phi(n+\mu)\rangle$.

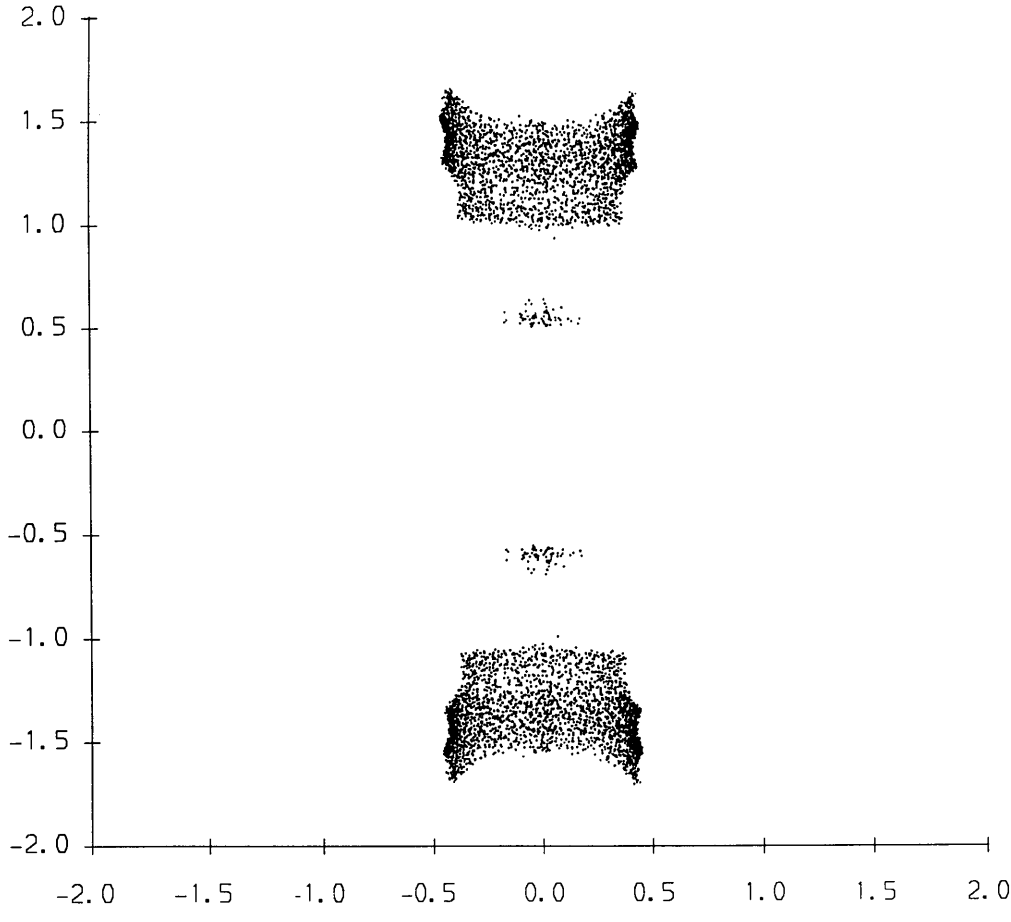

Fig. 4.2 The eigenvalue spectrum of M in the complex plane for a 6^4 lattice. Hopping parameter $\kappa = 0.04$, local Yukawa coupling $y = 0.5$.

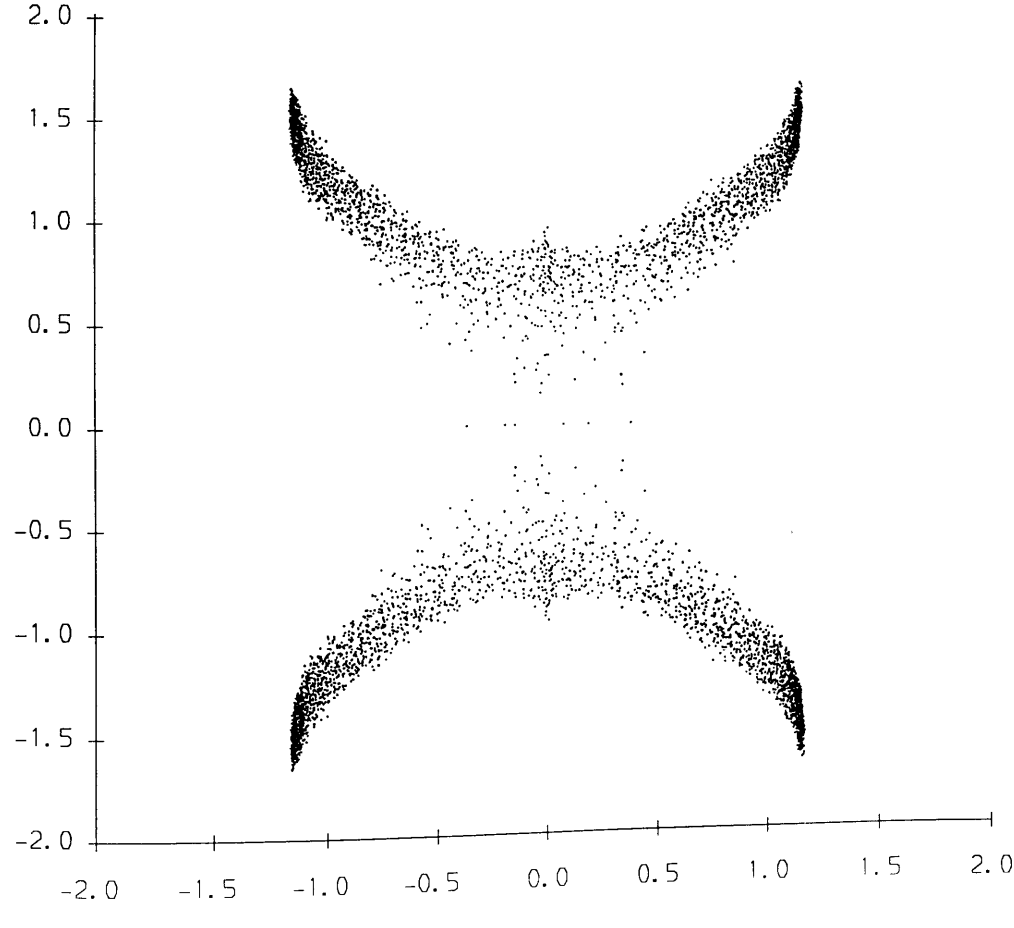

Fig. 4.3 The eigenvalue spectrum of M in the complex plane for a 6^4 lattice. Hopping parameter $\kappa = 0.04$, local Yukawa coupling $y = 1.2$.

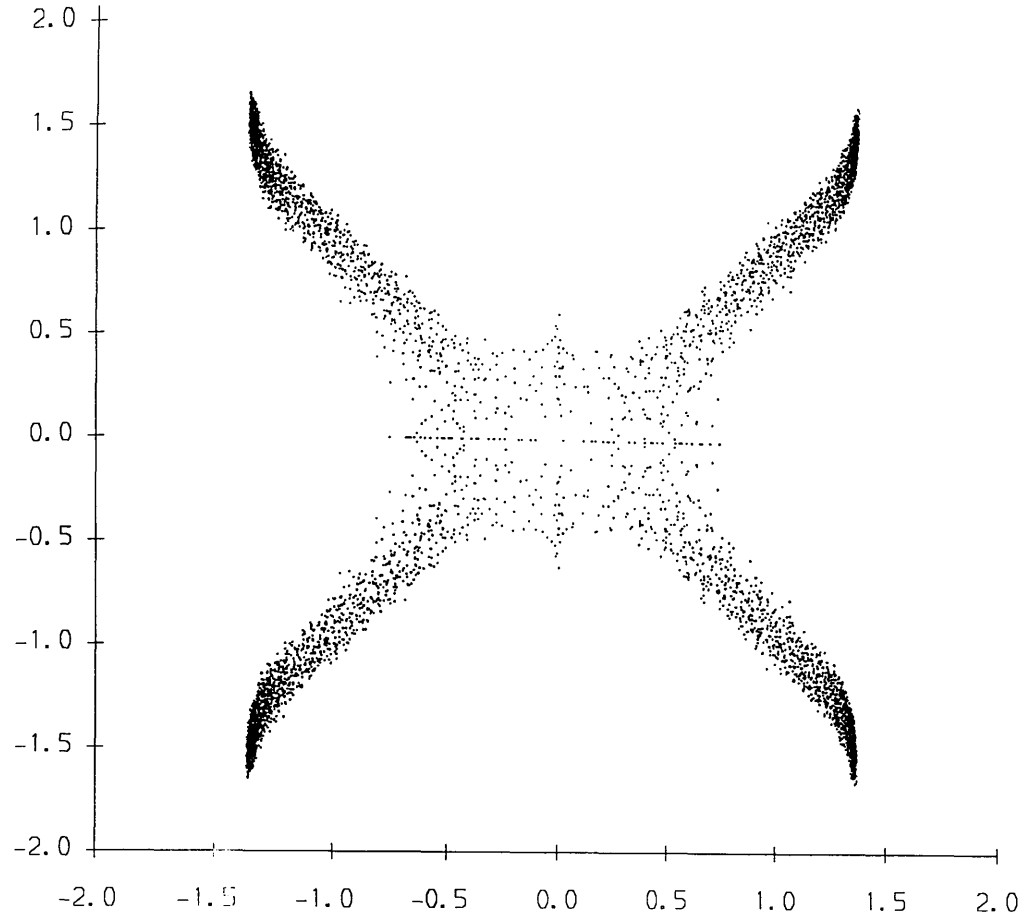

Fig. 4.4 The eigenvalue spectrum of M in the complex plane for a 6^4 lattice. Hopping parameter $\kappa = 0.04$, local Yukawa coupling $y = 1.4$.

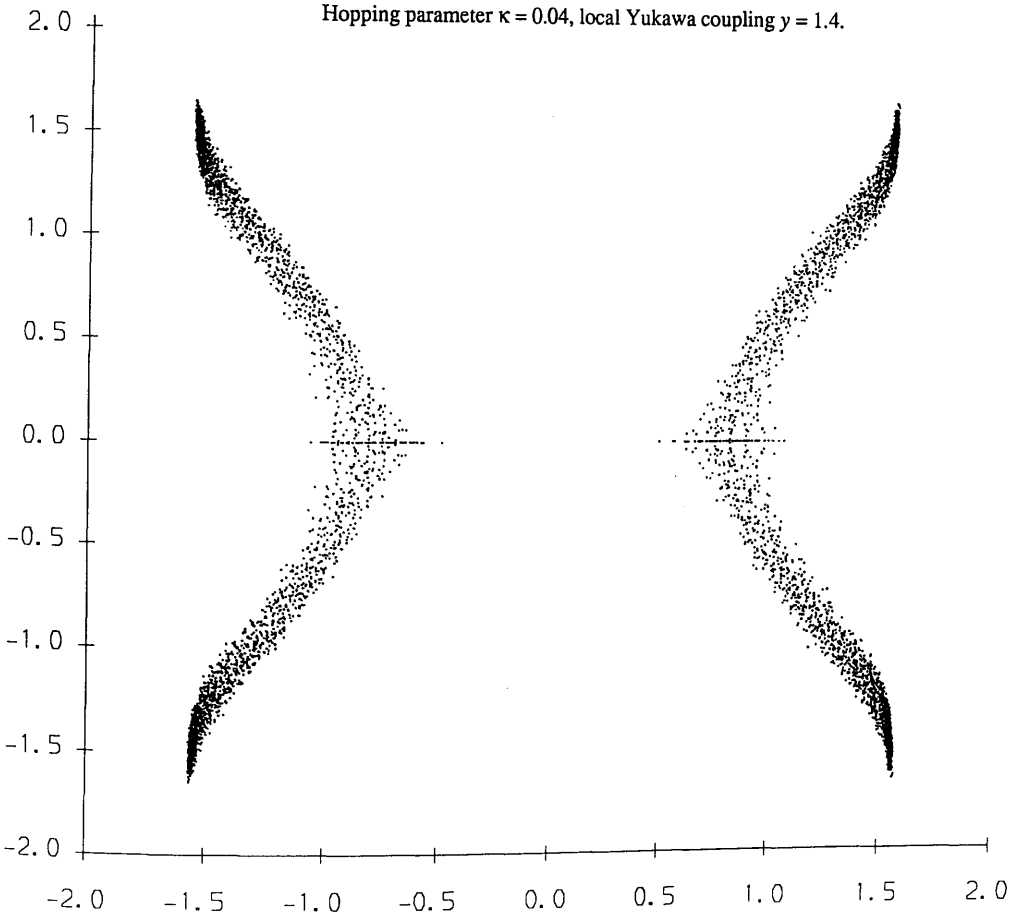

Fig. 4.5 The eigenvalue spectrum of M in the complex plane for a 6^4 lattice. Hopping parameter $\kappa = 0.04$, local Yukawa coupling $y = 1.6$.

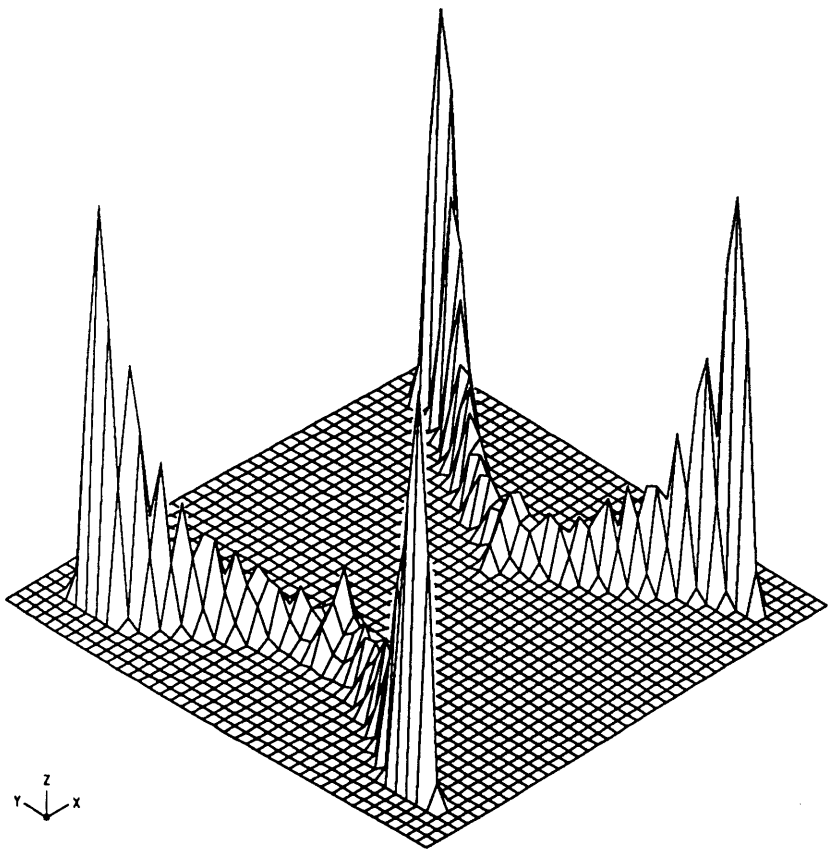

4.6 The density of eigenvalues of M in the complex plane for a 6^4 lattice. Hopping parameter $\kappa = 0.04$, local Yukawa coupling $y = 1.6$.

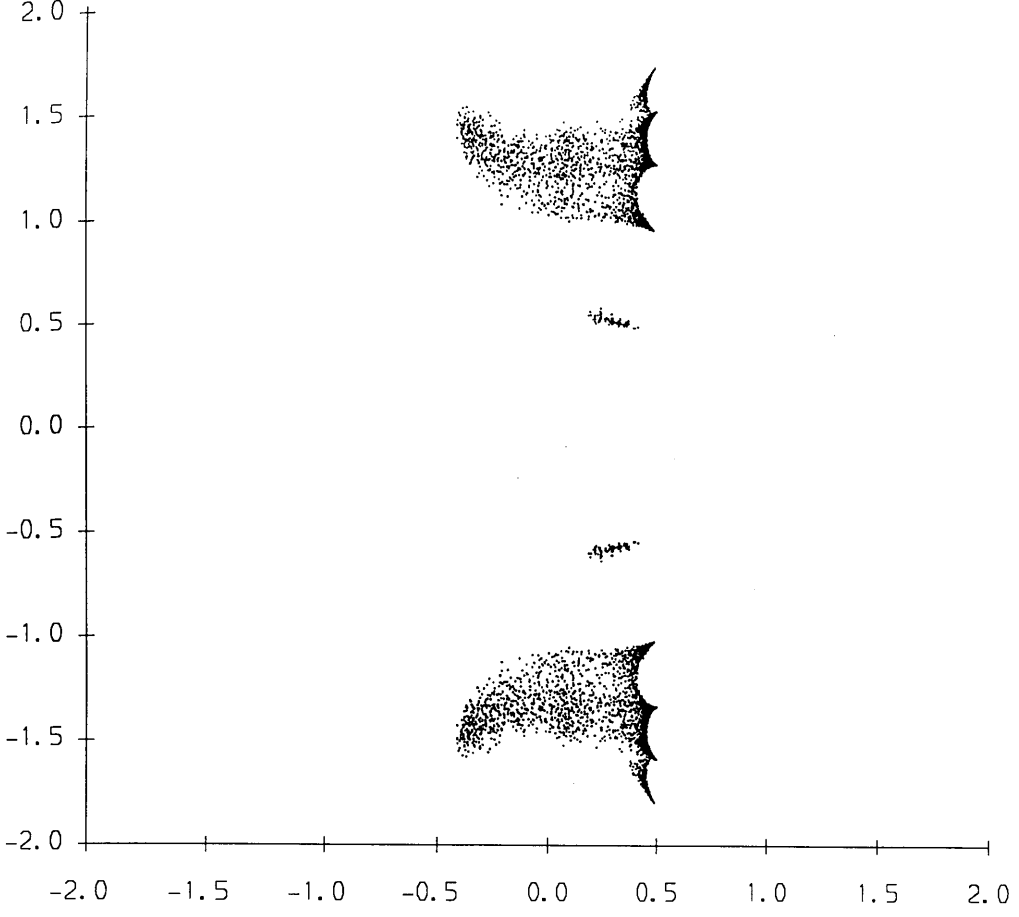

Fig. 4.7 The eigenvalue spectrum of M in the complex plane for a 6^4 lattice. Hopping parameter $\kappa = 0.08$, local Yukawa coupling $y = 0.5$.

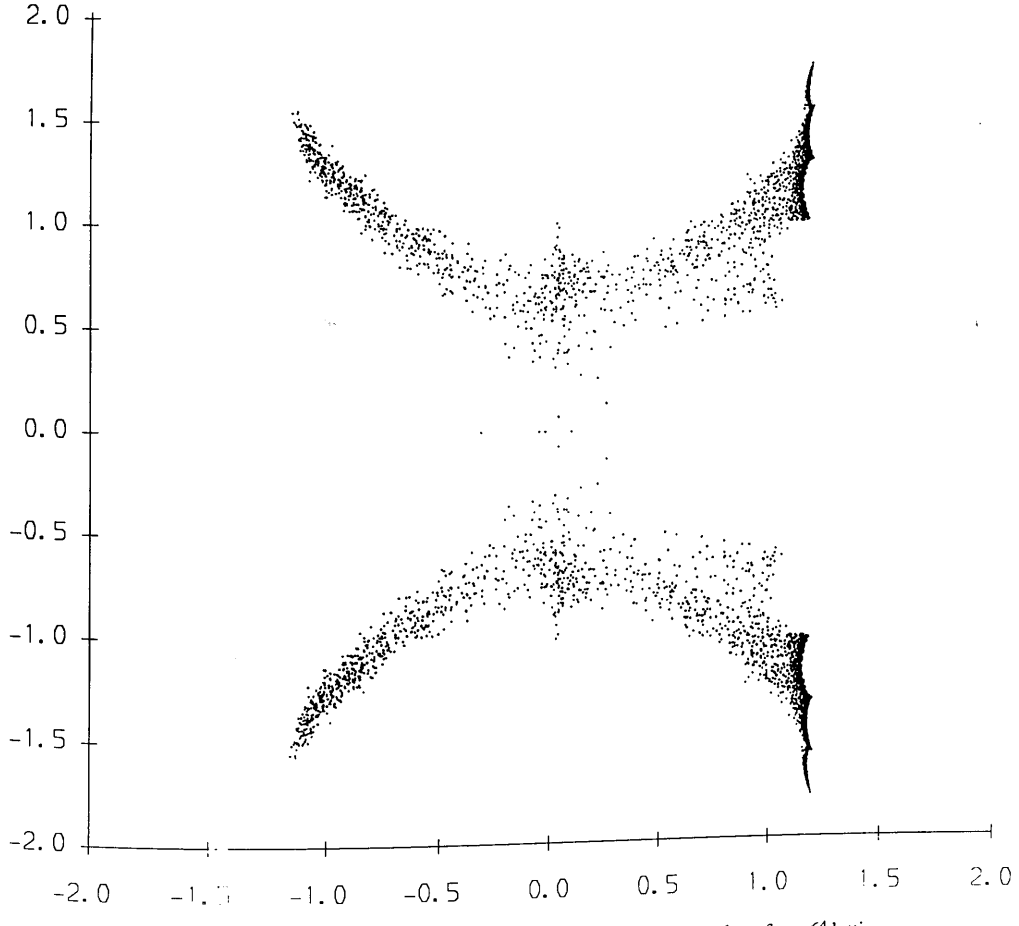

Fig. 4.8 The eigenvalue spectrum of M in the complex plane for a 6^4 lattice. Hopping parameter $\kappa = 0.08$, local Yukawa coupling $y = 1.2$.

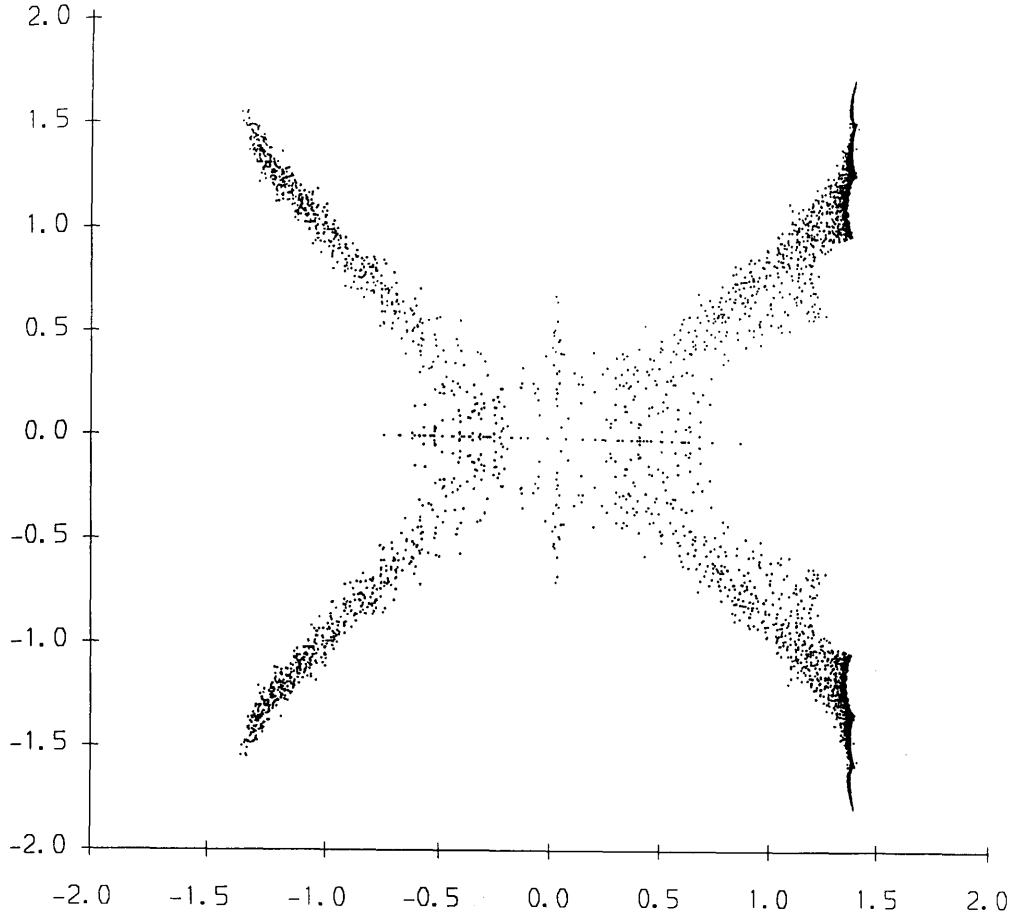

Fig. 4.9 The eigenvalue spectrum of M in the complex plane for a 6^4 lattice. Hopping parameter $\kappa = 0.08$, local Yukawa coupling $y = 1.4$.

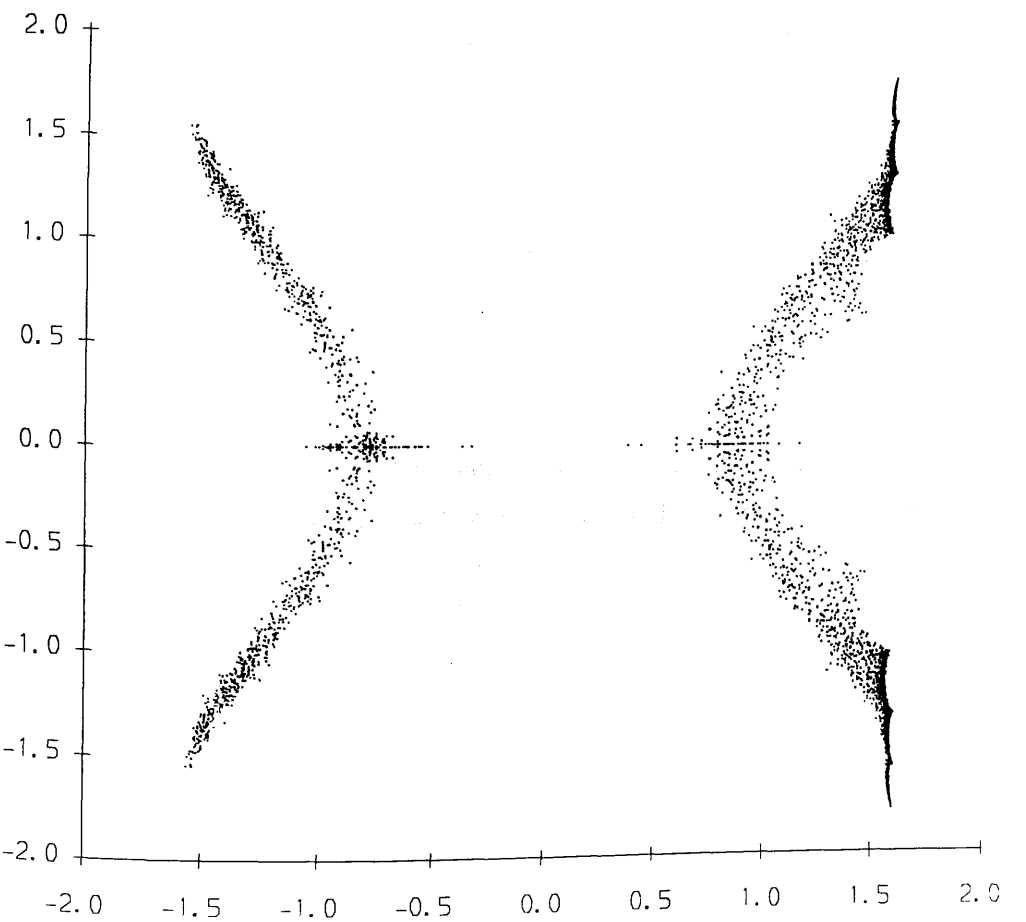

Fig. 4.10 The eigenvalue spectrum of M in the complex plane for a 6^4 lattice. Hopping parameter $\kappa = 0.08$, local Yukawa coupling $y = 1.6$.

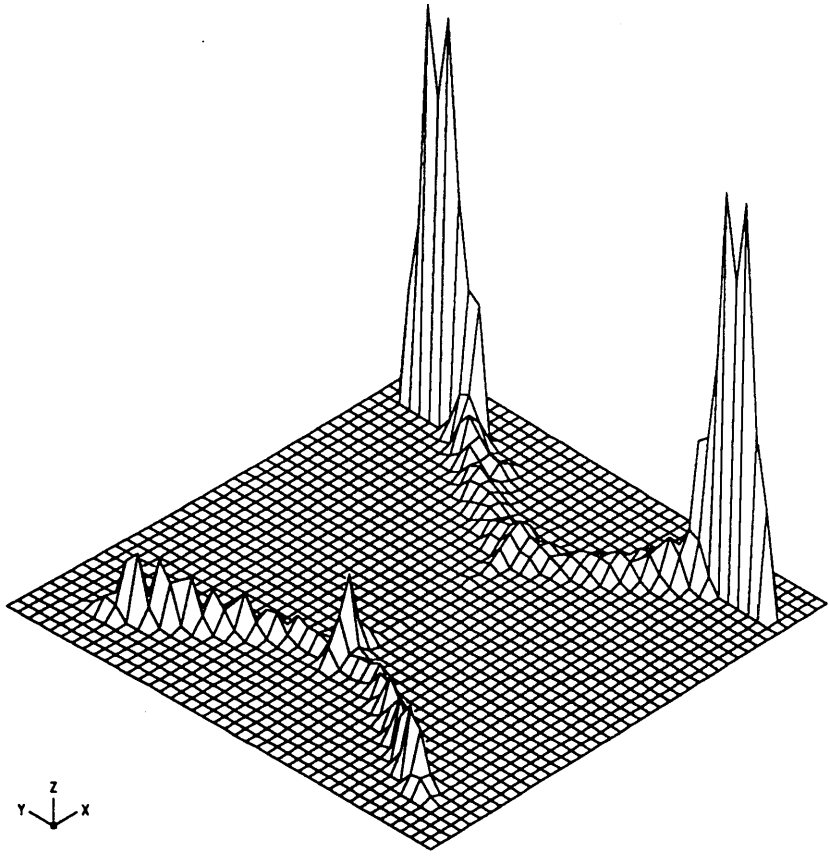

Fig. 4.11 The density of eigenvalues of M in the complex plane for a 6^4 lattice. Hopping parameter $\kappa = 0.08$, local Yukawa coupling $y = 1.6$.

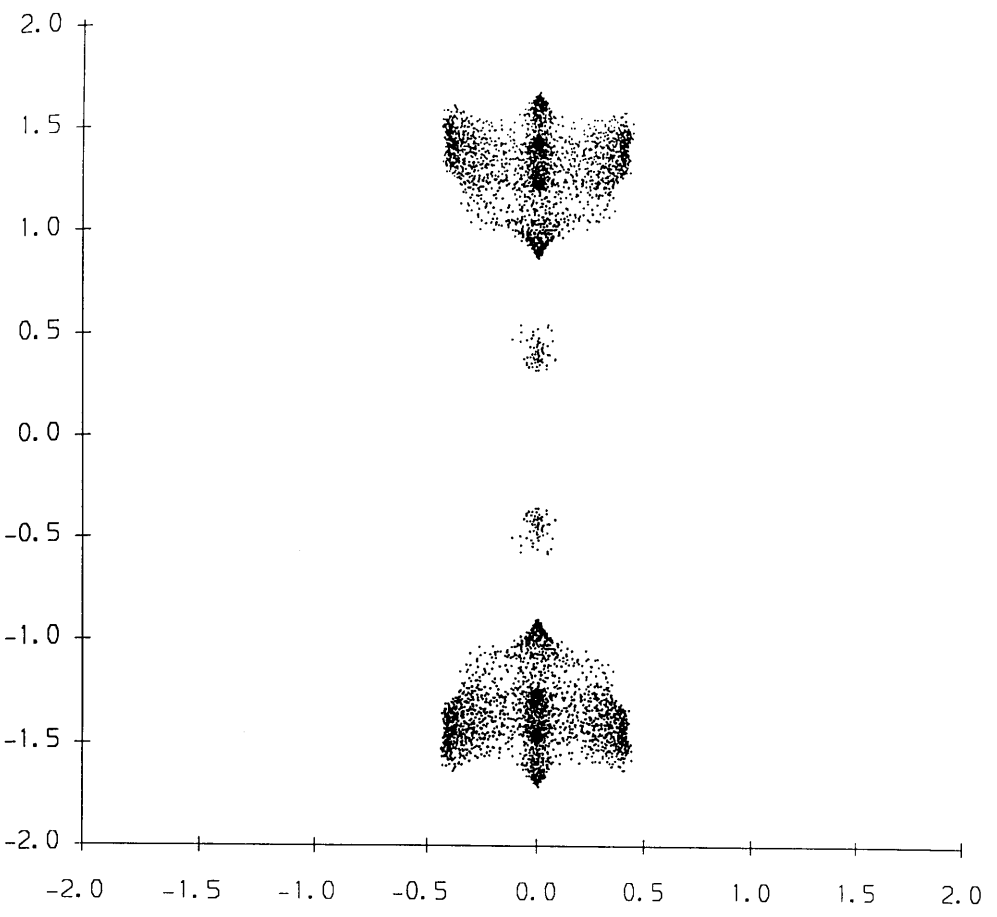

Fig. 4.12 The eigenvalue spectrum of M in the complex plane for a 6^4 lattice. Hopping parameter $\kappa = -0.08$, local Yukawa coupling $y = 0.5$.

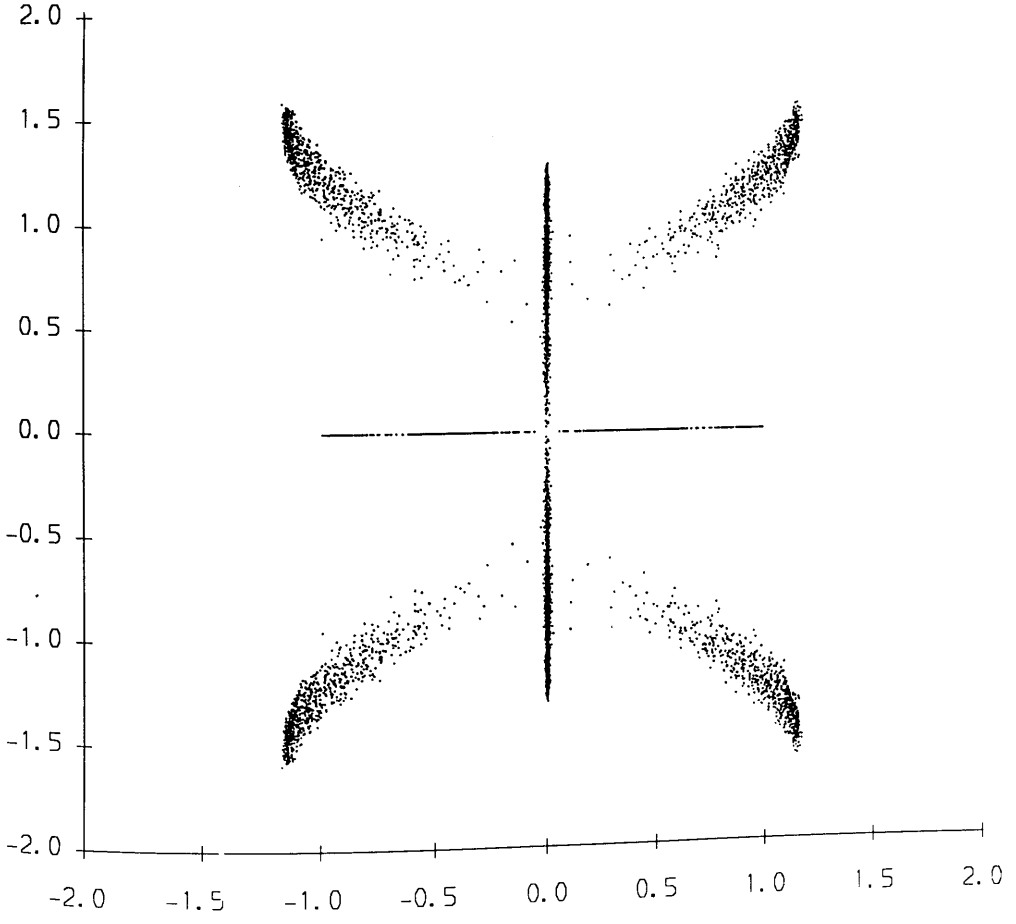

Fig. 4.13 The eigenvalue spectrum of M in the complex plane for a 6^4 lattice. Hopping parameter $\kappa = -0.08$, local Yukawa coupling $y = 1.2$.

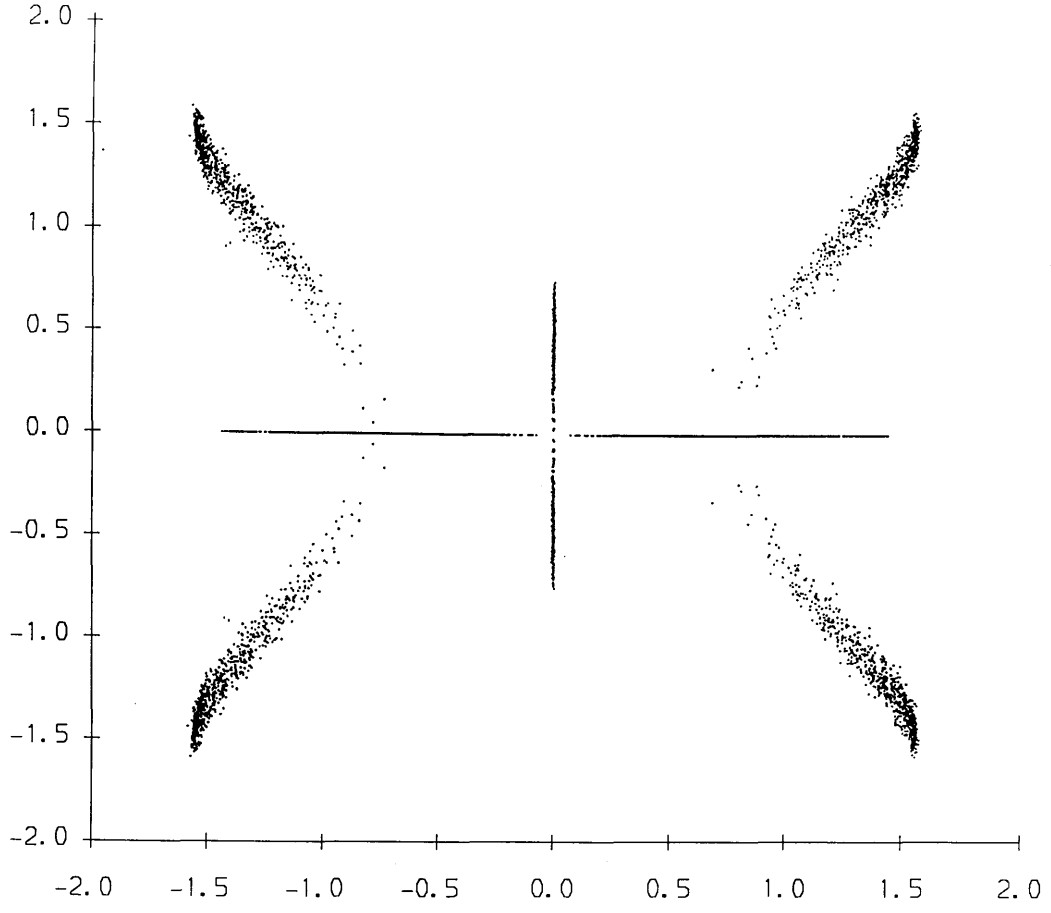

Fig. 4.14 The eigenvalue spectrum of M in the complex plane for a 6^4 lattice. Hopping parameter $\kappa = -0.08$, local Yukawa coupling $y = 1.6$.

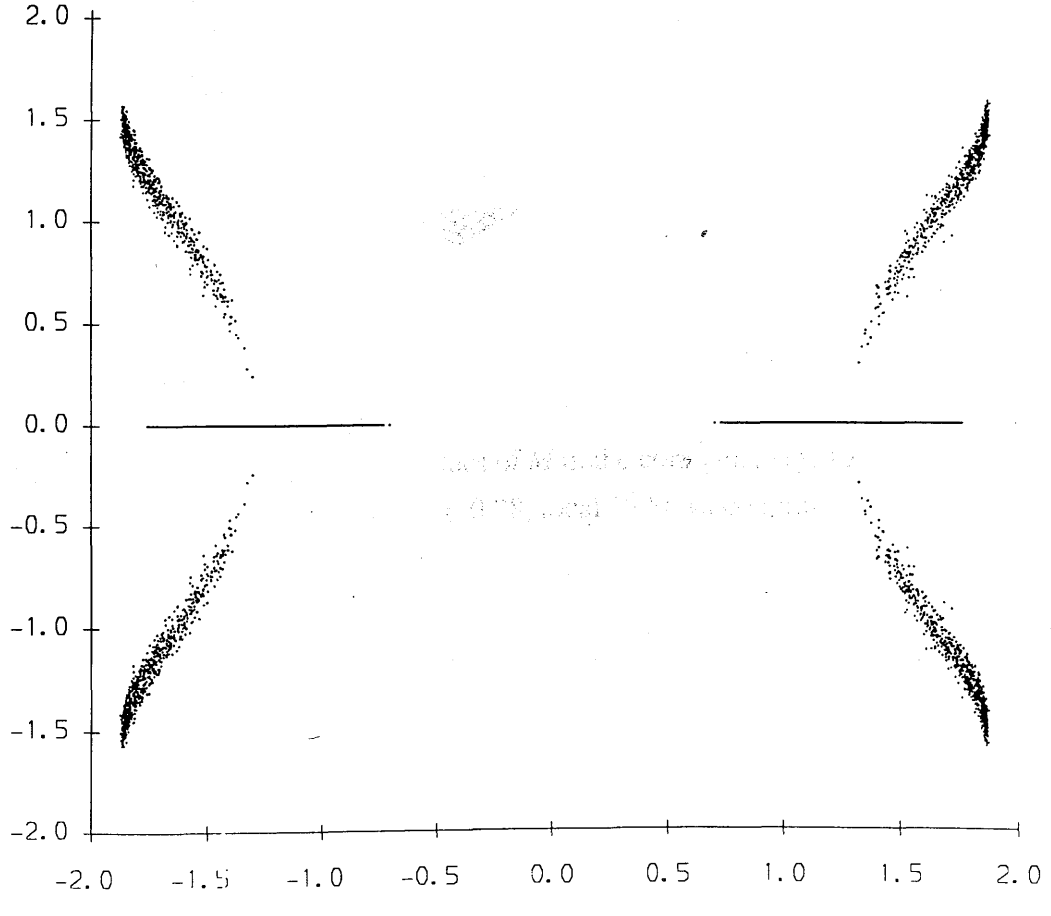

Fig. 4.15 The eigenvalue spectrum of M in the complex plane for a 6^4 lattice. Hopping parameter $\kappa = -0.08$, local Yukawa coupling $y = 1.9$.

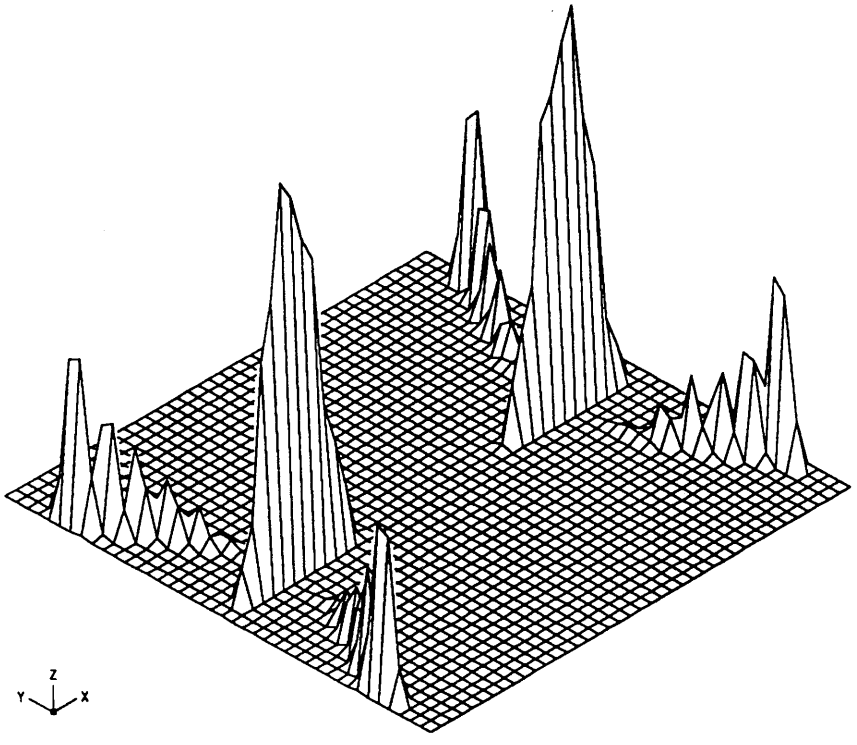

Fig. 4.16 The density of eigenvalues of M in the complex plane for a 6^4 lattice. Hopping parameter κ = -0.08, local Yukawa coupling y = 1.9.

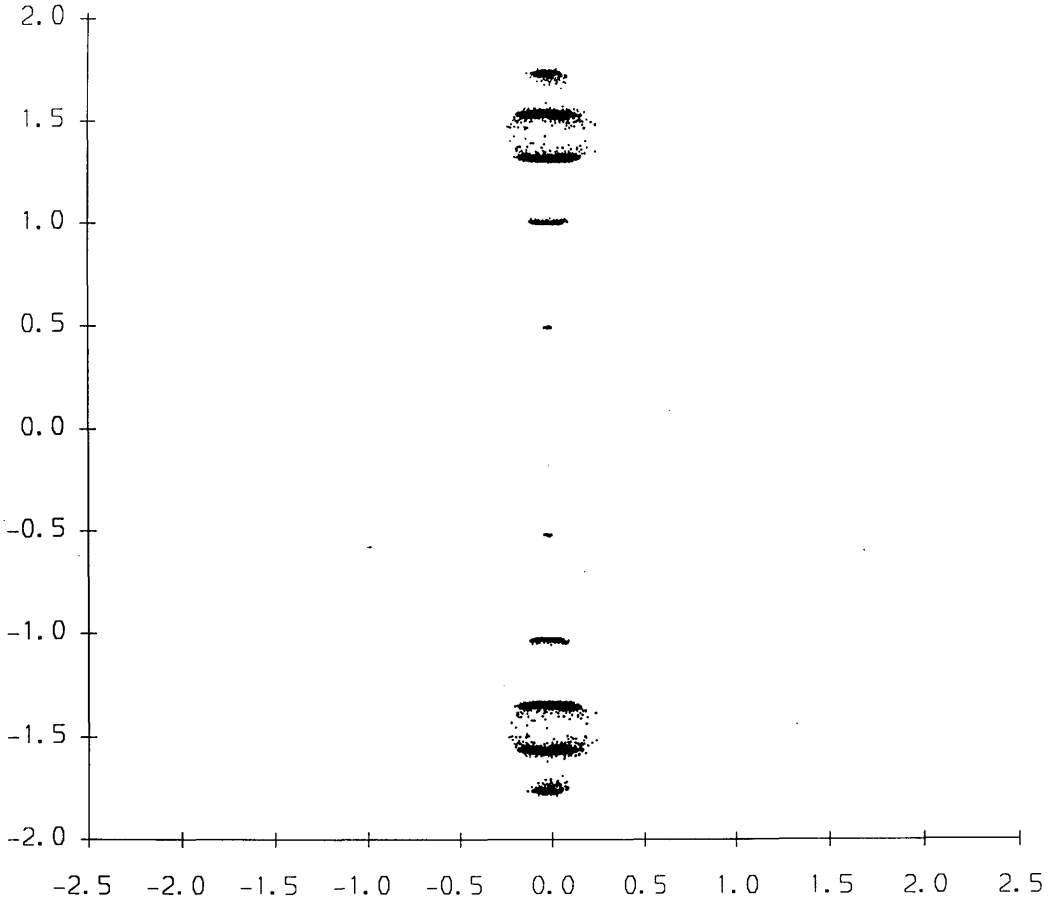

Fig. 4.17 The eigenvalue spectrum of M in the complex plane for a 6^4 lattice. Hopping parameter $\kappa = 0.04$, hypercubic Yukawa coupling $y = 0.5$.

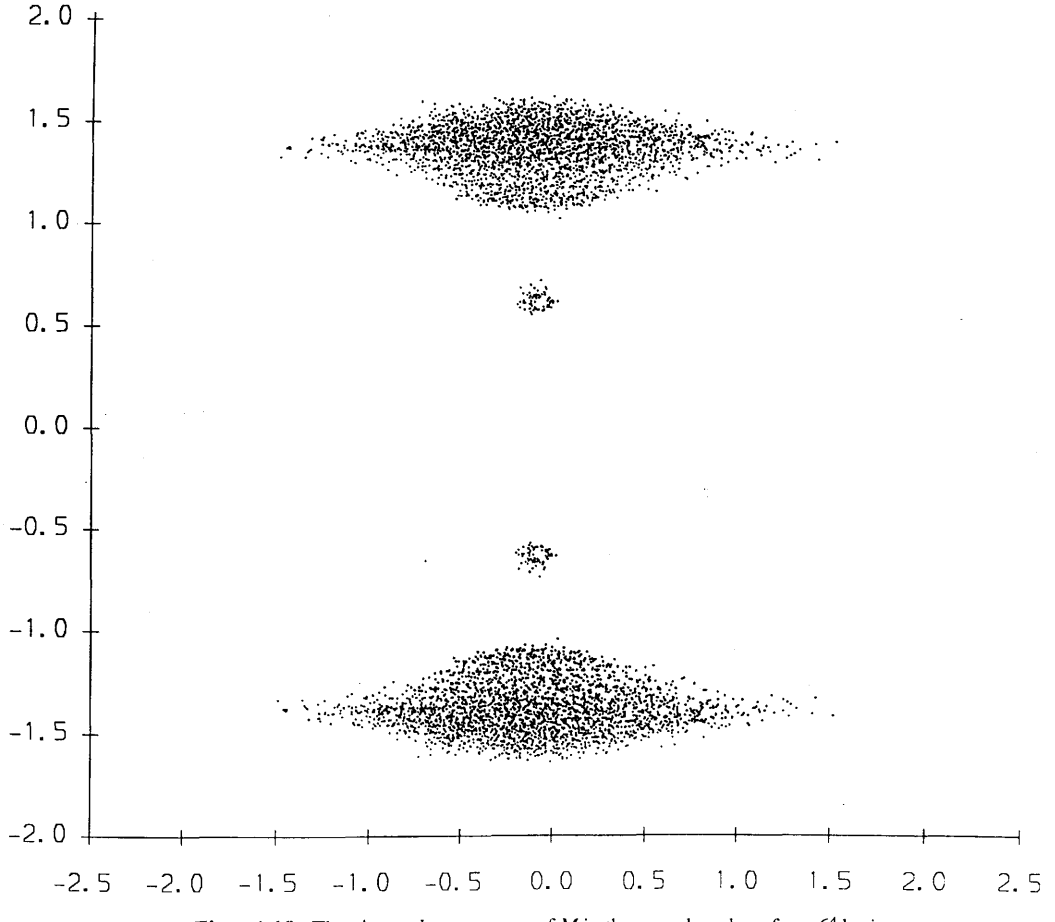

Fig. 4.18 The eigenvalue spectrum of M in the complex plane for a 6^4 lattice. Hopping parameter $\kappa = 0.04$, hypercubic Yukawa coupling $y = 2.0$.

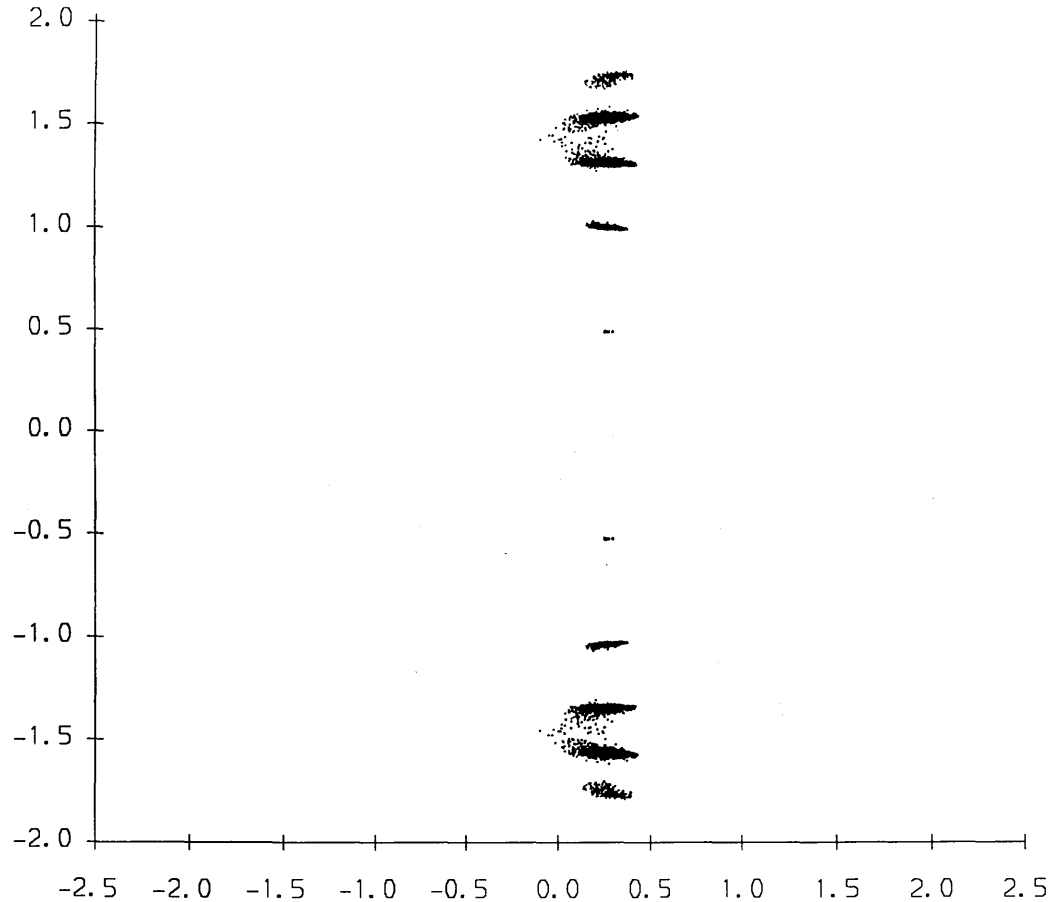

Fig. 4.19 The eigenvalue spectrum of M in the complex plane for a 6^4 lattice. Hopping parameter $\kappa = 0.08$, hypercubic Yukawa coupling $y = 0.5$.

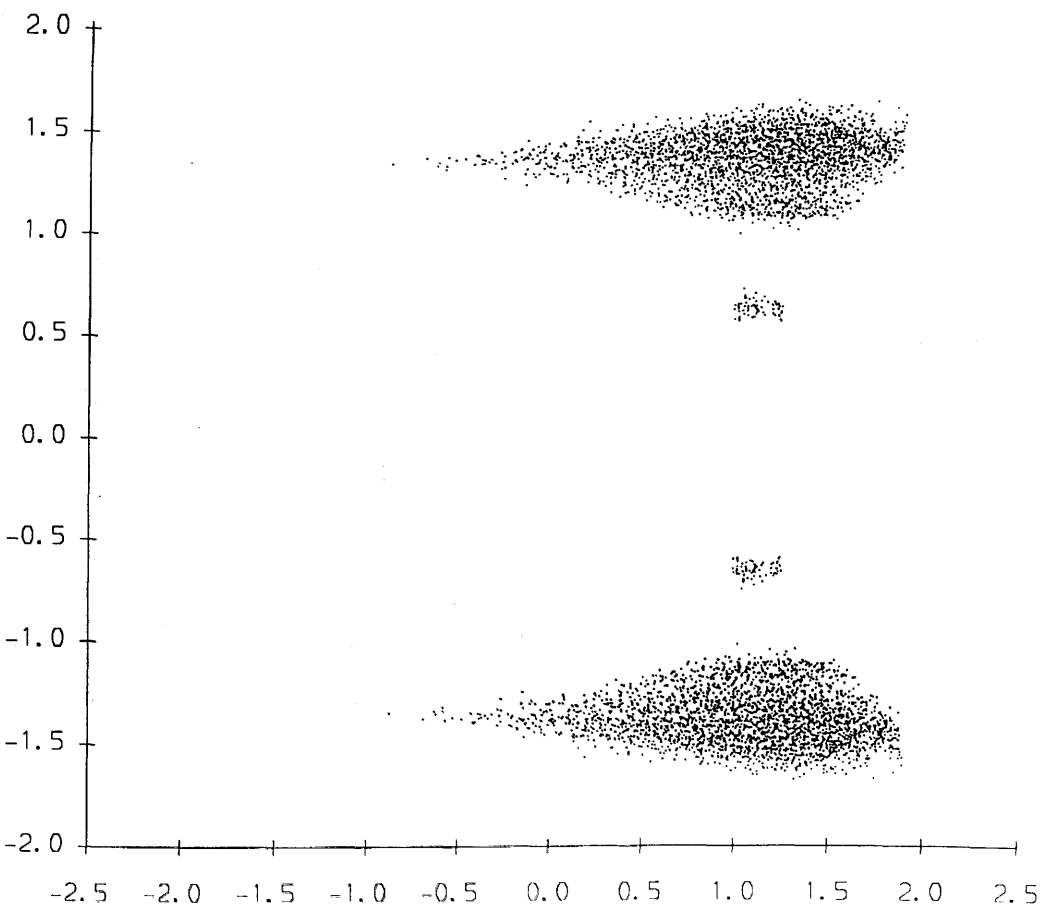

Fig. 4.20 The eigenvalue spectrum of M in the complex plane for a 6^4 lattice. Hopping parameter $\kappa = 0.08$, hypercubic Yukawa coupling $y = 2.0$.

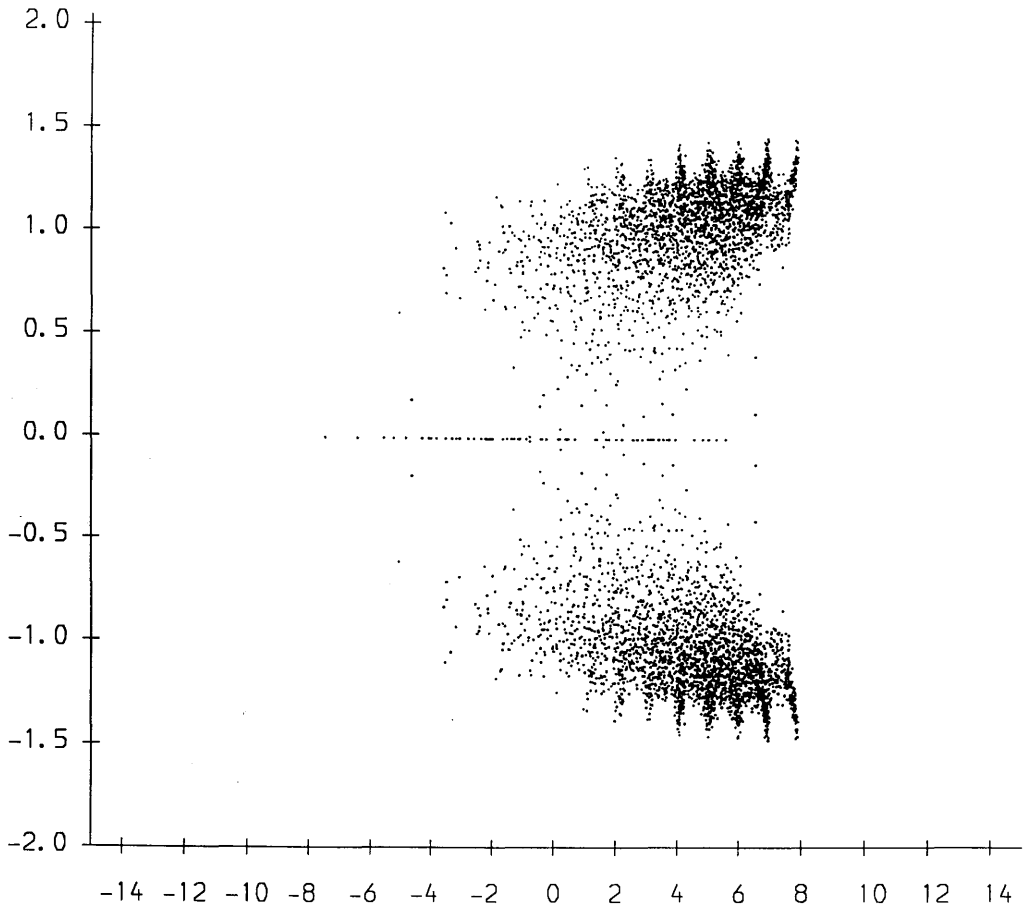

Fig. 4.21 The eigenvalue spectrum of M in the complex plane for a 6^4 lattice. Hopping parameter $\kappa = 0.08$, hypercubic Yukawa coupling $y = 8.0$.

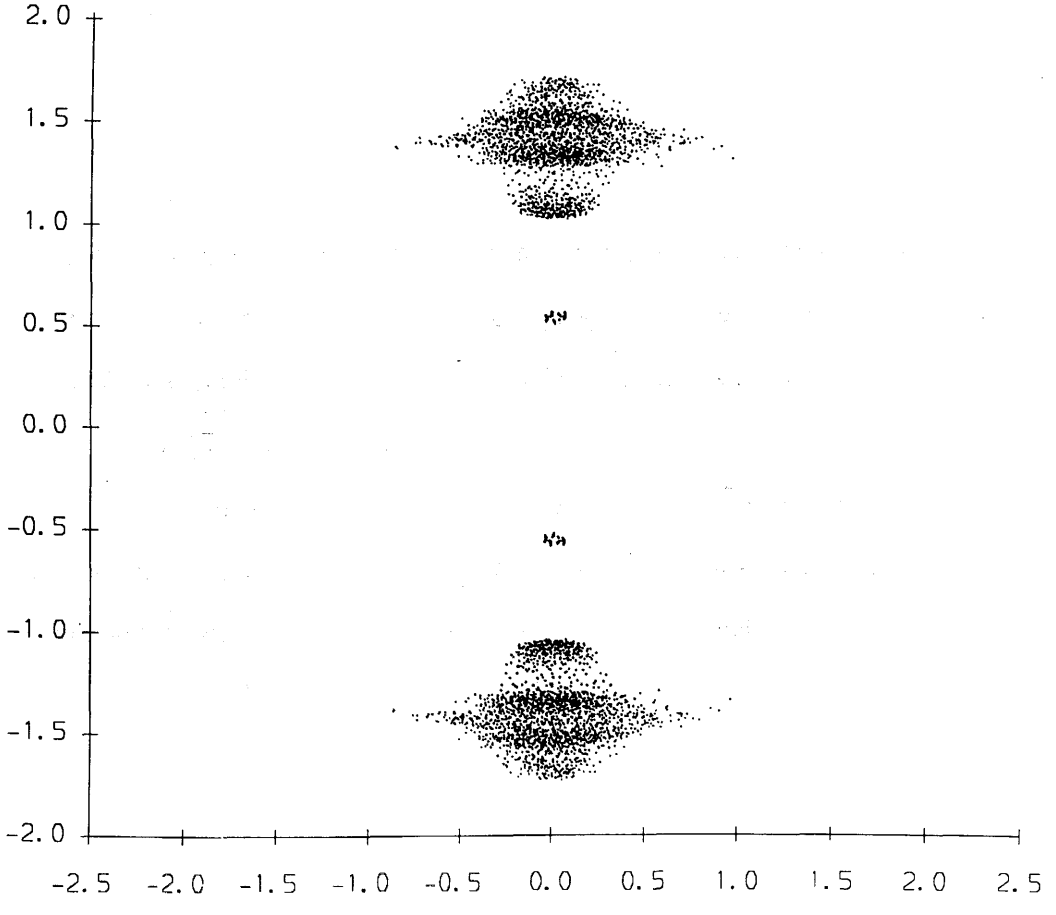

Fig. 4.22 The eigenvalue spectrum of M in the complex plane for a 6^4 lattice. Hopping parameter $\kappa = -0.08$, hypercubic Yukawa coupling $y = 2.0$.

Chapter 5

Fermion Masses with Local Coupling

5.1 Introduction

From the quenched studies of chapter 4 we have shown that for local coupling the PM1 / PM2 phases are distinguished by the absence / presence of real modes of M. Ideally we would like to be able to translate this into a statement about the renormalised fermion mass m_f since it was the behaviour of this quantity as a function of y that first indicated that the PM phase consisted of two different regions. This would be easy if the eigenvalue spectrum of M was always the free spectrum of M_{KS} shifted by some amount along the the real axis since we could then identify this shift as the mass m_f. However, we saw in chapter 4 that although this is qualitatively the case for hypercubic coupling it not true for the local form of the coupling that will concern us in this chapter.

From the eigenvalue spectra in the FM phase we can understand the generation of mass for all y (at least qualitatively) as being due to an overall shift in the eigenvalues to the right of the imaginary axis but it is difficult to make quantitative statements because the distribution is rather smeared compared to the free case. Since the spectra in the PM phase are always symmetric we cannot define a mass in this way. We could adopt a very simple definition such as

$$m_f = min(Re(\lambda) : Re(\lambda) > 0) \tag{5.1}$$

which is exact in the infinite volume free case. Such a definition would seem qualitatively correct in the PM phase since it gives $m_f = 0$ in the PM1 region and m_f increasing with y in PM2. However, it is not a reasonable definition in the FM phase since it would give $m_f = 0$ for $y < y^*$ which is not observed [37].

To achieve at least a qualitatively correct definition of the mass from the eigenvalue spectrum of M that is valid in both the PM and FM phases we first look at the behaviour of the renormalised fermion mass defined in the conventional way.

5.2 The Propagator Mass

The usual definition of the renormalised fermion mass comes from observing that the large time behaviour of the fermion two point function in the infinite volume limit is given by

$$\lim_{t \to \infty} \langle \overline{\Psi}(t)\Psi(0) \rangle = Z \, exp(-E_0 t) \tag{5.2}$$

where Ψ are the fermion operators in the theory, Z is some t independent constant and E_0 is the energy of the lowest lying state in the spectrum with the appropriate quantum numbers. If we take the zero momentum part of eqn. 5.2 then we can identify E_0 as the lowest mass state which is the renormalised fermion mass m_f. On the lattice we can use this as a practical definition since the LHS of eqn. 5.2 is given by the inverse of the fermion matrix (eqn. 1.37) which we can readily calculate by the methods of chapter 2.

In a finite volume there will be corrections to eqn. 5.2 due to particles propagating from the origin to t by going round the lattice in the negative time direction. Such particles travel a distance L_0-t and will feel the fermionic boundary conditions. Since we require the particle to be at rest we extract the zero momentum component by summing over all spatial sites $\boldsymbol{n}$ on a particular time-slice n_0, and for the particular case of antiperiodic boundary conditions in time the lattice forms of eqn. 5.2 are

$$\lim_{n_0 \to \infty} \sum_{\boldsymbol{n}} M^{-1}((n_0,\boldsymbol{n}), 0) = Z \{ (-1)^{n_0} exp(-E_0 n_0) - exp(-E_0(L_0 - n_0)) \} \tag{5.3a}$$

$$\text{or} \quad \lim_{n_0 \to \infty} \sum_{\boldsymbol{n}} M^{-1}((n_0,\boldsymbol{n}), 0) = Z \{ exp(-E_0 n_0) - (-1)^{n_0} exp(-E_0(L_0 - n_0)) \} \tag{5.3b}$$

The two contributions with differing phase come from particles travelling in different directions round the lattice and we use eqn. 5.3a (5.3b) if the origin is an even (odd) site. The rest mass m_f is given by

$$m_f = sinh(E_0) \tag{5.4}$$

In the $a \to 0, V \to \infty$ limit eqns 5.3a, 5.3b and 5.4 coincide with eqn. 5.2.

5.3 Evaluation of the Lattice Propagator

To evaluate the required inverse elements of M in eqn. 5.2 we use the block Lanczos algorithm of section 2.4.2 so that we can average over many (typically 10) origin sites at once for a given field configuration. The only difference between the algorithm we use and that described in section 2.4.2 is that the contribution to $MM^\dagger$ due to the local Yukawa term $y\phi$ is not in general a multiple of the identity and also connects even to odd and odd to even sites. Hence the Lanczos vectors depend on y and we cannot update simultaneously for several different values of y as was possible for a bare mass term m. Nor can we keep the Lanczos vectors purely even or odd and all our vectors are of length N and not $N/2$.

It might seem that the most efficient inversion method would be to apply the Lanczos algorithm to the matrix $M(P_e\text{-}P_o)$ which is a hermitian (but not positive definite) matrix whose square is $MM^\dagger$. We would recover the correct solution after a final (trivial) multiplication by $(P_e\text{-}P_o)$ and we could hope to halve the number of required multiplications by M provided the convergence was not adversely affected. However, this often leads to numerical problems due to $\alpha_2 = 0$ when we take a delta function for the source. This is exactly analogous to the observation in [55] that $\alpha_2 = 0$ when attempting to invert the hermitian (but not positive definite) matrix $\gamma_5 M_W$ where M_W is the Wilson fermion matrix of eqn. 1.26. Although a simple solution exists [55], we prefer to invert $MM^\dagger$ since the remedy complicates the algorithm slightly. In addition it was found that that the increase in the number of iterations taken to converge makes it only slightly faster to invert $\gamma_5 M_W$ as opposed to $M_W{}^\dagger M_W$, and since we are only working on moderate volumes time is not of over-riding importance.

As an initial test of the inversion program and of our fitting procedure for the propagator we first consider the free case $\kappa \rightarrow \infty$ on a 6^3 x 12 lattice with antiperiodic boundary conditions in time. The results are shown in figures 5.1 and 5.2 for $y = 0.4$ where we have taken either all even or all odd starting sites respectively and scaled the data such that the first point is normalised to unity. The

propagators fit the free forms of eqns. 5.3a and 5.3b perfectly for all values of t with $Z = 1$. As expected, we recover $m_f = sinh(E_0) = 0.4$. From now on we always consider only odd starting sites and therefore use eqn. 5.3b.

We now consider the interacting case. A typical propagator is shown in figure 5.3 for y = 0.4 and $\kappa = 0.08$. The data is averaged over 200 configurations each separated by 1000 sweeps where we use $B = 10$ in the block Lanczos algorithm to calculate 10 propagators on each configuration. Tunneling to a state with negative magnetisation is observed during the heatbath update but we always rotate the spins such that $\langle\phi\rangle \geq 0$. The remarkable fact is that the free propagator fits the interacting propagator so well for all values of t despite the fact that we only expect eqn. 5.3b to hold asymptotically for large t. This would be no surprise if the eigenvalue spectrum resembled a free one, but we know that this is far from true from the results of chapter 4 (for example see fig. 4.7).

In the crossover region we are able to perform the inversion (unlike ref. [37]) but the resulting propagator is not fitted at all by the free one. This is illustrated in figure 5.4 at $y = 1.2$. The error bars on the points are too small to show, but there is no way to sensibly define a mass via eqn. 5.3b. It appears that the very small eigenvalues present in the spectrum of M in the crossover region make the propagator mass ill-defined at least on these small volumes.

At larger values of y we can again fit the free propagator. Since the renormalised mass is large in this region the propagator drops to zero very rapidly, so we are effectively only fitting for $t \leq 2$. This would make the calculated mass meaningless if there was contamination due to other mass states, but we have seen for small y that the free propagator fits for all t. This means that we can define a mass for large y but whether this mass, which is larger than the lattice cutoff, has any physical meaning is another question. However, such large masses are required to be generated for the unphysical doubler fermions in Wilson-Yukawa models to decouple them from the physical spectrum [56].

The propagator mass as a function of y at $\kappa = 0.08$ is shown in figure 5.5. The

two regions $y < y^*$ and $y > y^*$ show very different behaviour. In the PM1 region the mass fits the relation $m_f = y\langle\phi\rangle$ for small y and hence will increase with κ ($\langle\phi\rangle = 0.54$ at $\kappa = 0.08$). In the PM2 region we have run at higher κ values and observed that the mass does indeed decrease with κ but the variation is much slower than predicted by eqn. 3.23. Much more extensive studies have been performed in ref [37] where the same results are obtained.

We can conclude from a comparison of the eigenvalue spectra with the propagators that it is the whole spectrum that influences the mass and not just a few of the smallest modes. If we are to define the fermion mass from the spectrum we must have a definition that includes the effects of all the eigenvalues

5.4 The Condensate Mass

A definition of the renormalised mass can be made from the observation that in a theory of free fermions the chiral condensate is zero when the bare mass term m is zero and becomes non-zero for finite m. We can therefore associate the breakdown of chiral symmetry in the interacting theory with the generation of some dynamical mass for the fermions. We call this mass the condensate mass to differentiate it from the normal propagator mass (the two definitions need not be equivalent). A numerical approach would be to calculate the condensate from the eigenvalue spectrum at various κ and y and solve the equation

$$\langle\bar{\chi}\chi\rangle = \left\langle \frac{1}{N}\sum_{i=1}^{N}\frac{1}{\lambda_i}\right\rangle = \langle\bar{\chi}\chi(m_f)\rangle_{free} \tag{5.5}$$

for m_f where the free condensate is given by

$$\langle\bar{\chi}\chi(m)\rangle_{free} = \frac{1}{N}\sum_{p_\mu}\frac{m}{m^2 + \sum_{\mu} sin^2 p_\mu} \tag{5.6}$$

The allowed momenta are determined by the lattice size and the boundary conditions from eqns. 4.16, 4.17 and 4.18.

This approach has been used successfully in dynamical studies of the FM phase of a one-component ϕ^4 model at large (but finite) quartic self-coupling [57].

However eqn. 5.5 will not even give qualitatively correct results in the PM phase. We have seen in figures 4.2 to 4.5 that the average eigenvalue spectrum of M exhibits a $(\lambda,-\lambda)$ symmetry throughout the PM phase for all values of y. Hence the chiral condensate will be zero and so will m_f derived from eqn. 5.5, and we will not distinguish the PM1 and PM2 phases.

In ref. [58] it is suggested that an order parameter for the PM1/PM2 transition which does detect the spontaneous generation of mass in the PM2 region might be

$$\frac{\partial<\bar{\chi}\chi(m)>}{\partial m}\Big|_{m=0} = <Tr(M^{-1})^2 - Tr(M^{-2})> - <Tr(M^{-1})>^2 \qquad (5.7)$$

which we could again fit to the value in a free theory at finite m_f. To show that this is a useful quantity the authors compute it in a free field theory to leading order in d. We find that the approximations used in [58] are entirely equivalent to assuming that to leading order all the free eigenvalues λ_i of M_{KS} take their RMS value, ie

$$\lambda_i^2(m=0) = \frac{1}{N}Tr(M_{KS}^2) = -\frac{d}{2} \qquad (5.8)$$

Using $\lambda = m \pm i\sqrt{d/2}$ gives

$$\frac{\partial<\bar{\chi}\chi(m)>_{free}}{\partial m} = \frac{2(d-2m^2)}{(d+2m^2)^2} \qquad (5.9)$$

Hence we could evaluate eqn. 5.7 from the eigenvalue spectrum of M at various κ and y and fit to the value in a free theory at finite bare mass to calculate m_f. Eqn 5.9 suggests that this quantity will change sign at the point where the renormalised mass becomes large, ie at the PM1/PM2 phase boundary (by evaluating the exact result for eqn. 5.9 from the free eigenvalues λ_0 we find that the leading order result is in fact a very good approximation).

Initial numerical studies were done in the symmetric phase at at $\kappa = 0.07$ on a 6^4 lattice with antiperiodic boundary conditions in time. The eigenvalue spectra of M were obtained on 8 configurations at values of y around y^*, and the values of m_f calculated by fitting $-Tr(M^{-2})$ to the exact result for a free field theory (the terms in eqn. 5.7 involving $Tr(M^{-1})$ were negligible as expected). The problems involved in performing the fit are obvious from the approximate result of eqn. 5.9.

Firstly, if the LHS is less than zero then there are two solutions for m. One is in the interval $d/2 < m^2 < 3d/2$, the other in the region $3d/2 < m^2 < \infty$. In addition, the RHS of eqn. 5.9 has a maximum of $2/d$ (at $m^2 = 0$) and a minimum of $-1/4d$ (at $m^2 = 3d/2$), and for values of $-Tr(M^{-2})$ outside this we cannot perform the fit. We should therefore include a wavefunction renormalisation factor of $Z(y)$ in front of eqn. 5.9 but this would leave us with only one equation for two unknowns. Since we are only interested in the qualitative behaviour of the mass as a function of y we set Z to unity and interpret $-Tr(M^{-2}) < -1/4d$ as a signal of $m_f^2 > 3d/2$. We also resolve the ambiguity in m_f for $-1/4d < -Tr(M^{-2}) < 0$ by assuming that m_f varies smoothly with y, ie we take the smaller solution for m_f. The most important fact is that eqn. 5.9 changes sign at $m^2 = d/2$ and hence we can tell whether m_f^2 is smaller or larger than $d/2$ from the sign of $Tr(M^{-2})$ independent of Z.

The results are shown in fig. 5.6 and indicate that the appearance of small real modes in the spectrum of M generates a large mass for the fermions. Although the numerical values for m_f would be affected by the wavefunction renormalisation that we have ignored, we can say without doubt that $m_f^2 > d/2$ for $y \geq 1.35$ and we are clearly able to qualitatively distinguish the PM1 and PM2 regions. However, the fact that we are unable to solve for m_f for $y \geq 1.40$ indicates that $Z > 1$ in this region and the method breaks down quantitatively.

Although this approach allows us to define the PM1 and PM2 regions in terms of the eigenvalue spectrum it has many disadvantages. The large fluctuations in $Tr(M^{-2})$ lead to relatively large error bars, and we cannot quantitatively investigate the behaviour of the mass in the PM2 region since here the method can only give a lower limit on m_f. In addition there is a huge amount of computation involved in fig. 5.6 which requires the calculation of the complete eigenvalue spectrum for every value of y on each of the 8 configurations. Despite all the data that we have generated, this approach gives us no real insight into the physics of the spontaneous mass generation in the PM2 region.

5.5 The M' Fermion Matrix

We would ideally like to relate the spontaneous generation of mass directly to the breaking of chiral symmetry since this is the most physically intuitive picture. The basic problem with the fermion matrix M is that it is not invariant under the $Z(2)$ symmetry of the Ising model $\phi \rightarrow -\phi$ and hence the chiral condensate cannot be non-zero in the PM phase. To distinguish the PM1 and PM2 regions we had to look at its first derivative with respect to the mass which is a rather indirect procedure that does nothing to clarify the physics. In addition we would like to be able to calculate results at all Yukawa couplings without the huge overhead of having to re-evaluate the eigenvalue spectrum for each value of y. This seems wasteful in the quenched approximation since the spin configuration itself is the same for all y.

This motivates the introduction of a new fermion matrix M' which is $Z(2)$ invariant and whose eigenvalues are a trivial function of the Yukawa coupling. Suppose we make a change of variables in the path integral 4.1 [33]

$$\chi' = (P_e + \phi P_o)\,\chi \tag{5.10}$$

$$\bar{\chi}' = \bar{\chi}\,(P_o + \phi P_e) \tag{5.11}$$

Then the new fermion matrix M' defined by

$$\bar{\chi}' M' \chi' = \bar{\chi} M \chi \tag{5.12}$$

is given by

$$\begin{aligned} M' &= (P_o + \phi P_e)\,(M_{KS} + y\phi)\,(P_e + \phi P_o) \\ &= \phi M_{KS} \phi P_o + M_{KS} P_e + y \end{aligned} \tag{5.13}$$

where we have used the fact that even and odd projectors interchange when we commute them through the fermionic derivative. We see immediately that the interaction term proportional to y has become a simple mass term (if we were using Wilson fermions and attempting to decouple the doublers via some Wilson-Yukawa coupling, this term would reduce to the normal Wilson term [53]). This has great benefits in the quenched approximation since we only need to calculate the eigenvalue spectrum at $y = 0$. From now on M' will *always* refer to eqn. 5.13

with $y = 0$.

M' can only be defined for the local form of the coupling matrix ($Y = y\phi$) since we make use of the fact that Y^{-1} is diagonal and trivial to calculate in order to remove the non-trivial y dependence of M. In the PM and AFM phases the hypercubic form of Y will typically have many zero diagonal elements and Y^{-1} will not exist. Although we may still be able to define M' deep in the FM phase it will not in general be of any more use to us than M.

We first summarise the important properties of this new fermion matrix. M' is non-hermitian and has complex eigenvalues. Since ϕ appears quadratically it is $Z(2)$ invariant as required and $Tr(M'^{-1})$ can be non-zero in the PM phase. As pointed out in ref [33], making the rotations 5.10 and 5.11 means that in the full model including gauge fields, $(\chi', \overline{\chi}')$ would be the fermion fields in the unitary gauge. It is only in this gauge, where $\phi = \mathbf{1}$, that the Higgs mechanism becomes manifest and the Yukawa term appears as a pure mass term just as it does in M'.

The transformations of eqns. 5.10 and 5.11 are not unitary since, using the integration rules for fermionic variables,

$$\begin{aligned} d\overline{\chi}d\chi &= (det(P_o + \phi P_e)\, det(P_e + \phi P_o))\, d\overline{\chi}'d\chi' \\ &= (det(\phi))\, d\overline{\chi}'d\chi' \\ &= \pm\, d\overline{\chi}'d\chi' \end{aligned} \tag{5.14}$$

Hence, for a single fermion, the M' chiral condensate will be zero on average in the PM phase due to the fluctuating nature of the sign of $det(\phi)$ and we seem to have achieved nothing. However, we have already noted that we cannot simulate the dynamical theory for an odd number of fermion species. If we take n_f even then the sign will square to one and the condensate can be non-zero. In the quenched approximation we monitor the behaviour of a single species but effectively set n_f to be even by ignoring the sign of $det(\phi)$ in the ensemble average.

We now consider the eigenvalue spectrum of M'. It is easy to see from eqn. 5.13 that for $y = 0$

$$(P_e\text{-}P_o)\, M'(P_e\text{-}P_o) = -M' \tag{5.15}$$

$$\phi M'\phi = -M'^{\dagger} \tag{5.16}$$

Since both of these are unitary transformations on M', each eigenvalue λ comes in a set of four $(\lambda, -\lambda, \lambda^*, -\lambda^*)$. The only exceptions will be purely real or imaginary eigenvalues which will come in $(\lambda, -\lambda)$ pairs and exact zero modes which can appear singly. It is worth noting here that had we chosen the transformation on the χ field to be that of eqn. 5.10 but with the even and odd projectors interchanged (and similarly for $\overline{\chi}$), we would have arrived at a new matrix M'' that is related to M' by the unitary transformation of eqn. 5.16. Hence M'' has the same eigenvalue spectrum as M' and the particular choice of transformation is purely a matter of convention.

In the quenched approximation the average eigenvalue spectrum of M' at $+\kappa$ is simply related to that at $-\kappa$. The symmetry of eqn. 3.13 means that the configuration $\phi(-\kappa)$ given by

$$\phi(-\kappa) = (P_e - P_o)\, \phi(\kappa) \tag{5.17}$$

has the same weight in the partition function of the theory defined at $-\kappa$ as $\phi(\kappa)$ does at κ. Given the matrix $M'(\kappa)$ on the configuration $\phi(\kappa)$ then an equally probable matrix at $-\kappa$ is, from eqns. 5.13 and 5.17,

$$\begin{aligned} M'(-\kappa) &= (P_e - P_o)\, \phi(\kappa) M_{KS} (P_e - P_o)\, \phi(\kappa) P_o + M_{KS} P_e \\ &= -\, \phi(\kappa) M_{KS} \phi(\kappa) P_o + M_{KS} P_e \end{aligned} \tag{5.18}$$

and therefore

$$(M'(-\kappa))^2 = -\,(M'(\kappa))^2 \tag{5.19}$$

In terms of the eigenvalues this means $\lambda(-\kappa) = i\lambda(\kappa)$ and hence the eigenvalue spectrum at $-\kappa$ is simply that at κ rotated by 90^0 in the complex plane.

We can work out the eigenvalues analytically in the cases $\kappa \to \pm\infty$. At $\kappa = +\infty$ the spins are frozen to $\phi = \mathbf{1}$ and hence $M' = M_{KS}$. The eigenvalues are therefore purely imaginary and equal to $\pm i\lambda_0$ with λ_0 given by eqn. 4.16. Due to eqn. 5.19 the eigenvalues at $\kappa = -\infty$ will purely real and equal to $\pm\lambda_0$. The overall picture is that as κ varies from $-\infty$ to $+\infty$ the eigenvalues move, via some path, from the real

to the imaginary axis. To discover the distribution between these limits and the direction of flow of the eigenvalues we perform monte carlo simulations and use the non-hermitian Lanczos algorithm described in section 4.4.

5.6 The Non-Hermitian Lanczos Algorithm for M'

Since the eigenvalues of M' come in $\pm$ pairs we use the non-hermitian Lanczos algorithm to evaluate the eigenvalues of $(M')^2$ and take the square root at the end. This means that the algorithm terminates after at most $N/2$ iterations. Given that the reorthogonalisation time grows as N^3 and the storage as N^2 we gain a factor of 8 in speed and 4 in storage on large volumes by this simple measure alone. Just as for M we can work in real arithmetic throughout since eqn. 5.16 implies

$$\phi\ (M'^2)\ \phi\ =\ (M'^2)^\dagger \tag{5.20}$$

The required hermitian unitary matrix U in eqn. 4.31 is given by the ϕ field itself and we can therefore use the real arithmetic algorithm of section 4.4.2. The basic feature of this implementation is that typical vector dot products are replaced by the combination

$$u^\dagger \phi v\ =\ \sum_{n=1}^{N} u^*(n)\ \phi(n)\ v(n) \tag{5.21}$$

for two vectors u and v. This expression is vectorisable and hence very fast.

We need some checks on the M' eigenvalues analogous to eqns 4.45 and 4.46 that were used to check the eigenvalues of M. Due to the $(\lambda, -\lambda)$ symmetry, $Tr(M')^{2n+1}$ is zero so we need to check quantities of the form $Tr(M')^{2n}$. These are most easily calculated by considering $(M')^2$ written in the form

$$(M')^2\ =\ M_{KS}\phi M_{KS}\phi\ P_o\ +\ \phi M_{KS}\phi M_{KS}\ P_e \tag{5.22}$$

and therefore

$$(M')^{2n}\ =\ (M_{KS}\phi)^{2n} P_o\ +\ (\phi M_{KS})^{2n} P_e \tag{5.23}$$

$$Tr(\ (M')^{2n})\ =\ Tr(\ (M_{KS}\ \phi)^{2n}) \tag{5.24}$$

due to the cyclic nature of the trace. Since ϕ is purely diagonal and M_{KS} connects nearest neighbour sites, eqn. 5.24 consists of closed loops comprising $2n$ 'hops'. At each vertex x, where the next hop is to site y, we associate a factor

$+\frac{1}{2}\alpha_\mu(x)\,\phi(x)$ if the hop is in the positive direction.
$-\frac{1}{2}\alpha_\mu(y)\,\phi(x)$ if the hop is in the negative direction.

The resulting expressions are particularly simple since all the α's and ϕ's on different sites commute, and $\alpha^2(x) = \phi^2(x) = 1$. Using these rules the value of $Tr(M'^2)$ is given by

$$(M'^2)_{nn} = n \quad \mu \tag{5.25}$$

$$\begin{aligned} Tr(M'^2) &= \sum_{n,\pm\mu} -\frac{1}{4}\alpha_\mu(n)\phi(n)\,\alpha_\mu(n)\phi(n+\mu) \\ &= -\frac{Nd}{2} < \phi(n)\phi(n+\mu) > \end{aligned} \tag{5.26}$$

The fourth order term comprises the following diagrams

$$(M'^4)_{nn} = \quad \mu \quad \nu \quad + \quad \mu \quad \nu \quad + \quad \mu \quad \nu \tag{5.27}$$

n n n

We pick up a minus sign for the fermion loop due to the product of the α_μ around a closed loop, and combining the first two terms we can write this as

$$Tr(M'^4) = \frac{1}{2^4}\left(-2Nd + 2\sum_{n,\pm\mu,\pm\nu} \phi(n+\mu)\phi(n+\nu) - 8\sum_{P} P_{\mu\nu}(n) \right) \tag{5.28}$$

where all other α_μ have squared to one. The last sum is over all *distinct* plaquettes $P_{\mu\nu}(n) = \phi(n)\phi(n+\mu)\phi(n+\mu+\nu)\phi(n+\nu)$. We could of course calculate even higher orders but eqns. 5.26 and 5.28 will be sufficient to test the accuracy of the eigenvalues to a high degree.

A final simple test comes from the observation that $det(M')$ is real due to the

(λ,λ^*) symmetry and hence

$$det(M'^2) = det(M'^\dagger M') = det(M_{KS}^\dagger M_{KS}) \tag{5.29}$$

We know the RHS from the free eigenvalues λ_0 of eqn. 4.16. To avoid numerical overflow we take logs and check the relationship

$$\sum_{i=1}^{N} 2\, log(\lambda_i) = \sum_{p_\mu} log\left(\sum_{\mu} sin^2(p_\mu)\right) \tag{5.30}$$

5.7 The Eigenvalue Spectrum of M'

As a result of the extra $(\lambda, -\lambda)$ symmetry present in M' but not in M, we can evaluate the complete eigenvalue spectrum of M' on volumes as large as 8^4. The eigenvalue spectra of M' at $\kappa = 0.00$, 0.04 and 0.09 are shown in figs. 5.7 to 5.12 where we show both scatter and density plots. The data comes from an 8^4 lattice with antiperiodic boundary conditions in time. Checks on the eigenvalues were performed by comparing the sum of λ^2, the sum of λ^4 and the determinant to eqns. 5.26, 5.28 and 5.30. Some typical numbers are given in table 5.1.

	κ = 0.04	κ = 0.09
$Tr\ (M'^2)$	- 613.999992	- 5322.000004
Eqn. 5.26 gives	- 614.000000	- 5322.000000
$Tr\ (M'^4)$	1988.006	14220.988
Eqn. 5.28 gives	1988.000	14221.000
$log\ (det\ (M'^2))$	2505.5112	2505.5092
Eqn 5.30 gives	2505.5177	2505.5177

Table 5.1 Tests of the numerical accuracy of the computed eigenvalues of M' on an 8^4 lattice compared to the exact analytic results.

Considering that each entry in table 5.1 is the sum of 2048 separately calculated quantities (remember we calculate λ^2) the agreement is good. We conclude that each eigenvalue is accurate to roughly one part in 10^6 from the values of $det(M'^2)$.

Figs. 5.7 to 5.14 confirm our prediction that the eigenvalues transfer from the real to the imaginary axis as κ increases, but what we could not predict was the path that the eigenvalues take. The figures show that the eigenvalues move along a circular path with a radius of approximately $\sqrt{2}$ and do not spread out until they have reached the imaginary axis where they then start to take up the free values $\pm i\lambda_0$. Although there is an increase in the number of imaginary modes at the phase transition the eigenvalues are moving gradually towards the imaginary axis throughout the PM phase. This is because the trace of M'^2 is related to $\langle\phi(n)\phi(n+\mu)\rangle$ and this $Z(2)$ invariant quantity increases with κ even in the symmetric phase. This is to be contrasted with the sudden onset of asymmetry in the spectrum of M at κ_c since $Tr(M)$ is related to $\langle\phi\rangle$.

A very important feature is evident in the density plots (figs. 5.8, 5.10 and 5.12). Although at large κ there is a very high density of eigenvalues on the imaginary axis there are still clumps of eigenvalues on and around the real axis near $\pm\sqrt{2}$. These real eigenvalues persist even at very large κ, analogous to the presence of eigenvalues of M with negative real part deep in the FM phase. We cannot extract their multiplicity at much higher κ due to the onset of degeneracy but the density is presumably decreasing since it must be zero at $\kappa = \infty$. We have studied the same spectra on 4^4 and 6^4 lattices and there is no sign that these real modes are a finite volume effect. We shall return to the fate of these eigenvalues in the infinite volume limit in the next chapter.

We have not displayed data at negative values of κ since these spectra can be obtained from figs 5.7 to 5.12 by rotating the plots by 90^0 about the origin. It is therefore obvious from the figures that as κ is decreased below $-\kappa_c$ the eigenvalues are migrating towards those of a pure AFM configuration given by $\pm\lambda_0$. However, there will still be small clumps of eigenvalues present on the imaginary axis.

The eigenvalue spectrum is qualitatively the same for different choices of boundary conditions with one important exception. For periodic boundary conditions in all directions there are exact zero modes present in M' (at $y = 0$) for

all values of κ. In figs. 5.13 and 5.14 we show the spectrum at $\kappa = 0.08$ with this choice of boundary conditions and the zero eigenvalues are obvious. We know that for $y = 0$ the matrix M has 2^d zero modes since $M(y = 0)$ is simply the free matrix M_{KS}, and obviously these are persisting in M' unaffected by the Yukawa interaction. This is easily explained since $M'^{\dagger}M'$ is a unitary transformation of $M^{\dagger}M$ for all y and hence has the same eigenvalues. Zero modes of M are also zero modes of $M^{\dagger}M$, and therefore there are zero modes in $M'^{\dagger}M'$ and hence in M' as well. This is *only* true for the zero modes since only those eigenvectors with zero eigenvalue are simultaneous eigenvectors of M' and $M'^{\dagger}M'$.

The notable feature of the zero eigenvectors of M_{KS} is that only these eigenvectors can be chosen to be purely even or purely odd. It is obvious from the definition of M' (eqn. 5.13) that the even zero eigenvectors of M_{KS} are also eigenvectors of M' with zero eigenvalue since the even part of M' is completely free. An odd eigenvector e_o of M_{KS} is not an eigenvector of M', but it is again obvious that the vector $e_o' = \phi e_o$ is an eigenvector of M' with zero eigenvalue since $\phi^2 = \mathbf{1}$. From the point of view of the eigenvectors the reason that all the non-zero eigenvalues of M' are perturbed (at finite κ) from their free values is that the corresponding free eigenvectors are mixed even/odd, and only the odd part feels the effects of the ϕ field when acted on by M'.

Numerically, we find n_0 eigenvalues in the spectrum of M'^2 with very small modulus (of the order of 10^{-10}) which we identify as corresponding to $2n_0$ zero modes of M' (typically $n_0 = 5$) . In such a case the Lanczos algorithm will have terminated prematurely after $N/2 - (2^{d-1} - n_0)$ iterations, indicating that there are $(2^d - 2n_0)$ degenerate eigenvalues of M' still to be found. The fact that all these unfound eigenvalues are zero modes is supported by the fact that eqns. 5.26 and 5.28 are very well satisfied by the incomplete set of known eigenvalues and also by the fact that, at this value of κ, there is never a degeneracy in the spectrum with any other set of boundary conditions. We can therefore identify all the expected 2^d zero modes numerically.

5.8 The Phase Diagram and the M' Condensate Mass

The appearance of zero modes in the eigenvalue spectrum of the usual fermion matrix M around $y = \sqrt{2}$ that was discovered in chapter 4 is easily explained from the eigenvalue spectra of M'. We know that a zero mode in $M'(y)$ implies a zero mode in M (remember that to obtain the eigenvalues of $M'(y)$ we simply shift the eigenvalues of M' a distance y along the real axis). The fact that there are real eigenvalues of M' in a narrow band around $-\sqrt{2}$ for all positive (finite) values of κ implies that there will be zero modes in M at $y \approx \sqrt{2}$ in the both the PM and FM phases. This confirms the results of chapter 4. In addition we know that in the AFM phase there will be eigenvalues of M' along the real line in a wide band around $-\sqrt{2}$ (this can be seen by rotating figure 5.11 by 90^0 to obtain the spectrum at $\kappa = -0.09$). This explains why there are zero modes in M for a much larger range of y in the AFM phase than in the PM of FM phases.

The eigenvalue spectra of M' explain the behaviour of the fermion mass and the existence of the PM1 /PM2 boundary if we associate a finite value of the $Z(2)$ invariant primed chiral condensate with the generation of a dynamical mass m_f for the fermions. This condensate at some value of the Yukawa coupling y is given by

$$\langle \bar{\chi}'\chi' \rangle = Tr((M' + y)^{-1}) = y \sum_{\lambda} \frac{1}{(y-\lambda_x)^2 + \lambda_y^2} \qquad (5.31)$$

where the sum runs over all the eigenvalues $\lambda = \lambda_x + i\lambda_y$. We can gain some insight into eqn. 5.31 if we consider the eigenvalues as being unit charges situated at the point (λ_x, λ_y) in some two-dimensional electrostatic system [59]. The chiral condensate is then proportional to the x-component of the electric field at the point $(y, 0)$ in the complex eigenvalue plane (the y-component is zero by symmetry).

If we consider first the case $\kappa = 0$ and approximate figure 5.7 by a perfectly circular ring of uniform density and radius $y^* = \sqrt{2}$ the situation becomes clear. For $y < y^*$ the condensate is zero since we know that the field inside a charged circular shell is zero by Gauss' law. At $y = y^*$ there will be singular behaviour. For $y > y^*$ the charge will be equivalent to a point source at the origin and the

condensate will be given exactly by $1/y$. This is to be compared with $<\bar{\chi}\chi(m_f)>_{free}$ which is zero for $m_f = 0$ and tends to $1/m_f$ as $m_f \rightarrow \infty$. Hence, at $\kappa = 0$, we identify the PM1 region for $y < y^*$ as having $m_f = 0$ and the PM2 region for $y > y^*$ as having m_f increasing with y. For $y = y^*$ we cannot define a mass due to the appearance of exact zero modes in $M'(y)$.

The other limit of interest is the free case where $\phi = \mathbf{1}$. As $\kappa \rightarrow \infty$ then $\lambda_x \rightarrow 0$ and $\lambda_y \rightarrow \lambda_0$. Hence eqn. 5.31 will be exactly the expression for the free chiral condensate and we identify $m_f = y$.

The procedure looks promising in these two idealised cases, but for intermediate values of κ we will have to evaluate eqn. 5.31 numerically and fit to the free case to calculate m_f. Allowing for a wave function renormalisation $\sqrt{Z(y)}$ we wish to solve

$$<\bar{\chi}\chi(m_f)>_{free} = Z^{-1}(y) <\bar{\chi}'\chi'(y)> \tag{5.32}$$

for m_f at different values of y. In the quenched approximation we can do this for all y once we know the eigenvalue spectrum of M'. At large y we can expand the RHS to leading order in $1/y$ to obtain the value of the primed chiral condensate in the PM2 region

$$\frac{1}{N} Tr\,(M' + y)^{-1} = \frac{1}{y}\left(1 - \frac{d}{2}\left(\frac{z}{y}\right)^2\right) + O(y^{-5}) \tag{5.33}$$

where we have used eqn. 5.26 and the fact that all traces of odd powers of M' are zero. Comparing this to the equivalent expansion of the LHS to leading order in $1/m_f$

$$\frac{1}{N} Tr\,(M_{KS} + m_f)^{-1} = \frac{1}{m_f}\left(1 - \frac{d}{2}\left(\frac{1}{m_f}\right)^2\right) + O\,(m_f^{-5}) \tag{5.34}$$

we can identify

$$m_f = \frac{y}{z} \tag{5.35}$$

$$Z(y) = \frac{1}{z} \tag{5.36}$$

which reproduces the expected large y result derived from the fermion propagator (eqn. 3.23).

However, there are two problems major in solving eqn. 5.32 in the general case. Firstly, we have one equation for two unknowns and we have already seen that $Z(y) \neq 1$ from our attempts to define m_f from the eigenvalues of M. Secondly, there will always be two solutions since the LHS is always positive and equal to zero at $m_f = 0$ and $m_f = \infty$.

A possible solution is again to consider the derivative of the condensate with respect to the mass which involves four fermion fields and so has a renormalisation factor of $Z^2(y)$. Hence we could fit the ratio R given by

$$R = \frac{Tr(M'^{-2})}{(Tr(M'^{-1}))^2} \tag{5.37}$$

which is independent of Z (we could not do this previously for M due to the vanishing of the denominator). If we evaluate this approximately in the free theory using the usual approximation $\lambda = m \pm i\sqrt{(d/2)}$ we find

$$R_{free}(m) = \frac{m^2 - \frac{d}{2}}{m^2} \tag{5.38}$$

which is a monotonically increasing function of m which varies from $-\infty$ to 1

This ratio has the disadvantage that it has no direct relevance to the static charge picture that is so helpful in understanding the mechanism for mass generation. In practice it is of no use since we find that we cannot fit R to the free theory for all values of y because R can become greater than one. Eqn. 5.38 shows that there is no solution for m in such a case

The solution we adopt is to realise that the fact that the condensate is real is due to the cancellation of the imaginary part of the sum over $1/\lambda$ between an eigenvalue $\lambda = \lambda_x + i\lambda_y$ above the real axis and its partner below the real axis $\lambda_x - i\lambda_y$. The condensate is completely determined by those eigenvalues above the real axis thanks to the (λ,λ^*) symmetry in the spectrum. Hence we define the complex quantity $\langle\bar{\chi}'\chi'\rangle_{uhp}$ where $\langle\rangle_{uhp}$ means that we evaluate the observable using only those eigenvalues in the upper half plane with $Im(\lambda) > 0$. We can then solve

$$<\bar{\chi}'\chi'(y)>_{uhp} = Z(y) <\bar{\chi}\chi(m_f)>^{free}_{uhp} \quad (5.39)$$

since we have two equations (real and imaginary parts) for the two unknowns Z and m_f. In practice we form the quantity R' by taking the ratio of real and imaginary parts to eliminate the renormalisation constant.

$$R' = \frac{Re(<\bar{\chi}'\chi'>_{uhp})}{Im(<\bar{\chi}'\chi'>_{uhp})} \quad (5.40)$$

and fit to a free theory with mass m_f. To see that this is a reasonable quantity to fit we evaluate R' approximately in the free case using $\lambda = m \pm i\sqrt{(d/2)}$ to obtain

$$R'_{free}(m) = -m\sqrt{\frac{2}{d}} \quad (5.41)$$

which is a nice linear relationship. To summarise, the procedure we use is to compute the eigenvalue spectrum of M' at a given κ and then solve

$$R'_{free}(m_f) = R'(y) \quad (5.42)$$

for all the required values of y to obtain the curve $m_f(\kappa,y)$. We evaluate the LHS of eqn. 5.42 exactly from the free eigenvalues of M_{KS} calculated on a lattice of the same size and with the same boundary conditions as that used for M'.

There are, however, difficulties involved in evaluating the LHS of eqn. 5.39 due to the presence of exactly real modes. These cause two main problems. Firstly, the LHS of eqn. 5.39 will behave in a singular fashion whenever $y = -\lambda_{real}$. This is in fact not a major problem since it only occurs (for $\kappa > -\kappa_c$) in the region around $y = y^*$ where we do not expect to be able to define a mass. Secondly, we have to decide how to include the real modes in eqn. 5.39 since they lie neither in the upper nor lower half plane. We choose to include the real eigenvalues in the sum over $1/\lambda$ but with a weight of 1/2. This has the advantage that it maintains the relationship

$$<\bar{\chi}'\chi'> = <\bar{\chi}'\chi'>_{uhp} + <\bar{\chi}'\chi'>^{*}_{uhp} \quad (5.43)$$

which holds in the free theory and means that we solve eqn. 5.32 exactly for Z and m_f by solving the related eqn. 5.39.

Another possible solution would be to ignore the real modes completely which allows us to define a mass throughout the crossover region. However, this mass will have little meaning. We cannot consistently define a mass in the crossover

region because the condensate can become negative and there is therefore no solution to eqn. 5.32 for positive m_f.

The need to know the renormalisation constant Z in order to calculate m_f is a disadvantage of our procedure compared to the usual definition of m_f from the fermion propagator. The value of Z in the latter case is irrelevant since we are only interested in the rate of decay of the propagator and not its actual value. Whether our particular method of determining Z is a consistent one will only be decided by performing the simulation and calculating m_f.

5.9 Numerical Results for the Fermion Mass

The results obtained on a 6^3 x 12 lattice at $\kappa = 0.08$ with antiperiodic boundary conditions in time are shown in figure 5.15 alongside our own data for the propagator mass. There is qualitative agreement for small and large y and although there is not exact numerical agreement we conclude that the condensate mass is a very useful indicator of the value of m_f. The results obtained at $\kappa = 0.04$ in the PM phase and $\kappa = 0.0775$, 0.0800, 0.0825 and 0.0850 in the FM phase are shown in figure 5.16. Each curve is averaged over 50 configurations (100 at $\kappa = 0.0775$ and 0.0800) each separated by 10,000 heatbath sweeps. The error bars (not shown in the figure) are all less than $\pm 2\%$ for $y < y^*$ and roughly constant at ± 0.008 for $y > y^*$. The gaps in figure 5.16 occur where we are unable to define m_f either because the condensate becomes negative or because it fluctuates so wildly that the errors in m_f are huge. This region coincides with the region in y for which the propagator mass is not defined and suggests that the failure of both methods is due to the appearance of very small eigenvalues in the appropriate fermion matrix.

As expected, we find that in the FM phase the fermion mass increases with increasing κ for $y < y^*$ and decreases with increasing κ for $y > y^*$. The mass continues to increase as κ is reduced across the FM / PM2 phase boundary, whereas in the PM1 region we observe a very small (but non-zero) fermion mass. From the perturbative and large y expressions for m_f (eqns. 3.3 and 3.23) we

expect the curves to approach the lines $m_f = y \langle\phi\rangle$ as $y \to 0$ and $m_f = yz^{-1}$ as $y \to \infty$. In table 5.2 we compare these predictions to the actual gradients where we assume that the curves are linear in y for $y \geq 3.0$ and quadratic in for $y \leq 0.2$.

κ	$\langle\phi\rangle$	$\frac{\partial m_f}{\partial y}\Big\|_{y=0}$	$\frac{1}{z}$	$\frac{\partial m_f}{\partial y}\Big\|_{y=\infty}$
0.0400			3.425(9)	1.653(1)
0.0775	0.409(8)	0.372(5)	1.805(6)	1.422(1)
0.0800	0.533(5)	0.483(4)	1.603(5)	1.349(1)
0.0825	0.613(6)	0.565(5)	1.477(4)	1.291(1)
0.0850	0.672(5)	0.629(5)	1.393(4)	1.245(1)

Table 5.2 Comparison of the values of the condensate mass obtained on a $6^3 \times 12$ lattice to the expected small and large y expressions. We do not give results in the PM1 region where $\langle\phi\rangle = 0$.

We see from table 5.2 that, for small y, the condensate mass is only between five and ten percent smaller than one would expect from the perturbative relation. However, at large y the agreement is much worse. Although the condensate mass decreases with κ as predicted the quantitative agreement is very bad. There are, however, some signs that the large y expansion is becoming more accurate with increasing κ but we are unable to check this any further because we encounter degeneracy in the spectrum of M' for $\kappa > 0.850$.

Comparison with the extensive data for m_f in ref [37] (obtained on an $8^3 \times 16$ lattice) shows that the disagreement does not represent a discrepancy with the propagator mass. The propagator gives a large y gradient of 1.44 at $\kappa = 0.0800$ and of 1.30 at $\kappa = 0.0850$ and we see that the condensate results are only about five percent less than this.

An interesting feature of fig. 5.16 is that as y approaches y^* from below the mass curve flattens off and eventually the mass decreases with y close to the PM1 /

PM2 boundary. In the electrostatic picture this is because our test charge at $(y,0)$ is approaching the clump of positive charges around $(\sqrt{2},0)$ from the left. The effect of these charges is to reduce the x-component of the electric field since their field is in the $-x$ direction, and the chiral condensate (and hence m_f) decreases with increasing y. This effect is also seen in the propagator mass which flattens off with y up to the point where it can no longer be defined around $y = 1.0$. In ref [37] there is evidence, unfortunately from a single point, that the propagator mass does indeed turn over and decrease for $y > 1.0$ at $\kappa = 0.08$, so it seems that this effect is not purely an artifact of the condensate method.

It is instructive to plot the wave function renormalisation constant $\sqrt{Z}$ against y. The results are shown in fig 5.17 and we see that $\sqrt{Z}$ becomes greater than one in the PM2 region. Fig. 5.17 supports our previous conclusion, drawn from the study of the eigenvalues of M, that the wave function renormalisation is greater than one in the region $y > 1.5$.

5.10 Conclusions

These studies have shown that it is possible to gain much information about the behaviour of the renormalised fermion mass m_f in all regions of the phase diagram from the eigenvalues of the $Z(2)$ invariant fermion matrix M'. It has been shown that it is possible to qualitatively predict the behaviour of m_f from the knowledge of a very few eigenvalue spectra via a simple electrostatic analogy, and also to obtain reasonable quantitative results from higher statistics studies. Our purely local definition of m_f agrees with the non-local propagator definition because we have seen that only one mass state contributes to the fermion propagator.

In quenched studies the method allows results at all Yukawa couplings to be calculated with no additional overheads. In dynamical studies this definition of the mass will be of great use in very small volumes where full simulations are possible but the usual propagator method is unworkable, and we should be able to very rapidly sketch out the phase diagram of the dynamical $Z(2)$ model.

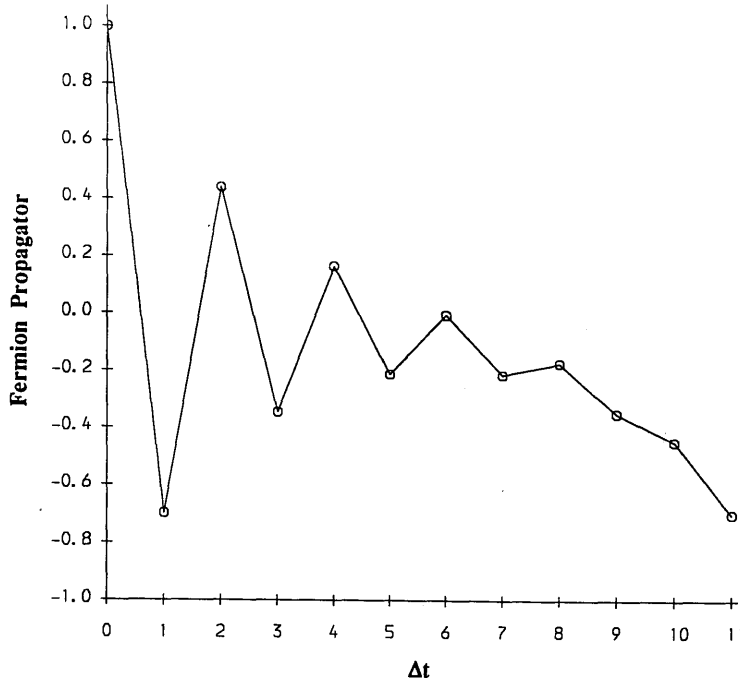

Fig. 5.1 The fermion propagator vs. time difference Δt on a $6^3 \times 12$ lattice starting from an even site. Points (o) calculated at $\kappa = \infty$, $y = 0.4$. Solid line is fit from eqn. 5.3 with $E_0 = 0.390$.

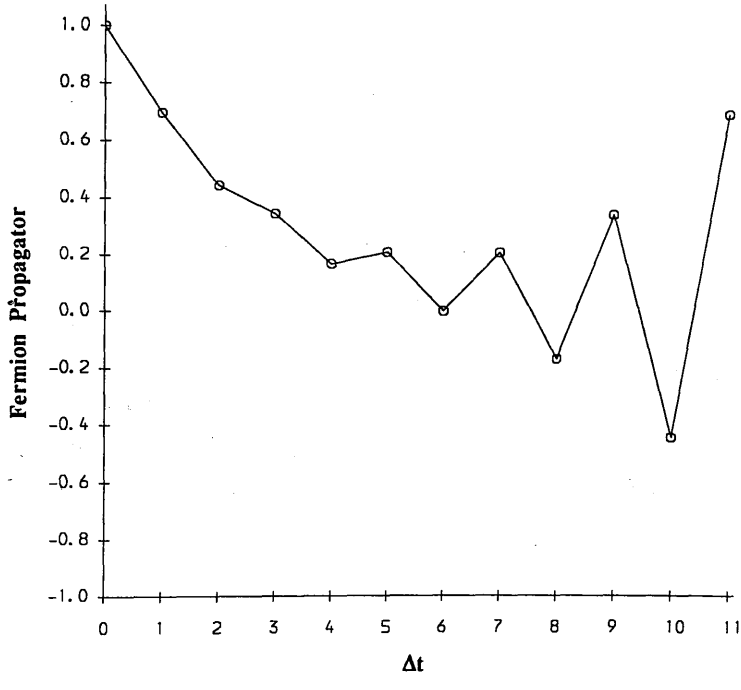

Fig. 5.2 The fermion propagator vs. time difference Δt on a $6^3 \times 12$ lattice starting from an odd site. Points (o) calculated at $\kappa = \infty$, $y = 0.4$. Solid line is fit from eqn. 5.3 with $E_0 = 0.390$.

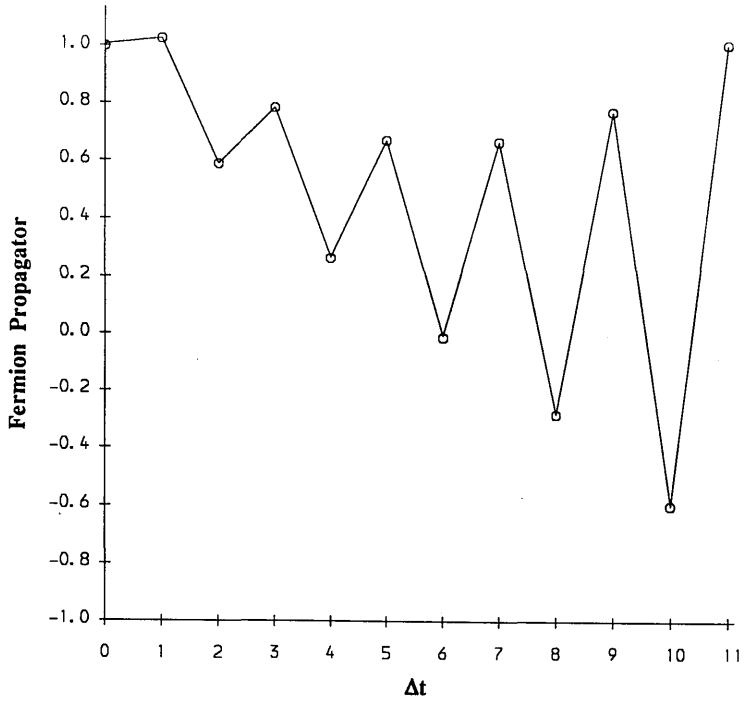

Fig. 5.3 The fermion propagator vs. time difference Δt on a $6^3 \times 12$ lattice starting from an odd site. Points (o) calculated at $\kappa = 0.08$, $y = 0.4$. Solid line is fit from eqn. 5.3 with $E_0 = 0.200$.

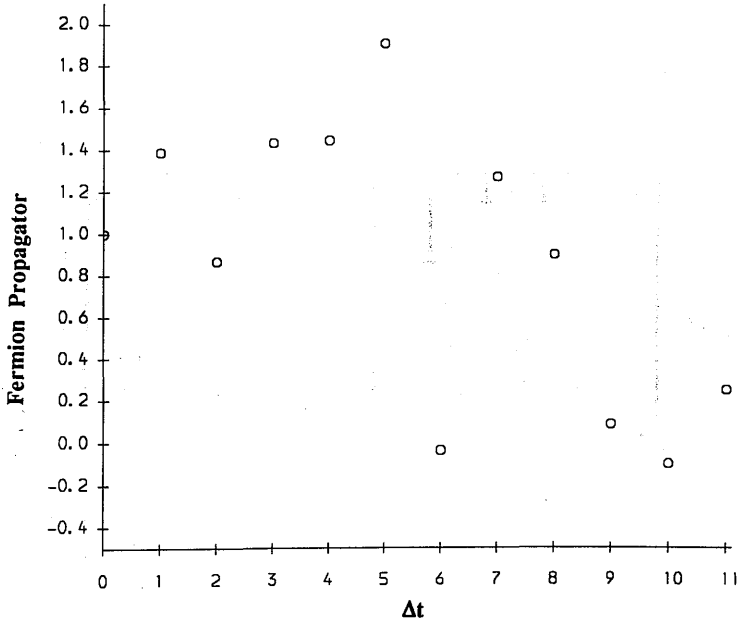

Fig. 5.4 The fermion propagator vs. time difference Δt on a $6^3 \times 12$ lattice starting from an odd site. Points (o) calculated at $\kappa = 0.08$, $y = 1.2$. Fit to the free form of eqn. 5.3 is not possible.

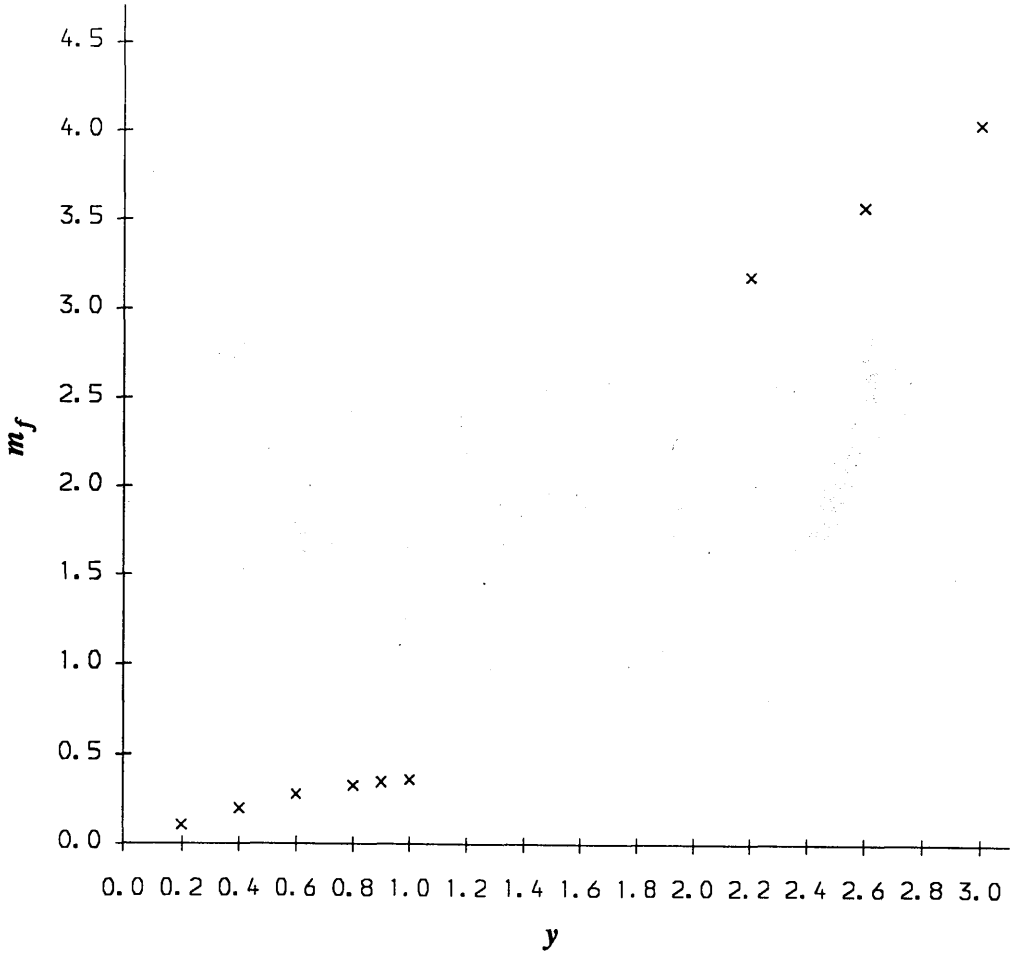

Fig. 5.5 The fermion propagator mass m_f vs. local Yukawa coupling y on a $6^3 \times 12$ lattice at $\kappa = 0.08$.

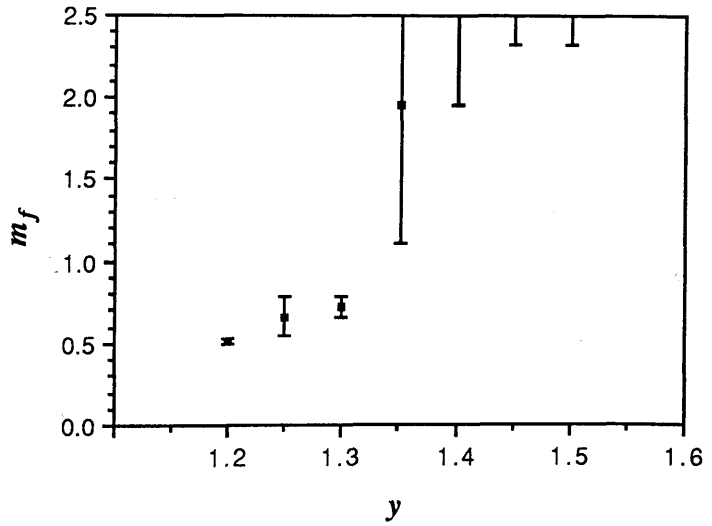

Fig. 5.6 The fermion mass m_f calculated from the eigenvalue spectrum of M vs. local Yukawa coupling y on a 6^4 lattice at $\kappa = 0.07$.

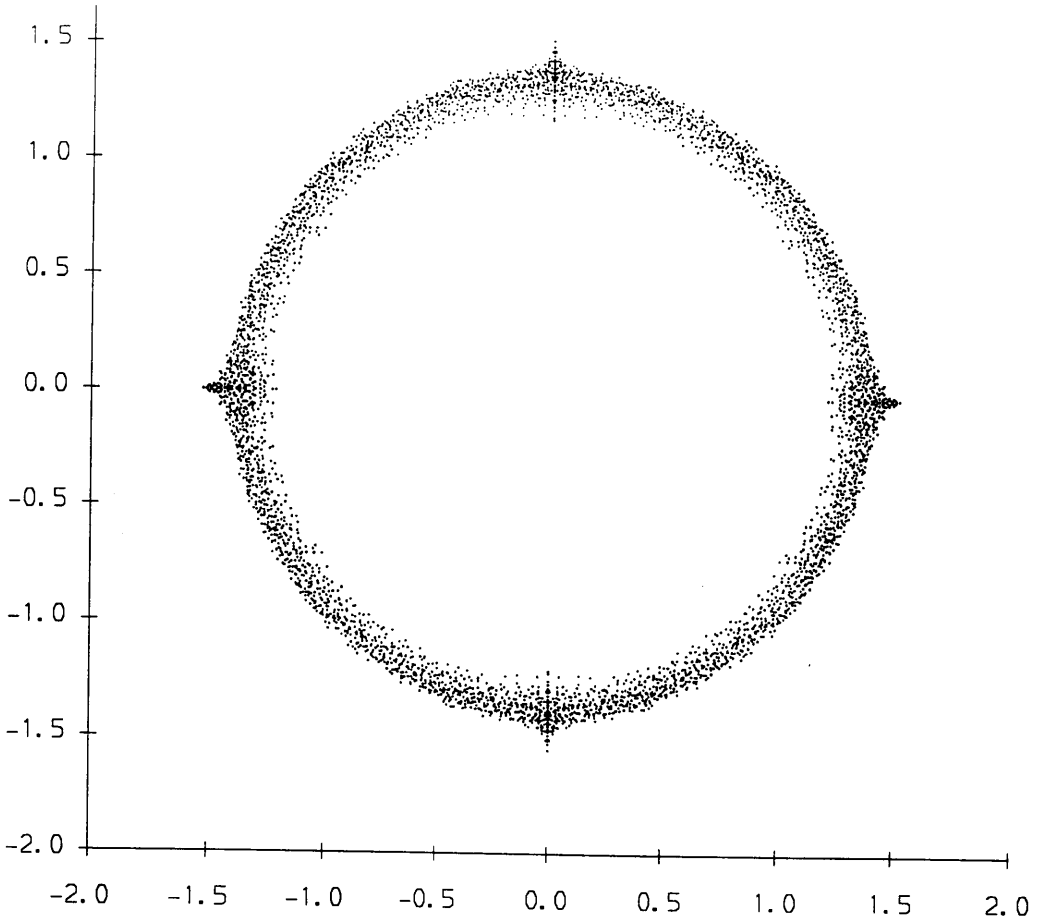

Fig. 5.7 The eigenvalue spectrum of M' in the complex plane for an 8^4 lattice Hopping parameter $\kappa = 0.00$.

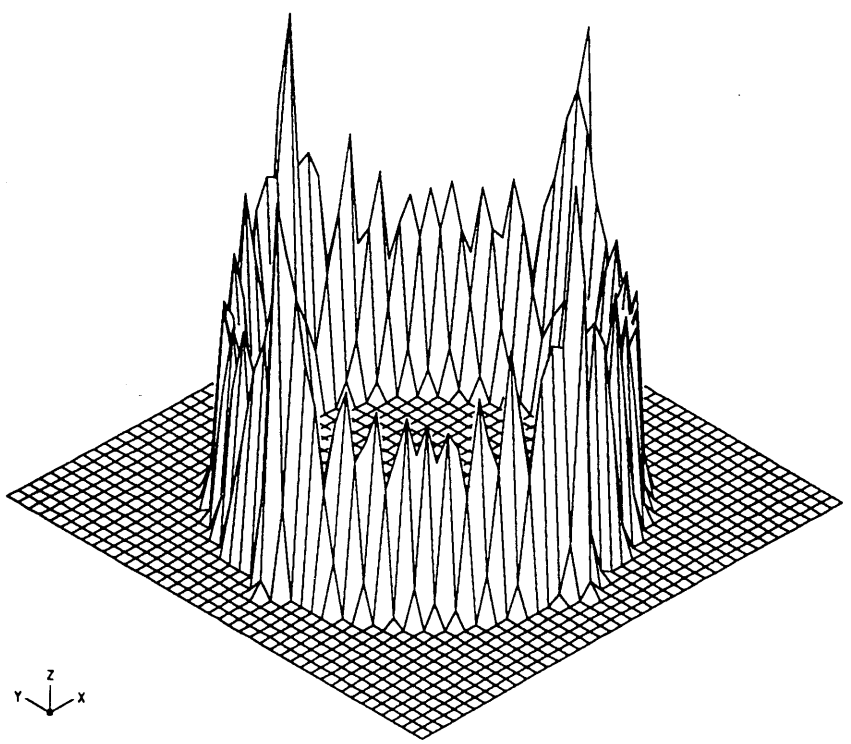

Fig. 5.8 Density of eigenvalues of M' in the complex plane for an 8^4 lattice. Hopping parameter $\kappa = 0.00$.

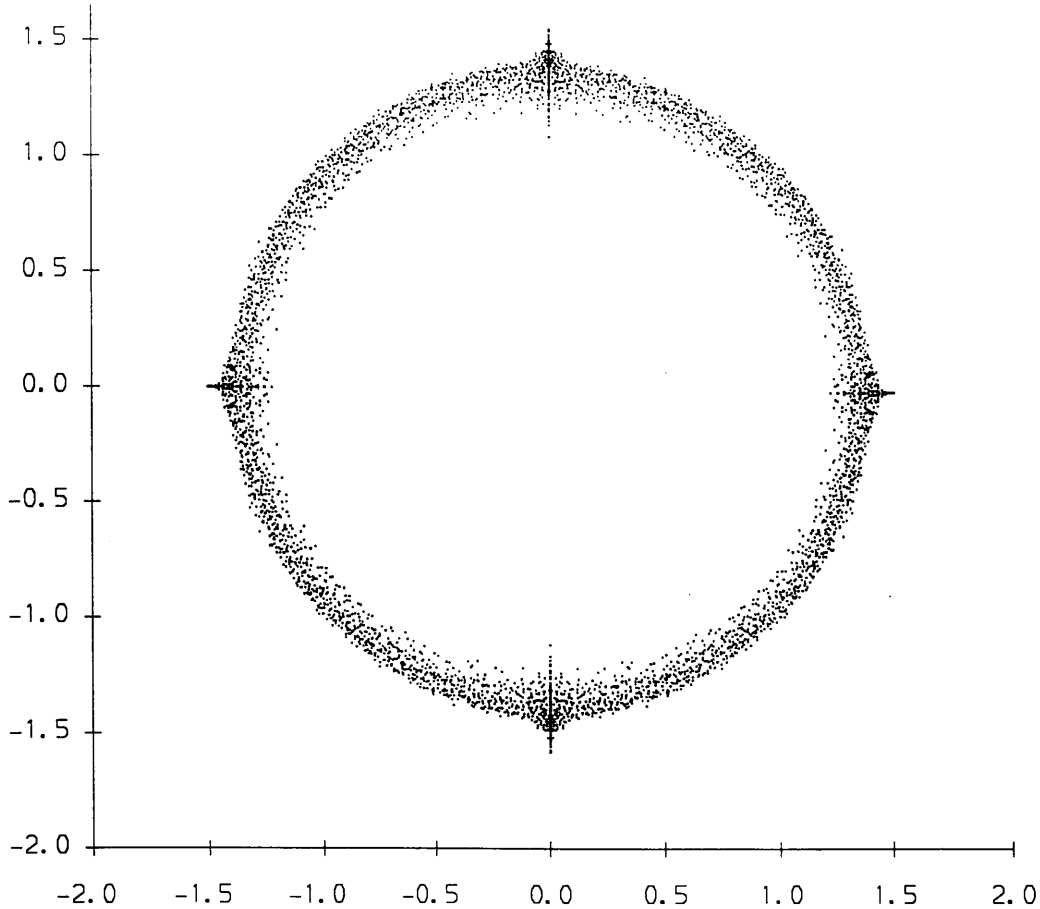

Fig. 5.9 The eigenvalue spectrum of M' in the complex plane for an 8^4 lattice. Hopping parameter $\kappa = 0.04$.

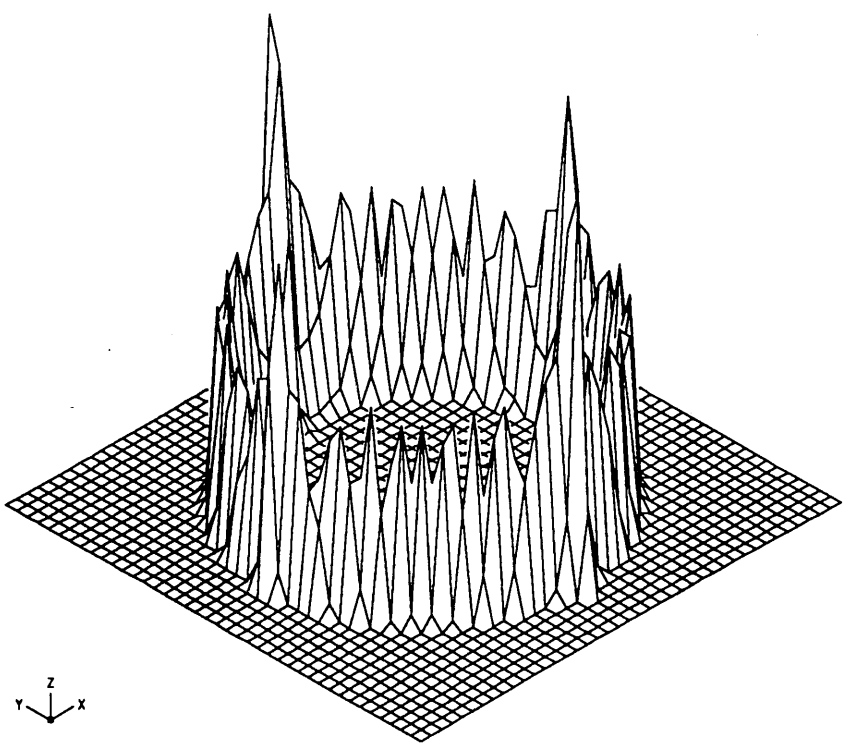

Fig. 5.10 Density of eigenvalues of M' in the complex plane for an 8^4 lattice. Hopping parameter $\kappa = 0.04$.

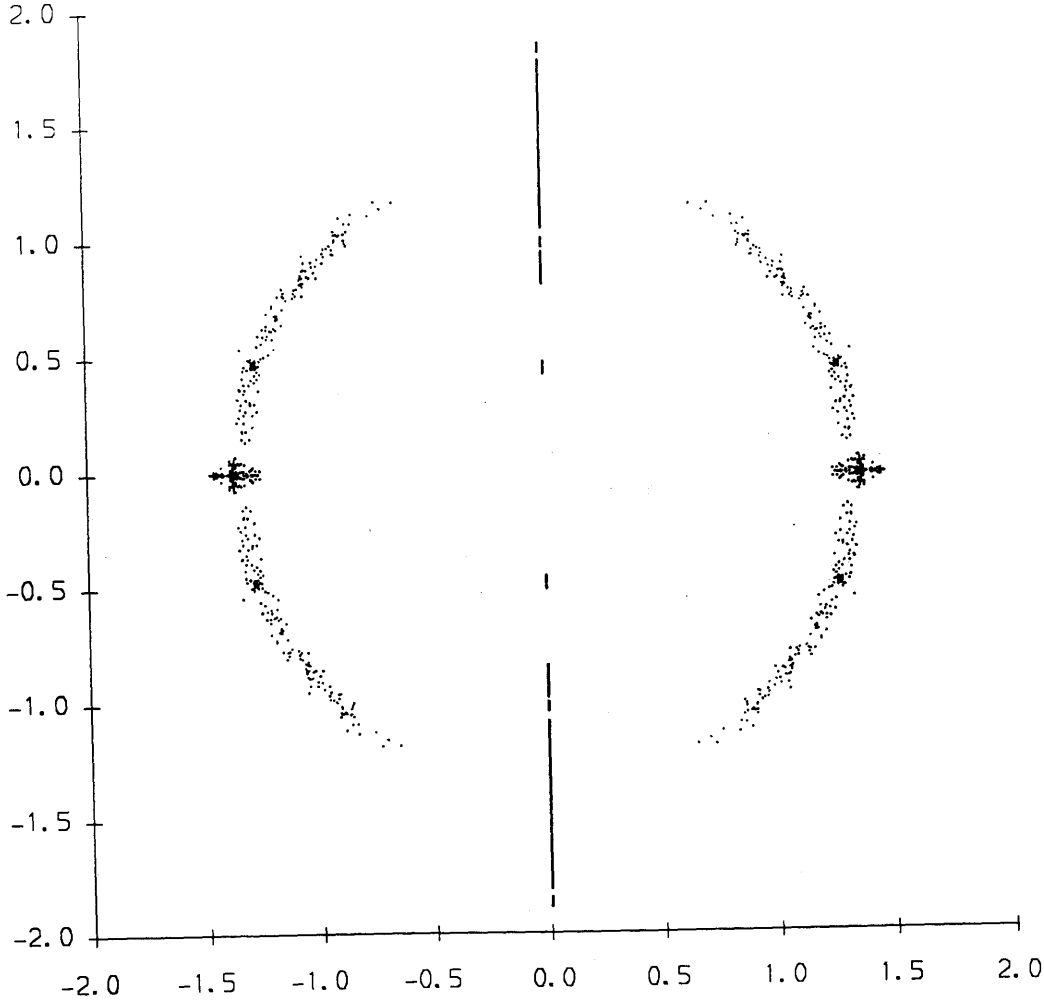

Fig. 5.11 The eigenvalue spectrum of M' in the complex plane for an 8^4 lattice. Hopping parameter $\kappa = 0.09$.

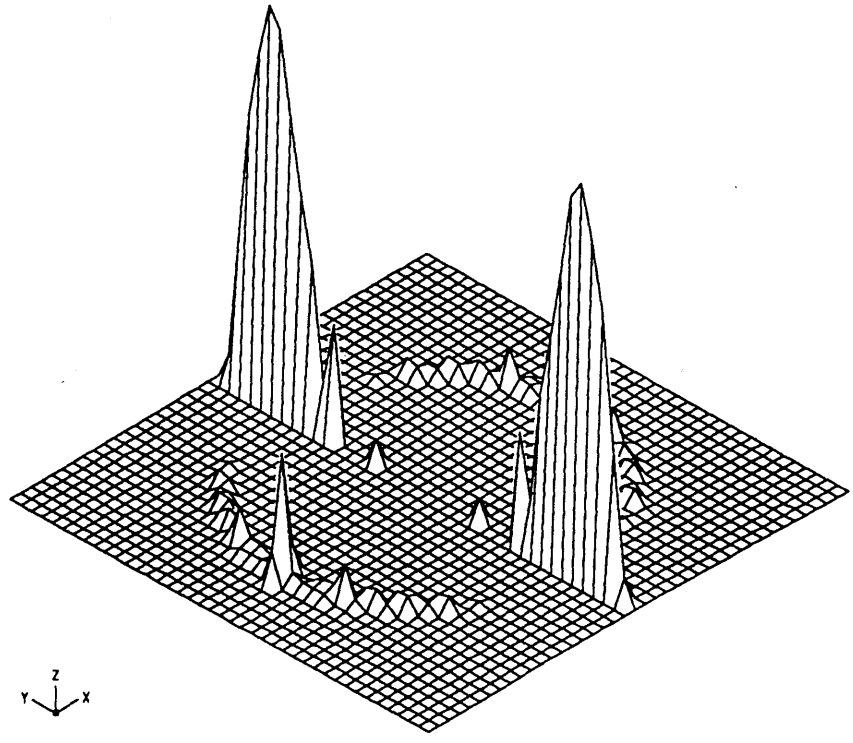

Fig. 5.12 Density of eigenvalues of M' in the complex plane for an 8^4 lattice. Hopping parameter $\kappa = 0.09$.

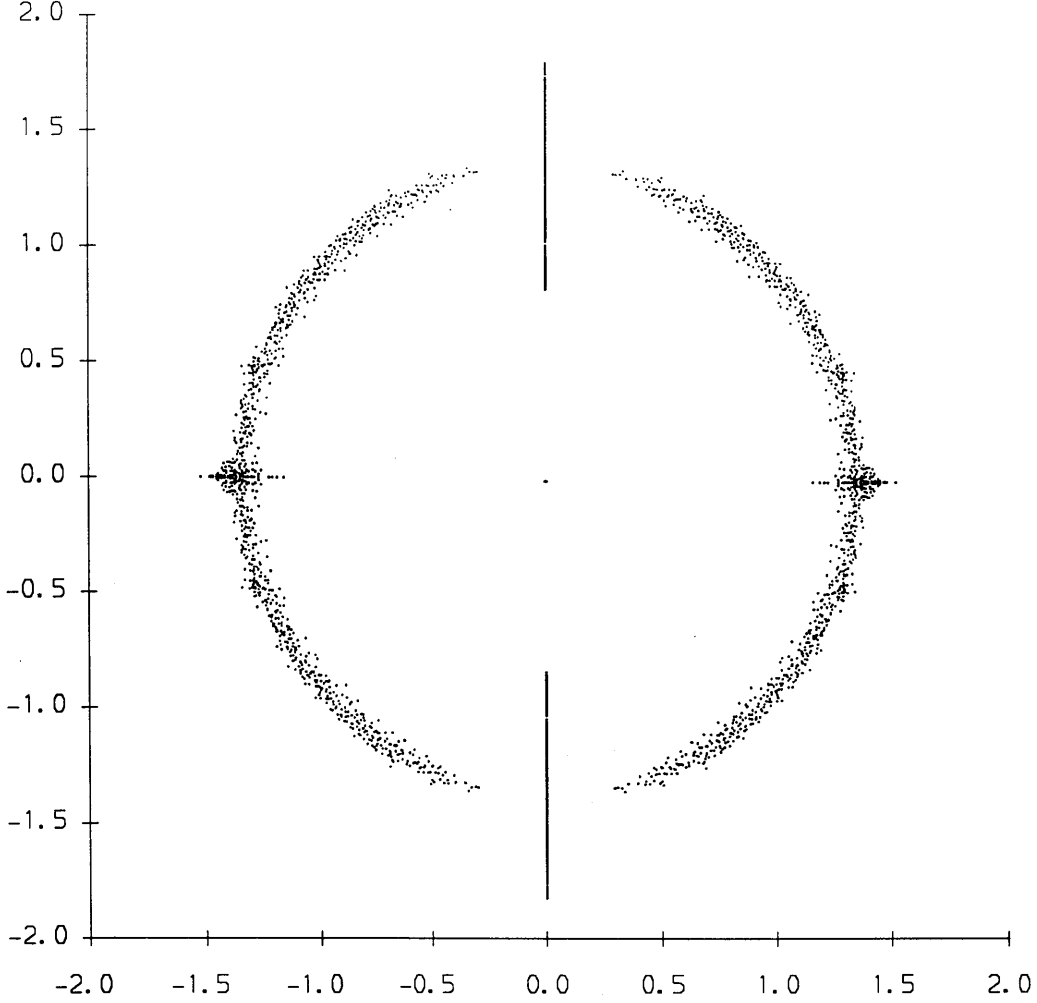

Fig. 5.13 The eigenvalue spectrum of M' in the complex plane for an 8^4 lattice using periodic boundary conditions. Hopping parameter $\kappa = 0.08$.

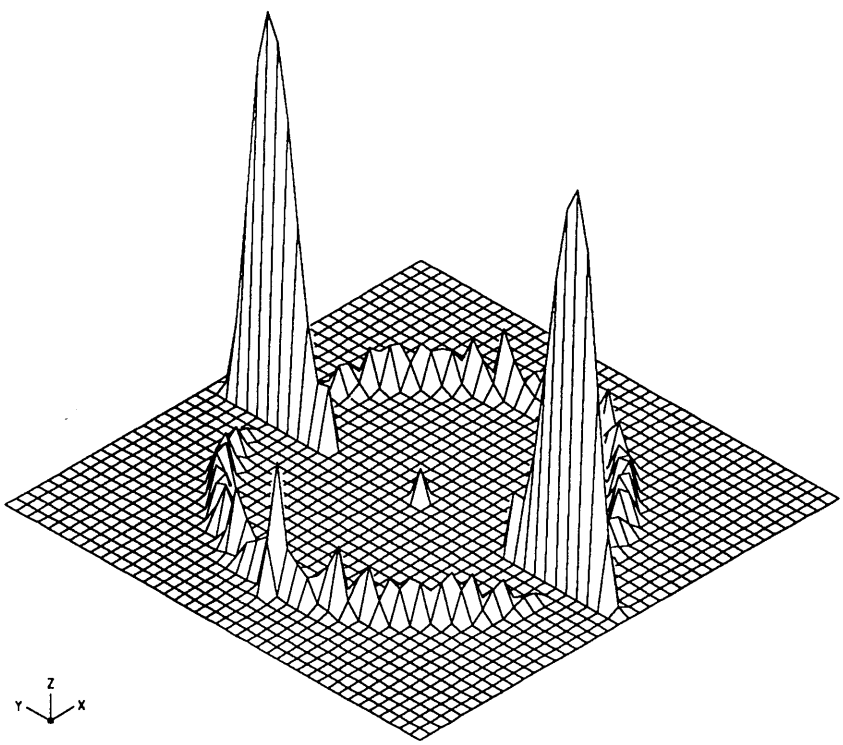

Fig. 5.14 Density of eigenvalues of M' in the complex plane for an 8^4 lattice using periodic boundary conditions. Hopping parameter $\kappa = 0.08$.

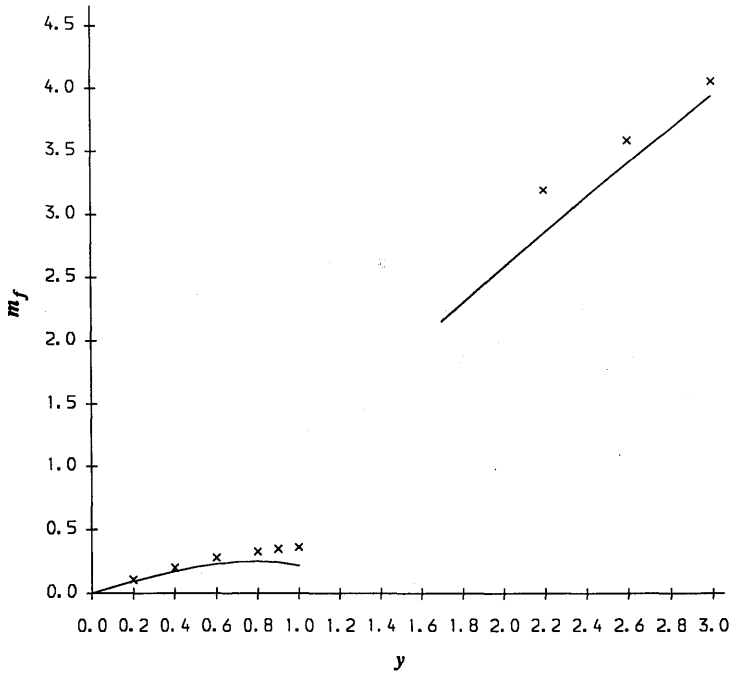

Fig. 5.15 The fermion mass m_f vs. local Yukawa coupling y on a $6^3 \times 12$ lattice at $\kappa = 0.08$. Points ($\times$) are from the fermion propagator, solid line is from the fit to the M' condensate.

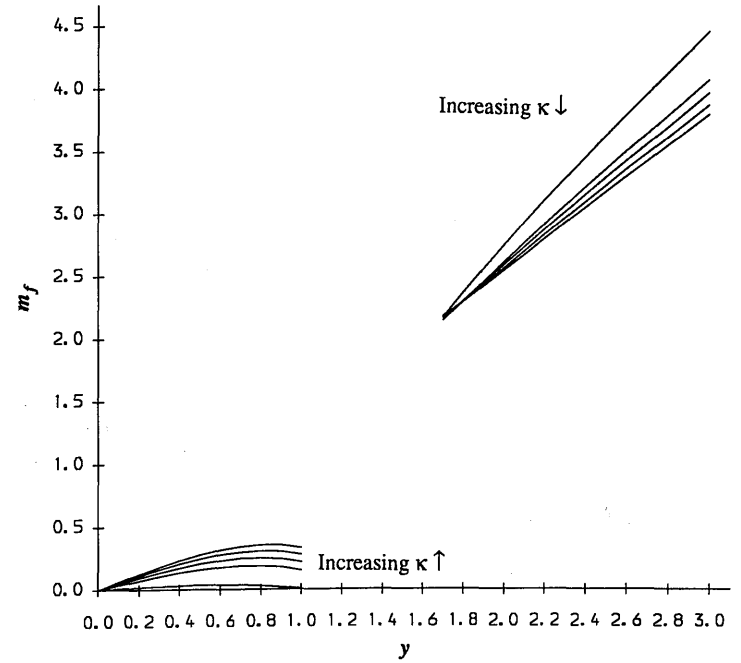

Fig. 5.16 The fermion mass m_f vs. local Yukawa coupling y on a $6^3 \times 12$ lattice at $\kappa = 0.0400$, 0.0775, 0.0800, 0.0825 and 0.0850.
Note that the order of the curves is reversed at small and large y.

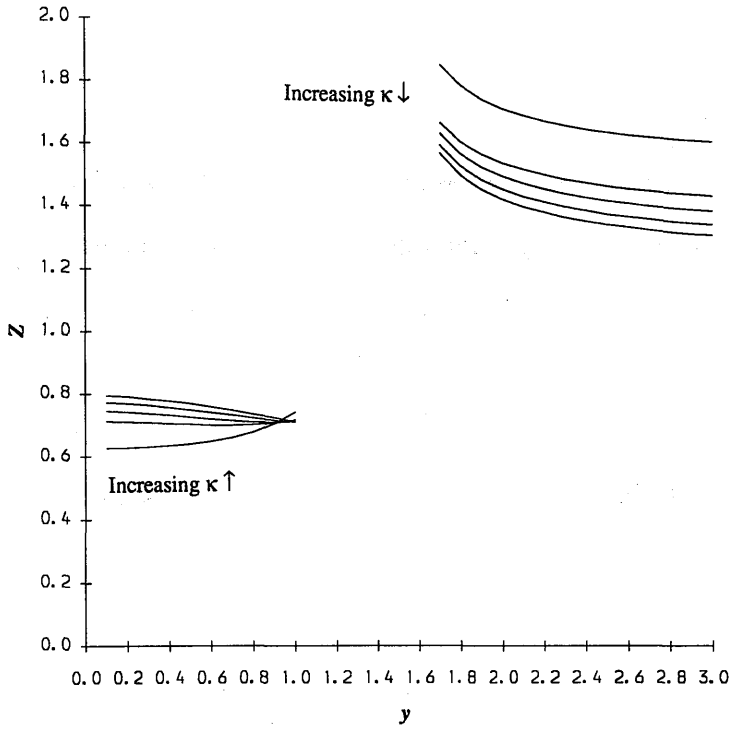

Fig. 5.17 The fermion renormalisation Z vs. local Yukawa coupling y on a $6^3 \times 12$ lattice at κ = 0.0400, 0.0775, 0.0800, 0.0825 and 0.0850. Note that the order of the curves is reversed at small and large y.

Chapter 6

The Quenched Infinite Volume Limit

6.1 Introduction

From the eigenvalue spectra of both M and M' we have seen that in Higgs / fermion systems defined with local Yukawa coupling y the crossover region around $y^* \approx \sqrt{2}$ is the region where there are many small eigenvalues present in the spectrum of the fermion matrix. We have seen from the studies of M' that the total number of small modes present for y around y^* decreases as κ is increased above κ_c, but we still observe a finite number even for very relatively large κ on the volumes studied so far (up to 8^4). The continued existence of zero modes in the $Z(2)$ model means that the crossover region (where we are unable to define the fermion mass) persists well into the FM phase unlike some other related models, eg. the $SU(2)_L \times SU(2)_R$ model of ref [53]. Hence it is an important question whether or not these modes will persist in the infinite volume limit.

6.2 The Hermitian Lanczos Algorithm

Our previous studies have been concerned with the complex eigenvalues of M and M' and we have been limited to rather small volumes by the need to use the non-hermitian Lanczos algorithm. A crucial feature of this algorithm is that we have to perform a global reorthogonalisation of the Lanczos vectors after each iteration. This requires that we store all N Lanczos vectors simultaneously and we are therefore forced to consider small lattices due to limited computer memory. In addition the huge computational overhead of the reorthogonalisation step makes studies on lattices larger than 8^4 unfeasible due to limited computer time. If we were to consider a hermitian matrix H then we would be able to use the hermitian algorithm [60]. The advantage of this algorithm for determining real eigenvalues is that we do not need to reorthogonalise, and at each iteration storage is only required

for the two most recent Lanczos vectors x_i and x_{i-1} and one additional vector for workspace. For the hermitian algorithm the time taken grows as N^2 if H is sparse, which is to be compared with the N^3 behaviour of the non-hermitian algorithm at large N.

In order to be able to use the hermitian algorithm we study the low lying eigenvalues of the hermitian matrix $M^\dagger M$. These small eigenvalues are relevant since if $M^\dagger M$ has a zero mode then so will M, and since the matrix $M'^\dagger M'$ is a unitary transformation of $M^\dagger M$ this implies a zero mode for M' as well. The price we pay is that, unlike M', the eigenvalues of $M^\dagger M$ are not a trivial function of the Yukawa coupling and we have to do a completely separate calculation for each value of y. Fortunately we already know the region of y for which $M^\dagger M$ will have small eigenvalues from the small volume studies of M and M'.

To calculate the eigenvalues of some hermitian matrix H we use the iterative procedure of eqns. 2.27 to 2.30 as for the block algorithm but we set $B = 1$ to generate a real, symmetric tridiagonal matrix that is a unitary transformation of H. The α's and β's that comprise the tridiagonal form written in the manner of eqn. 2.10 are therefore real scalar quantities and the implementation is much simpler than the general case $B \neq 1$. However, because we no longer reorthogonalise the Lanczos vectors we will never have $\beta_i = 0$ for some $i \leq N$, and the problem is that we must decide at which iteration N' to terminate the algorithm. We can then easily calculate the eigenvalues of the resulting tridiagonal form T' by some standard procedure, but the problem is then one of deciding which eigenvalues λ' of T' are true eigenvalues of T (and hence of H).

6.2.1 Sturm Sequencing

Let us postpone the question of exactly when to terminate the algorithm and assume that we have generated some real symmetric tridiagonal matrix T' consisting of N' α's and β's. We extract the eigenvalues of this matrix by the process of Sturm sequencing [61] which relies on the following theorem:

The number of eigenvalues λ of some N' dimensional hermitian matrix T' less than a certain value λ_0 is given by the number of changes of sign in the sequence $[d_0, d_1 \ldots d_{N'}]$, where d_i is the minor determinant of $T' - \lambda_0 \mathbf{1}$ formed from the first i rows and columns and we set $d_0 = 1$.

This theorem is obvious in the case where T' is diagonal and fortunately holds in the general case. To find the n^{th} eigenvalue of T' to some desired accuracy $\pm\delta\lambda_n$ we use the theorem to find a value λ_n such that there are n-1 eigenvalues below $\lambda_n - \delta\lambda_n$ and n below $\lambda_n + \delta\lambda_n$. This can be done very simply with a bisection procedure. The advantage of this method over an exact method (such as the QL algorithm [52]) is that if we are only interested in the eigenvalues of T' within a limited range we only have to calculate those particular eigenvalues. The QL algorithm becomes prohibitively time consuming for the very large values of N' that we will encounter, but we are forced to use it for non-hermitian matrices because there is no generalisation of this crucial sequencing theorem to the case of complex eigenvalues. The use of Sturm sequencing to calculate eigenvalues is very efficient for the specific case of the tridiagonal form T' since we can generate d_i iteratively from d_{i-2} and d_{i-1} using the known values of α_i and β_{i-1}. Since we are only interested in the changes of sign of d_i we calculate the ratio d_i/d_{i-1} which eliminates overflow problems.

The problem now is to decide whether λ_n is a true eigenvalue of T as well as T' or whether it is a spurious eigenvalue that is only present in the spectrum of T'. This is done by realising that if λ_n has converged at iteration N' it should be unchanged by running the algorithm for one more iteration and stopping at iteration $N'' = N' + 1$. We identify the true eigenvalues λ_n of T as those which are eigenvalues (to within the desired accuracy $\delta\lambda_n$) of both T' and T''. This is easily checked for each eigenvalue without performing a separate calculation of the spectrum of T'' since it only depends on the relative signs of $d_{N'}$ and $d_{N'+1}$.

As well as these spurious eigenvalues which we identify and remove due to

their instability, 'ghost' eigenvalues can also appear. These are stable degenerate partners of true eigenvalues that occur because we typically have $N' >> N$ and some eigenvalues of H can therefore appear more than once in T'. We identify and remove these by demanding that the true eigenvalues should be separated by some minimum amount.

6.2.2 Implementation for $M^\dagger M$

We wish to find the eigenvalues of $M^\dagger M$. This is most efficiently done by calculating the eigenvalues of $UM = (P_e - P_o)M$, which is hermitian but not positive definite. From eqn. 4.31 we see that $(UM)^2 = M^\dagger M$ and hence we can square up the eigenvalues of UM as we calculate them. This implementation requires only one multiplication of a Lanczos vector by M per iteration compared to two such multiplications required to evaluate the eigenvalues of $M^\dagger M$ directly. The fact that the eigenvalues are not necessarily positive causes no complications in Lanczos algorithm or in the Sturm sequencing. An approach similar to this was considered in section 5.3 for the inversion of M but was rejected since inversion requires x_1 to be a delta function and this can cause the problem $\alpha_2 = 0$. When we only wish to produce some tridiagonal form T we are free to choose x_1 arbitrarily, and taking it to be a random vector normalised to unity removes this problem.

There is no exact symmetry in the eigenvalue spectrum of UM except in the case $y = 0$. In this limit the eigenvalues are given by $\pm\lambda_0$, with λ_0 given by eqn. 4.16. For finite y the high degeneracy of these free modes will be removed and we should obtain N distinct eigenvalues.

By the above procedure we can extract all the eigenvalues of T' that are eigenvalues of H and we can work in real arithmetic throughout if x_1 is chosen to be real. The only remaining question is when to stop the algorithm in order to guarantee that all the desired (in our case small) eigenvalues of H are contained in T'. We could of course run for many iterations, say $N' = 10N$, but this would take prohibitively long and we therefore require some reliable lower bound on N'.

6.2.3 Convergence of the Eigenvalues

If we suspend the Lanczos algorithm at regular intervals and extract all the stable eigenvalues contained in the tridiagonal T we can monitor the order in which the eigenvalues of UM are being determined. We find that the eigenvalues of smallest and largest absolute value converge first, and subsequently the spectrum fills in from the edges towards the centre in a smooth fashion as the algorithm proceeds. We find that the small eigenvalues of UM are distributed roughly symmetrically about the origin and also that the positive and negative modes converge in a symmetric fashion. Since we are interested in those eigenvalues of $M^\dagger M$ below some cutoff Λ^2 we should halt the algorithm when those of UM around Λ have converged. From the order in which the eigenvalues converge we can then guarantee that we will have found all the eigenvalues of UM in the interval $[-\Lambda, \Lambda]$ and hence all the required eigenvalues of $M^\dagger M$ - but how do we know when the modes around Λ have converged without the overhead of suspending the algorithm and calculating the eigenvalue spectrum ?

To answer this question we appeal to the results of chapter 2 where it was shown that the convergence of the solution in an inversion algorithm is governed by the convergence of the smallest eigenvalues. If we consider attempting to solve

$$(UM - \Lambda \mathbf{1})\, \psi = x_1 \qquad (6.1)$$

then we know that the residue $|r|$ from the solution of eqn. 6.1 will be small when the smallest eigenvalues of the matrix $UM - \Lambda\mathbf{1}$ have converged, ie when those eigenvalues of UM around Λ have converged. We do not actually have to construct a solution vector and solve eqn. 6.1 since the Lanczos algorithm gives us $|r|$ at this 'mass' $-\Lambda$ purely as a function of the α's and β's (which we calculate anyway) via eqns. 2.32 to 2.39. We can monitor the convergence of the eigenvalues across the whole spectrum since we can calculate the residue at many masses simultaneously by the simple replacement $\alpha_i(-\Lambda) = \alpha_i(\Lambda=0) - \Lambda$. Here we are making use of the fact that neither the Lanczos vectors nor the β_i are affected by the addition of any multiple of the identity matrix to UM.

6.3 Numerical Results

The program was initially checked in three ways. Firstly, it was verified that at $y = 0$ the correct free eigenvalues $\pm\lambda_0$ were produced for a variety of different volumes and boundary conditions. Secondly, on a small 6^4 lattice at $\kappa = 0$ all the eigenvalues were computed at some non-zero value of y and the relationship

$$Tr(M^\dagger M) = \sum_{i=1}^{N} \lambda_i^2 = N\,(\frac{d}{2} + y^2) \qquad (6.2)$$

was checked. The fact that exactly 6^4 eigenvalues were found and that eqn. 6.2 was satisfied to a very high accuracy shows that the Sturm sequencing procedure finds the correct eigenvalues and also that it discards all of the spurious eigenvalues and degenerate ghosts. As a final check, the low lying eigenvalues of UM were computed on a large volume and their squares were found to agree with the eigenvalues of $M^\dagger M$ found using an independently written program. However, by considering the matrix UM rather than $M^\dagger M$ the time taken for the calculation was significantly reduced.

The low eigenvalues (typically at least the smallest 40) were calculated on 8^4, 10^4 and 14^4 lattices with antiperiodic boundary conditions in time alone. Values of y slightly below, in and above the expected location of the crossover region ($y^* \approx \sqrt{2}$) were used and data was collected both in the PM phase at $\kappa = 0.06$ and in the FM phase at $\kappa = 0.10$ (where $<\phi> = 0.88$). Both the time taken to produce a representative spin configuration and the time taken by the Lanczos algorithm grow quickly with the volume. Although the precise number of iterations taken for the Lanczos algorithm to converge varies significantly with V, κ and$y$ it always peaks around $y = y^*$ due to the appearance of very small eigenvalues. There was typically an order of magnitude increase in the number of iterations taken on the 14^4 lattice compared to the 8^4 lattice with the maximum number being 50,000 (occurring at $\kappa = 0.06$ and $y = 1.4$). As a result we considered 50, 25 and 5 configurations respectively on the three volumes.

Since we are ultimately interested in the zero eigenvalues of M and M' we take the square root of the eigenvalues of $M^\dagger M$ to ensure the same normalisation in both cases. This amounts to taking the absolute value of the eigenvalues of UM, and from now on 'λ' will *always* refer to this positive quantity.

6.3.1 Behaviour of the Small Eigenvalues

A simple observable to study would be the average value of the smallest eigenvalue $<\lambda_1>$, but this fluctuates too much to be of quantitative use particularly on the largest volume where only 5 eigenvalues were obtained. However, the second lowest eigenvalue is much more stable and in figs. 6.1 and 6.2 we plot $<\lambda_2>$ against y for the three volumes considered at $\kappa = 0.06$ and 0.10 respectively. Although the magnitude of $<\lambda_2>$ is somewhat larger in the FM than in the PM phase in all cases, there is no evidence to suggest that the quenched crossover region is absent in the FM phase for $V \rightarrow \infty$ since $<\lambda_2>$ drops significantly at the same value of y independently of the volume. Figs. 6.1 and 6.2 already suggest that the results obtained on small volumes (that there are only zero modes for $\kappa > 0$ in a small region around $y \approx y^*$) may be valid in the infinite volume limit. This is somewhat surprising since we know that for $y = 0$ zero modes must appear in the limit $V \rightarrow \infty$ regardless of the boundary conditions. We might naively expect these zero eigenvalues to persist all the way up to $y = y^*$ and only disappear in the large y region.

To make more quantitative statements about the infinite volume limit we plot $<\lambda_2>$ against $1/V$ for constant y at $\kappa = 0.06$ in figs. 6.3 to 6.6, and at $\kappa = 0.10$ in figs. 6.7 to 6.10. We see that there is an approximately linear relationship in the crossover region and a straight line fit allows us to extrapolate to $V = \infty$. We cannot really extract meaningful numbers for the infinite volume values of the small eigenvalues due to the large error bars. However, we can draw the useful qualitative conclusion from figs. 6.3 to 6.10 that the data is consistent with there only being zero modes in the region $y = 1.3$ to $y = 1.5$ in the infinite volume at

both values of κ. Hence we conclude that there are no zero modes for $0 < y \leq 1.2$ and $y \geq 1.6$ in the PM or FM phases, and also that the crossover region extends at least as far as $\kappa = 0.10$ into the broken phase.

6.3.2 The Density of Zero Modes

The relationship $\langle\lambda_2(V)\rangle = a + bV^{-1}$ that we have found to be valid in the crossover region is a rather empirical one and we would like to be able to have more systematic control of the finite size effects. We therefore look for an observable which, unlike $\langle\lambda_2\rangle$, should be independent of the volume in the continuum limit. Such a quantity is the normalised eigenvalue density since we expect the shape of the eigenvalue spectrum and the distribution of eigenvalues within it to become independent of the volume as $V \rightarrow \infty$. We are particularly interested in the small modes so we study the infinite volume limit of the quantity $\rho(0)$ given by

$$\rho(0) = \frac{1}{V}\frac{\partial n(\lambda)}{\partial \lambda}\Big|_{\lambda=0} \tag{6.3}$$

where $n(\lambda)$ is the number of eigenvalues less than λ. Since we have already computed all of the eigenvalues below some cutoff and not just the smallest one or two, we can attempt to calculate this quantity. This is done by binning the eigenvalues into bins of width $\Delta\lambda$ and counting the number $n(\lambda)$ in each bin centered on λ. By plotting the approximation to $\rho(\lambda)$ given by

$$\rho(\lambda) \approx \frac{1}{V}\frac{n(\lambda)}{\Delta\lambda} \tag{6.4}$$

against λ we can make some appropriate extrapolation to calculate $\rho(0)$ [62, 63].

Some typical plots of $\rho(\lambda)$ taken from the $V = 8^4$ eigenvalues at $\kappa = 0.06$ ($y = 1.3$ and $y = 1.4$) and at $\kappa = 0.10$ ($y = 1.3$) are shown in figure 6.11 (the points for $\kappa = 0.10$ and $y = 1.4$ overlap those at $y = 1.3$ and are not shown). The relative errors on the points are taken to be $\pm n^{-1/2}$ where n is the number of eigenvalues in the bin of width $\Delta\lambda$ at λ. We see from fig. 6.11 that a linear fit to $\rho(\lambda)$ is possible for small enough values of λ allowing us to determine $\rho(0)$ even though no exact zero eigenvalues are actually present. Unfortunately not all the data is good enough

to obtain such good fits due particularly to the limited number of eigenvalues available on the larger volumes. In addition the very low number of small eigenvalues present outside the crossover region again makes it difficult to obtain quantitative results. However, we find conclusively that $\rho(0)$ drops very rapidly to zero for y outside the range $1.3 \rightarrow 1.4$. Within this narrow band we can obtain stable fits on all three volumes and we plot $\rho(0)$ against $1/V$ in fig. 6.12 for the same values of κ and y as in fig. 6.11. As expected the density of zero modes is lower in the FM phase than in the PM phase but is still definitely non-zero. The important conclusion that we draw from fig. 6.12 is that there are no strong finite size effects in $\rho(0)$ in the crossover region and that the zero modes persist with non-vanishing density in the infinite volume limit in both the PM and FM phases for $y \approx y^*$.

6.4 The Large Kappa Limit

The fact that there are zero modes in the crossover region in the FM phase is slightly surprising since we know that at least in the limit $\kappa \rightarrow \infty$ the eigenvalues of $M^\dagger M$ will become the free eigenvalues $\lambda_0^2 + y^2$ and in the infinite volume limit the smallest value of λ will therefore be equal to y. Either the density of zero modes drops smoothly with κ (but always remains non-zero) in which case the crossover phenomenon will persist throughout the FM phase, or it reaches zero at some finite κ at which point the crossover will cease. The results of section 6.3.2 have shown that we can actually answer this question in the infinite volume limit by simply considering the case $V = 8^4$ since $\rho(0)$ shows little volume dependence in the crossover region.

We have calculated the low eigenvalues at values of κ starting from just above the PM/FM phase boundary and increasing deep into the FM phase. The value of y was chosen to be 1.37 which is the point at which the density of small modes is maximal in the 8^4 case in the PM phase, and hence is the expected value of y^* on this volume. However, the major obstacle to calculating $\rho(0)$ from the eigenvalues

is that for large κ they become degenerate for the same reasons that degeneracy was encountered in the spectra of M and M' at high magnetisation. There is no easy way of deciding during the Sturm sequencing procedure if two very closely spaced eigenvalues represent a true degeneracy or whether one is a ghost. We cannot perturb the fermion matrix by the methods of section 4.5.3 since we do even attempt to calculate all N eigenvalues. We could therefore never be certain that a perturbation chosen to be small enough not to destroy the spectrum of UM completely is large enough to split all the degeneracies. Although we can still obtain the eigenvalues very accurately we do not know their multiplicities so we cannot calculate the eigenvalue density.

We cannot calculate the density of zero modes but we can plot the number of eigenvalues less than some small value to give an indication of the behaviour of $\rho(0)$. Fig. 6.13 shows the number of distinct eigenvalues less than 0.075 as a function of κ averaged over 50 configurations, but due to the possible degeneracies each point is only a lower bound on the true number of small modes. Despite this, fig. 6.13 is useful in that it shows that the small eigenvalues go away very slowly with κ even though at $\kappa = 0.15$ the magnetisation $\langle\phi\rangle$ is already 0.98 and we would appear to be very close to the free case where $\langle\phi\rangle = 1$ and there would be no eigenvalues λ less than y. If we make the reasonable assumption that the degeneracy of the eigenvalues increases with κ then the small eigenvalues will actually go away even more slowly than fig. 6.13 would suggest. We therefore conclude that the zero modes in M present at $y = y^*$ persist deep into the FM phase in the infinite volume limit though with decreasing number.

This is consistent with the result quoted in ref. [58] where it is shown analytically that there is an exact zero mode in M at $y = 1.3647...$ on an infinite volume configuration where all but one of the spins are up (this is similar to a real configuration at very large κ). It is difficult to extend the analysis to a system with a lesser magnetisation, but our data shows that the conclusions obtained from this artificial configuration are applicable throughout the FM region.

6.4 Conclusions

Our study of the smallest eigenvalues of $M^\dagger M$ on large volumes shows that, in the infinite volume limit, the fermion matrix has zero modes around $y = y^*$ in both the PM and FM phases where y^* is between 1.3 and 1.4. The presence of only a very few spins pointing down in an otherwise completely magnetised configuration is enough to produce many small eigenvalues in the crossover region, and from the results of chapter 5 this means that fermion mass will not be defined in the crossover region of the quenched model for any finite value of κ. By studying the density of eigenvalues around zero we have also shown that the finite volume effects in the spectrum of $M^\dagger M$ are very small in this region of y. We conclude that the zero modes definitely appear with non-vanishing density in the infinite volume limit between $y = 1.3$ and 1.4. This region may extend as far as from 1.2 to 1.6 but the density of zero modes is much reduced. For $0 < y \leq 1.2$ and $y \geq 1.6$ we see no evidence for there being any zero modes at all.

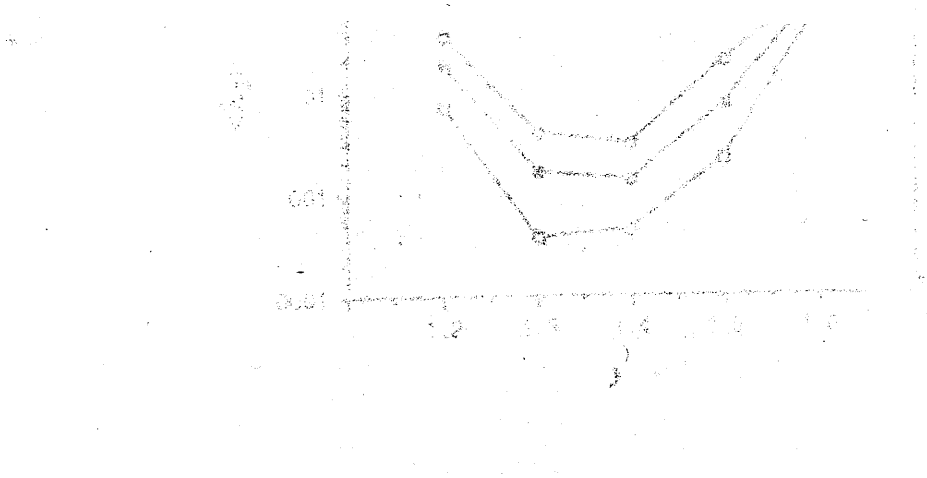

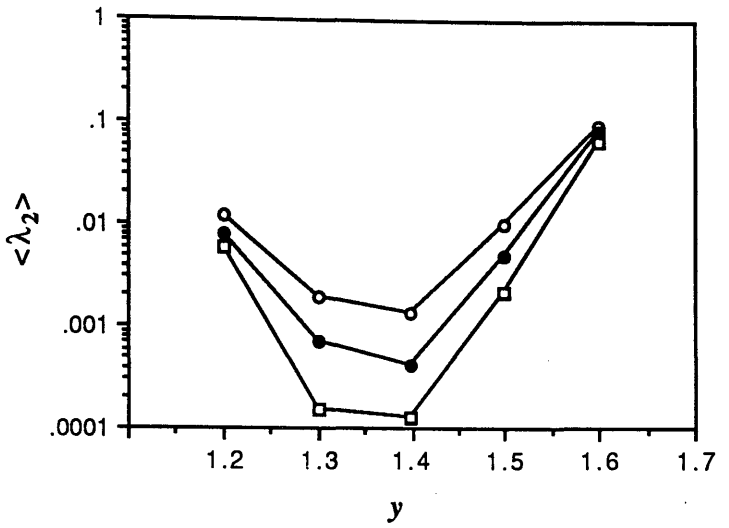

Fig. 6.1 The average of the square root of the second lowest eigenvalue of $M^\dagger M$ vs. local Yukawa coupling y. Hopping parameter $\kappa = 0.06$. (o) $V = 8^4$, (•) $V = 10^4$, (▫) $V = 14^4$.

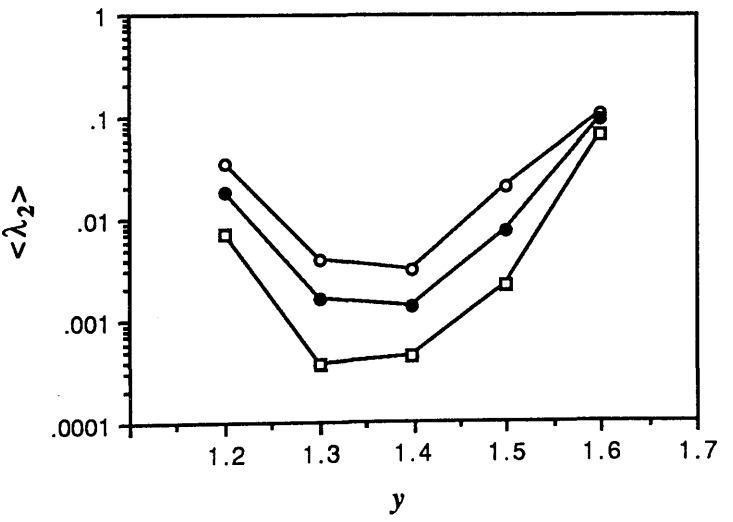

Fig. 6.2 The average of the square root of the second lowest eigenvalue of $M^\dagger M$ vs. local Yukawa coupling y. Hopping parameter $\kappa = 0.10$. (o) $V = 8^4$, (•) $V = 10^4$, (▫) $V = 14^4$.

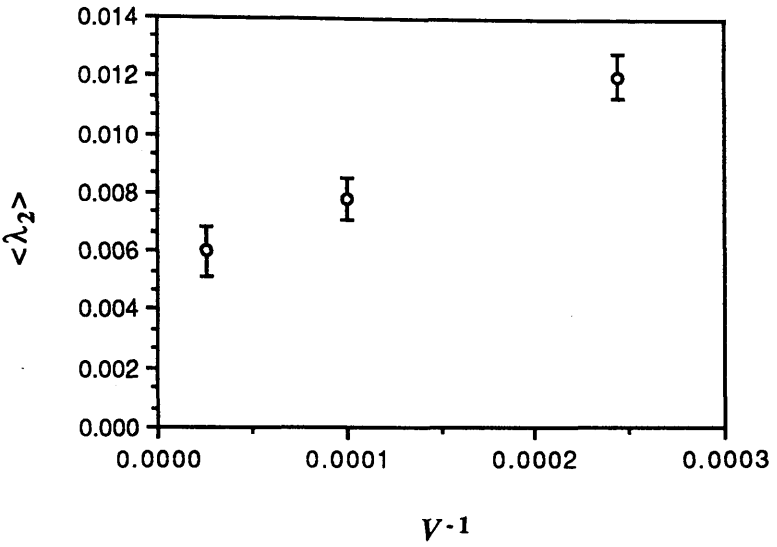

Fig. 6.3 The average of the square root of the second lowest eigenvalue of $M^\dagger M$ vs. the inverse volume. Hopping parameter $\kappa = 0.06$.
(o) $y = 1.2$.

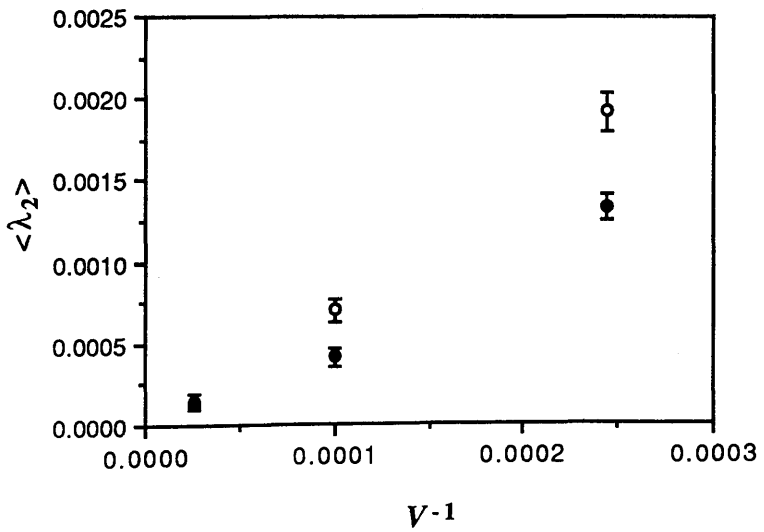

Fig. 6.4 The average of the square root of the second lowest eigenvalue of $M^\dagger M$ vs. the inverse volume. Hopping parameter $\kappa = 0.06$.
(o) $y = 1.3$, (•) $y = 1.4$.

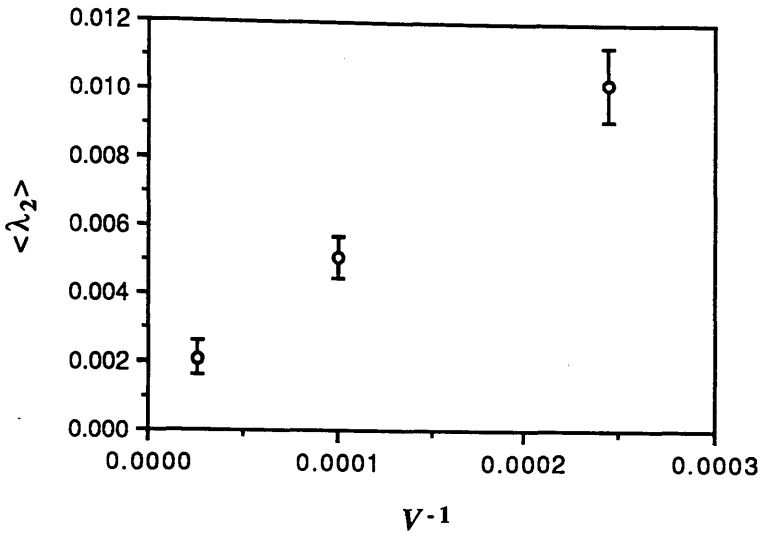

Fig. 6.5 The average of the square root of the second lowest eigenvalue of $M^\dagger M$ vs. the inverse volume. Hopping parameter $\kappa = 0.06$.
(o) $y = 1.5$.

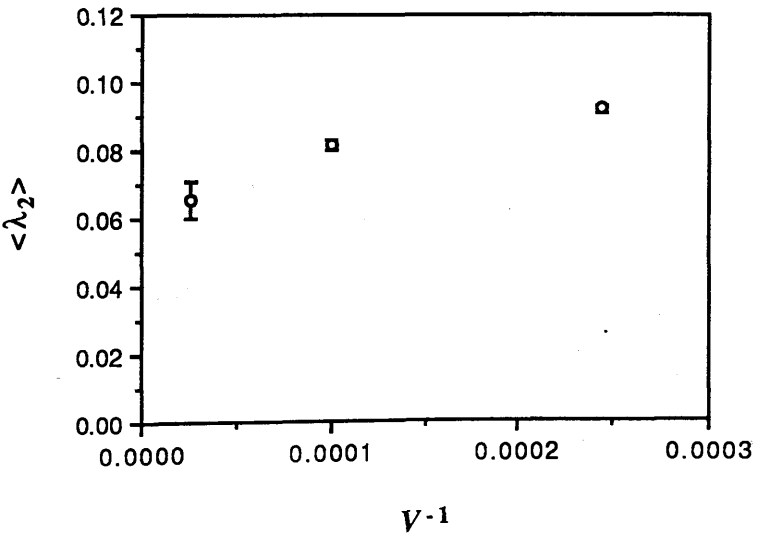

Fig. 6.6 The average of the square root of the second lowest eigenvalue of $M^\dagger M$ vs. the inverse volume. Hopping parameter $\kappa = 0.06$.
(o) $y = 1.6$.

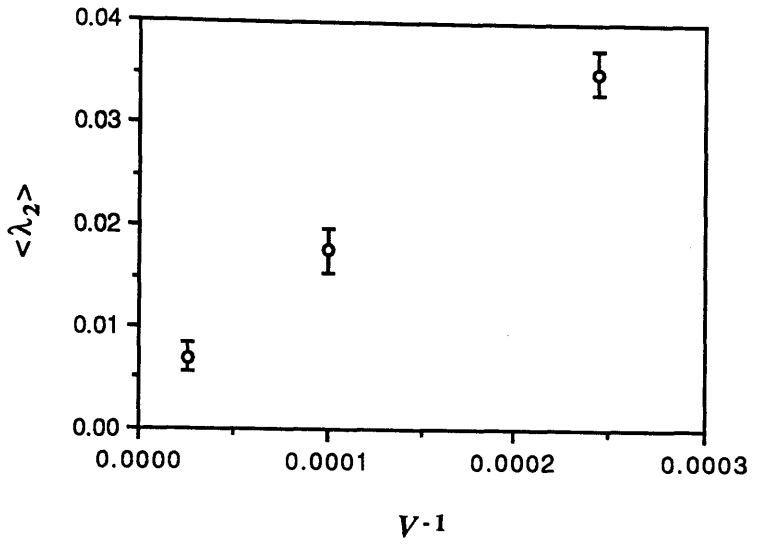

Fig. 6.7 The average of the square root of the second lowest eigenvalue of $M^\dagger M$ vs. the inverse volume. Hopping parameter $\kappa = 0.10$.
(o) $y = 1.2$.

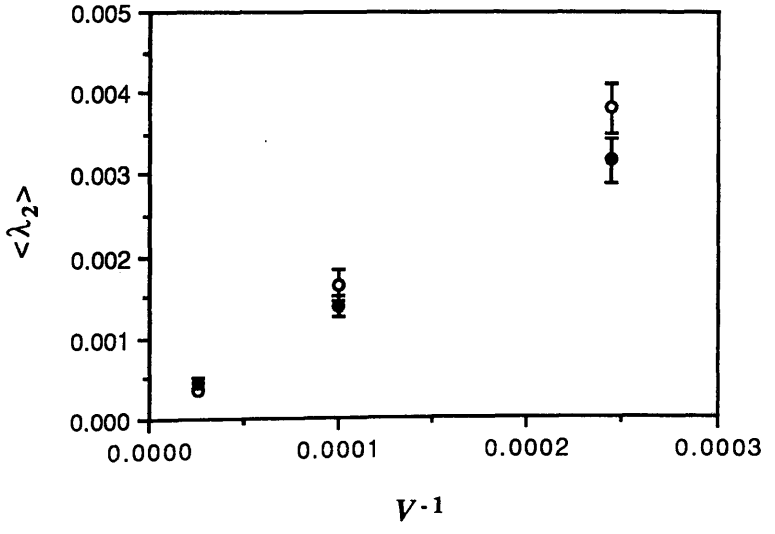

Fig. 6.8 The average of the square root of the second lowest eigenvalue of $M^\dagger M$ vs. the inverse volume. Hopping parameter $\kappa = 0.10$.
(o) $y = 1.3$, (•) $y = 1.4$.

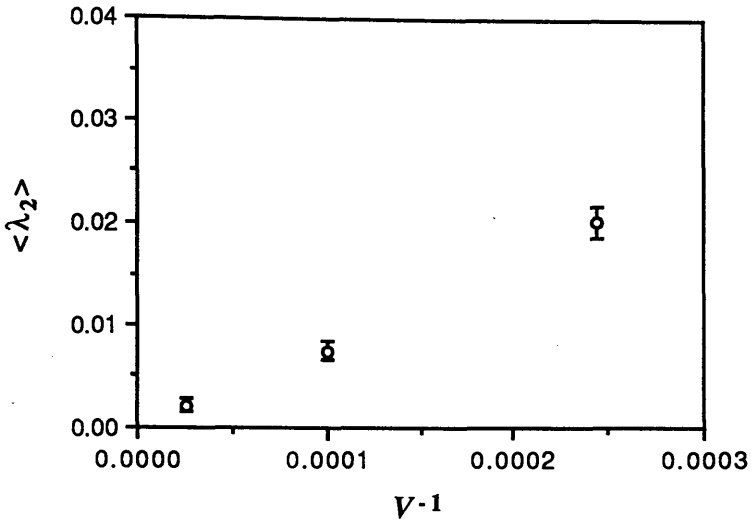

Fig. 6.9 The average of the square root of the second lowest eigenvalue of $M^\dagger M$ vs. the inverse volume. Hopping parameter $\kappa = 0.10$.
(o) $y = 1.5$.

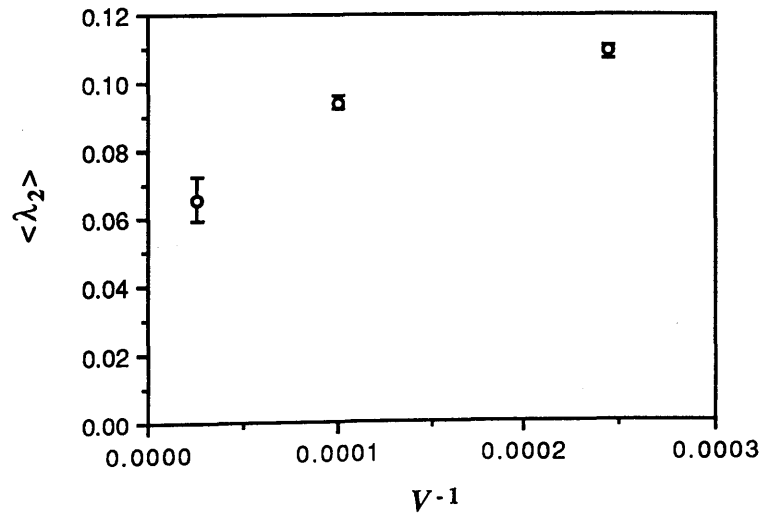

Fig. 6.10 The average of the square root of the second lowest eigenvalue of $M^\dagger M$ vs. the inverse volume. Hopping parameter $\kappa = 0.10$.
(o) $y = 1.6$.

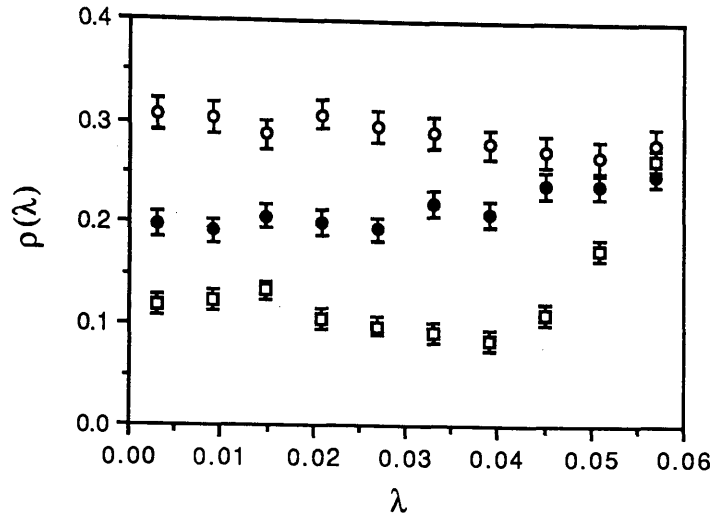

Fig. 6.11 The local density of small eigenvalues vs. eigenvalue for an 8^4 lattice. (o) $y = 1.4$, $\kappa = 0.06$; (•) $y = 1.3$, $\kappa = 0.06$; (▫) $y = 1.3$, $\kappa = 0.10$

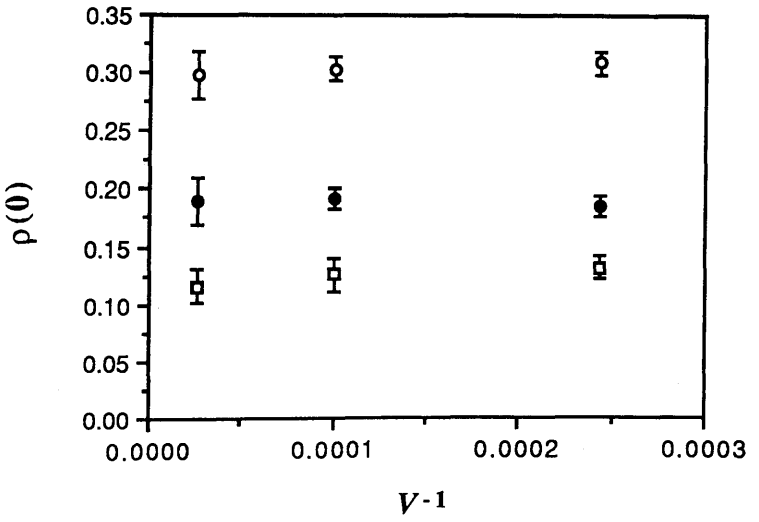

Fig. 6.12 The density of zero modes ρ(0) vs. the inverse volume. (o) $y = 1.4$, $\kappa = 0.06$; (•) $y = 1.3$, $\kappa = 0.06$; (▫) $y = 1.3$, $\kappa = 0.10$

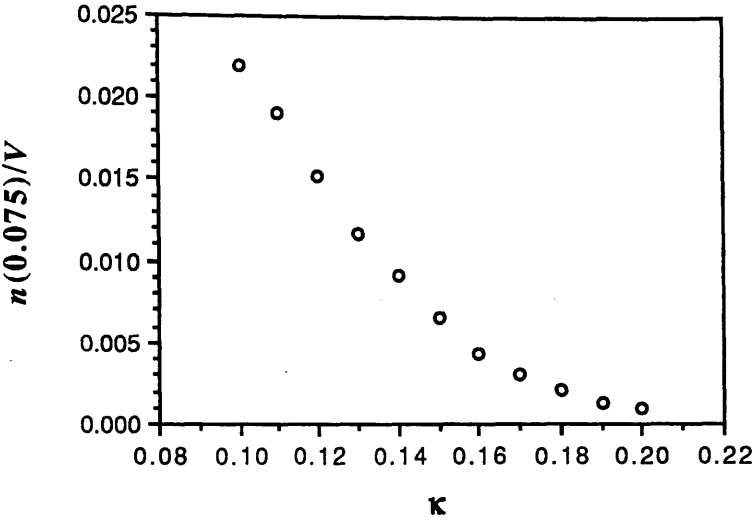

Fig. 6.13 The number of eigenvalues less than 0.075 divided by the volume vs. hopping parameter κ on an 8^4 lattice at $y = 1.37$.

Chapter 7

Dynamical Simulations

7.1 Introduction

We have seen from the quenched studies of chapters 4, 5 and 6 that in lattice Higgs models defined with local Yukawa coupling y the crossover region around $y = \sqrt{2}$ is caused by the appearance of small eigenvalues in the spectrum of the fermion matrix. However, we know that in a full simulation the field configurations that give rise to these small modes will be heavily suppressed by a factor $det(M)^{n_f}$ and the quenched approximation may cease to give results that are in any way applicable to the full theory with dynamical fermions. It is therefore possible that our inability to define the renormalised fermion mass m_f in this region is simply due to the failure of the quenched approximation. To establish whether or not the quenched results are relevant in the crossover region we need to evaluate m_f on spin configurations that are generated including the effects of closed fermion loops. In the Ising model we noted previously that there is no obvious way of using an efficient algorithm such as the Hybrid Monte Carlo algorithm of section 1.7.2 due to the discrete nature of the field variables, and the need to use some other more costly algorithm restricts us to working on very small volumes indeed. On such small volumes it will be impossible to define m_f from the exponential decay of the fermion propagator (eqn. 5.2) due to the small size of the lattice in the time direction, but we can appeal to the results of chapter 5 to define m_f via the eigenvalue spectrum of the $Z(2)$ invariant fermion matrix M'.

Using this definition of m_f and the values of the bosonic observables $<\phi>$, $<\phi_{st}>$ and $z^2 = <\phi(n)\phi(n+\mu)>$ we will endeavour to clarify the phase diagram in the (κ, y) plane. The quenched results will still be useful guides to the behaviour as $y \rightarrow 0$ and $y \rightarrow \infty$ since in these limits the fermions decouple from the dynamics of the model. For intermediate values of y the phase diagram is not

known and although we are unable to systematically scan the entire parameter space due to limited computer time there are several key points that we wish to clarify.

Firstly, we know that the fermionic determinant favours ferromagnetic ordering for all finite y [40]. Hence for $\kappa < -\kappa_c$ the bosonic and fermionic actions will be acting in opposition and we wish to know whether there is some region of y in which the system does not adopt the AFM phase and if so whether or not this region extends to very large negative κ. This is a question on which there is some disagreement between Lee, Shigemitsu and Shrock [40] who envisage anti-ferromagnetism at all y for some sufficiently negative κ, and Stephanov and Tsypin [58] who predict intermediate PM1 and PM2 phases around $y = \sqrt{2}$.

Secondly, we wish to know whether the direct PM1/PM2 boundary persists in the full model or whether there is always some other intervening phase. Lee *et al.* discuss several possibilities including the possible existence of a multi-critical point whereas Stephanov and Tsypin predict that the boundary occurs at $y = \sqrt{2}$ for all values of $\kappa < -\kappa_c$. If the boundary does exist it will presumably become a genuine phase transition line and we would like to investigate the behaviour of the fermion mass close to it. This was not possible in the quenched studies where we were unable to define m_f due to the appearance of very small fermionic modes, but the inclusion of the fermion dynamics may now allow us to follow the behaviour of m_f right through the phase transition. If this is possible we will want to determine the critical value of the Yukawa coupling $y_c(\kappa)$.

Thirdly, it will be interesting to see if the introduction of the fermion dynamics simply results in a rescaling of κ, $\kappa \rightarrow \kappa\,(y)$, or whether the full theory generates genuinely new field configurations not present in the quenched model. Such configurations might exhibit novel spin orderings, for example a ferrimagnetic phase due to the competition between the fermion and boson dynamics at negative κ. Alternatively there might be new fermionic behaviour that we could detect by observing new forms of the eigenvalue spectrum of M.

7.2 Simulating the Dynamical Theory

We wish to generate field configurations $\{\phi\}$ with the correct probability distribution including the full fermionic contributions. After integrating out the fermionic degrees of freedom this amounts to generating $\{\phi\}$ with the probability

$$P\{\phi\} \approx \prod_{i=1}^{n_f} det(M_i\{\phi\})\ exp\ (-S_B\{\phi\}) \tag{7.1}$$

where M_i is the fermion matrix associated with the i^{th} fermion species with Yukawa coupling y_i and S_B is the pure Ising action of eqn. 4.2 with critical points at $\pm\kappa_c$. From now on we consider an even number n_f of fermion species all with the same Yukawa coupling y and drop the species subscript.

To employ a heatbath algorithm we need to know the probability $P_u(n)$ that a given spin $\phi(n)$ will be 'up' with all the other spins held constant. From eqn. 1.40 this is given by

$$P_u(n) = \frac{det(M_u)^{n_f} P_u^Q}{det(M_u)^{n_f} P_u^Q + det(M_d)^{n_f} P_d^Q} \tag{7.2}$$

where M_u (M_d) is the fermion matrix evaluated with $\phi(n)$ up (down) and P^Q are the corresponding quenched probabilities coming purely from the Ising action. Dividing through by $det(M_u)^{n_f}$ we see that the effect of the fermion loops is to multiply P_d^Q in eqn. 7.2 by a factor D^{n_f} where the dynamical factor D is given by

$$D = det \left(\frac{M_d}{M_u}\right) = det\ (\mathbf{1} + M_u^{-1}(M_d - M_u)\ ) \tag{7.3}$$

This is simple to calculate for the hypercubic and local forms of the Yukawa coupling since in both cases the difference $M_d - M_u$ is a sparse diagonal matrix and we therefore only have to evaluate a few elements of $(M_u)^{-1}$ (the evaluation of this inverse will be the major computational task). For the local form, $M_d - M_u$ has only one non-zero element

$$(M_d - M_u)\ (p, q) = -\ 2y\ \delta(p, n)\ \delta(q, n) \tag{7.4}$$

whereas for the hypercubic form there are 2^d non-zero diagonal entries given by

$$(M_d - M_u)\,(p,q) \;=\; -\frac{2y}{2^d}\,\delta(p,\, n+h)\,\delta(q,\, n+h) \qquad (7.5)$$

where $\{h\}$ are the 2^d vectors spanning a hypercube that were introduced in eqn. 3.24. We only consider the local form from now on since it is only with this coupling that the fermion mass exhibits singular behaviour in the quenched approximation. The expression for D becomes particularly simple in this case

$$D \;=\; 1 - 2y\, M_u^{-1}(n,n) \qquad (7.6)$$

By pulling out a factor of M_d^{-1} in eqn. 7.3 we arrive at the equivalent expression

$$D^{-1} \;=\; 1 + 2y\, M_d^{-1}(n,n) \qquad (7.7)$$

Hence the problem of dynamical simulation reduces to one of calculating diagonal elements of the inverse fermion matrix which we do this using the Lanczos algorithm of chapter 2.

7.2.1 Rank Annihilation

It is the fact that we have to run the inversion algorithm once for each update of a single spin that makes the dynamical algorithm so time consuming. The Lanczos algorithm gives us a whole column of the inverse matrix and it seems wasteful to utilise only one inverse element (the diagonal one). We can make use of more of the information contained in the inverse if, rather than hitting each spin on the lattice once per entire sweep, we hit all the spins in a given sub-lattice more than once before moving on to a new sub-lattice. This would be a pointless procedure in the quenched case since each spin only couples to its nearest neighbours, but $det(M)$ is a highly non-local object and hence couples all the spins on the lattice. We can therefore hope to gain by thermalising whole subsets of the lattice at once.

The above is a computationally efficient approach since we can systematically update all the diagonal inverse elements relevant to a particular sub-lattice while updating the spins in the sub-lattice without having to perform any more Lanczos inversions. This is done by a procedure known as rank annihilation and requires knowledge of the off-diagonal elements.

As we 'lap' over a given sub-lattice we need to calculate the new diagonal elements of M^{-1} after each spin flip. It can be shown [51] that the change δM^{-1} in M^{-1} due to the change of one element $M(p_0, q_0)$ by an amount c is given by

$$\delta M^{-1}(p,q) = -c \frac{M^{-1}(p,q_0)\, M^{-1}(p_0,q)}{1 + c\, M^{-1}(p_0,q_0)} \tag{7.8}$$

This is an exact expression that can be checked by back substitution. We use eqn. 7.8 to continually update all the elements of the propagator connecting the sites in a given sub-lattice, and the required off-diagonal elements are precisely those that we get 'for free' when we initially calculate the inverse once for each site. Rounding errors build up very slowly during the rank annihilation process so we can lap over a given sub-lattice many times provided that the inverse is initially calculated to a reasonably high accuracy.

7.2.2 The Dynamical Heatbath Algorithm

The algorithm we use to simulate the dynamical theory with a local Yukawa coupling y comprises the following steps:

1) Divide the whole lattice into N_s sub-lattices each containing n_s points.
2) Consider each subset in turn and evaluate the $n_s \times n_s$ block of the inverse that connects all the sites in the sublattice.
3) Lap over all the sites in the sub-lattice N_{lap} times. For each site n, calculate the probability $P_u(n)$ from eqn. 7.2 where D is given by eqn. 7.6 (7.7) if $\phi(n)$ is initially up (down). Set the new value of $\phi(n)$ accordingly and if the spin has been flipped correct all the inverse elements (diagonal and off-diagonal) that connect sites in the sub-lattice using eqn. 7.8 with $c = \pm 2y$ depending on the direction of the flip, and $p_0 = q_0 = n$.
4) Steps 1 to 3 comprise one sweep of the lattice. Repeat these steps a total of N_{sweep} times.

An important feature of this procedure is that step 2 permits the use of the block algorithm with block size $B = n_s$. Whether we use the block algorithm once or the single algorithm n_s times will depend on which is more efficient, ie whether or not M has small eigenvalues. If M possesses many small eigenvalues then the block algorithm will be much faster than the single algorithm for calculating the required inverse block. In such a case it is advantageous to partition the lattice into sub-lattices even if we subsequently take N_{lap}= 1 since the time required per site for inversion is much reduced by the use of the block form.

If M has few small eigenvalues the most efficient approach will be to run the single algorithm n_s times, once for each site in the sub-lattice. Partitioning the lattice will still be advantageous since we can then lap over the sublattice many times with little extra computation.

As a final remark, eqn. 7.8 shows that the change in $M^{-1}(n,n)$ caused by flipping $\phi(n)$ depends only on $M^{-1}(n,n)$ itself and therefore we can calculate M_d^{-1} from M_u^{-1}. Doing this shows that eqns. 7.6 and 7.7 are consistent.

7.2.3 Numerical Details

All studies were done on a 4^4 lattice using two species of dynamical staggered fermions with antiperiodic boundary conditions in time unless otherwise stated. When running the Lanczos algorithm a convergence criterion of $|r| < 1.0 \times 10^{-5}$ was used. At the start of every sweep the lattice was divided randomly into 16 sublattices each containing 16 sites, and we set $N_{lap} = 2$. This random partitioning was chosen in preference to, say, dividing the lattice into 16 hypercubes so that we could be confident that any ordering of the system was a real effect and not purely due to the particular choice of the sub-lattices. This random choice is only possible because the change in M due to one spin flip is restricted to a single diagonal element when using the local Yukawa coupling. If we were using the hypercubic coupling then all the diagonal elements of M on a whole hypercube would be affected by a spin flip and the natural choice of sub-lattice would therefore be this

hypercube. Any other choice of sub-lattice would make the updating prohibitively slow because many of the off-diagonal elements required for rank annihilation would have to be calculated by a separate Lanczos inversion (the same situation occurs when the dynamical heatbath algorithm is applied to SU(3) gauge theory [12]). By choosing a hypercube as the sub-lattice we would already know all the necessary off-diagonals from the calculation of the diagonal elements.

7.3 Results at κ = -0.15

The first question we consider is the nature of the phase diagram for large negative κ. We know that the fermionic determinant prefers ferromagnetic over anti-ferromagnetic ordering, but at negative κ the bosonic action prefers the AFM state. We wish to find out if the fermionic effects are strong enough such that, at some y, some other phase occurs at large negative κ. The numerical studies were performed at $\kappa \approx -2\kappa_c = -0.15$. For $y = 0$ or $y = \infty$ we will recover the quenched result $\langle\phi_{st}\rangle = 0.98$, and y values ranging from 0.2 to 2.8 were chosen for the dynamical simulations at intermediate y. Since we are interested in the persistence of the AFM phase, all runs were started from a pure AFM state and data accumulated for 200 sweeps after 100 thermalisation sweeps.

We plot $\langle\phi_{st}\rangle$ and $-z^2$ as a function of y in fig. 7.1 (z^2 is always negative at this value of κ), and although the data set is rather small it is obvious that the fermionic effects are dominant for a very large interval of y from 1.0 to 2.2. The magnetisation $\langle\phi\rangle$ is always smaller than 0.01 so the intermediate phase seems to be a paramagnetic one. For $y \approx \sqrt{2}$ the system is seen to adopt a PM state after a few tens of sweeps from an initial AFM state so the fermionic effects are indeed very strong. Although not strong enough to keep the system in the AFM phase, the bosonic effects prevent the system from taking up the FM state which would be preferred in a purely fermionic system. We always start updating from deep within the AFM phase so any effects due to incomplete equilibration would tend to reduce the apparent size of the PM region. As a result fig. 7.1 at worst represents a

conservative estimate as to the extent of the symmetric region.

The problem with fig. 7.1 is that the curves show strange behaviour around what we might expect to be the AFM/PM1 boundary where $<\phi_{st}>$ drops more rapidly and $-z^2$ more slowly than one would expect given the very small size of the lattice and our prior experience with the quenched AFM/PM transition. The curve for $-z^2$ shows a small peak around $y = 1.3$ which represents a local *minimum* of the purely bosonic action $S_B = -2\kappa N z^2$. We would expect S_B to be rising across an AFM/PM boundary since the fermion dynamics are forcing the system into a state that is not the preferred state of the purely bosonic (quenched) model.

Further investigation shows that at $y = 1.2$ and $y = 1.3$ the system is approaching a state where the spins are anti-ferromagnetically ordered in space but ferromagnetically ordered in time, ie the value of the observable

$$<\phi_{mixed}> \; = \; < (-1)^{n1+n2+n3} \, \phi(n) > \qquad (7.9)$$

becomes large. We call such a state a mixed AFM / FM state but it should not be confused with the ferrimagnetic (FI) state where $<\phi>$ and $<\phi_{st}>$ are both non-zero. A genuine FI phase is in fact observed at this position in the phase diagram in ref. [64] in dynamical simulations of a U(1) Higgs model on a 6^4 lattice. No reasons are given as to why it should be the preferred state and unfortunately the fermionic boundary conditions are not stated. It is therefore not clear if the two phenomena are in any way related.

A pure mixed state (with $<\phi_{mixed}> = 1$) has $<\phi> = <\phi_{st}> = 0$ and $z^2 = -0.5$ which explains the behaviour of the curves around $y = 1.3$. The reason that the time direction was singled out as the direction of ferromagnetic ordering can only be because it is in this direction that the fermionic boundary conditions are antiperiodic rather than periodic. The same final mixed state was obtained starting from AFM, PM and FM initial states which proves that the choice of the time direction is not a random one and it must therefore be related in some way to the boundary conditions. This behaviour is only observed for $y < 1.4$ and for $1.4 \leq y < 2.4$ the system is genuinely in a PM state where $<\phi_{mixed}>$ is small.

We believe that the existence of the mixed state is a finite size effect since in the infinite volume the boundary conditions will become irrelevant. In an attempt to discover the true phase structure in this region we performed simulations around the first AFM / PM phase boundary using antiperiodic boundary conditions in all directions. The results are shown in fig. 7.2 and show much smoother behaviour than those obtained with antiperiodic boundary conditions in time alone. For $1.0 \leq y \leq 1.4$ the system is in a genuine PM state where all three quantities $\langle\phi\rangle$, $\langle\phi_{st}\rangle$ and $\langle\phi_{mixed}\rangle$ are small. The bosonic observables vary smoothly across the phase boundary around $y = 0.9$ indicating that the mixed state has been eliminated by this change of boundary conditions. To prove conclusively that fig. 7.2 represents the infinite volume behaviour more accurately than fig. 7.1 would of course require simulations on much larger lattices, but it seems very unlikely that the mixed state can persist in the continuum limit.

Although we have found a large PM region we are unfortunately unable to use the fermion mass m_f to discover whether or not it consists of two distinct regions PM1 and PM2. This is because for $0.8 \leq y \leq 1.2$ the M' condensate is negative (we only consider the case of antiperiodic boundary conditions to avoid problems with the mixed state) and there is no way we can perform a fit to a free theory with positive m_f. Despite this problem the results do clarify the phase diagram to some extent. We believe that this study is evidence that the PM region extends to much larger negative κ at some value of the Yukawa coupling close to $\sqrt{2}$ since the only way that the system can exclude the exact zero modes found in an AFM state around this value of y is to take up some other spin ordering. Ferromagnetic ordering has too high a bosonic action so a PM state is chosen. Although a PM state still has a large bosonic action compared to an AFM state, PM configurations are preferable to AFM configurations since for the latter the fermion determinant can become arbitrarily small due to the very high density of small eigenvalues. We conclude that for $\kappa < 0$, the phase structure therefore resembles that proposed by Stephanov and Tsypin [58] rather than that by Lee *et al.*[40].

7.3.1 The Eigenvalue Spectrum

It is instructive to examine the eigenvalue spectrum of M in the AFM and PM phases. In both AFM regions (small and large y) the eigenvalue spectra are the same as in the quenched AFM studies where for small y there is a very high density of eigenvalues along the imaginary axis with no real eigenvalues, and for large y there is a high density of real eigenvalues but no imaginary ones. It is at the intermediate values of y that the fermion dynamics become important. In quenched simulations the eigenvalues of M transfer from the imaginary to the real axis via the origin but this is impossible in the dynamical case due to the presence of the fermion determinant. The dynamical system therefore adopts PM ordering since such configurations have, even in the quenched theory, a much lower density of small eigenvalues.

The actual eigenvalue spectrum is shown in fig. 7.3 where three configurations are superimposed at $y = 1.4$. We see that this PM state is not simply a quenched PM state where we would expect at least some small eigenvalues - the fermion dynamics have completely excluded the small modes. Although the same effect would be achieved in an FM state the much higher bosonic action for such a state gives a PM configuration a much larger weight in the partition function, and it is the latter state that we observe. The introduction of fermion dynamics has therefore done a lot more than simply distorting the quenched phase diagram and has produced an eigenvalue spectrum that is never observed in the quenched model.

The eigenvalue spectrum for the mixed state found at $y = 1.3$ is shown in fig. 7.4. We see that this configuration is chosen because it manages to exclude the small eigenvalues but with less of an increase in the bosonic action than a PM state due to the smaller value of z^2. The eigenvalue spectrum for the PM state observed at $y = 1.3$ with antiperiodic boundary conditions in all directions is not shown since it is of exactly the same form as would be obtained in the quenched theory in the PM region.

7.4 Results for $\kappa > 0$

Two runs were performed in the upper half of the phase plane, one at at $\kappa = 0.04$ and the other at $\kappa = 0.085$. At $\kappa = 0.04$ we ran for 1000 sweeps after 300 thermalisations from a hot start. In addition to the continual monitoring of various bosonic variables the eigenvalue spectrum of M' was calculated every 100 sweeps so that m_f could be calculated by the methods of chapter 5. At $\kappa = 0.085$ we ran for 2000 sweeps after 500 thermalisations from a cold start and calculated the spectrum of M' every 200 sweeps.

The results for the bosonic variables $<\phi>$ and z^2 are shown in fig. 7.5 and 7.6 for $\kappa = 0.04$ and 0.085 respectively. We see from fig. 7.5 that, as expected, the quenched phase diagram is recovered in the small and large y limits and the system is in the PM phase. However we know that in the quenched model there are small eigenvalues in M at intermediate values of y. In this region the system excludes these small modes and increases the fermionic determinant by adopting an FM state.

At $\kappa = 0.085$ we know from the quenched studies that zero modes can still appear for $y \approx \sqrt{2}$ and we see from fig. 7.6 that the dynamical system attains a very high magnetisation in this region. However, we know from section 6.4 that a high magnetisation is not in itself sufficient to ensure that there are no small modes in M. By looking at the eigenvalue spectrum of M we observe that these dynamical configurations do not exhibit the small modes that would still appear around $y \approx \sqrt{2}$ in the quenched system deep in the FM phase. As expected the the curves approach the quenched results for small and large values of y.

7.5 Comparison with Mean Field Theory

A simple mean field approach to the pure Ising model [36] gives an estimate of the critical hopping parameter $\kappa_c = 1/4d$, valid to leading order in $1/d$. This calculation can be extended in a simple manner to finite y by the inclusion of the effective fermionic action $n_f \, ln(det(M))$. In the limit of small and large y the

fermion determinant can be evaluated approximately to give the following estimates for the locations of the PM/FM phase boundaries in the (κ, y) plane [58]

$$\kappa = \kappa_c \left(1 - \frac{2n_f y^2}{d + 2y^2} \right) \quad \text{valid for } y^2 < d/2. \tag{7.10}$$

$$\kappa = \kappa_c \left(1 - \frac{dn_f}{d + 2y^2} \right) \quad \text{valid for } y^2 > d/2. \tag{7.11}$$

The same approach gives the following equations for the positions of the AFM/PM phase boundaries

$$\kappa = -\kappa_c \left(1 + \frac{2n_f y^2}{d - 2y^2} \right) \quad \text{valid for } y^2 < d/2. \tag{7.12}$$

$$\kappa = -\kappa_c \left(1 - \frac{dn_f}{d - 2y^2} \right) \quad \text{valid for } y^2 > d/2. \tag{7.13}$$

If we use $\kappa_c = 0.075$ then we can obtain the critical (mean field) Yukawa couplings y_c^{MF} from eqns. 7.10, 7.11 at $\kappa = 0.04$ and eqns. 7.12, 7.13 at $\kappa = -0.15$. Extracting the critical couplings y_c from figs. 7.1, 7.2 and 7.5 is rather difficult due to the extremely small volume and hence the absence of any real discontinuity in the bosonic observables, but we can make rough estimates. The results are presented in table 7.2 and we see that the mean field results are good estimates of the true positions of the phase boundaries.

	Phase Boundary	y_c^{MF}	y_c
$\kappa = 0.04$	PM / FM	0.8	0.6 ± 0.1
	FM / PM	2.6	2.5 ± 0.1
$\kappa = -0.15$	AFM / PM	0.8	0.9 ± 0.1
	PM / AFM	2.4	2.3 ± 0.1

Table 7.1 Comparison of the critical Yukawa couplings at $\kappa = 0.04$ and -0.15 calculated from mean field theory (y_c^{MF}) and from numerical simulations on a 4^4 lattice (y_c).

7.6 The Renormalised Fermion Mass

We now turn our attention to the behaviour of the fermion mass as a function of y for these positive values of κ so we can compare to the quenched results of chapter 5 and look for the the PM1 and PM2 phases in the dynamical model. We have already seen how the dynamical configurations exclude the zero modes from the spectrum of M and hence also from M'. We therefore expect that we will be able to define m_f for all values of y since it was the appearance of small eigenvalues in the quenched crossover region that made it impossible to define m_f from either the fermion propagator or the chiral condensate.

We calculate m_f from the eigenvalue spectrum of M' evaluated on 10 representative spin configurations for each value of κ and y. This was done in exactly the same way as in chapter 5 except that it was necessary to perturb the fermion matrix as described in section 4.5.3 in order to extract the multiplicities of degenerate eigenvalues in the FM phase. The perturbation was made as small as possible whilst still giving N distinct eigenvalues and we took $\Delta = 500$ in eqn. 4.47. The spectra have to be calculated many more times than in the quenched studies since we can no longer shift the eigenvalues of M' along the real axis at will and obtain the correct spectrum for all values of y. Although in practice we initially calculate the spectrum at $y = 0$ for computational simplicity, the only value of y at which the eigenvalues are physically meaningful is the y value used in the dynamical updating. This means that the only *computational* advantage of considering M' rather than M is due to the extra $(\lambda,-\lambda)$ symmetry present in the eigenvalue spectrum and this is not a critical factor when considering so small a lattice. However, it is still necessary to use the M' condensate to define m_f since only this condensate can give a non-zero m_f in the PM phase at large y. The usual condensate $<\bar{\chi}\chi>$ always vanishes in the PM phase and would give a corresponding zero value for m_f.

In fig. 7.7 we plot m_f and the wavefunction renormalisation constant Z evaluated at $\kappa = 0.04$ against y. Fig. 7.7 shows that unlike the quenched model we

can define m_f for all values of y. We are not troubled by the appearance of zero modes in the eigenvalue spectrum so $<\bar{\chi}'\chi'>$ is stable and positive. The errors are therefore small despite the limited data set. As in the quenched studies we see that there are two distinct paramagnetic phases PM1 and PM2. In PM1 the fermion mass is small which we would expect from the perturbative result $m_f = y <\phi>$, whereas in PM2 it is large and increases with y as expected from the large y expression $m_f = y/z$. For intermediate y the system is in the FM phase where m_f, $<\phi>$ and z are all large. The crossover from small y behaviour (where m_f is always less than y) to large y behaviour (m_f always greater than y) occurs around $y = 1.4$.

Fig. 7.7 also shows that the behaviour of Z for small and large y is much as in the quenched case. However, Z is continuous throughout the crossover region and as expected approaches unity at $y = 1.4$ where the system is highly magnetised. As $<\phi> \rightarrow 1$ the Yukawa term becomes a pure mass term and we have a free fermion with $Z = 1$ and $m_f = y$. As y is increased into the PM2 phase the fermions rapidly decouple from the dynamics and we recover the quenched result that $Z \approx 1.6$ independent of y.

In fig. 7.8 we plot m_f and the wavefunction renormalisation constant Z against y evaluated at $\kappa = 0.085$ where the system is always in the FM phase. We see that m_f is non-zero for all values of y and exhibits the expected small and large y behaviour. For $y = 1.4$ the system is almost completely magnetised ($<\phi> = 0.998$) and we find $m_f = y$ and $Z = 1$ with very small error. The fermion dynamics are still important at much larger values of y than at $\kappa = 0.04$ (as is obvious from a comparison of figs. 7.5 and 7.6) and Z continues to increase with y even as far as $y = 4.2$.

If we compare figs. 7.7 and 7.8 we see that as κ is increased across the PM/FM phase boundaries, m_f increases for small y but decreases for large y as in the quenched model. The results show that the small and large y approximations to m_f given by eqns 3.3 and 3.23 are qualitatively correct. To check the quantitative

agreement we first plot $m_f\, zy^{-1}$ against y for $y \geq 1.4$ and $\kappa = 0.04$ in fig. 7.9. This quantity should be exactly one if the first order hopping parameter expansion is valid. Although there are signs of it becoming constant at large y it is far from unity except in the trivial region near $y = 1.4$ where the system is almost free.

At $\kappa = 0.085$, m_f is non-zero for all y and in fig. 7.10 we plot $m_f(y\langle\phi\rangle)^{-1}$ against y for $y \leq 1.4$ and $m_f\, zy^{-1}$ for $y \geq 1.4$. The agreement is reasonable for small y, especially so given that the very small volume of the system will make light fermions particularly susceptible to finite size effects. For large y we see that the hopping parameter expansion gives excellent quantitative agreement. To show that this is not a chance result we performed a simulation at $\kappa = 0.1$ and $y = 4.2$ which gave the result $m_f = 4.510$, $z = 0.927$ and $m_f\, zy^{-1} = 1.00 \pm 0.01$.

7.7 The PM1/PM2 Phase Boundary

The studies at positive κ have shown that m_f can be defined and is continuous for all values of y. However, this is because in the intermediate region of y the system excludes the problematic fermionic zero modes by adopting a highly magnetised FM state. In the quenched studies we were unable to define m_f at the direct PM1 / PM2 boundary due to the presence of small eigenvalues and we wish to see if this problem is still present in the dynamical model when there is no intervening FM phase. We first have to locate the PM1 / PM2 phase transition if indeed it exists. We want to perform simulations at a value of κ where the system does not adopt FM ordering even for $y \approx \sqrt{2}$, but we do not want to take κ so large and negative that we encounter the mixed state seen previously at $\kappa = -0.15$ instead of the PM1 phase that is of interest.

Simulations were performed at $\kappa = -0.04$ with values of y taken between 1.0 and 1.8. The FM phase was never encountered, the maximum value of $\langle\phi\rangle$ being only 0.073 at $y = 1.4$. We can therefore be confident that the system remained in the PM phase throughout and we will be able to ascertain whether the PM1/PM2 phase boundary was crossed by examining the behaviour of the renormalised

fermion mass. The results for m_f and Z are shown in fig. 7.11, taken from 10 configurations separated by 100 sweeps, and there is an obvious signal for a phase transition at $y \approx 1.3$. Although this is the same qualitative conclusion that was reached from the quenched simulations of chapter 5, we have for the first time been able to calculate the fermion mass close to the phase boundary. We now have direct evidence of the PM1/PM2 phase transition rather than having to infer its existence from the different behaviour of m_f in the small and large y regimes.

To obtain a value for the critical Yukawa coupling y_c for the PM1/PM2 phase transition we first remember that, in the language of statistical mechanics, m_f represents the inverse of some correlation length ξ. In general, if some second order phase transition which occurs as a function of a parameter β is well described by mean field theory we expect the correlation length to scale as [70]

$$\xi^{-1}(\beta) \approx \sqrt{(\beta - \beta_c)} \tag{7.14}$$

where β_c is the critical point. We might therefore expect m_f to obey the relation

$$m_f(y) \approx \sqrt{(y - y_c)} \tag{7.15}$$

for y close to the phase boundary on the PM2 side. Motivated by this, we plot m_f^2 against y in fig. 7.12. We see that eqn. 7.15 is very well obeyed and from a straight line fit for $y > y_c$ we estimate $y_c^{PM1/PM2} = 1.30 \pm 0.05$ at $\kappa = -0.04$.

7.7.1 The Eigenvalue Spectrum

Fluctuations in the condensate are slightly larger than in the previous dynamical simulations due to the presence of smaller eigenvalues. However, the fact that we are able to define m_f smoothly across the phase boundary indicates that the very small modes have been excluded from the eigenvalue spectrum throughout the crossover region. Figs. 7.13 to 7.16 show the variation of the eigenvalue spectrum of M as y is increased from 1.2 to 1.5 across the phase transition and confirm this prediction - the spectrum shows the characteristic 'X' shape that we expect at these values of y but there are no eigenvalues at all in the very centre of the distribution. Unlike in the quenched case, the eigenvalues in the full theory are transferring from

the imaginary to the real axis via a path that avoids the origin and this removes the singularities present in the quenched chiral condensate. To illustrate that these conclusions (drawn from the eigenvalues of M) are relevant to the calculation of m_f (from the eigenvalues of M') we plot the chiral condensate evaluated on 10 quenched configurations in the PM phase at $\kappa = 0.04$ for values of y close to the PM1/PM2 boundary in fig. 7.17. The huge fluctuations present in the data and the fact that the condensate can become negative are to be compared with fig. 7.18 where we plot the same quantity in the dynamical model. We see that it is indeed the exclusion of the very small modes of M that makes the dynamical model so much better behaved around $y = \sqrt{2}$.

Given our prior experience of the quenched model on much larger volumes (where we were unable to define m_f from the propagator or the M' condensate in the same range of y) these results lead us to believe that it would also be possible to define m_f from the fermion propagator close to the PM1/PM2 phase transition in the full theory if a large-scale simulation of the dynamical model was performed.

7.8 Use of the Block Algorithm in Dynamical Simulations

We know that the block algorithm will be the most efficient way of inverting the fermion matrix whenever small eigenvalues are present. On the small lattice used in the dynamical simulations it always converges after exactly N/B iterations and hence takes the same time regardless of the matrix under consideration. In contrast the time taken by the single algorithm can vary by over an order of magnitude depending on the eigenvalue spectrum.

It is when the system is in a PM state at intermediate y that the block algorithm will be of most use. The block algorithm was therefore used (with $B = 16$) for all the simulations around the PM1/PM2 phase transition at $\kappa = -0.04$. The reduction in the time taken per sweep compared to the time taken using the single algorithm is shown in table 7.2 and we see that there is a dramatic improvement especially around $y = \sqrt{2}$ (using the block algorithm a sweep always took 9 seconds).

y	Speed up factor
1.0	2.4
1.2	2.8
1.4	4.5
1.6	2.8
1.8	1.7

Table 7.2 The improvement in the time taken per sweep of the lattice achieved by using the block algorithm with $B = 16$ compared to $B = 1$. Data is taken from simulations on a 4^4 lattice at $\kappa = -0.04$.

For positive κ there are never any small eigenvalues present in the spectrum of M and we always use the single algorithm for inversion. The single algorithm is faster at small y since the fermion matrix is almost free, and also at large y where all the eigenvalues become large. At intermediate y the fermion dynamics intervene and the system adopts a highly magnetised FM state which again means that there are no small eigenvalues.

The only problem with the block algorithm was due to the very small size of the lattice. It is always possible that one of the solution vectors in the block solution will converge before the final iteration (iteration 16 in our case). This is not a problem when the convergence is gradual, but on the small 4^4 lattice used in the dynamical simulations convergence is always very sudden since exact orthogonality of the Lanczos vectors is maintained throughout. If all the solutions converge prematurely then the algorithm will terminate properly , but if one or more solutions converge early at iteration i then this introduces some very small diagonal elements into the matrix β_i and the algorithm fails at the point where the inversion of β_i is attempted.

It was found that the solution vectors tend to converge prematurely whenever there is a degeneracy in the eigenvalue spectrum of M. In the $Z(2)$ model this is

synonymous with the system being in a highly magnetised state where the single inversion algorithm is preferable, so it is not a major problem. However, some degeneracy can always appear even in the PM phase especially with such a small lattice and occasionally (typically once every 400 sweeps) the block algorithm did indeed fail. It would in principle be possible to reduce the block size at this point so that the block solution contains only those solution vectors that have not converged and continue the algorithm with a smaller value of B. However, this turns out to be very difficult in practice and the solution we adopt is simply to perform the required inversion with B= 1.

The block algorithm fails most frequently precisely in those regions where we would not wish to use it anyway. The fact that it fails at all is due to the extremely small lattice volume and the degenerate eigenvalues that arise due to the discrete nature of the Ising spins. The numerical studies close to the PM1/PM2 phase boundary were only possible through the use of the block Lanczos algorithm and its very occasional failure was a minor problem.

7.9 Conclusions

Although the general phase structure of the $Z(2)$ model for positive κ was never in doubt, there was doubt as to the behaviour for large negative κ. Our results point to the correct phase structure being that of ref [58] with the PM phase perhaps extending to $\kappa = -\infty$ at some value of y close to 1.4.

Our studies of the renormalised fermion mass m_f (defined in terms of the chiral condensate calculated from the $Z(2)$ invariant fermion matrix M') have shown that the small and large y behaviour are the same as the quenched model. However, the fact that m_f cannot be defined for a large range of intermediate values of y in quenched simulations has been shown to be due to a complete breakdown of the quenched approximation due to the appearance of very small fermionic eigenvalues. The dynamical system does not exhibit these small modes near $y = \sqrt{2}$ in either the PM or FM phases and as a result m_f can be defined for all values of y. Small and

large y expansions for m_f have been shown to be qualitatively valid in the appropriate regions of the phase plane and are quantitatively accurate whenever the system is in the FM phase for large y. We have been able to distinguish the PM1 and PM2 phases (occurring at small and large y respectively) from whether m_f increases or decreases as κ is increased across the PM/FM phase boundary. We have shown that there is a direct PM1/PM2 phase transition in the full theory and that m_f exhibits smooth behaviour across the phase boundary. At $\kappa = -0.04$ we find a critical Yukawa coupling y_c for this transition of $y_c = 1.30 \pm 0.05$, and we expect y_c to be very weakly dependent on κ. The proposed phase diagram is shown in fig. 7.19.

These studies have shown that as well as giving valuable qualitative information on the fermionic behaviour of dynamical systems, looking at the eigenvalue spectrum is a useful means of obtaining results for the fermion mass m_f on very small volumes where its definition via the fermion propagator is inapplicable. We believe that the same results would be obtained if m_f were calculated in this conventional way on much larger lattices since it was found in the large volume quenched studies that there is qualitative agreement between the two definitions. More importantly, it was found that both definitions break down in the same regions of the phase plane and we therefore expect that the propagator will fit to some free propagator for all values of y in the full theory on a large volume.

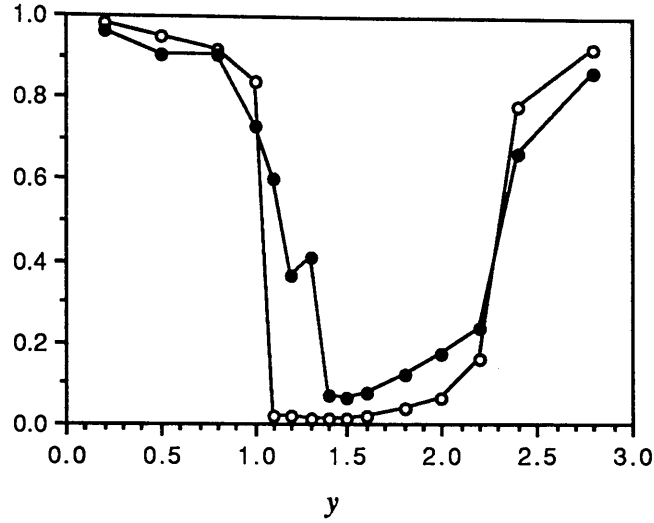

Fig. 7.1 The values of relevant bosonic observables vs.Yukawa coupling y at $\kappa = -0.15$. Data taken from a 4^4 lattice with 2 species of dynamical fermion with antiperiodic boundary conditions in time.
(o) $\langle\phi_{st}\rangle$, (•) $-z^2$.

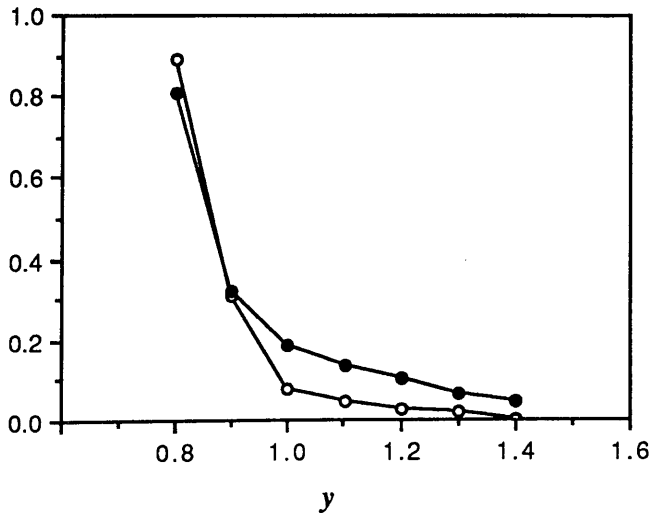

Fig. 7.2 The values of relevant bosonic observables vs.Yukawa coupling y at $\kappa = -0.15$. Data taken from a 4^4 lattice with 2 species of dynamical fermion with antiperiodic boundary conditions in all directions.
(o) $\langle\phi_{st}\rangle$, (•) $-z^2$.

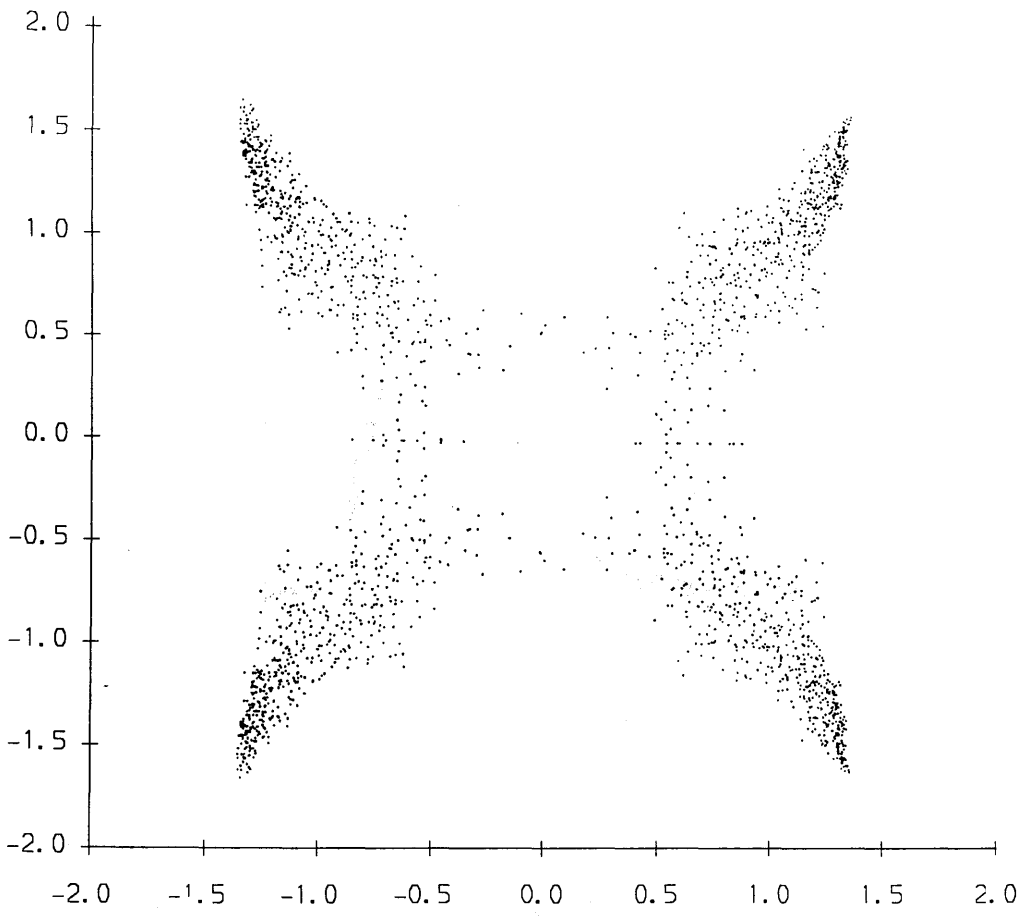

Fig. 7.3 The eigenvalue spectrum of M in the complex plane for a 4^4 lattice. Data taken at $\kappa = -0.15$ with two species of dynamical fermion with antiperiodic boundary conditions in time. Yukawa coupling $y = 1.4$.

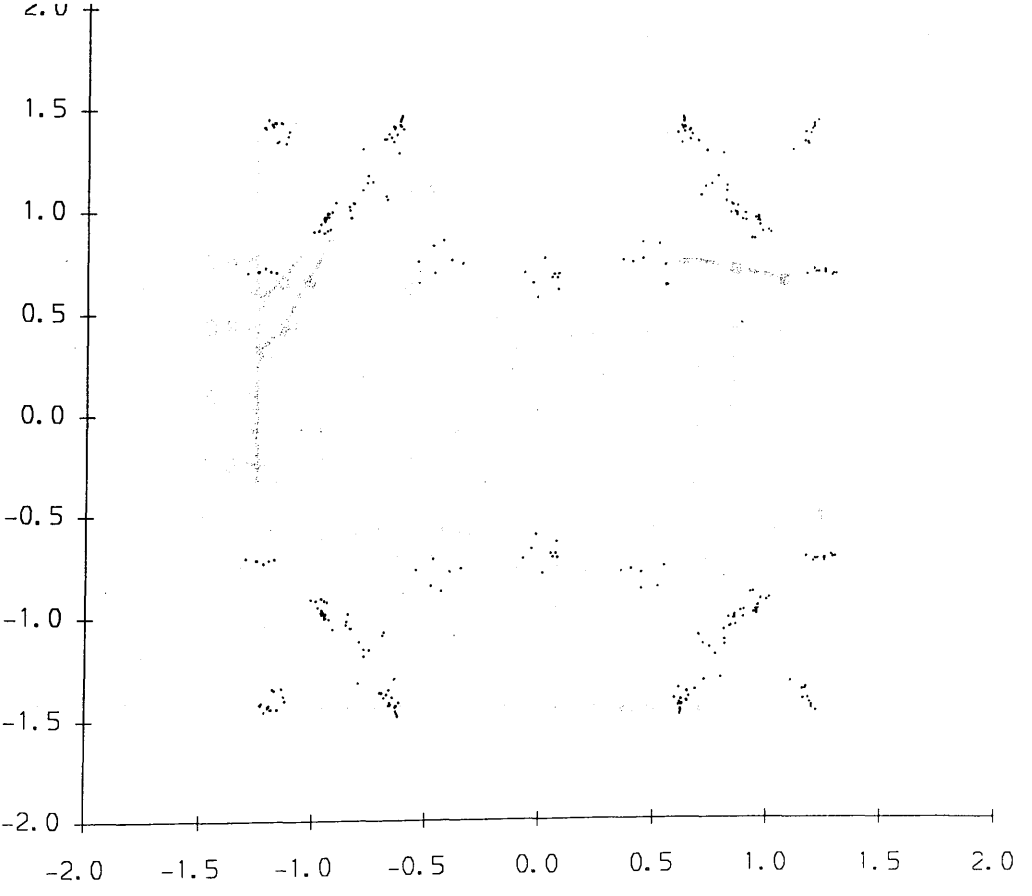

Fig. 7.4 The eigenvalue spectrum of M in the complex plane for a 4^4 lattice. Data taken at $\kappa = -0.15$ with two species of dynamical fermion with antiperiodic boundary conditions in time. Yukawa coupling $y = 1.3$.

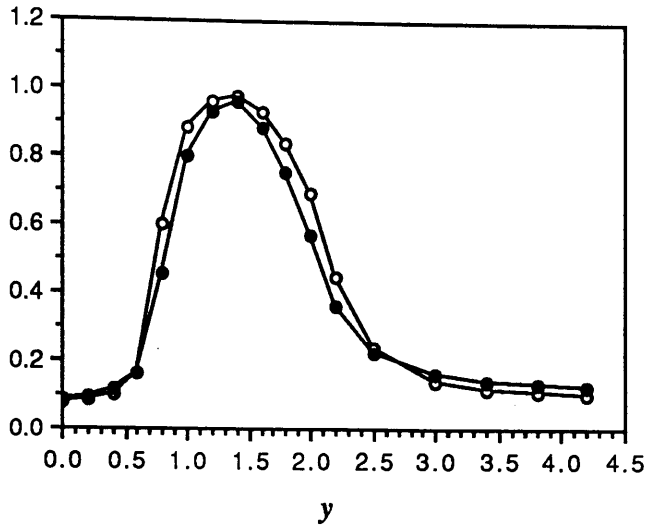

Fig. 7.5 The values of relevant bosonic observables vs.Yukawa coupling y at $\kappa = 0.04$. Data taken from a 4^4 lattice with 2 species of dynamical fermion with antiperiodic boundary conditions in time.
(o) $\langle\phi\rangle$, (•) z^2.

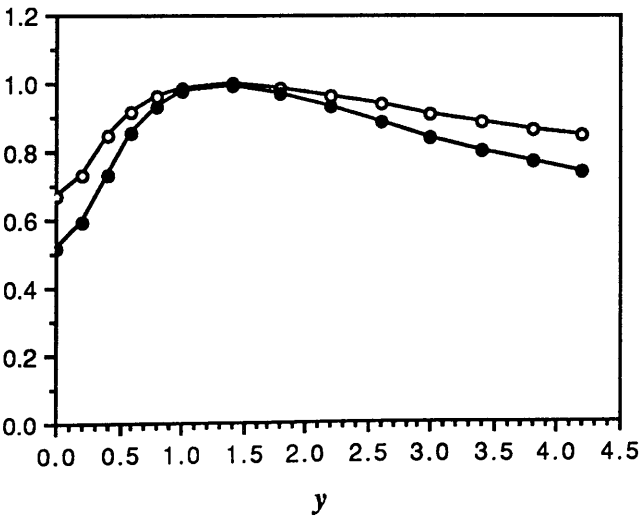

Fig. 7.6 The values of relevant bosonic observables vs.Yukawa coupling y at $\kappa = 0.085$. Data taken from a 4^4 lattice with 2 species of dynamical fermion with antiperiodic boundary conditions in time.
(o) $\langle\phi\rangle$, (•) z^2.

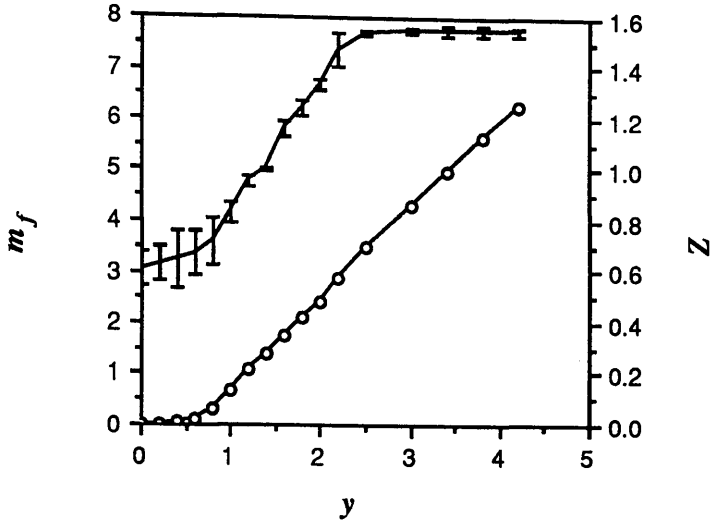

Fig. 7.7 The fermion mass m_f and the fermion renormalisation constant Z vs. Yukawa coupling y at $\kappa = 0.04$. Data taken from a 4^4 lattice with 2 species of dynamical fermion with antiperiodic boundary conditions in time. (o) m_f, (I) Z.

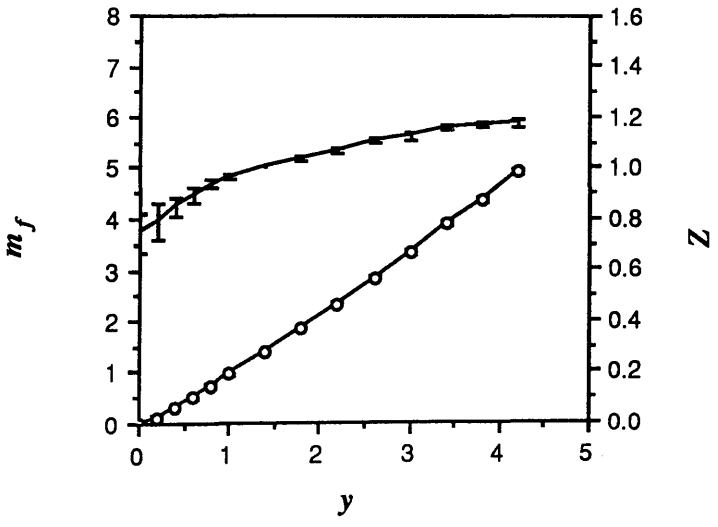

Fig. 7.8 The fermion mass m_f and the fermion renormalisation constant Z vs. Yukawa coupling y at $\kappa = 0.085$. Data taken from a 4^4 lattice with 2 species of dynamical fermion with antiperiodic boundary conditions in time. (o) m_f, (I) Z.

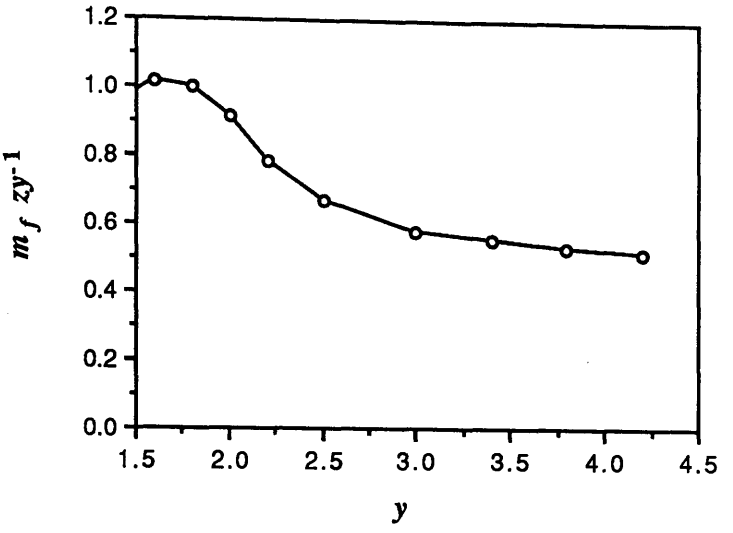

Fig. 7.9 The combination $m_f\, zy^{-1}$ against y at $\kappa = 0.04$. This quantity should appoach unity at large y if the large y expression for m_f is valid.

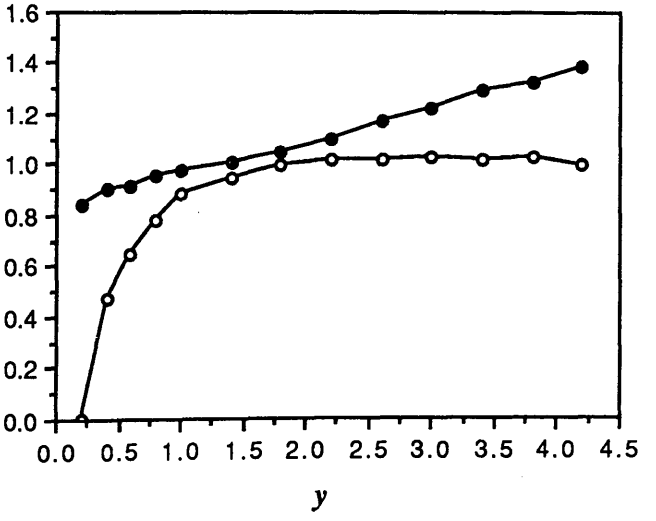

Fig. 7.10 The combinations $m_f(y\langle\phi\rangle)^{-1}$ and $m_f\, zy^{-1}$ against y at $\kappa = 0.085$. These should approach unity at small and large y respectively if the perturbative and large y expressions for m_f are valid.
(•) $m_f(y\langle\phi\rangle)^{-1}$, (o) $m_f\, zy^{-1}$.

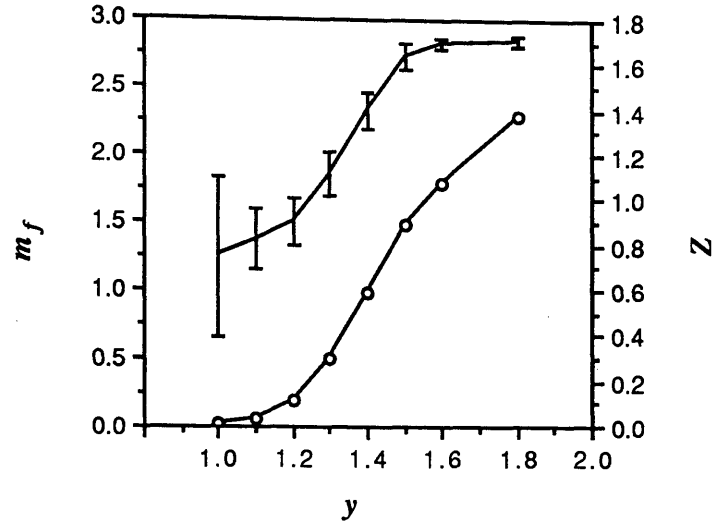

Fig. 7.11 The fermion mass m_f and the fermion renormalisation constant Z vs. Yukawa coupling y at $\kappa = -0.04$. Data taken from a 4^4 lattice with 2 species of dynamical fermion with antiperiodic boundary conditions in time. (o) m_f, (|) Z.

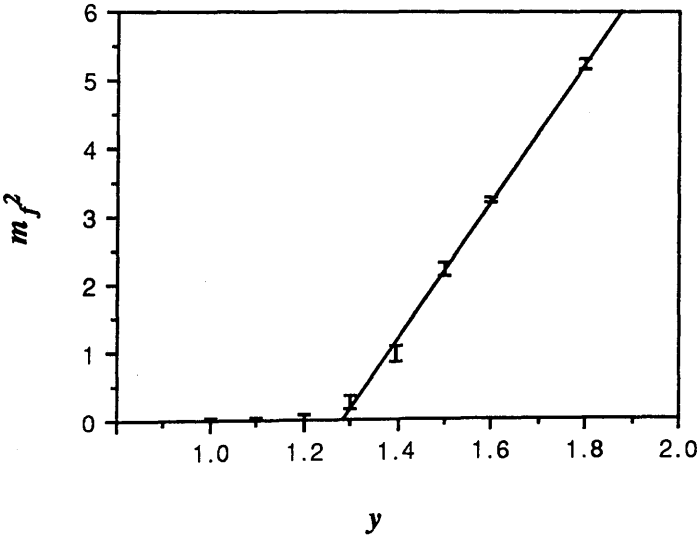

Fig. 7.12 The square of the fermion mass vs. Yukawa coupling y at $\kappa = -0.04$. Straight line fit is $m_f^2 = 10.17 \times (y - 1.29)$.

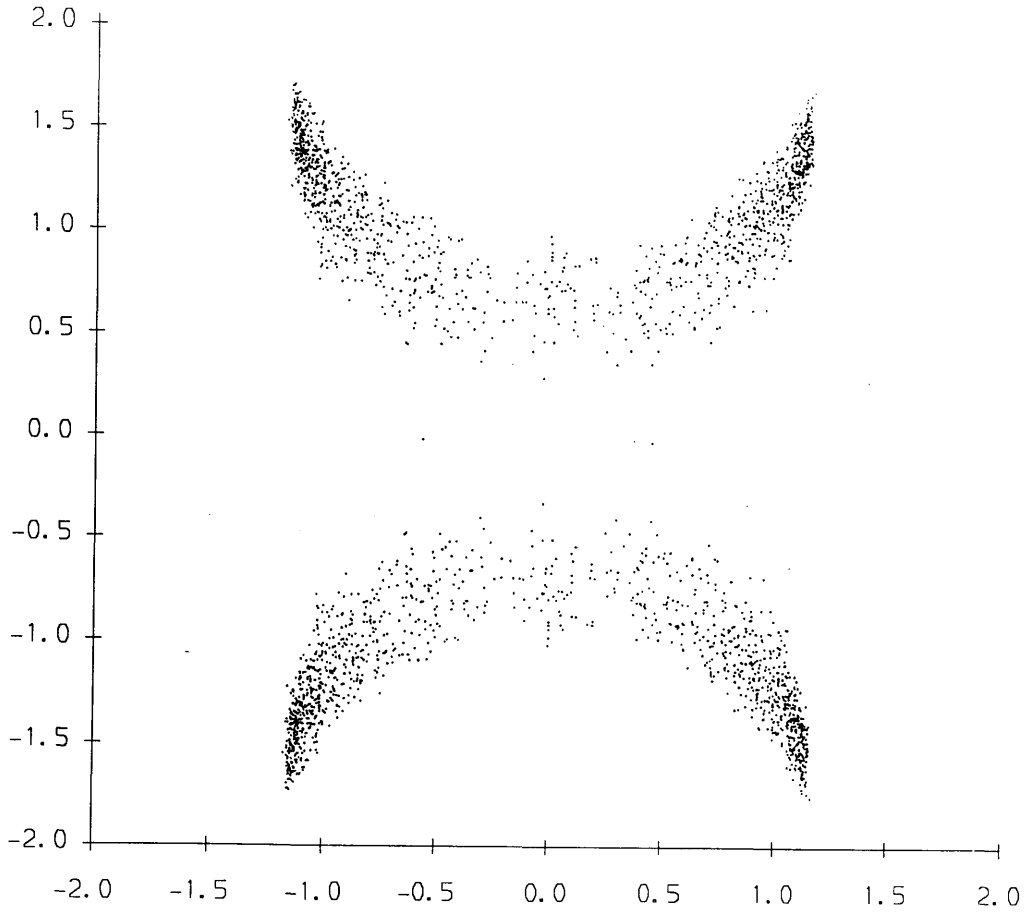

Fig. 7.13 The eigenvalue spectrum of M in the complex plane for a 4^4 lattice. Data taken at $\kappa = -0.04$ with two species of dynamical fermion with antiperiodic boundary conditions in time. Yukawa coupling $y = 1.2$.

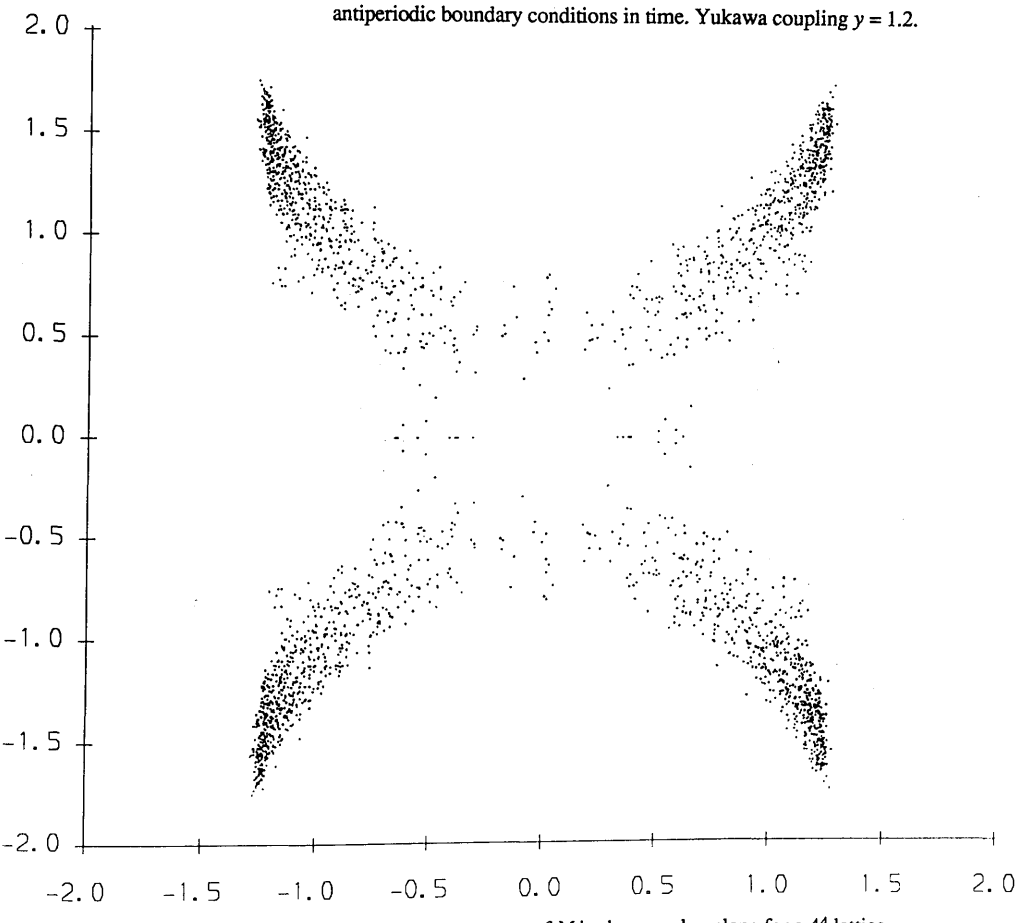

Fig. 7.14 The eigenvalue spectrum of M in the complex plane for a 4^4 lattice. Data taken at $\kappa = -0.04$ with two species of dynamical fermion with antiperiodic boundary conditions in time. Yukawa coupling $y = 1.3$.

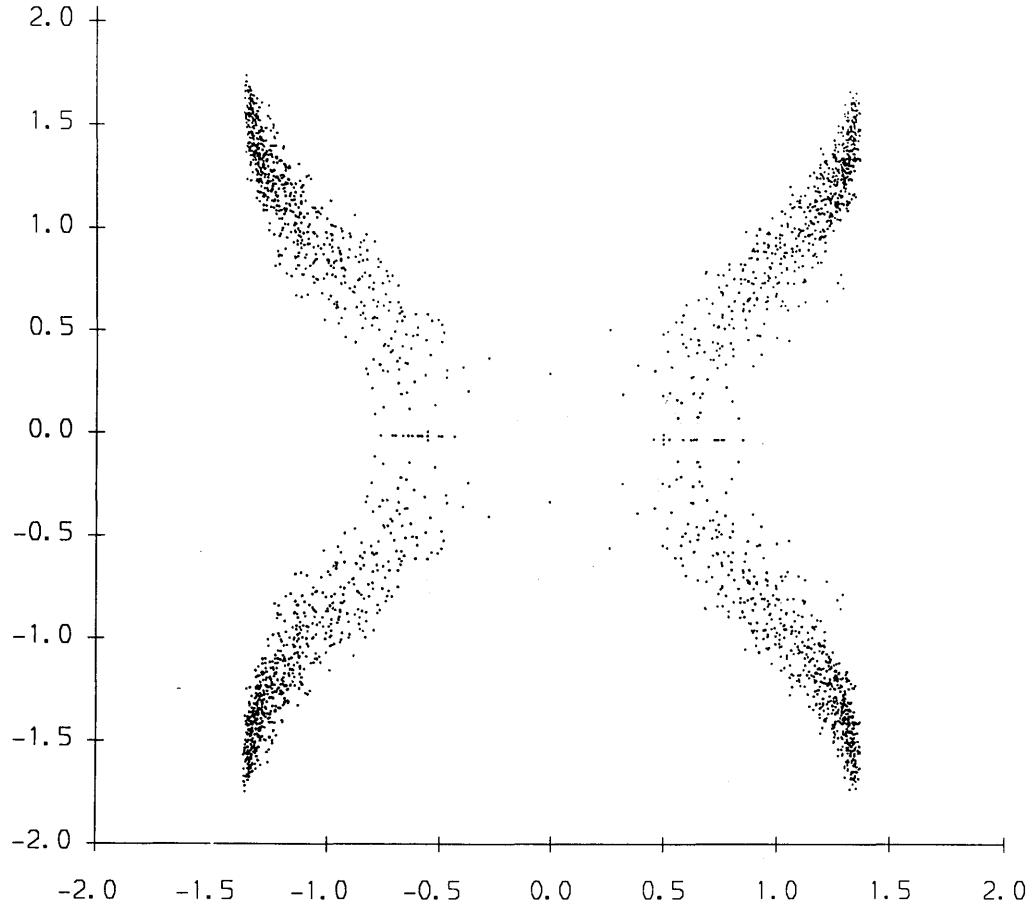

Fig. 7.15 The eigenvalue spectrum of M in the complex plane for a 4^4 lattice. Data taken at $\kappa = -0.04$ with two species of dynamical fermion with antiperiodic boundary conditions in time. Yukawa coupling $y = 1.4$.

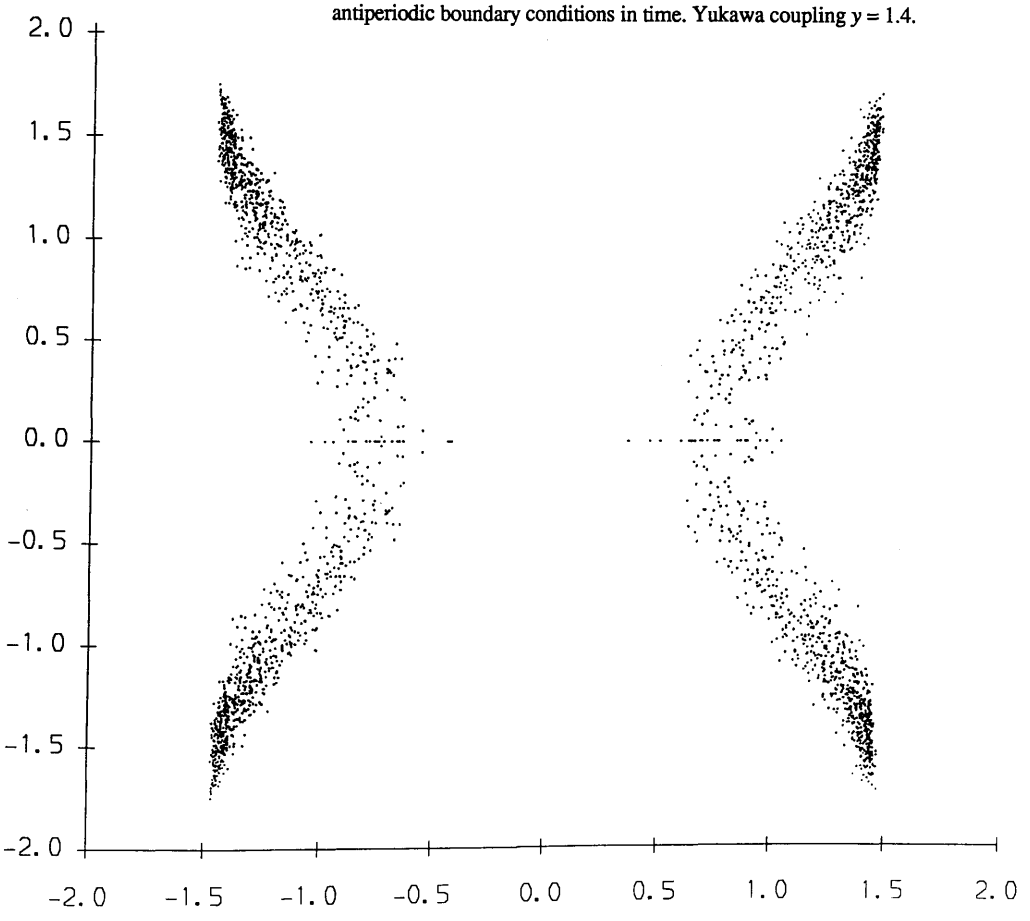

Fig. 7.16 The eigenvalue spectrum of M in the complex plane for a 4^4 lattice. Data taken at $\kappa = -0.04$ with two species of dynamical fermion with antiperiodic boundary conditions in time. Yukawa coupling $y = 1.5$.

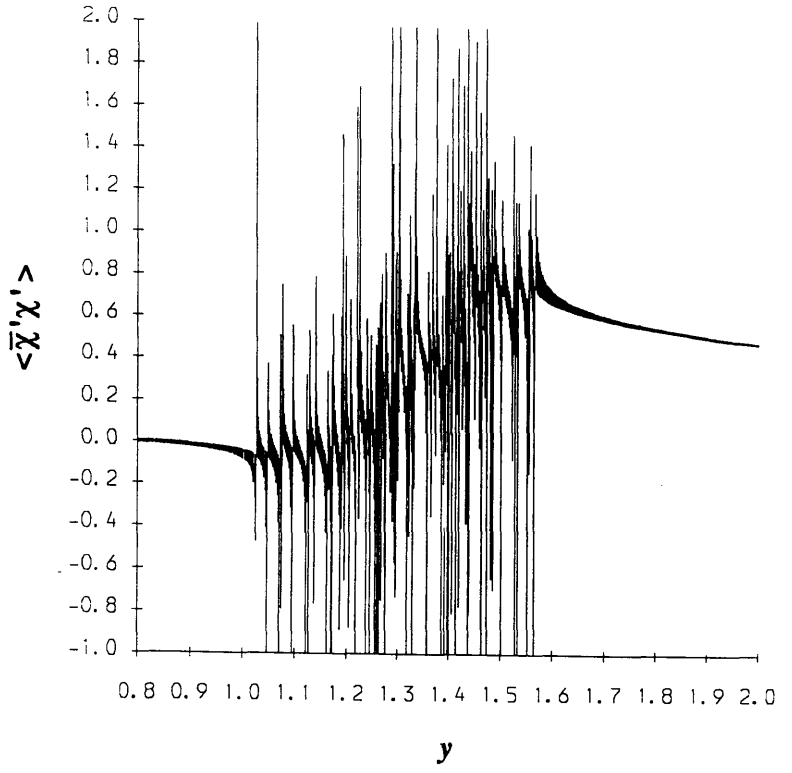

Fig. 7.17 The primed chiral condensate vs. Yukawa coupling y averaged over 10 quenched PM configurations generated at $\kappa = 0.04$.

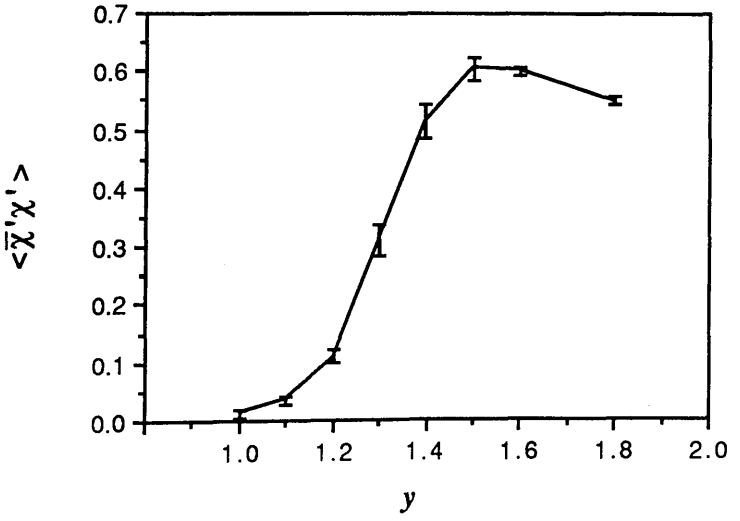

Fig. 7.18 The primed chiral condensate vs. Yukawa coupling y averaged over 10 dynamical PM configurations generated at $\kappa = -0.04$.

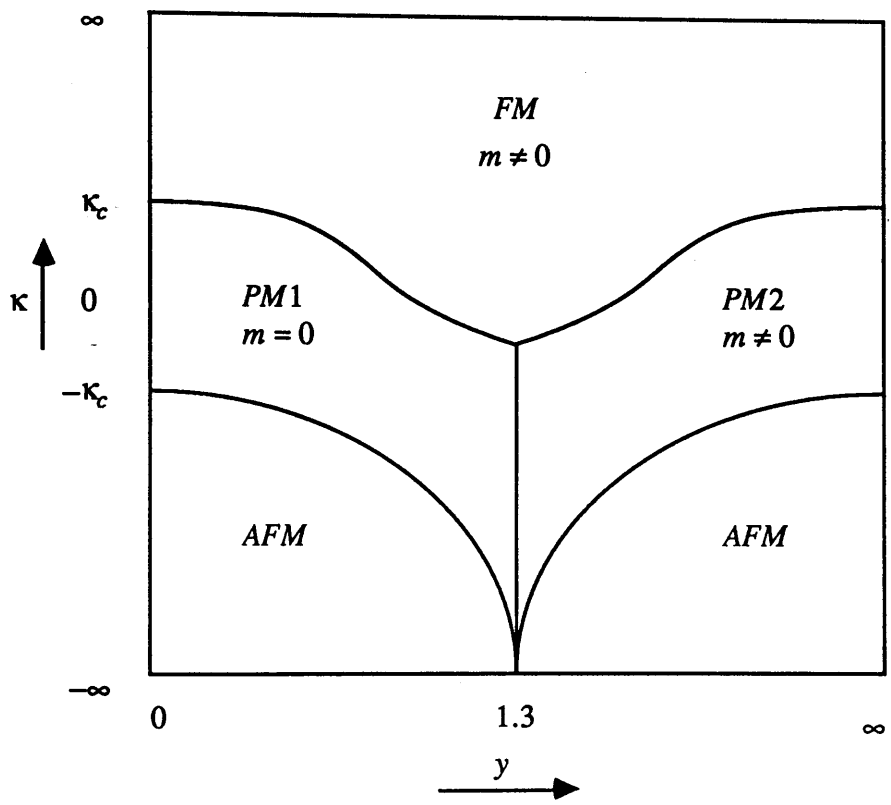

Fig. 7.19 The phase diagram of the dynamical $Z(2)$ model defined with local Yukawa coupling y showing the behaviour of the fermion mass m. Our numerical studies suggest that the PM1/ PM2 phase boundary lies at $y = 1.3$ and extends from $\kappa = -\infty$ at least as far as $\kappa = -0.04$.

Chapter 8

Conclusion

We have shown that by studying the eigenvalue spectrum of the staggered fermion matrix M it is possible to make useful qualitative statements about the fermionic behaviour of lattice systems from only a few configurations. For the specific case of a $Z(2)\times Z(2)$ scalar-fermion system with local Yukawa coupling y we were able to clearly differentiate between the weak and strong coupling regimes from the distribution of the eigenvalues in the complex plane on 6^4 lattices. The same spectra clearly showed whether the system was in a chirally symmetric or broken phase. It was also shown that numerical problems that have been encountered by other authors at intermediate y are due to the appearance of very small eigenvalues in M. Using the same methods we clarified why the alternative hypercubic formulation of the Yukawa interaction term removes the singular behaviour seen in the quenched model defined with local Yukawa coupling.

Although the eigenvalues of M yield qualitatively very useful information it was shown that a consistent quantitative definition of the renormalised fermion mass m_f from the eigenvalues of M is problematic because M is not invariant under the $Z(2)$ symmetry of the bosonic action. Performing a transformation on the fermion fields, we defined a new fermion matrix M' that is $Z(2)$ invariant. By associating a non-zero value of the M' chiral condensate with the generation of a finite mass for the fermions we were immediately able to explain the behaviour of m_f in all regions of the quenched phase diagram from very limited studies on an 8^4 lattice. We were further able to obtain numerical values for m_f by performing much more extensive studies on a $6^3\times 12$ lattice. Our results were in good agreement with data obtained by other authors who define m_f in the conventional manner from the fermion propagator. However, our method requires far less computation in the quenched approximation and will also be applicable on much smaller volumes.

On large volumes it is not feasible to compute all the eigenvalues of the fermion matrix. However, it was shown that useful information can be gained by studying only the small eigenvalues of $M^\dagger M$ on lattices of varying size up to a maximum volume of 14^4. We have shown that the existence of small eigenvalues of M on finite systems implies that, in the quenched infinite volume limit, M will have exact zero modes for values of y between 1.3 and 1.4 regardless of whether the scalar field is in a symmetric (PM) or magnetised (FM) phase. We have also shown that these eigenvalues appear with a non-vanishing density. The fact that zero modes exist at some y throughout the FM phase of the $Z(2)$ model is a major difference between it and other related models. For example, the $SU(2)_L \times SU(2)_R$ model of ref. [53] exhibits the same behaviour as the $Z(2)$ model in the PM phase but has no zero modes at all in the FM phase.

We have performed full dynamical studies on a small 4^4 lattice and have been able to map out the phase diagram in several important regions. We have demonstrated the validity of various mean field results for the positions of the phase boundaries derived in ref. [58]. Our most important result is that a PM phase exists (for values of y close to 1.4) for all values of the scalar field hopping parameter κ less than -0.04. By using the methods of calculating m_f that were developed and checked in the quenched approximation we have shown that, as in the quenched model, this PM phase is split into two regions PM1 and PM2. In PM1 the fermions are massless, whereas in PM2 they spontaneously acquire a mass despite the fact that the scalar field has zero expectation value. Close to the phase boundary we have shown that m_f scales with mean field exponents and we have calculated the critical Yukawa coupling for the PM1/PM2 phase transition as $y_c = 1.30 \pm 0.05$ at $\kappa = -0.04$. By computing the eigenvalue spectrum of M on dynamical configurations generated close to y_c we have shown that the effect of the inclusion of closed fermion loops is to exclude the small modes from M. It is this feature of the fermion dynamics that makes the full theory so much better behaved than the quenched theory in the region of intermediate y.

The existence of a PM2 phase is very important in models where Wilson-Yukawa couplings are used to give the unwanted doubler fermions a large mass and decouple them from the theory. In the continuum limit $<\phi> \rightarrow 0$, and it might seem that it is impossible to give the doublers a mass of order the cutoff using the Higgs mechanism. However, if the continuum limit is taken at the FM/PM2 phase boundary (from within the FM region) it is possible to arrange for the doublers to acquire a large mass whilst leaving the physical fermions light by choosing the Yukawa and Wilson-Yukawa couplings appropriately [42]. This is because, as we have seen in the $Z(2)$ model, the PM2 phase is a non-perturbative region where the fermion mass need not vanish as the magnetisation goes to zero.

These studies have again shown the value of the Lanczos algorithm in lattice field theory. It was only through the use of the non-hermitian and hermitian Lanczos algorithms that the small and large volume studies of the fermionic eigenvalues were possible. In addition, the block Lanczos algorithm has been shown to be the most efficient method of inverting the Kogut-Susskind fermion matrix. In the dynamical studies of the $Z(2)$ scalar-fermion model the use of the block form of the algorithm was seen to result in a reduction by a factor larger than 4 in the time taken per sweep of the lattice in regions where very small eigenvalues were present in M.

There are many possibilities for further application of the techniques developed in this thesis. Firstly it would be interesting to examine the dynamical $Z(2)$ model defined with hypercubic Yukawa coupling. This model has the interesting feature that the introduction of fermion dynamics produces a new phase of simultaneous ferromagnetic and antiferromagnetic bosonic order that is not observed in the quenched model. The existence of this ferrimagnetic state at large y and large negative κ is presumably due to the competition between the fermionic and bosonic actions which tend to align and anti-align neighbouring bosonic fields respectively. A study of the eigenvalue spectrum of M in this phase might well clarify the precise reasons for its existence.

Secondly, it would be desirable to perform a much more extensive exploration of the phase diagram of the dynamical $Z(2)$ model with local coupling. We have only been able to do very limited studies (with the number of staggered fermion species n_f always equal to 2) due to the need to perform an entirely separate numerical simulation for each value of κ, y and n_f. However, a technique exists that allows the positions of the phase boundaries to be determined from a single simulation at a given κ without the need to sweep in y or n_f. The procedure is to use the Lanczos algorithm to calculate the complex eigenvalues of M at some arbitrary value of the Yukawa coupling y_0. It is then possible to calculate the value of $det(M)^{n_f}$ analytically for all values of y by expanding it about y_0 in powers of $(y - y_0)$. Knowledge of the eigenvalues allows us to determine the coefficient C_n in front of the term $(y - y_0)^n$. After averaging over a sufficient number of configurations such that the C_n are known to some desired accuracy we can then calculate the (in generally complex) zeroes of this polynomial of degree $N+1$. A real root implies that the determinant will vanish at some real value of y and hence the partition function will be zero at this point in the phase plane (we see from eqn. 4.7 that $Z = < det(M)^{n_f} >$, where the average is a quenched one). We can than use the powerful theorems of Lee and Yang [65] to identify this as a phase transition point and to investigate its properties. A very similar approach has been used successfully in studies of QCD at finite chemical potential μ [66, 67] where the expansion parameter is $exp(\mu)$.

Initial studies have shown some promising results with there being some signs of real roots of the determinant at the expected values of y. However, the major conclusion of these preliminary investigations is that it will be necessary to perform dynamical updating at some values $y = y_0$, $n_f = n_{f0}$ close to the phase transition of interest in order to eliminate the large fluctuations in the values of C_n that occur when quenched configurations are used. These fluctuations are caused by the huge variation in the possible values of the eigenvalues and especially by the appearance of very small modes of M. We have already seen how the inclusion of fermion

dynamics removes these small modes and hopefully it will allow the C_n to be determined to very high accuracy. It is important to note that although we may produce dynamical configurations at some particular values of y and n_f we are still able to expand the value of the determinant for arbitrary values of these parameters. We can therefore locate all the phase transitions in the (n_f, y) plane for a given value of κ, although we would expect the errors to be smallest for those transitions happening close to the point (n_{f0}, y_0).

Finally, there are other lattice models where an investigation of the eigenvalue spectrum of M would clarify certain points. One example is a model which attempts to decouple the unwanted doublers present in the naive fermion formulation by coupling the fermions to a scalar field $z_\mu(n)$ which has a Gaussian distribution with dispersion σ. The coupling is via a formally irrelevant second derivative term much like the Wilson term of eqn. 1.26 and we see immediately that this has parallels with the use of Wilson-Yukawa couplings in lattice Higgs systems. This model was studied by Bernaschi *et al.* [68] and the feature that is of interest to us is that they find a very sudden increase in the number of conjugate gradient iterations required to invert the fermion matrix as σ is increased from 0.1 to 1.0. This interval in σ separates the small σ region where species doubling is observed from the large σ region where the doublers seem to be localised and hence very massive. In addition, within this interval they are unable to define the fermion mass from the propagator. This is remarkably similar to the behaviour seen around $y = 1.4$ in the $Z(2)$ scalar-fermion model and we therefore expect that the fermion matrix is developing small eigenvalues in this region. Some studies of the eigenvalues (and eigenvectors) of M for this model have already been performed by Weingarten and Velikson [69]. However, they only consider the eigenvalues on small 2-d systems of size 20×20. Our experience with the $Z(2)$ model would allow us to investigate much larger lattices and perhaps make the origins of the crossover behaviour around $\sigma = 0.1 \rightarrow 1.0$ more clear.

References

[1] R.P. Feynman and A.R.Hibbs, *Quantum Mechanics and Path Integrals* (McGraw-Hill 1965)

[2] K.G. Wilson, Phys. Rev. D10 (1974) 2445

[3] H.B. Nielsen and M. Ninomiya, Nucl. Phys. B193 (1981)173

[4] K.G. Wilson in *New Phenomena in Subnuclear Physics*, ed. A. Zichichi (Plenum 1977)

[5] N. Kawamoto, Nucl. Phys. B190 (1981) 617

[6] L. Susskind, Phys. Rev. D10 (1977) 3031

[7] N. Kawamoto and J. Smit, Nucl. Phys. B192 (1981) 100

[8] J. P. Gilchrist *et al.*, Nucl. Phys. B248 (1984) 29

[9] N. Metropolis, A.W. Rosenbluth, A.M. Teller and E. Teller, J. Chem. Phys. 21 (1953) 1087

[10] J. Polonyi and H.W. Wyld, Phys. Rev. Lett. 51 (1983) 2257

[11] S. Duane *et al.*, Phys. Lett. B195 (1987) 216

[12] I. M. Barbour *et al.*, J. Comp. Phys. 68 (1987) 227

[13] R. Gupta, Nucl. Phys. B (Proc. Suppl.) 4 (1988) 562

[14] D.S. Scott, *Sparse Matrices and their Uses*, ed. I.S. Duff (Academic Press, New York, 1981)

[15] D. O'Leary, Lin. Algebra and Appl. 29 (1980) 63

[16] M. Hestenes and E. Stiefel, J. Res. Nat. Bur. Stand. 49 (1952) 409

[17] W.H. Press, B.P. Flannery, S.A. Teukolsky, and W.T. Vetterling, *Numerical Recipes - The Art of Scientific Computing* (Cambridge University Press 1986) p. 302.

[18] C. Lanczos, J. Res. Nat. Bur. Stand. 45 (1952) 409

[19] I. M. Barbour *et al.*, *The Recursion Method and its Applications* (Springer-Verlag 1985)

[20] A. S. Householder in *The Theory of Matrices in Numerical Analysis* (Blaisdell, New York, 1964) p. 139;
C. Paige and M. Saunders, Siam J. Numer. Analysis 12 (1975) 617
A. N. Burkitt and A. C. Irving, Phys. Lett. B205 (1988) 69

[21] G. R. Katz *et al.*, Phys. Rev. D37 (1988)

[22] L. A. Hagemann and D. M. Young, *Applied Iterative Methods* (Academic Press, New York, 1981) p. 33

[23] J. F. McCarthy, Phys. Rev. D40 (1989) 2149

[24] J. Smit and J. C. Vink, Nucl. Phys. B286 (1987) 485

[25] K. C. Bowler *et al.*, Nucl. Phys. B240 (1984) 213

[26] I. M. Barbour *et al.*, *Lattice Gauge Theory, A Challenge in Large-Scale Computing* (Plenum 1986) p.89

[27] S. L. Glashow, Nucl. Phys. 22 (1961) 579;
A. Salam in *Elementary Particle Theory*, ed. N. Svartholm (Amqvist and Wiksell, Stockholm 1968);
S. Weinberg, Phys. Lett 19 (1967) 1264

[28] P. W. Higgs, Phys. Lett. 12 (1964a) 132

[29] J. F. Gunion, H. E. Huber, G. L. Kane and S. Dawson, *The Higgs Hunters Guide*, University of California Davis preprint UCD-89-4

[30] E. S. Abers and B. W. Lee, Phys. Rep. 9C (1973) 1

[31] D. Baillin and A. Love, *An Introduction to Gauge Field Theories* (Adam Hilger, 1986) p. 233

[32] G. Arnison *et al.*, Phys. Lett. B122 (1983) 103;
M. Banner *et al.*, Phys. Lett. B122 (1983) 476;

[33] J. Smit, *Standard Model and Chiral Gauge Theories on the Lattice*, talk presented at the International Conference Lattice '89, Capri Sept. 1989, to be published in Nucl. Phys. B (Proc. Suppl.)

[34] A. Hasenfratz, *The Standard Model - From Action to Answers*, talk given at the TASI-89 Summer School, Boulder Co., Jun 4-30 1989

[35] J. Smit, Acta Phys. Polon. B17 (1986) 531

[36] G. Parisi, *Statistical Field Theory* (Addison-Wesley 1988) p. 35

[37] A. Hasenfratz and T. Neuhaus, Phys. Lett. B220 (1989) 435

[38] D. Stephenson and A. Thornton, Phys. Lett. B212 (1988) 479

[39] D. Stephenson and A. Thornton, Phys. Lett. B214 (1988) 577

For a review of other work see J. Jersak, *Lattice Studies of the Higgs System* (DESY preprint 89-115), review talk given at the INFN Eloisatron Project Workshop on Higgs Particles, Erice, Italy Jul. 15-26 1989

[40] I-H Lee, J. Shigemitsu and R.E. Shrock, Nucl. Phys. B334 (1990) 265

[41] Y. Cohen, S. Elitzur and E. Rabinovici, Phys. Lett. B104 (1981) 289

[42] W. Bock *et al.*, DESY preprint DESY-90-030

[43] I-H Lee, J. Shigemitsu and R.E. Shrock, Nucl. Phys. B330 (1990) 225

[44] A. Hasenfratz, University of Arizona preprint AZPH-TH/89-74

[45] For a discussion of the relationship between the Ising model and continuum scalar field theory see A.M. Polyakov, *Gauge Fields and Strings* (Harwood Academic 1989) p. 5-11

[46] D.S. Gaunt, M.F. Sykes and S. McKenzie, J. Phys. A12 (1979) 871

[47] J. Berlin, A. Hasenfratz, M.U. Heller and M. Klomfass, Florida State University preprint FSU-SCRI-90-15

[48] M. Luscher and P. Weisz, Nucl. Phys. B290 (1987) 25;
Nucl. Phys. B295 (1988) 65;
Nucl. Phys. B318 (1989) 705

[49] L. A. Hagemann and D. M. Young, *Applied Iterative Methods* (Academic Press, New York, 1981) p.15

[50] I. Montvay, G. Munster and U. Wolff, Nucl. Phys. B305 (1988) 143;
U. Wolff, Phys. Lett. B228 (1989) 379

[51] P.E. Gibbs, Ph.D. thesis, University of Glasgow (1985)

[52] J. Cullum and R.A. Willoughby, *A QL Algorithm for Complex Symmetric Tridiagonal Matrices*, IBM Research Report 1984;

W.H. Press, B.P. Flannery, S.A. Teukolsky, and W.T. Vetterling, *Numerical Recipes - The Art of Scientific Computing* (Cambridge University Press 1986) p. 360

[53] I.M. Barbour, W. Bock, C.T.H. Davies, A.K. De, D. Henty, J. Smit and T. Trappenberg, preprint Julich HLRZ-90-42, Glasgow GUPTA/90/5-1

[54] S. Aoki, I-H Lee, D. Mustaki, J. Shigemitsu and R.E. Shrock, preprint ITP-SB-89-93

[55] D. Henty, R. Setoodeh and C.T.H. Davies, Nucl. Phys. B337 (1990) 487

[56] S. Aoki, I-H Lee, J. Shigemitsu and R.E. Shrock, Phys. Lett. B243 (1990) 403

[57] J. Kuti, Nucl. Phys. B (Proc. Suppl.) 9 (1989) 55

[58] M.A. Stephanov and M.M. Tsypin, Moscow State University Lebedev Institute preprint LEBEDEV-89-184

[59] M.Rafiq, Ph.D. thesis, University of Glasgow (1987)

[60] J. Cullum and R.A. Willoughby, J. Comp. Phys. 44 (1981) 329

[61] A. Jennings, *Matrix Computation for Engineers and Scientists* (Wiley, New York) p.281

[62] S. Hands, *The Chiral condensate and Topology in SU(2) Lattice Gauge Theory*, presented at the International Symposium Lattice '88, Batavia, IL. Sep 22-25 1988

[63] S. Hands, J.B. Kogut and E. Dagotto, Nucl. Phys. B333 (1990) 551

[64] A. Hasenfratz, W. Liu and T. Neuhaus, Phys. Lett. B236 (1990) 339

[65] C.N. Yang and T.D. Lee, Phys. Rev. D87 (1952) 404

[66] I.M. Barbour, C.T.H. Davies and Z. Sabeur, Phys. Lett. B215 (1988) 567

[67] I.M. Barbour and Z. Sabeur, Nucl. Phys. B342 (1990) 269

[68] M. Bernaschi, S Cabasino, E Marinari and R. Sarno, University of Rome preprint ROM2F-89-009

[69] D. Weingarten and B. Velikson, Nucl. Phys. B270 (1986) 10

[70] G. Parisi, *Statistical Field Theory* (Addison-Wesley 1988) p.39